The University of Nottingham

Thesis submitted to the University of Nottingham for the degree of Doctor of Philosophy

Photoelectron spectroscopy as a probe of intramolecular vibrational dynamics in electronically excited toluene

Alistair Malcolm Green, MChem

August 2011

Supervisors: Professors Katharine Reid and Tim Wright

Abstract

Intramolecular vibrational energy redistribution (IVR) is a commonly-observed phenomenon whereby vibrational energy can be transferred between different parts of a polyatomic molecule. This process has profound implications for the understanding of chemical reactivity. In this work, IVR is studied in the S_1 electronic state of toluene using time-resolved and frequency-resolved techniques. Both experiments are based upon laser photoelectron spectroscopy in the collision-free environment of a molecular beam.

The time-resolved experiments employ laser pulses of $\sim$1 ps duration and $\sim$15 cm^{-1} bandwidth. In a pump-probe scheme, the molecule is first excited to a chosen superposition of vibrational states in the S_1 manifold and then ionised by a second photon. The photoelectrons produced by the probe laser pulse are detected using velocity map imaging in order to obtain a vibrationally resolved photoelectron spectrum. Changes in the spectrum as a function of time give a direct view of the evolution of the vibrational state. The use of a two-colour ionisation scheme substantially improves the resolution compared with previous work.

High resolution zero kinetic energy (ZEKE) photoelectron spectra have also been obtained for the first time from excited vibrational levels in the S_1 electronic state of toluene. These experiments employed laser pulses of $\sim$5 ns duration and $\sim$0.3 cm^{-1} bandwidth, allowing the excitation of individual S_1 vibrational levels rather than a superposition. The nanosecond and picosecond experiments therefore give complementary information.

A Fermi resonance at $\sim$460 cm^{-1} above the S_1 origin in toluene is shown to be more complicated than previously thought, and provides the first demonstration of the use of time-resolved photoelectron spectroscopy to gain quantitative measurements of vibrational coupling matrix elements. Lifetimes of dissipative IVR have been determined following the preparation of high-frequency vibrations, and at intermediate energies several "doorway states" which mediate the IVR mechanism have been identified for the first time.

Acknowledgements

I owe a great debt to my supervisors, Professors Katharine Reid and Tim Wright, for offering me the chance to study for a PhD and making this whole project possible. Their support and guidance have been invaluable over the last three and a half years. Special thanks must also go to Dr Julia Davies, without whose tireless efforts in the lab the research programme would never have got off the ground. She has been my mentor throughout, instructing me in the practical aspects of research, helping me to make sense of the results and showing endless patience in the face of my beginner's mistakes.

I am grateful to my fellow PhD students for their friendship, advice and sometimes bizarre conversations over tea. Adrian "I ♡ ZEKE" Gardner graciously allowed me to spend a summer in his lab working on the nanosecond experiments, and our many late night foraging expeditions in search of coffee will not be forgotten. Paul Hockett and Mick Staniforth were on hand to help me settle in when I first arrived in Nottingham, and gave me many valuable pointers for getting started with Matlab. Thanks are also due to Jonny Midgley and Steve Daly for moral support and pulling me away from thesis writing in time for afternoon tea.

The technical staff in the School of Chemistry play an essential part in keeping the equipment going, none more so than the living legend that is Neil Barnes. During the course of this project, he has been a great provider of technical know-how, spare parts, elbow grease and after-hours pyrotechnic entertainment. David Lichfield and James Warren gave us valuable assistance with the electronics.

I must also thank my parents for their unwavering support, encouragement and belief that I could succeed.

This project was funded by EPSRC Grant EP/E046150 and a DTA studentship from the University of Nottingham. Computer time and access to the *Gaussian 09* quantum chemistry software package were provided by the National Service for Computational Chemistry Software.

Last but not least, thanks must go to Sue for supplying an estimated 1500 cups, or 400 litres of life-giving tea. These contained roughly 40 grams of caffeine, or 12.5 times the lethal dose for an adult human.

"I love deadlines. I like the whooshing sound they make as they fly by."

—*Douglas Adams*

Contents

List of Figures viii

List of Tables xii

I Principles 1

1 Introduction 2
- 1.1 What is a vibrational state? . . . 5
  - 1.1.1 The harmonic oscillator model . . . 6
  - 1.1.2 Coupling of vibrational modes . . . 8
- 1.2 The simplest case of IVR: a Fermi resonance . . . 9
  - 1.2.1 Fermi resonance in the frequency domain . . . 9
  - 1.2.2 Fermi resonance in the time domain . . . 10
- 1.3 The regimes of IVR dynamics . . . 11
- 1.4 Frequency-resolved studies of IVR . . . 12
- 1.5 Time-resolved studies of IVR . . . 13
  - 1.5.1 Chemical timing . . . 13
  - 1.5.2 Time-resolved dispersed fluorescence . . . 15
  - 1.5.3 Time-resolved fluorescence depletion . . . 16
  - 1.5.4 Picosecond IR pump, UV probe spectroscopy . . . 17
  - 1.5.5 Time-resolved photoelectron spectroscopy . . . 18
- 1.6 Aims, objectives and overview . . . 22

2 Theories and models for the study of IVR 25
- 2.1 Notation for the normal modes of toluene . . . 25
- 2.2 Mechanisms of vibrational coupling . . . 26
  - 2.2.1 Anharmonic coupling . . . 27
  - 2.2.2 Rotation-vibration coupling . . . 27
- 2.3 Mode coupling versus mode mixing . . . 28
- 2.4 Competition between IVR and other processes . . . 29
- 2.5 IVR dynamics in the statistical limit: Fermi's Golden Rule . . . 30
- 2.6 Doorway states and the tier model . . . 31
- 2.7 Influence of methyl rotors . . . 33
  - 2.7.1 Unhindered rigid rotor model . . . 33
  - 2.7.2 Hindered rotors . . . 34
  - 2.7.3 Symmetry considerations . . . 35
  - 2.7.4 Torsion-vibration coupling and the acceleration of IVR . . . 36
  - 2.7.5 Thermal population of torsional levels in toluene . . . 37
  - 2.7.6 Torsional selection rules upon electronic excitation . . . 38

II Techniques 39

3 Time-resolved photoelectron spectroscopy: velocity map imaging 40
- 3.1 Picosecond laser system . . . 41
- 3.2 Velocity map imaging spectrometer . . . 43
- 3.3 Image analysis . . . 45
  - 3.3.1 Recovery of the photoelectron spectrum . . . 45

3.3.2 Background subtraction . . . 46
3.3.3 Calibration . . . 47
3.3.4 Distortion correction . . . 48
3.4 Improving resolution: the SEVI technique . . . 49
3.5 Characterisation of the S_1 electronic state: REMPI . . . 51

4 High resolution photoelectron spectroscopy: ZEKE 53
4.1 Principle of ZEKE spectroscopy . . . 53
4.2 ZEKE apparatus . . . 55
4.3 Laser wavelength calibration . . . 57

5 Computational methods 58
5.1 Vibrational frequencies . . . 58
5.1.1 Neutral and ion ground states . . . 58
5.1.2 Neutral S_1 excited state . . . 62
5.1.3 Deuterated toluene . . . 65
5.2 Simulation of photoelectron spectra . . . 69
5.3 Density of vibrational states . . . 70
5.3.1 Total density of states: the Beyer-Swinehart Algorithm . . . 71
5.3.2 Density of states with symmetry restrictions . . . 73

III Results and Discussion 76

6 Nano- and picosecond photoelectron spectroscopy of toluene 77
6.1 REMPI spectra via S_1 . . . 78
6.2 Photoelectron spectra via the S_1 origin . . . 79
6.3 Photoelectron spectra via S_1 15^1 (0^0 + 332 cm^{-1}) . . . 80
6.4 Photoelectron spectra via S_1 $6b^1$ (0^0 + 532 cm^{-1}) . . . 81
6.5 Photoelectron spectra via S_1 1^1 / 4^1 $16b^1$ Fermi resonance (754 / 736 cm^{-1}) 83
6.6 Photoelectron spectra via S_1 $18a^1$ (0^0 + 935 cm^{-1}) and 12^1 (0^0 + 966 cm^{-1}) 85
6.7 Summary . . . 89

7 Restricted IVR: a "Fermi resonance" 90
7.1 A Fermi resonance in toluene . . . 90
7.2 Nanosecond REMPI and ZEKE studies . . . 92
7.3 Time-resolved spectra . . . 94
7.4 Interpretation . . . 99
7.4.1 Fourier analysis . . . 99
7.4.2 Empirical model for the quantum beats . . . 103
7.4.3 Three-level picture . . . 105
7.4.4 Effect of pump wavelength . . . 107
7.4.5 Role of the methyl group . . . 109
7.5 The eigenvector coupling matrix . . . 111
7.6 Deuteration of the methyl group . . . 117
7.7 Conclusions . . . 123

8 Dissipative IVR following excitation to high vibrational levels 125
8.1 S_1 $6b^1$ (1^1 / 4^1 $16b^1$) Fermi resonance . . . 126
8.1.1 Assignments . . . 126
8.1.2 Time-resolved spectra via S_1 "$6b^1$ 4^1 $16b^1$" level (0^0 + 1263 cm^{-1}) 127
8.1.3 Time-resolved spectra via S_1 "$6b^1$ 1^1" level (0^0 + 1284 cm^{-1}) . . . 131
8.2 S_1 $6b^1$ $18a^1$ level (0^0 + 1466 cm^{-1}) . . . 133
8.3 S_1 $6b^1$ 12^1 level (0^0 + 1494 cm^{-1}) . . . 138
8.4 Discussion . . . 140
8.5 Conclusions . . . 141

9 IVR in the intermediate regime 143
9.1 A C−CH_3 stretch in toluene: 13^1 . . . 143

9.1.1 Nanosecond REMPI and ZEKE studies . . . 144
9.1.2 Picosecond time-resolved SEVI spectra . . . 145
9.1.3 Assignment of the "doorway" state . . . 149
9.2 C−CD_3 stretch: 13^1 in toluene-D_3 . . . 156
9.3 Ring breathing: $1^1 6a^1$ in toluene-D_3 . . . 162
9.4 Conclusions . . . 167

10 Conclusions and future work **169**
10.1 Spectroscopy of the toluene cation . . . 170
10.2 Regimes of IVR dynamics . . . 170
10.2.1 Restricted IVR . . . 171
10.2.2 Intermediate IVR . . . 173
10.2.3 Dissipative IVR . . . 174
10.3 Future directions . . . 175

IV Appendices **177**

A Normal modes of toluene **178**

B Normal modes of toluene-D_3 **184**

Bibliography **190**

List of Figures

1.1 An early demonstration of non-random IVR: "Rabinovitch's Bicycle". . 4
1.2 Normal modes of the water molecule. 7
1.3 Example of Fermi resonance coupling in CO_2. 9
1.4 Summary of relative IVR rates observed by Parmenter and co-workers. . 15
1.5 Fluorene. 16
1.6 *Para*-n-butylaniline. 18

2.1 Example of Coriolis coupling between bending and stretching vibrations. 28
2.2 The tier model of IVR. 32
2.3 Torsional potential function for toluene in the S_0 electronic state. 35

3.1 Schematic of the picosecond laser system. 41
3.2 Optical delay line and beam path into the VMI chamber. 42
3.3 Schematic of the VMI spectrometer. 44
3.4 Electrostatic lens for velocity map imaging. 44
3.5 Example of background subtraction. 47
3.6 Example of distortion correction. 50
3.7 SEVI spectrum *via* the S_1 vibrational origin in toluene. 52

4.1 Principle of the ZEKE experiment. 53
4.2 Nanosecond REMPI and ZEKE apparatus. 55
4.3 Schematic of the combined REMPI / ZEKE spectrometer used in the nanosecond experiments. 56

5.1 Example of simulated photoelectron spectra using CIS and TD-B3LYP methods for the S_1 normal mode analysis. 71
5.2 Calculated density of states for S_1 toluene and deuterated toluene. . . . 74

6.1 Picosecond and nanosecond REMPI spectra of toluene recorded in this work *via* the S_1 electronic state. 78
6.2 Photoelectron spectra and Franck-Condon simulation *via* the S_1 origin in toluene. 79
6.3 Comparison of ZEKE spectra *via* the S_1 origin in the two isotopomers. . 80
6.4 Photoelectron spectra and Franck-Condon simulation via S_1 15^1. 81
6.5 ZEKE spectra *via* S_1 15^1 for the two isotopomers. 81
6.6 Photoelectron spectra and Franck-Condon simulation *via* S_1 $6b^1$. 82
6.7 ZEKE spectra *via* S_1 $6b^1$ in the two isotopomers. 82
6.8 SEVI and ZEKE spectra and Franck-Condon simulations *via* the S_1 1^1 / $4^1 16b^1$ Fermi resonance. 84
6.9 ZEKE spectra *via* the two components of the 1^1 / $4^1 16b^1$ Fermi resonance in S_1 $C_6H_5CD_3$. 85
6.10 Comparison of modes 12 and 18*a* in the three electronic states. 86
6.11 Photoelectron spectra and Franck-Condon simulations *via* the S_1 "$18a^1$" and "12^1" vibrational levels. 87
6.12 Nanosecond REMPI spectra in the vicinity of $18a^1$ and 12^1 for the two isotopomers. 87
6.13 ZEKE spectra *via* S_1 $18a^1$ in the two isotopomers. 88
6.14 ZEKE spectra *via* the S_1 vibrational levels at 957 and 973 cm^{-1} in $C_6H_5CD_3$. 88

7.1 Coupling of ring stretch and bends in a Fermi resonance of S_1 toluene. . 91
7.2 Portion of the REMPI spectra of toluene in the vicinity of the S_1 $6a^1$ / $10b^1 16b^1$ Fermi resonance. 92
7.3 ZEKE spectra via the three S_1 vibrational levels, compared with simulations via the zero-order states. 93
7.4 Comparison of 1- and 2-colour spectra at 0 ps. 95
7.5 Photoelectron spectra from the Fermi resonance for time delays of 0–12 ps. 95
7.6 Comparison of SEVI and ZEKE spectra via S_1 $6a^1$ / $10b^1 16b^1$. 97
7.7 Examples of Gaussian fits to time-resolved spectra. 98
7.8 Peak integrals as a function of time delay, determined from the Gaussian fit. 98
7.9 Time-dependent intensity of the ion origin peak from 0 to 400 ps. 99
7.10 Fourier transforms of the oscillations shown in Fig. 7.8 and Fig. 7.9. . . 102
7.11 Origin peak intensity from 0-400 ps, with fit to Equation (7.3). 104
7.12 Cosine fits to the peak oscillations in the time-resolved spectra. 106
7.13 Effect of changing pump wavelengths on the oscillations of the ion $16a^2$ peak. 108
7.14 Schematic representation of the two "torsional ladders" excited in the S_1 electronic state. 110
7.15 Real part of Fourier transform for the $16a^2$ peak, with assignments of the frequency components. 111
7.16 Simulations of the peak oscillations for on-resonance pump wavelength, based upon the fitted coupling matrix. 118
7.17 Comparison of nanosecond REMPI spectra in the vicinity of S_1 $6a^1$ / $10b^1 16b^1$ / $16a^2$ for $C_6H_5CH_3$ and $C_6H_5CD_3$. 119
7.18 Nanosecond ZEKE spectra recorded *via* the four vibrational levels in the vicinity of S_1 $6a^1$ in $C_6H_5CD_3$. 120
7.19 Comparison of energy spacing of the "Fermi resonance" components in $C_6H_5CD_3$ with the bandwidth of the picosecond laser. 121
7.20 Picosecond two-colour VMI photoelectron spectra *via* the Fermi resonance in S_1 $C_6H_5CD_3$ for time delays of 0–12 ps. 121
7.21 Time-resolved oscillations of the origin peak for the Fermi resonance in $C_6H_5CD_3$, with fit to Equation (7.3). 122
7.22 Fourier transform of the time–resolved oscillations of the origin peak for the Fermi resonance in $C_6H_5CD_3$. 123

8.1 Calculated density of vibrational states superimposed upon the picosecond REMPI spectrum of toluene. 125
8.2 Comparison of energy spacing of the $6b^1\left(1^1/4^1 16b^1\right)$ Fermi resonance components with the bandwidth of the picosecond laser. 126
8.3 Confirmation of the assignment of the S_1 vibrational levels at 1263 and 1284 cm^{-1}. 127
8.4 Time-resolved two-colour VMI photoelectron spectra *via* S_1 $6b^1 4^1 16b^1$, taken with a probe wavelength of 290 nm. 128
8.5 Decay of bright state population following excitation to S_1 $6b^1 4^1 16b^1$. . . 129
8.6 Increase of dark state population following excitation to S_1 $6b^1 4^1 16b^1$. . 130
8.7 Fit to bright and dark state populations as a function of time following excitation to S_1 $6b^1 4^1 16b^1$, using an averaged value for the IVR lifetime. 130
8.8 Time-resolved two-colour VMI photoelectron spectra *via* S_1 $6b^1 1^1$, taken with a probe wavelength of 290 nm. 131
8.9 Decay of bright state population following excitation to S_1 $6b^1 1^1$, with fits to Equation (8.1). 132
8.10 Increase of dark state population following excitation to S_1 $6b^1 1^1$. 132
8.11 Fit to bright and dark state populations as a function of time following excitation to S_1 $6b^1 1^1$, using an averaged value for the IVR lifetime. . . 133
8.12 Time-resolved SEVI spectra *via* S_1 $6b^1 18a^1$. 134

8.13 Decay of bright state population following excitation to S_1 $6b^1 18a^1$, with fits to Equation (8.1). . . . 136
8.14 Increase of dark state population following excitation to S_1 $6b^1 18a^1$, with fits to Equation (8.1). . . . 137
8.15 Comparison of the SEVI spectrum at 0 ps with a Franck-Condon simulation via S_1 $6b^1 12^1$. . . . 138
8.16 Time-resolved SEVI spectra via the S_1 $6b^1 12^1$ level in toluene. . . . 139
8.17 Decay of bright state population following excitation to S_1 $6b^1 12^1$. . . . 140

9.1 S_1 mode 13. . . . 143
9.2 Nanosecond REMPI spectrum of toluene in the vicinity of S_1 13^1. . . . 144
9.3 Nanosecond ZEKE spectra via two S_1 vibrational levels in the vicinity of 13^1, compared with a Franck-Condon simulation via 13^1. . . . 145
9.4 Picosecond SEVI spectra via S_1 13^1 at short time delays. . . . 146
9.5 Picosecond SEVI spectra via S_1 13^1 at long time delays. . . . 147
9.6 Bright state population as a function of time, with fit to Equation (9.1). 148
9.7 Fits of peak oscillations to Equation (9.2), with $\omega_1 = 0.975\ \mathrm{rad\,ps^{-1}} = 5.2\,\mathrm{cm^{-1}}$ and $\omega_2 = 1.293\ \mathrm{rad\,ps^{-1}} = 6.9\,\mathrm{cm^{-1}}$. . . . 150
9.8 Isolation of the photoelectron spectrum from the "doorway" vibrational state. . . . 151
9.9 Comparison of the "doorway" SEVI spectrum with Franck-Condon simulations from possible doorway states which could give rise to a peak at $\sim$1290 $\mathrm{cm^{-1}}$. . . . 154
9.10 Comparison of the ZEKE and "doorway" SEVI spectra with Franck-Condon simulations from six candidate doorway states that could give rise to a peak at $\sim$1475 $\mathrm{cm^{-1}}$. . . . 155
9.11 Comparison of atomic motions for Varsányi mode 13 in the two isotopomers. . . . 156
9.12 Portion of the nanosecond REMPI spectrum of $C_6H_5CD_3$ in the vicinity of S_1 13^1. . . . 157
9.13 SEVI spectra at 0 ps *via* S_1 13^1 in the two isotopomers. . . . 158
9.14 Two-colour VMI photoelectron spectra *via* S_1 13^1 in toluene-D_3 at selected pump-probe time delays. . . . 159
9.15 Time-resolved oscillations of the $\Delta v = 0$ peak (1160–1347 $\mathrm{cm^{-1}}$) in spectra via S_1 13^1 in toluene-D_3. . . . 160
9.16 Time-resolved picosecond SEVI spectra *via* S_1 13^1 in toluene-D_3. . . . 160
9.17 Comparison of SEVI spectrum *via* S_1 13^1 in toluene-D_3 at 6 ps with simulations from the candidate doorway states. . . . 161
9.18 Simulation *via* a state which could potentially couple to S_1 $|13^1, m = 1\rangle$ in $C_6H_5CD_3$. . . . 162
9.19 Portion of the nanosecond REMPI spectrum of toluene-D_3 in the vicinity of the $1^1 6a^1$ vibrational level. . . . 163
9.20 Picosecond SEVI spectra via S_1 1^1 $\left(6a^1/10b^1 16b^1/16a^2\right)$ in $C_6H_5CD_3$ at short time delays. . . . 164
9.21 Picosecond SEVI spectra via S_1 1^1 $\left(6a^1/10b^1 16b^1/16a^2\right)$ in $C_6H_5CD_3$ at long time delays. . . . 165
9.22 Comparison of SEVI spectra *via* S_1 $1^1 6a^1$ in $C_6H_5CD_3$ with Franck-Condon simulations. . . . 166
9.23 Oscillations of the 1^1 peak in the SEVI spectra via S_1 1^1 $\left(6a^1/10b^1 16b^1/16a^2\right)$ for $C_6H_5CD_3$, with fit to Equation (9.1). . . . 167

10.1 Picosecond REMPI spectrum of toluene and calculated density of vibrational states, showing the three distinct regimes of IVR observed in this work. . . . 171

A.1 Normal modes of toluene in the S_0 electronic state (part 1) . . . 178
A.2 Normal modes of toluene in the S_0 electronic state (part 2) . . . 179
A.3 Normal modes of toluene in the S_1 electronic state (part 1) . . . 180
A.4 Normal modes of toluene in the S_1 electronic state (part 2) . . . 181

A.5 Normal modes of the toluene cation (part 1) 182
A.6 Normal modes of the toluene cation (part 2) 183

B.1 Normal modes of $C_6H_5CD_3$ in the S_0 electronic state (part 1) 184
B.2 Normal modes of $C_6H_5CD_3$ in the S_0 electronic state (part 2) 185
B.3 Normal modes of $C_6H_5CD_3$ in the S_1 electronic state (part 1) 186
B.4 Normal modes of $C_6H_5CD_3$ in the S_1 electronic state (part 2) 187
B.5 Normal modes of $C_6H_5CD_3^+$ (part 1) 188
B.6 Normal modes of $C_6H_5CD_3^+$ (part 2) 189

List of Tables

2.1 Symmetries of torsional levels in toluene. 36
2.2 Torsional levels in the S_0 state of toluene. 38

5.1 Calculated and measured frequencies for toluene in the S_0 electronic state. 60
5.2 Calculated and measured frequencies for the toluene cation. 61
5.3 Calculated and measured frequencies for S_1 toluene. 64
5.4 Frequencies for deuterated toluene ($C_6H_5CD_3$) in the S_0 electronic state. . 66
5.5 Frequencies for S_1 deuterated toluene ($C_6H_5CD_3$). 67
5.6 Calculated and measured frequencies for $C_6H_5CD_3^+$. 68
5.7 Parameters used to find torsional levels in the S_1 electronic state for the density of states calculations. 73

6.1 Cation vibrational frequencies determined in this work, with comparisons to a previous time-of-flight study of toluene-H_8. 89

7.1 Gaussian functions used to fit the time-resolved spectra. 96
7.2 Parameters given by fit of origin peak intensity (0-400 ps) to Equation (7.3). 104
7.3 Parameters given by fit of time-resolved peak oscillations to Equation (7.3). 105
7.4 Energies of the allowed torsional transitions on $S_1 \leftarrow S_0$ excitation. 109
7.5 Franck-Condon factors, $|\langle\gamma|\chi\rangle|^2$, used in the calculation of the coupling matrix. 115
7.6 Quantum beat modulation depths given by the fitted coupling matrix. . . 117
7.7 Composition of the eigenstates, derived from the squares of the matrix elements given in Equation (7.22). 117
7.8 Parameters obtained from a fit of the origin peak oscillations for $C_6H_5CD_3$ to Equation (7.3). 122

8.1 Comparison of IVR rates with number of potential doorway states. 141

9.1 Parameters given by fit of peak oscillations to Equation (9.2). 149
9.2 List of vibrational states with suitable energy and symmetry for coupling to $|13^1, m = 0\rangle$. 152
9.3 List of vibrational states with suitable energy and symmetry for coupling to $|13^1, m = 1\rangle$. 153
9.4 Summary of the most plausible candidates for the identity of the doorway state(s) coupled to 13^1. 154
9.5 Parameters obtained from fits of 13^1 peak oscillations to Equation (9.1) for the two isotopomers. 158
9.6 Candidate doorway states with suitable energy and symmetry for coupling to $|13^1, m = 0\rangle$ in S_1 toluene-D_3. 162

Part I.

Principles

1. Introduction

One of the ultimate goals of physical chemistry is to understand how chemical reactions occur. Ideally, we would like to obtain a complete description of the motion of the reactants across the potential energy surface. This motion consists not only of translation and rotation of the molecules, but also the vibrations of their chemical bonds, which often have profound implications for the reactivity. A simple illustration is provided by light atom transfer reactions of the form $\mathrm{A} + \mathrm{BC} \longrightarrow \mathrm{AB} + \mathrm{C}$, which are governed by *Polanyi's rules* [1–3]. If the activation barrier occurs early on the reaction coordinate, as A approaches BC, then a large amount of translational energy is needed to surmount it and AB will be formed in a highly vibrationally excited state; we can picture the vibration of AB as a "slalom" motion down the long exit valley of the potential energy surface. Conversely if the barrier occurs at a later stage, as AB and C are separating, then BC must be initially vibrationally excited in order for the reaction to succeed. In the exit valley the vibrational energy is converted into translational kinetic energy, producing fast-moving products.

The rates of chemical reactions are frequently rationalised in terms of *transition state theory*, which assumes that there is a "point of no return" on the reaction coordinate. This configuration of the reactants, known as the *transition state* or *activated complex*, corresponds to the maximum potential energy along the reaction coordinate. It is assumed to undergo a particular vibration which leads to irreversible dissociation into the products, so that the lifetime of the transition state determines the rate of the reaction.

Suppose that the transition state has a specified internal energy, E, and that this energy can flow freely between the different vibrational degrees of freedom, becoming statistically distributed amongst many kinds of motion. The transition state will decompose into the products when, by chance, enough energy accumulates in the vibration of the bond that is going to break. This idea is the key to the *Rice-Ramsperger-Kassel-Marcus (RRKM) theory*, which is one of the most commonly used approaches to predicting the rates of unimolecular reactions. It can be shown [4, 5] that the rate constant is given by the RRKM expression:

$$k\left(E\right) = \frac{W^{\dagger}\left(E\right)}{h\rho\left(E\right)}, \tag{1.1}$$

where $W^{\dagger}\left(E\right)$ is the total number of vibrational states in the activated complex which

have an energy less than or equal to E, and h is Planck's Constant. $\rho(E)$ is the density of vibrational states in the reactant molecule, which is defined as the number of states that exist within the infinitessimal energy range E to $(E + \mathrm{d}E)$.

The postulated transfer of energy between the different modes of vibration is known as *intramolecular vibrational energy redistribution*, or IVR. When RRKM theory was first proposed in 1952, the concept of IVR was pure conjecture. However, the success of the theory in reproducing observed rates of reaction inspired chemists to investigate whether or not IVR is a real phenomenon, and under what circumstances it might occur fast enough for the RRKM assumptions to be valid.

Experimental evidence for the reality of IVR was unearthed in 1960 by Butler and Kistiakowsky [6] during the course of an investigation into the properties of methylene (CH_2), which is a highly reactive carbene that can be generated by the photolysis of ketene ($H_2C{=}C{=}O$). Methylene reacts with cyclopropane by inserting itself into one of the C−H bonds, forming methylcyclopropane in which the C−CH_3 bond is highly vibrationally excited. Butler and Kistiakowsky found that, unless it achieved vibrational relaxation through colliding with another molecule, the methylcyclopropane would rapidly decompose into a mixture of butene isomers. An alternative way to prepare methylcyclopropane was through the reaction between methylene and propylene, in which CH_2 would add itself across the double bond to form the ring. In this case the ring would be vibrationally excited instead of the C−CH_3 bond. Remarkably, however, the mixture of butene isomers produced by decomposition remained the same. This result suggested that the vibrational energy had become randomly distributed amongst the vibrational modes of methylcyclopropane within ten picoseconds, before the molecule could decompose.

Once it had been established that rapid IVR can indeed occur as required by RRKM theory, the search was on for situations in which the distribution of vibrational energy does *not* become rapidly randomised. The first demonstration of non-random vibrational energy flow, violating the assumptions of RRKM theory, came from an elegant experiment by Rynbrandt and Rabinovitch [7] using the reaction scheme depicted in Fig. 1.1. The addition of the deuterated carbene CD_2 to a double bond produced an isotopically labelled compound containing two cyclopropane rings, which has become known as "Rabinovitch's Bicycle" [3]. Either one of the rings could then open to eliminate CF_2, leading to two possible alkene products. Although both alkenes have the same chemical formula, they can be distinguished by mass spectrometry due to their different fragmentation patterns.

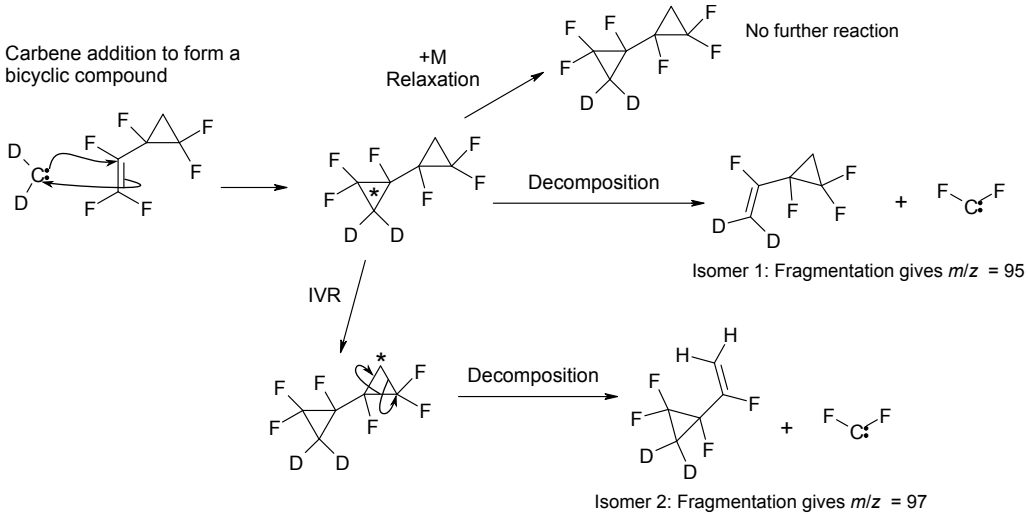

Fig. 1.1. An early demonstration of non-random IVR: "Rabinovitch's Bicycle" [7]. Asterisks denote vibrational excitation.

Crucially, the vibrations of the molecule determine which of the rings will open. Initially, the newly-formed ring containing CD_2 will be vibrationally excited; this is denoted by an asterisk in Fig. 1.1. If the non-deuterated ring is to open, producing isomer 2, then the vibrational energy must be transferred into it before CF_2 elimination takes place. At low pressures, Rynbrandt and Rabinovitch observed roughly equal yields of the two alkene products, as would be expected if IVR is fast compared with the elimination reaction. However, above about 100 Torr, collisions between molecules led to vibrational relaxation on a time-scale faster than IVR and so isomer 1 was dominant. From the pressure dependence of the product ratio, it was possible to deduce an IVR rate constant of $3 \times 10^9\,\mathrm{s}^{-1}$, which is equivalent to a lifetime of $\sim$330 ps. This was the first example of the direct experimental determination of an IVR rate.

If the vibrations of a molecule do not become too rapidly randomised, then there exists the tantalising possibility of controlling its reactivity by selectively exciting particular bonds, for instance using laser radiation [3, 8, 9]. Such control has been achieved in a number of simple reactions; for instance the $\mathrm{H}\cdot + \mathrm{HOD}$ reaction produces mainly $\mathrm{H_2} + \mathrm{OD}$ if the O−H stretch is excited, or $\mathrm{HD} + \mathrm{OH}$ if the energy is instead placed into the O−D bond [9]. Extending such control schemes to larger molecules, however, remains challenging. Only certain vibrational levels — the so-called "bright states" — can be prepared directly by the absorption of light. If the desired localised vibration does not correspond to one of these, then we must instead find a bright state that will undergo IVR into a "dark" state involving vibration of the correct bond. However, IVR can also frustrate our efforts to control the reaction by depopulating the required vibrational state [8].

The far-reaching consequences of IVR have attracted much interest among physical chemists, and numerous studies have been carried out in the past in an effort to obtain a better understanding of how and when this process occurs. Reviews can be found in, for example, Refs. [10–13]. The remainder of this chapter will give a brief overview of the basic quantum mechanics underlying IVR, the techniques that can be used to study it experimentally and the aims and objectives of the present investigation. A discussion of the theoretical approaches and models used to rationalise the observed IVR behaviour follows in Chapter 2. First, however, we must consider the nature of molecular vibrational states themselves.

1.1. What is a vibrational state?

In order to define the concept of a "vibrational state" in a molecule, we must first make the *Born-Oppenheimer approximation* in which the motions of the nuclei and electrons are treated separately. Due to their lower mass, the electrons move on a much shorter time-scale than the nuclei and so can respond almost immediately to any change in the nuclear positions. The Hamiltonian operator of the molecule can therefore be separated into a sum of electronic and nuclear parts:

$$\hat{\mathrm{H}} \approx \hat{\mathrm{H}}_{\mathrm{el}} + \hat{\mathrm{H}}_{\mathrm{nuc}} \,. \tag{1.2}$$

In a further approximation, we then separate out the contributions to $\hat{\mathrm{H}}_{\mathrm{nuc}}$ from translation, vibration, rotation and nuclear spin:

$$\hat{\mathrm{H}} \approx \hat{\mathrm{H}}_{\mathrm{el}} + \hat{\mathrm{H}}_{\mathrm{trans}} + \hat{\mathrm{H}}_{\mathrm{vib}} + \hat{\mathrm{H}}_{\mathrm{rot}} + \hat{\mathrm{H}}_{\mathrm{spin}}, \tag{1.3}$$

and the total wavefunction becomes a product:

$$\Psi = \psi_{\mathrm{el}}\, \psi_{\mathrm{trans}}\, \psi_{\mathrm{vib}}\, \psi_{\mathrm{rot}}\, \psi_{\mathrm{spin}}, \tag{1.4}$$

in which ψ_{vib} defines the vibrational state of the molecule.

Next we must find a set of basis functions which can be used to describe the vibrations. Ideally we would use the eigenfunctions of the vibrational Hamiltonian, but these are not generally known. Instead we will employ the eigenfunctions arising from an approximate form of $\hat{\mathrm{H}}_{\mathrm{vib}}$, which enable us to picture the vibrational motion intuitively.

1.1.1. The harmonic oscillator model

Traditionally a vibrating molecule is pictured as behaving like a collection of point masses (atoms) connected by springs which obey Hooke's Law: when a bond is stretched or compressed, the atoms experience a restoring force proportional to their displacement from the equilibrium position. This is the *harmonic oscillator model*. If a heteronuclear diatomic molecule is modelled as two masses m_1 and m_2 connected by a spring with a force constant k, then it is possible to reduce its classical equations of motion down to a one-body problem by introducing the concept of the *reduced mass*, $\mu = m_1 m_2 / (m_1 + m_2)$. If the displacement from the equilibrium bond length is x then the potential and kinetic energies of the oscillator are given by:

$$V = \frac{1}{2} k x^2 \tag{1.5}$$

$$T = \frac{1}{2} \mu \left(\frac{\mathrm{d}x}{\mathrm{d}t} \right)^2 . \tag{1.6}$$

By analogy with these classical expressions, the Hamiltonian for a quantum mechanical harmonic oscillator is of the form:

$$\hat{\mathrm{H}}_{\mathrm{harm}} = \frac{-\hbar^2}{2\mu} \frac{\mathrm{d}^2}{\mathrm{d}x^2} + \frac{1}{2} k x^2 . \tag{1.7}$$

The corresponding Schrödinger equation, $\hat{\mathrm{H}}_{\mathrm{harm}}\, \psi(x) = E\, \psi(x)$, is analytically soluble [14]. There are infinitely many eigenstates, equally spaced in energy, which are characterised by the vibrational quantum number v. The energy eigenvalues are given by the relation:

$$E_v = \left(v + \frac{1}{2} \right) h\nu, \tag{1.8}$$

where $\nu = (1/2\pi)\sqrt{k/\mu}$ is the fundamental frequency of the oscillator.

At first sight, the treatment of polyatomic molecules seems far more complicated due to the greater range of possible motions. However a simplification can be achieved by taking certain combinations of atomic motions which are known as the *normal modes*. For a non-linear molecule with N atoms there are $(3N - 6)$ normal modes of vibration, each of which can be treated as a single, independent harmonic oscillator. A simple example is provided by the water molecule, whose normal modes consist of a symmetric stretch, an anti-symmetric stretch and a bend (see Fig. 1.2). Any possible vibration of the molecule can be expressed as a combination of these motions.

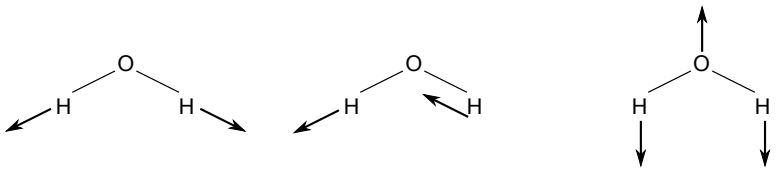

(a) Symmetric stretch. (b) Anti-symmetric stretch. (c) Bend.

Fig. 1.2. Normal modes of the water molecule.

By analogy with Equations 1.5 and 1.6, we can write:

$$V = \frac{1}{2}\sum_{i=1}^{3N-6} \lambda_i Q_i^2, \tag{1.9}$$

$$T = \frac{1}{2}\sum_{i=1}^{3N-6} \left(\frac{\mathrm{d}Q_i}{\mathrm{d}t}\right)^2, \tag{1.10}$$

where λ_i is the force constant of the i^{th} oscillator, and Q_i is the mass-weighted *normal coordinate* which describes the atomic displacements associated with that mode. In quantum mechanics, the Hamiltonian becomes:

$$\hat{\mathrm{H}}_{\text{harm}} = \sum_{i=1}^{3N-6} \left(-\frac{\hbar^2}{2}\frac{\mathrm{d}^2}{\mathrm{d}Q_i^2} + \frac{1}{2}\lambda_i Q_i^2\right), \tag{1.11}$$

and the wavefunction is a product of one-dimensional harmonic oscillator eigenfunctions. Each normal mode has its own vibrational quantum number, v_i, and an associated frequency ν_i. The vibrational state of the molecule is completely specified by the numbers of quanta in each normal mode. Conventionally vibrational states are represented using a notation of the form "1^2", where "1" is a number identifying a particular normal mode and the superscript is the number of quanta. Transitions are denoted by using a subscript to give the initial number of quanta. The mode numbering scheme used for toluene is illustrated in Appendix A, and will be described in more detail in Section 2.1.

This ability to picture the molecule's vibrational motion intuitively is the great advantage of the harmonic oscillator basis: we can say precisely *which* bonds are vibrating. The reality, however, is somewhat more complicated due to a number of effects which the harmonic oscillator model does not take into account. Since they result from a simple approximation, the harmonic basis states are sometimes referred to as the *zero-order vibrational states*. Next we shall consider how real molecules differ from the harmonic model, and how those differences lead to the phenomenon of IVR.

1.1.2. Coupling of vibrational modes

The main shortcoming of the harmonic model is that Hooke's Law is valid only for small displacements from the equilibrium geometry. Beyond a certain point, the restoring force decreases with increasing bond length and so a real chemical bond will eventually break if it is stretched far enough. This deviation from Hooke's Law is known as *anharmonicity*. Another complication arises due to the molecule's rotation, which causes the atoms to experience a Coriolis force. For these and other reasons, which will be discussed further in Section 2.2, the zero-order states given by the harmonic oscillator model are not eigenstates of the full vibrational Hamiltonian and the motions corresponding to the normal modes are not truly independent of one another. Nonetheless, since the wavefunctions of the zero-order states $|a\rangle, |b\rangle, |c\rangle \cdots |\gamma\rangle$ are orthogonal to one another, *any* other function can be expressed as a linear combination of them. We can therefore write the "true"[1] vibrational eigenstates $|1\rangle, |2\rangle, |3\rangle, \cdots |n\rangle$ in the form:

$$|n\rangle = \sum_{\gamma=a,b,c\cdots} \alpha_{n\gamma}|\gamma\rangle, \tag{1.12}$$

where the coefficients $\alpha_{n\gamma}$ are known as the *coupling matrix elements*. These determine how closely the eigenstate resembles each of the zero-order states, and are subject to the normalisation conditions:

$$\sum_{\text{Eigenstates, } n=1,2,3\cdots} \alpha_{n\gamma}^2 = 1 \text{ for each zero-order state } \gamma = a, b, c\cdots, \tag{1.13a}$$

$$\sum_{\text{Zero-order states, } \gamma=a,b,c\cdots} \alpha_{n\gamma}^2 = 1 \text{ for each eigenstate } n = 1, 2, 3\cdots. \tag{1.13b}$$

Two zero-order states are said to be "coupled" to one another if they both make a significant contribution to the same eigenstate.

We can also look at Equation (1.12) the other way around, and express a given zero-order state as a linear combination of eigenstates. This picture shows that the normal mode vibrations predicted by the harmonic oscillator model can exist in a real molecule *if a coherent superposition of eigenstates is excited*. In quantum mechanics, the preparation of a coherent superposition results in a "wavepacket" which has a non-trivial evolution in time. The zero-order state will therefore have only a fleeting existence. At some later time, when the phase differences between the eigenstates have evolved, the wavefunction may resemble a different vibrational state altogether. This change in the vibrational wavefunction can be regarded as a manifestation of IVR.

[1] Within the framework of the Born-Oppenheimer approximation.

1.2. The simplest case of IVR: a Fermi resonance

The effects of coupling can be most easily understood in the simple case where just two zero-order states are coupled together. This situation is in fact commonly observed in vibrational spectroscopy, and is known as a *Fermi resonance* when a fundamental harmonic vibration is coupled to an overtone or combination which accidentally has a similar frequency.[2] The effects of the coupling can be seen in both frequency-resolved and time-resolved experiments.

1.2.1. Fermi resonance in the frequency domain

A classic example of a Fermi resonance is found in the Raman spectrum of CO_2, where the fundamental of the symmetric stretch ($v_1 = 1330\ \mathrm{cm}^{-1}$) accidentally falls very close in energy to the first overtone of the bending mode ($2v_2 = 1334\ \mathrm{cm}^{-1}$) [15]. Within the harmonic oscillator approximation, Raman transitions are subject to the selection rule $\Delta v = \pm 1$. We would therefore expect to see a strong Raman band for the fully allowed 1_0^1 stretching transition at $1330\,\mathrm{cm}^{-1}$. No band should be observed for the forbidden bending transition 2_0^2 at $1334\,\mathrm{cm}^{-1}$. In reality, however, the Raman spectrum contains two bands of roughly equal intensity at 1285 and $1385\,\mathrm{cm}^{-1}$. These are further apart than expected, although the average of their wavenumbers is at about $1330\,\mathrm{cm}^{-1}$, where 1_0^1 "should" have been. Furthermore, 2_0^2 appears to have "stolen" intensity from 1_0^1 [15]. The bands in fact correspond to a pair of eigenstates which are some mixture of the zero-order states $|1^1\rangle$ and $|2^2\rangle$, as illustrated in Fig. 1.3.

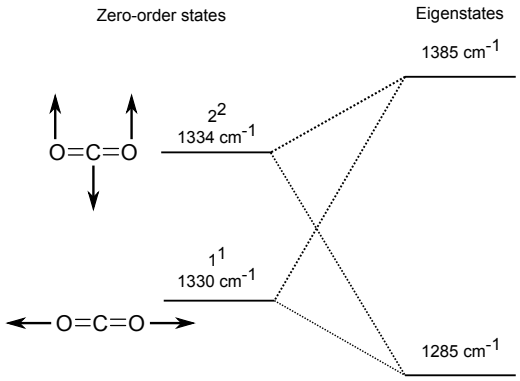

Fig. 1.3. Example of Fermi resonance coupling in CO_2. The Raman spectrum shows two bands which correspond to the eigenstates at 1285 and $1385\,\mathrm{cm}^{-1}$.

In this instance, Raman scattering leads to the preparation of a single vibrational eigenstate in any given molecule. By their very nature, eigenstates are *stationary*: that

[2] Another possibility is the coupling of two accidentally near-degenerate overtones, which is called a *Darling-Dennison resonance.*

is to say the expectation values of the observables do not change with time. Consequently, there can be no IVR *dynamics* in an experiment where individual eigenstates are prepared. Nonetheless, the shifts of the Raman bands from their expected positions and the changes in their intensities enable us to deduce the nature of the vibrational couplings, and so could be said to be indicative of IVR.

A possible source of confusion arises from the naming of the eigenstates, as they are often (loosely) referred to by the label of the zero-order state which they most closely resemble. In this example, the Raman band at $1285\,\mathrm{cm}^{-1}$ might be described as "1^1"; however it is important to remember that the eigenstate does not correspond to the pure symmetric stretching motion that this label suggests. Further clarification of some commonly misunderstood points regarding vibrational coupling and IVR can be found in a review article by Nesbitt and Field [12].

1.2.2. Fermi resonance in the time domain

An analogy can be drawn between a Fermi resonance and two classical pendulums hanging from a single bar [15]. Since the two pendulums have frequencies that are close to resonance with one another, energy can be transferred between them. If the first pendulum is set in motion then the second will also begin to swing, eventually taking all of the energy away from the first. The oscillation then gradually transfers back to the first pendulum, and so on.

In order to see a similar dynamical process in a molecule, we need to excite just one of the *zero-order* states that contribute to the Fermi resonance. In Section 1.1.2 we saw that a zero-order state can be expressed as a linear combination of the vibrational eigenstates. Certain zero-order states, known as *bright states*, can therefore be prepared by exciting a coherent superposition of the eigenstates. One way to achieve this is through the absorption of a laser pulse with sufficient spectral bandwidth to encompass both of the eigenstates.

Consider a Fermi resonance between a zero-order bright state $|b\rangle$ and a dark state $|d\rangle$. Although $|b\rangle$ can be prepared directly by the absorption of light, photoexcitation into $|d\rangle$ is prevented by symmetry selection rules or an unfavourable Franck-Condon factor. Their coupling produces a pair of eigenstates $|1\rangle$ and $|2\rangle$:

$$|1\rangle = \alpha_{1b}|b\rangle + \alpha_{1d}|d\rangle, \tag{1.14a}$$

$$|2\rangle = \alpha_{2b}|b\rangle + \alpha_{2d}|d\rangle. \tag{1.14b}$$

In accordance with the time-dependent Schrödinger equation, coherent excitation of $|1\rangle$ and $|2\rangle$ will produce a wavepacket of the form:

$$\begin{aligned}\Psi(t) &= c_1|1\rangle e^{-iE_1t/\hbar} + c_2|2\rangle e^{-iE_2t/\hbar} \\ &= c_1 e^{-iE_1t/\hbar}\left(\alpha_{1b}|b\rangle + \alpha_{1d}|d\rangle\right) + c_2 e^{-iE_2t/\hbar}\left(\alpha_{2b}|b\rangle + \alpha_{2d}|d\rangle\right), \end{aligned} \tag{1.15}$$

where E_1 and E_2 are the energies of the two eigenstates. The coefficients c_1 and c_2 take values such that $\Psi(t=0) = |b\rangle$, *i.e.* the molecule is initially in the zero-order bright vibrational state.

If $|b\rangle$ and $|d\rangle$ are orthonormal then the overlap integral with the zero-order bright state at a given later time t is:

$$\langle b|\Psi\rangle = c_1\alpha_{1b}e^{-iE_1t/\hbar} + c_2\alpha_{2b}e^{-iE_2t/\hbar} \tag{1.16}$$

$$\begin{aligned}|\langle b|\Psi\rangle|^2 &= \left(c_1\alpha_{1b}e^{-iE_1t/\hbar} + c_2\alpha_{2b}e^{-iE_2t/\hbar}\right)\left(c_1\alpha_{1b}e^{+iE_1t/\hbar} + c_2\alpha_{2b}e^{+iE_2t/\hbar}\right) \\ &= c_1^2\alpha_{1b}^2 + c_2^2\alpha_{2b}^2 + c_1c_2\alpha_{1b}\alpha_{2b}e^{i(E_2-E_1)t/\hbar} + c_1c_2\alpha_{1b}\alpha_{2b}e^{i(E_1-E_2)t/\hbar}. \end{aligned} \tag{1.17}$$

Taking the real part, and noting that in general $\cos(\theta) \equiv \cos(-\theta)$, we arrive at an expression for the probability of finding the molecule in the bright vibrational state at a given time t:

$$\mathrm{Re}\,|\langle b|\Psi\rangle|^2 = c_1^2\alpha_{1b}^2 + c_2^2\alpha_{2b}^2 + 2c_1c_2\alpha_{1b}\alpha_{2b}\cos\left(\left(E_2 - E_1\right)t/\hbar\right). \tag{1.18}$$

Thus, if we perform an experiment that is sensitive to the population of the bright state then we will see an oscillation in time, also known as a *quantum beat*, whose frequency depends upon the difference in energy between the two eigenstates. The vibrational energy is being transferred back and forth between the bright and dark states, just as in the classical analogy the energy flowed from the first pendulum to the second and back again. We can see these quantum beats using a variety of time-resolved techniques, some of which will be discussed in Section 1.5.

1.3. The regimes of IVR dynamics

The behaviour that we see in either a frequency-resolved or a time-resolved experiment will depend upon the number of coupled zero-order states. In the simplest case, where there is no significant coupling, an absorption spectrum will show a single peak and no time dependence can be observed if an individual bright state is prepared. It should be noted, however, that under some circumstances multiple bright states can be coherently

excited, leading to time dependence that is not due to IVR. For example, in a diatomic molecule where there is only one normal mode and all zero-order states are bright, a femtosecond laser pulse can be used to create a vibrational wavepacket which is a superposition of vibrational overtones [13]. Although IVR is clearly not possible in this instance, the expectation value of the bond length oscillates in time due to the evolving phase relationship between the coherently excited eigenstates. If a second laser pulse is used to ionise the molecule, then the ion yield may show a quantum beat as a function of the time delay between the excitation and ionisation pulses, as the changing bond length alters the Franck-Condon factor for ionisation [13].

Restricted IVR occurs when the number of coupled states is small but greater than one, as in the Fermi resonance example above. In a time-resolved experiment, the hallmark of restricted IVR is the observation of quantum beats and recurrences; that is to say the molecule periodically returns to the initially prepared bright state. In a frequency resolved experiment, the spectrum will be well structured but the positions and intensities of the peaks will betray the presence of coupling. One example of restricted IVR encountered in this work will be considered in detail in Chapter 7.

At the opposite extreme, if the number of coupled states is sufficiently large, *dissipative* or *statistical* IVR may occur. In a time-resolved experiment, population is lost irreversibly from the initially prepared bright state, usually in the form of an exponential decay (see Section 2.5). Frequency-resolved experiments will generally produce a spectrum containing a broad, unresolved feature. Dissipative IVR is usually seen at relatively high levels of vibrational excitation, and some examples will be studied in Chapter 8.

In between the two limits, it is sometimes possible to observe an intermediate case where a time-resolved experiment shows quantum beats superimposed upon an exponential decay of the bright state population. A frequency-resolved experiment would give a few well-resolved peaks on top of a broad, raised baseline. Some examples of intermediate IVR will be examined in Chapter 9.

1.4. Frequency-resolved studies of IVR

The Fermi resonance example in Section 1.2.1 showed how it is possible to infer the presence of vibrational couplings from a spectrum in which the individual eigenstates are resolved. Although no dynamics take place in such an experiment, we can nonetheless obtain detailed information about IVR. Even dissipative IVR lifetimes can be determined through a careful analysis of the spectral line widths [10]. Eigenstate-resolved experi-

ments are often "safer" to interpret than their time-resolved counterparts, as they are less sensitive to the precise way in which the vibrational states are prepared [13]. An additional advantage of frequency-resolved studies is the ability to select molecules in a particular rotational level, whereas time-resolved experiments show an average over a range of rotational and other quantum states because of the need for a relatively broad excitation bandwidth [10].

Most frequency-resolved studies of IVR to date have taken place in the ground electronic state. Reviews of the extensive literature on this subject can be found in, for example, Refs. [10, 16] and Section 2.2 of Ref. 11. The present investigation, however, is primarily concerned with excited electronic states. Comparatively few frequency-resolved studies have been made of IVR in excited states, as eigenstate resolution is much more difficult to achieve than in the ground state [13]. Nonetheless, in a pioneering fluorescence excitation study with a resolution of $30\,\mathrm{MHz} \equiv 0.001\,\mathrm{cm}^{-1}$, Borst and Pratt [17] have succeeded in observing individual eigenstates resulting from the internal rotation of the methyl group in the S_1 electronic state of toluene. These results gave insights into the possible mechanisms by which a methyl rotor can facilitate IVR, and will be discussed further in Section 2.7.

1.5. Time-resolved studies of IVR

Notwithstanding the potential advantages of frequency-resolved experiments, it is often desirable to obtain a more direct view of the IVR dynamics in real time. Over the past thirty years a number of different spectroscopic techniques have been developed in order to achieve the necessary time resolution, with progress being driven by improvements in both laser and detection technology.

1.5.1. Chemical timing

By 1980 it had become clear that IVR processes sometimes occur on a time-scale of a few tens of picoseconds, making them difficult to observe directly using the technology of the day. Parmenter and co-workers devised an ingenious method, dubbed *chemical timing*, to circumvent this problem [18, 19]. In the first chemical timing experiment [18], which took place in a cell at room temperature, a frequency-doubled continuous-wave argon ion laser[3] was used to excite *para*-difluorobenzene (pDFB) to a vibrational level $2191\,\mathrm{cm}^{-1}$ above the S_1 origin and a dispersed fluorescence spectrum was obtained. The

[3] By a fortunate coincidence, the Ar^+ laser was able to produce the required wavelength directly and so a tuneable laser source was not required in this instance.

spectrum was seen to be highly congested, indicating that IVR was taking place on a time-scale shorter than the fluorescence lifetime of ∼8 ns. The experiment was then repeated in the presence of varying partial pressures of oxygen. Collisions with O_2 can non-radiatively quench the excited pDFB molecules back to the ground electronic state, suppressing the fluorescence. With an oxygen partial pressure of 31.2 ktorr, the S_1 pDFB molecules were on average quenched within 11 ps. Consequently, only those molecules which happened to fluoresce after less than 11 ps were able to contribute to the observed dispersed fluorescence spectrum, and considerably more vibrational structure could be resolved. By examining the ratio of structured to unstructured emission as the oxygen partial pressure was lowered, it was possible to deduce an IVR lifetime of the order of 10 ps.

In a follow-up study, Holtzclaw and Parmenter [20] carried out chemical timing experiments following the excitation of eleven different vibrational levels between 1615 and 3310 cm^{-1} in the S_1 electronic state of pDFB. All showed evidence of IVR, suggesting that the phenomenon is near-universal for vibrational states above ∼1600 cm^{-1} in this molecule. One surprise in that work was the observation of IVR at state densities of just a few levels per cm^{-1}, compared with tens to hundreds of states per cm^{-1}in many non-aromatic molecules. Holtzclaw and Parmenter proposed that, in these cases, the total density of states might have been boosted by rotation-vibration coupling.

A chemical timing comparison of pDFB and its close relative *para*-fluorotoluene (pFT) by Parmenter and Stone [21] proved to be particularly revealing. Thirty of the 38 normal modes in pFT involve mainly motion of the benzene ring, and have near-identical frequencies to their counterparts in pDFB. The two molecules are therefore very similar, apart from the addition of a methyl group in pFT which is free to rotate. This extra degree of freedom was found to lead to dramatic increases in the IVR rates observed following the preparation of four different S_1 vibrational levels. The degree of acceleration depended upon the vibrational level initially excited, but on average was about a factor of 40 [22]. Replacing the CH_3 group with CD_3 had a smaller effect, increasing the rate of IVR by a factor of 2–4 [22]; this was taken as evidence that the spacing of the energy levels of the methyl rotor is of minor importance. Moving the methyl group to the *meta* position, however, led to a further order of magnitude increase in the IVR rate compared with *para*-fluorotoluene [23]. These results are summarised in Fig. 1.4, and possible explanations will be discussed in Section 2.7.

The principal advantage of the chemical timing method is its simplicity, as it does not require time-resolved detection or ultra-fast laser pulses. However, since the observed

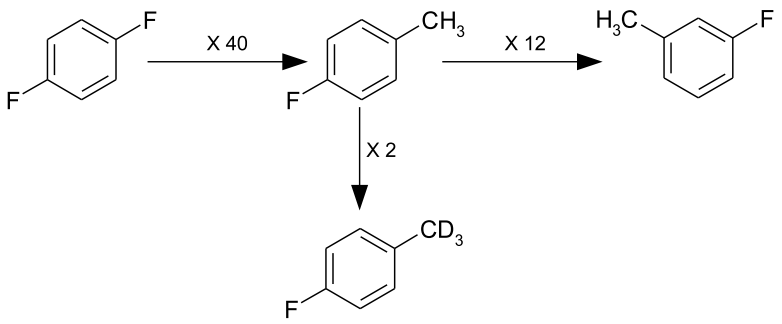

Fig. 1.4. Summary of relative IVR rates observed by Parmenter and co-workers. (Based upon Fig. 1 of Ref. 23.)

fluorescence is time-integrated, this technique is not sensitive to quantum beats such as those predicted by Equation (1.18). An additional disadvantage is that the molecules undergo collisions during the experiments, potentially allowing intermolecular vibrational energy transfer to compete with the purely intramolecular process that we wish to study.

1.5.2. Time-resolved dispersed fluorescence

At about the same time as the first chemical timing experiments, in the early 1980s Zewail and co-workers began developing the "picosecond jet" technique for studying IVR by time-resolved fluorescence [24, 25]. The molecule of interest was cooled in a supersonic jet expansion and excited to a chosen vibrational level in the S_1 electronic state by a laser pulse of $\sim$15 ps duration. A monochromator was used to disperse the resulting fluorescence, which was then recorded by a photomultiplier tube with a time resolution of $\sim$150 ps. (In later experiments, the photomultiplier was replaced by a microchannel plate with $\sim$80 ps resolution.) As a result of changes in the S_1 vibrational state, the intensities of the fluorescence bands showed quantum beats superimposed upon the usual exponential decay. Moreover, bands due to emission from different vibrational states in S_1 were found to oscillate with different phases.

Using this method, in 1984 Felker and Zewail [26] reported the first direct observation of non-chaotic energy flow among multiple vibrational levels in a polyatomic molecule, anthracene. In a classic series of papers [27–30], the same authors went on to develop a formalism to describe and interpret the observed quantum beat patterns. Fourier transformation of the quantum beats yielded a set of frequency components which could be identified with the energy separations of the coherently-excited vibrational eigenstates. From the amplitudes of these frequency components, it was possible to determine the coupling matrix elements connecting the zero-order states. In other words, the time-resolved fluorescence was able to give *quantitative* information about the strength of the

coupling, and the composition of the vibrational eigenstates in terms of the zero-order basis states. Felker and Zewail later summarised these findings in two reviews [31, 32].

In order to compare their picosecond jet method with earlier chemical timing results, Zewail and co-workers undertook a study of IVR in *para*-difluorobenzene and *para*-fluorotoluene [33]. Following the excitation of a C−F stretch at $\sim$1200 cm^{-1} in the S_1 state of pFT, a chemical timing study by Moss and Parmenter [22] had indicated dissipative IVR with a lifetime of 15 ps. By contrast, Zewail and co-workers saw no quantum beats in the fluorescence decay, suggesting a complete absence of IVR. These authors attributed the discrepancy to the difference in sample temperature between the two experiments [33], although it is also possible that their detection time resolution may have been insufficient to observe the beats.

1.5.3. Time-resolved fluorescence depletion

Felker and Zewail's experiments relied upon gating of the signal from a photodetector in order to achieve time resolution. The precision of this gating was therefore the limiting factor, giving a temporal resolution of $\sim$80 ps. In order to achieve more precise timing, McDonald and co-workers developed the technique of *time-resolved fluorescence depletion* (TRFD) [34]. This method uses a "pump-dump" scheme with two laser pulses of equal wavelength and duration (7.9 ps). The "pump" pulse prepares a chosen bright vibrational state in the S_1 manifold. After a variable time delay, the "dump" pulse has two effects: as well as exciting molecules from S_0 into the S_1 bright state, it also causes stimulated emission from the S_1 bright state down to S_0. Crucially, however, any molecules that have undergone IVR into an S_1 dark state will not participate in stimulated emission at this stage.

Following the second laser pulse, the spontaneous $S_1 \rightarrow S_0$ fluorescence is monitored. The intensity of the fluorescence reflects the flow of vibrational energy out of the bright state during the time interval between the two pulses. If extensive IVR took place and few molecules remained in the bright state, then the stimulated emission process will have been inefficient and many molecules remain in S_1, leading to strong spontaneous fluorescence. Conversely, in the absence of IVR, the dump pulse leads to efficient stimulated emission and the subsequent spontaneous fluorescence is weaker.

TRFD was first applied to the study of IVR in the S_1 electronic state of the fluorene molecule [35]. The structure of fluorene is shown in Fig. 1.5. In that work, nineteen different S_1 vibrational levels were examined. No evidence of IVR was observed for

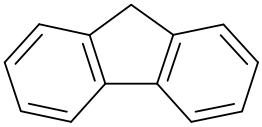

Fig. 1.5. Fluorene.

vibrational levels below 800 cm^{-1}. However clear quantum beats were seen following the preparation of vibrational levels between 800 and 1600 cm^{-1} above the S_1 origin, indicating restricted IVR. Above 1600 cm^{-1} the TRFD results showed that the dissipative IVR regime had been accessed, and could be used to measure the IVR lifetime.

McDonald and co-workers also successfully used their TRFD technique to investigate the IVR dynamics of *para*-cyclohexylaniline [36]. As in fluorene, they were able to detect quantum beats following the preparation of several different vibrational levels. A bright state at 484 cm^{-1} showed a particularly interesting beat pattern in which two frequency components could be resolved, suggesting coupling to two different dark states. In a follow-up study on the same molecule [37], the IVR rates and quantum beat patterns were shown to be temperature-dependent, suggesting that low-frequency vibrations and molecular rotations may play a role in the IVR mechanism.

1.5.4. Picosecond IR pump, UV probe spectroscopy

A common feature of all the time-resolved techniques discussed above is a focus on IVR dynamics in an excited electronic state. Ebata and co-workers [38] have developed a pump-probe spectroscopic technique for direct time-resolved study of IVR dynamics in the *ground* electronic state. In these experiments, the molecule of interest is cooled in a supersonic molecular beam and an infra-red laser pulse of $\sim$12 ps duration is used to prepare a chosen bright vibrational state. An ultra-violet probe pulse, also of 12 ps duration, then ionises the molecule using a $(1+1)$ resonance-enhanced multi-photon ionisation (REMPI) scheme. REMPI is a two-step process in which the molecule is first excited to the S_1 electronic state, and then ionised by a second UV photon. The ion yield is recorded as a function of both the UV wavelength and the time delay between the IR and UV pulses. The efficiency of ionisation is dramatically enhanced when the UV photon energy is resonant with the transition to one of the vibrational levels in the S_1 electronic state, and so for a given time delay a plot of ion yield against wavelength gives information equivalent to a UV absorption spectrum. From this, it is possible to infer the nature of the vibrational state in S_0 at the moment when the first UV photon was absorbed.

Ebata and co-workers have focussed their experiments mainly on phenol, aniline and various deuterated isotopologues. Following the excitation of the O−H stretch in isolated phenol, dissipative IVR was observed with a lifetime of 14 ps [38]. A comparison of the IVR rates for different isotopomers suggested that the mechanism for IVR is mediated

via a C−H stretch or bend in this instance. These authors were also able to gain insights into the IVR dynamics of phenol clusters and a series of phenyl alcohols with varying carbon chain lengths; details can be found in Ref. 38 and references therein.

1.5.5. Time-resolved photoelectron spectroscopy

In recent years, time-resolved photoelectron spectroscopy has gained considerable popularity for studies of molecular dynamics in excited electronic states (see, for example, reviews in Refs. [39–41]). Many of these experiments have made use of femtosecond laser pulses, which allow the observation of various ultra-fast processes. However, the Fourier transform-limited bandwidth of such pulses is typically $\sim$100 cm^{-1}, which is not sufficient to resolve vibrational levels in the cation. For this reason, picosecond pulses represent a more suitable compromise between time- and energy resolution for studies of IVR [13].

In a pump-probe scheme, the molecule is first excited to a chosen vibrational level, usually in the S_1 electronic state, and then ionised by a second photon. The ionisation step projects the vibrational state in S_1 onto the vibrational levels of the cation. The photoelectron spectrum consists of a series of peaks which correspond to the formation of different cation vibrational levels, and their relative intensities are determined by the Franck-Condon factors connecting the S_1 state to the cation. These in turn depend upon the nature of the vibration in the S_1 state at the time of the probe laser pulse's arrival. Changes in the photoelectron spectrum as a function of the time delay between the two laser pulses therefore give a direct view of the progress of IVR, with a temporal resolution limited by the pulse duration.

One of the earliest experiments of this kind was carried out by Reilly and co-workers [42] in 1990. In that work, laser pulses of approximately 10–15 ps duration were used to excite and ionise *para*-n-butylaniline (Fig. 1.6), with time-of-flight (TOF) measurements to determine the velocity distribution of the photoelectrons. The photoelectron spectrum was shown to be time-dependent, with the $\Delta v = 0$ peak becoming broadened and other peaks corresponding to the "bright state" decreasing in intensity as the pump-probe time delay was increased.

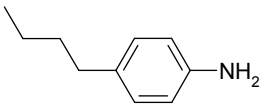

Fig. 1.6. *Para*-n-butylaniline.

At about the same time, Knee and co-workers published a pioneering study of IVR in fluorene (Fig. 1.5) in a molecular beam, using time-resolved zero electron kinetic energy (ZEKE) spectroscopy with laser pulses of 10–15 ps duration [43, 44]. ZEKE is a very high resolution variant of photoelectron spectroscopy which will be explained fully in Chapter 4. In those experiments, a fixed pump laser wavelength was used to prepare a

chosen vibrational level in the S_1 electronic state. The yield of electrons produced at the ionisation threshold (*i.e.* with no kinetic energy) was then recorded as the probe laser wavelength was scanned. By avoiding the requirement to measure the velocity of the photoelectrons, a resolution of $\sim$6 cm^{-1} was achieved.

Clear vibrational structure could be seen in the spectra taken at 0 ps time delay. With the excitation laser tuned to an S_1 vibrational feature at 834 cm^{-1} above the origin, the intensities of two photoelectron peaks were seen to oscillate in time with a period of 125 ps. One of these corresponded to ionisation from the 'bright' vibrational state and was maximised at time zero, whereas the other was due to ionisation from a 'dark' state and oscillated with the opposite phase. These quantum beat patterns were interpreted as the result of couplings amongst a small number of zero-order vibrational states. Different behaviour was seen on excitation of a higher S_1 vibrational level at 1707 cm^{-1}, with a loss of structure in the spectrum over time. A measurement of the intensity of the major photoelectron peak revealed an exponential decay, indicating dissipative IVR with a lifetime of 80 ps.

This early experiment served as a proof of concept for the study of IVR with picosecond time-resolved photoelectron spectroscopy. Knee and co-workers went on to apply the technique to acenaphthene [45], van der Waals complexes [45–47], *para*-difluorobenzene [45, 48] and benzene [49]. Unfortunately, although the ZEKE experiments were able to give very detailed spectra, they were extremely time-consuming to perform because of the need to scan the probe laser wavelength. Full ZEKE spectra could therefore only be obtained at a few selected time delays, as each one took several hours to complete. In order to obtain more detailed information about the time dependence, the probe laser wavelength was fixed to a selected feature in the spectrum and the ZEKE signal monitored as the time delay was scanned.

An additional problem was the relatively long pulse duration, which meant that only IVR processes on a time-scale of more than 15 ps could be studied. The chemical timing experiments of Parmenter and co-workers had demonstrated that in many cases IVR proceeds faster than this, with lifetimes of around 10 ps being observed [18]. In 2002, Reid and co-workers pioneered the use of $\sim$1 ps laser pulses for time-resolved photoelectron spectroscopy, in order to observe IVR processes in *para*-fluorotoluene [50]. Due to the relatively broad bandwidth of the laser used in that work, it was not possible to select an individual bright vibrational state in S_1; instead a mixture was prepared comprising approximately 80% of a C$-$F stretching fundamental at 1230 cm^{-1} and 20% of a C$-$CH$_3$ stretching fundamental at 1194 cm^{-1}. Time-of-flight measurements were used to obtain

a photoelectron spectrum, which had well-resolved vibrational structure when the pump and probe laser pulses were overlapped in time. As the pump-probe time delay was increased up to a maximum of 1000 ps, the photoelectron spectrum was seen to become increasingly congested due to dissipative IVR. These results were consistent with the IVR lifetime of ∼15 ps previously measured in the chemical timing experiments of Parmenter and co-workers [21, 51].

In a follow-up study, Whiteside *et al.* [52, 53] applied time-of-flight photoelectron spectroscopy to investigate the IVR dynamics following the preparation of four different S_1 vibrational levels in toluene. When nanosecond laser pulses were used to excite and ionise, little structure could be resolved in the photoelectron spectrum. In three of the four cases more structure emerged on reducing the pulse duration to 1 ps, although some congestion still remained. The spectra from a $C-CH_3$ stretching vibration at $\sim 1193\,cm^{-1}$ were shown to be highly time-dependent, with the vibrational structure being rapidly lost as the pump-probe time delay was increased.

More recent studies of IVR carried out within our research group have relied mainly on the use of *velocity map imaging* (VMI) [54] to record time-resolved photoelectron spectra. This technique is central to the present investigation, and will be explained in detail in Chapter 3. In essence, an electric field is used to focus the photoelectrons onto a phosphor screen, forming an image that contains information about their velocity distribution. Fast-moving electrons strike close to the edges of the screen, whereas slower electrons arrive nearer the centre of the image. Since the electrons are actively pushed towards the detector, a collection efficiency of almost 100% is achieved. By contrast, a time-of-flight photoelectron spectrometer can only detect the small fraction of photoelectrons that happen to be ejected along the axis of the flight tube. A second advantage of VMI is the ability to record the complete photoelectron angular distribution in a single measurement. Although this angular information is valuable in studies of photoionisation dynamics [55], it has so far proved to be of limited utility to our investigations of IVR in aromatic species [13].

In the first of these time-resolved VMI studies, King *et al.* [56] compared the IVR behaviour of three different initially-prepared vibrational levels in the S_1 electronic state of *para*-fluorotoluene. In each case, when the pump and probe pulses were overlapped in time, the photoelectron spectrum showed a series of partially resolved peaks which could be assigned to vibrational levels in the cation. As the pump-probe time delay was increased, the spectra became more congested due to IVR. The spectra following the preparation of a C−F stretching vibration at $1230\,cm^{-1}$ in S_1 proved to be particularly

interesting. After 2 ps a peak appeared at $\sim$1150 cm^{-1} which had not been present at 0 ps, and was assigned to a single quantum of a totally symmetric in-plane "pinching" motion of the C−H bonds on the benzene ring. This suggested that a similar motion was taking place in the S_1 electronic state, and is believed to be the first example of the identification of a dark state involved in IVR. After 4 ps the spectrum had become more complicated, but by 6 ps the structure was remarkably similar to that seen at 2 ps. This hinted at the possibility of an oscillation between two different zero-order vibrational states.

Clearer evidence for oscillatory behaviour was later seen in a study of a Fermi resonance in toluene by Hammond *et al.* [13, 57, 58], which demonstrated the ability of picosecond time-resolved VMI to follow the evolution in time of a simple vibrational wavepacket. In that work, laser pulses of $\sim$1 ps duration were used to excite a coherent superposition of the eigenstates created by the coupling of a ring stretching fundamental ($6a^1$) to a combination of bending motions ($10b^1 16b^1$) in the S_1 electronic state.[4] Partial vibrational resolution was achieved in the photoelectron spectrum, which at 0 ps was characteristic of ionisation out of the $6a^1$ zero-order bright state. As the time delay between the pump and probe pulses was increased up to a maximum of 10 ps, the intensities of two of the peaks showed a regular oscillation with a period of 3 ps. The origin peak, which resulted mainly from ionisation out of $6a^1$, was maximised at 0 and 6 ps. Conversely, a peak at $\sim$500 cm^{-1} oscillated with the opposite phase, indicative of ionisation from the $10b^1 16b^1$ dark state. Although this experiment was an important milestone showing the utility of time-resolved VMI in studies of IVR, it did not reveal the full story. In Chapter 7 of the present work, the $6a^1$ / $10b^1 16b^1$ system is revisited with higher spectral resolution and a greater range of pump-probe time delays, revealing some complications that were not apparent in the original study.

More recent work by our group has employed a refinement of VMI in which different laser wavelengths are used for the excitation and ionisation steps. By lowering the probe photon energy, and hence the kinetic energies of the photoelectrons, it is possible to achieve substantially better energy resolution in the photoelectron spectrum. This technique is known as *slow electron velocity map imaging* (SEVI) [59, 60], and will be explained in detail in Section 3.4. In the first application of time-resolved SEVI to the study of IVR dynamics, Hammond and Reid [13, 58, 60] re-investigated the C−F stretching vibration in *para*-fluorotoluene that had previously been studied with time-resolved one-colour VMI [56]. The resolution achieved was improved by roughly a factor of three

[4] This notation for the normal modes of toluene is explained in Appendix A.

[60] compared with the earlier work, revealing three small peaks that had not previously been observed. By examining the time dependence of these features, it was possible to infer a coupling between the initially prepared bright state and dark state consisting of three quanta in a ring stretching mode [60]. This result demonstrated that the improved resolution offered by SEVI over one-colour VMI could allow significantly more information about the dynamics to be deduced.

1.6. Aims, objectives and overview

This work is aimed at achieving a better understanding of the IVR mechanisms that operate in the S_1 excited electronic state of toluene, by comparing the dynamics from different initially-prepared vibrational levels. Comparisons are also drawn with the isotopologue $C_6H_5CD_3$, in which the methyl group is fully deuterated. The choice of molecule is inspired by the chemical timing studies of Parmenter and co-workers (see Section 1.5.1), who showed that the rate of IVR in benzene derivatives is strongly influenced by structural factors such as the position of the substituents on the aromatic ring. The addition of a methyl rotor was seen to have a particularly dramatic effect, increasing the IVR rate by a factor of 40. Substituted benzenes are therefore interesting targets for investigations into the mechanisms of IVR, since families of related molecules may readily be compared. These compounds also have a practical advantage for the experimentalist, in that their $S_1 \leftarrow S_0$ electronic transitions fall within a wavelength range easily accessed by ultraviolet lasers.

The techniques employed will be explained in Part II. Photoelectron spectroscopy is used to look for the signatures of IVR in both the time and frequency domains, supported by theoretical calculations to assist with the interpretation and assignment of the spectra.

Chapter 3 describes the equipment and methods used to perform picosecond time-resolved experiments, which build upon our research group's preliminary studies discussed above in Section 1.5.5. That early work demonstrated the ability of photoelectron velocity map imaging, in conjunction with laser pulses of 1 ps duration, to identify a dark vibrational state involved in IVR [56] and to observe the evolution of a vibrational wavepacket in real time [57]. Those experiments were carried out in the Lasers for Science facility of the Rutherford-Appleton Laboratory, but for the current project a new picosecond laser system was delivered to Nottingham in December 2007. In addition to the increased beam time available, the in-house laser system gives us the capability to produce pump and probe beams with independently-tuneable wavelengths, facilitating

the use of the SEVI technique to improve the resolution of the photoelectron spectra (see Section 3.4).

Frequency-resolved studies require a combination of a high resolution photoelectron detection scheme and a laser source with sufficiently narrow bandwidth to prepare a single vibrational level in S_1, rather than the superposition created by a picosecond pulse. The solution, described in Chapter 4, is to obtain zero kinetic energy (ZEKE) photoelectron spectra with laser pulses of $\sim$5 ns duration. This work is believed to be the first study of the ZEKE spectra *via* excited vibrational levels in S_1 toluene.

Chapter 5 describes the use of density functional theory and the configuration interaction singles (CIS) method to calculate the vibrational frequencies and normal coordinates of toluene in each of the electronic states of interest. These calculations are performed for the neutral species in the S_0 and S_1 electronic states, as well as the D_0 ground state of the cation. The calculated frequencies and normal modes are then used to derive the Franck-Condon factors connecting the S_1 state to the ion, in order to simulate the appearance of the photoelectron spectra from different S_1 vibrational levels. Two methods are also presented for finding the vibrational density of states as a function of internal energy, which is one of the important quantities to be considered when attempting to rationalise the observed IVR behaviour from different initially prepared states.

The experimental results and conclusions are presented in Part III. Chapter 6 focusses upon the vibrational levels for which no time dependence was observed in the picosecond experiments; these spectra are primarily of interest as a means of characterising the vibrational levels of the toluene cation. The picosecond SEVI spectra are compared side by side with the corresponding nanosecond ZEKE spectra. Accurate frequencies are established for eight normal modes in the cation, three of which had not been measured previously.

The remaining results are divided up according to the regime of IVR dynamics observed. Chapter 7 examines the restricted IVR regime, re-visiting a Fermi resonance that was first studied in the preliminary experiments at the Rutherford-Appleton Laboratory [13, 57, 58]. With the increased resolution achieved through the use of SEVI, and the ability to measure spectra over a greater range of time delays, this system has been revealed to be more complicated than previously thought. Furthermore, by adapting the equations originally developed by Felker and Zewail [27] to describe fluorescence quantum beats, it has been possible to derive the elements of the vibrational coupling matrix from the time-resolved photoelectron spectra [61].

Chapter 8 deals with three examples of the opposite limiting case, in which the coupling

of many vibrational levels leads to dissipative IVR. The time-resolved photoelectron spectra show an irreversible loss of population from the initially prepared bright vibrational state, and can be used to derive a rate constant for the IVR process. A comparison of the observed rates suggests that they depend upon the nature of the vibrational motion initially excited, and are not simply determined by the internal energy or the density of states.

Two interesting intermediate cases are presented in Chapter 9. These vibrational levels initially display the quantum beats expected for restricted IVR, but at longer time delays the photoelectron spectra show a loss of structure which indicates dissipative IVR. This behaviour suggests that the IVR mechanism proceeds *via* a so-called "doorway state" which is strongly coupled to the initially prepared zero-order bright state. One of the doorway states can be assigned with confidence, and several possible candidates for the identity of the other doorway state are proposed.

Finally, in Chapter 10 the conclusions reached from this work are summarised and future research directions are suggested.

2. Theories and models for the study of IVR

In Chapter 1 a brief overview was given of the phenomenon of intramolecular vibrational energy redistribution and the methods by which it can be studied. This chapter provides further details of the theoretical foundations upon which the present investigation relies, including a discussion of the mechanisms by which IVR can occur and the models that can be used to rationalise the observed dynamics.

2.1. Notation for the normal modes of toluene

The toluene molecule, $C_6H_5CH_3$, has fifteen atoms and hence $3 \times 15 - 6 = 39$ normal modes. Thirty-eight of these are true vibrations. The one remaining degree of freedom is the internal rotation of the methyl group, which will be considered further in Section 2.7. Several different notation schemes have been developed by various authors to label the vibrational modes, which can lead to confusion when consulting the literature on the spectroscopy of toluene. In this section, a brief overview will be given of the most common labelling systems and the conventions adopted in the present work will be established.

One of the simplest schemes is the Mulliken convention [62], in which the normal modes are first sorted according to their symmetry classification and then numbered in order of decreasing frequency. Such a system was adopted by Hickman *et al.* [63] for a dispersed fluorescence study of toluene which established several normal mode frequencies in the S_1 electronic state. Although the assignment of Mulliken labels to normal modes is systematic and unambiguous, this numbering scheme is difficult to use when comparing different molecules. Any change to the substituents on the benzene ring may result in a change in the energy ordering of the normal modes, and thus a given normal mode in toluene may have a different Mulliken number from its closest equivalent in, say, *para*-fluorotoluene. Similar problems can arise when considering different electronic states of a single molecule.

An alternative approach is based upon the work of Wilson [64], who was the first to derive the normal modes of benzene using group theory. In Wilson's notation, which pre-dates the establishment of the Mulliken convention, the normal modes are numbered from 1 to 20. Pairs of degenerate modes are distinguished by the suffixes a and b to give

a total of thirty labels. Some of the normal modes of other benzene derivatives, such as toluene, can therefore be given labels by analogy with the diagrams given in Wilson's paper. However, as Hickman *et al.* [63] have noted, the normal modes of toluene are sufficiently different from those of benzene as to make some of the choices of Wilson labels rather ambiguous. Certain modes have therefore been given different names by different authors; the conversions between some of these schemes are listed in Table 1 of Ref. 63.

The convention adopted in the present work is an extended version of the Wilson notation developed by Varsányi [65]. Recognising the ambiguities which can arise when making comparisons with benzene, Varsányi gives a separate set of normal mode diagrams for each class of benzene derivatives (*e.g.* monosubstituted, *para*-disubstituted etc.), and also provides extra labels for modes that have no equivalent in benzene. Toluene has eight normal modes that are primarily associated with the methyl group, and these are represented by using the Greek letters ν and δ to denote methyl C−H stretches and bends respectively. Symmetric and asymmetric bends and stretches are distinguished by the subscripts 's' and 'as'. Among the asymmetric bending (δ_{as}) modes, a '+' superscript indicates a rocking motion of the whole methyl group, whereas a '−' superscript is used for bends within the CH_3 unit.

The normal mode motions associated with each Varsányi label are shown for toluene in Appendix A, and for the deuterated isotopologue $C_6H_5CD_3$ in Appendix B. These diagrams are derived from density functional theory and Configuration Interaction Singles (CIS) calculations which will be described in Section 5.1. Since a full calculation of the normal modes was not possible at the time of Varsányi's work, some of the modes do not exactly match the approximate diagrams given in Ref. 65 (see Section 5.1.1). Separate sets of diagrams are given for the neutral S_0 and S_1 electronic states and for the cation, since the normal modes of each electronic state are slightly different. The implications of these differences will be considered further in Section 2.3.

2.2. Mechanisms of vibrational coupling

In Section 1.1.2 it was noted that the zero-order vibrational states given by the harmonic oscillator model are not eigenstates of the real molecule, and in many cases are therefore coupled to one another. In this section, the mechanisms by which couplings take place will be examined in more detail. Selection rules will also be presented that determine which combinations of zero-order states are able to couple. Couplings arise for two

reasons: failure of the harmonic model for the potential energy, and failure of Equation (1.3) which separates the vibrations from other degrees of freedom.

2.2.1. Anharmonic coupling

In the harmonic oscillator picture, the vibrational energy can be separated out into a sum of contributions from a set of normal modes. However, this separation relies on the assumption that the potential has a quadratic form; that is to say the potential energy increases with the square of the atomic displacement from the equilibrium position. For small displacements the quadratic potential is a reasonable approximation; however at larger displacements a real chemical bond will weaken and eventually break. If a more realistic, anharmonic potential is used then cross terms containing the quantum numbers of two or more modes begin to appear in the expression for the energy: the normal modes are no longer independent of one another [66]. These cross terms lead to *anharmonic coupling*, which can in some cases be very strong; one example is the Fermi resonance in CO_2 that was discussed in Section 1.2.1. Anharmonic coupling is possible among sets of zero-order states which have similar frequencies and share the same symmetry irreducible representation.

2.2.2. Rotation-vibration coupling

The concept of a "vibrational state" can only be defined if we assume that the vibrational motion is independent of the other degrees of freedom (see Section 1.1). This separation is, however, not rigorous. If a molecule is rotating, then its atoms will experience the two pseudo-forces which appear in rotating reference frames. A *centrifugal force* pushes the atoms away from the centre of rotation. In addition, due to the vibrations, some of the atoms are moving with respect to the rotating molecular reference frame. They will therefore experience a *Coriolis force*, which acts perpendicularly to the direction of motion and to the axis of rotation.

The Coriolis forces lead to a coupling between rotation and vibration. In a classical picture of a bond stretching motion, the atoms no longer move in straight lines, but in ellipses because they are being pushed sideways by the Coriolis force [66]. The normal mode frequencies are therefore affected by the rotational quantum number. More interestingly, however, Coriolis interactions can also cause different zero-order vibrational states to couple together. One simple example, shown in Fig. 2.1, is a coupling between the bending and anti-symmetric stretching vibrations of a linear triatomic molecule.

According to *Jahn's rule*, Coriolis coupling is allowed if the direct product of the

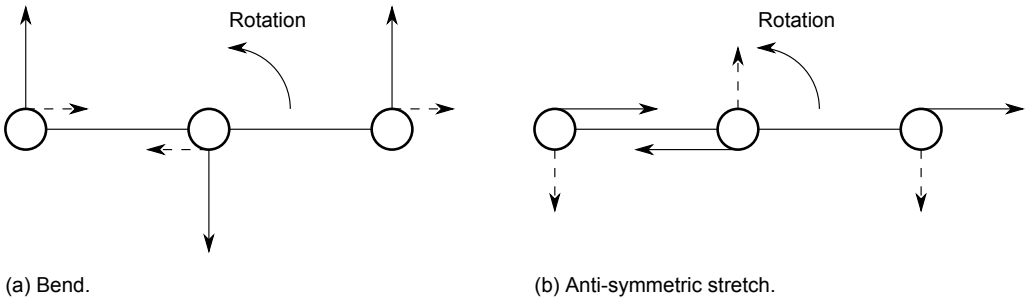

Fig. 2.1. Example of Coriolis coupling between bending and anti-symmetric stretching vibrations in a linear triatomic molecule. The solid arrows represent atomic displacements and the dashed arrows indicate the direction of the Coriolis forces. (This diagram is based upon Fig. 100 of Herzberg's textbook [66].)

symmetries of the two vibrations contains the species of a rotation [66]. For the purposes of vibrational analysis, it is convenient to regard toluene as belonging to the point group C_{2v}. This is an approximation which neglects the structure of the methyl group. In C_{2v}, the three rotations transform as A_2, B_1 and B_2. Examination of the direct product table [67] reveals that Coriolis coupling is allowed between any two vibrational states whose symmetries differ. Thus, *in C_{2v} molecules, Coriolis coupling is allowed if anharmonic coupling is forbidden and vice-versa.*

Lawrance and Knight [68] have carried out a detailed theoretical examination of the relative importance of Coriolis and centrifugal coupling in IVR processes. Centrifugal coupling of zero-order states is subject to a different selection rule: the direct product of the vibrational symmetries must be the same as the direct product of the symmetries of any two rotations. In C_{2v}, this means that centrifugal coupling is always allowed by symmetry. Coriolis coupling is the stronger of the two interactions in low rotational levels, but for rotational quantum numbers $J \approx 40$ to 100 centrifugal coupling becomes comparable to Coriolis coupling. In higher rotational levels, centrifugal coupling is the dominant mechanism. However, in the rotationally cool environment of a supersonic molecular beam, only low J levels are populated and centrifugal coupling is negligible. In the present work, the experiments were carried out at a rotational temperature of $\sim$10 K (see Section 3.2) and we should not expect to see any effects from centrifugal coupling.

2.3. Mode coupling versus mode mixing

Coupling of zero-order states is a consequence of the breakdown of the harmonic oscillator approximation. However, even when the harmonic oscillator model remains valid, the

normal modes of a given molecule will change if it undergoes a transition to a different electronic state. For instance, as can be seen from the diagrams in Appendix A, some of the normal modes of a toluene molecule in the S_0 electronic state differ significantly from their counterparts in the S_1 electronic state and the cation. This effect arises because the change of electronic structure affects the force constants of the chemical bonds.

In the experiments described in this work, photoelectron spectra are recorded following ionisation from the S_1 electronic state, thus projecting the vibrational state in S_1 onto the vibrational levels of the cation. It is therefore convenient to regard the cation normal modes as "mixtures" of the S_1 normal modes. Although this mixing is unrelated to coupling or IVR, it must be taken into account when interpreting the spectrum. The mixing is usually expressed in terms of the *Duschinsky transformation* [69]:

$$\vec{Q'} = \mathbf{S}\vec{Q} + \vec{d}, \tag{2.1}$$

where $\vec{Q}$ and $\vec{Q'}$ are the normal coordinates of the two electronic states, $\mathbf{S}$ is a rotation matrix and $\vec{d}$ is an offset vector. The off-diagonal elements of the $\mathbf{S}$ matrix quantify the extent of the mixing between the normal modes.

It should be noted that the Duschinsky transformation is not exact, because it assumes that the molecular axis system is the same for both electronic states. Özkan [70] has pointed out that this is not strictly true, and so in general a non-linear transformation is more accurate. However, this subtlety is beyond the scope of the present work.

2.4. Competition between IVR and other processes

The picosecond experiments carried out in this work are sensitive to the population of the initially prepared bright vibrational state as a function of time. It is therefore important to consider all of the possible processes, in addition to IVR, which could potentially cause a loss of population from the bright state. These include fluorescence and internal conversion from the S_1 to the S_0 electronic state, and inter-system crossing (ISC) from S_1 to a triplet state. The time-scale of the experiments is typically $\sim$500 ps, and so processes with a lifetime substantially longer than this are unlikely have a significant influence on the results.

The fluorescence lifetime of toluene varies according to the vibrational level excited in S_1. Hickman *et al.* [63] have reported lifetimes ranging from 86 ns for the S_1 vibrational origin to 48 ns at an S_1 vibrational energy of 1900 cm^{-1}. Even the shortest of these is almost two orders of magnitude greater than the longest pump-probe time delay used in

the present time-resolved experiments, suggesting that the loss of S_1 population due to fluorescence is negligible.

Smalley and co-workers [71] have measured the rate of inter-system crossing in toluene using two-colour laser photoionisation. In that work, the molecules were initially excited to the vibrational origin of the S_1 electronic state and the ion yield was measured as a function of the time delay between the excitation and ionisation laser pulses. The second laser pulse was capable of achieving ionisation either from S_1, or from the T_1 electronic state produced by inter-system crossing. A biexponential decay of ion yield was therefore observed, reflecting the separate decays of population from the S_1 and T_1 states. Analysis of this decay indicated an ISC rate constant of $8.5\,(\pm 0.2) \times 10^{-6}$ s^{-1}, which is equivalent to a lifetime of approximately 12 µs. Furthermore, the combined quantum yields of fluorescence and ISC were able to account for $94 \pm 14\%$ of the decay of S_1 population, suggesting that $S_1 \rightsquigarrow S_0$ internal conversion is relatively unimportant in toluene.

It therefore seems likely that, on the 500 ps time-scale of the experiments, any loss of population from the bright state will be almost entirely due to IVR as the competing processes are too slow to have any significant effect.

2.5. IVR dynamics in the statistical limit: Fermi's Golden Rule

One of the most basic factors influencing IVR is the *density of states*, $\rho(E)\,\mathrm{d}E$, which is defined as the number of vibrational levels that exist within an energy range E to $E + \mathrm{d}E$. This depends upon both the structure of the molecule and the degree of vibrational excitation, rising sharply as the internal energy is increased. Methods for calculating $\rho(E)$ will be discussed in Section 5.3.

Density of states arguments are frequently used to rationalise the existence of the different regimes of IVR that were discussed in Section 1.3. When the density of states is low, each zero-order state will have few neighbours sufficiently close in energy for coupling and so we can expect to see restricted, or possibly no IVR. At higher densities of states, the number of zero-order states available for coupling to an initially prepared bright state is larger and dissipative IVR becomes a possibility. This explains why, in most molecules, a certain threshold energy can be identified at which IVR begins [11].

Bixon and Jortner [72] have developed a model to quantify the effect of the density of states upon the rates of non-radiative transitions, including but not limited to IVR, in the limit where $\rho(E)$ is large. The following simplifying assumptions are made:

- The vibrational levels are equally spaced in energy.
- All of the zero-order dark states have equal coupling strength to the bright state.
- The interaction energies of the zero-order states (*i.e.* off-diagonal elements of $\hat{\mathrm{H}}_{\mathrm{vib}}$ in the harmonic oscillator basis) are much greater than the spacing between the zero-order vibrational levels.

Bixon and Jortner showed that, when these approximations are valid, the population of the initially prepared bright state will decay exponentially over time:

$$|\langle \Psi(t) | \Psi(t=0) \rangle|^2 = \exp(-k_{\mathrm{IVR}} t), \tag{2.2}$$

$$k_{\mathrm{IVR}} = 2\pi \left\langle V^2 \right\rangle \rho. \tag{2.3}$$

Equation (2.3) is equivalent to Fermi's Golden Rule, which is more commonly derived by perturbation theory in order to describe the rates of radiative transitions [14]. In this expression, ρ is the averaged density of states and $\left\langle V^2 \right\rangle$ is the mean square of the off-diagonal elements of the vibrational Hamiltonian matrix.

At first sight, it might appear that the IVR rate should be directly proportional to ρ. However, this is only true if *all* of the dark states have roughly equal coupling strength to the bright state. If ρ is increased by adding states which are not significantly coupled to the bright state, then there will be a corresponding decrease in $\left\langle V^2 \right\rangle$ and little change in the IVR rate [12].

The C−H stretches of terminal acetylenes provide an interesting example of this type of behaviour [12]. In 1-butyne ($\mathrm{H_3C{-}CH_2{-}C{\equiv}CH}$) there are 22 states per $\mathrm{cm^{-1}}$Ḟollowing the preparation of a single quantum of the terminal C−H stretch, the IVR lifetime inferred from a high resolution infra-red spectrum is 270 ps. Adding an extra carbon atom to the chain (1-pentyne) increases the state density by more than two orders of magnitude, to 2400 levels per $\mathrm{cm^{-1}}$. However the IVR rate following excitation of the C−H stretch increases by less than a factor of two, with measured lifetimes of 240 ps for the *gauche* conformer and 440 ps for the *trans* conformer. An extreme case is $\mathrm{(CF_3)_3C{-}C{\equiv}CH}$, which has 10^{11} states per $\mathrm{cm^{-1}}$, yet has an IVR rate only four times faster than *gauche*-pentyne (lifetime of 60 ps).

2.6. Doorway states and the tier model

If the IVR rate constant is found to be relatively insensitive to the density of states, then that suggests an IVR mechanism which is dominated by "local" couplings between the

bright state and a few particular dark states. Some of these may be so-called *doorway states*,[1] from which many other dark states can be accessed [12].

The *tier model* is a refinement of the doorway state picture in which the dark states are organised into a hierarchy according to the strength of their coupling to the bright state (see Fig. 2.2). In the first tier are the doorway states, which couple relatively strongly to the bright state. From here, the vibrational energy flows sequentially through the series of tiers, each of which contains more states than the previous one and has a weaker coupling to the bright state. Typically the change in the total number of vibrational quanta compared with the bright state (Δv) increases from one tier to the next; for instance the first tier might have mainly $\Delta v = 3$ or 4, the second tier $\Delta v \leq 8$ and so on [12].

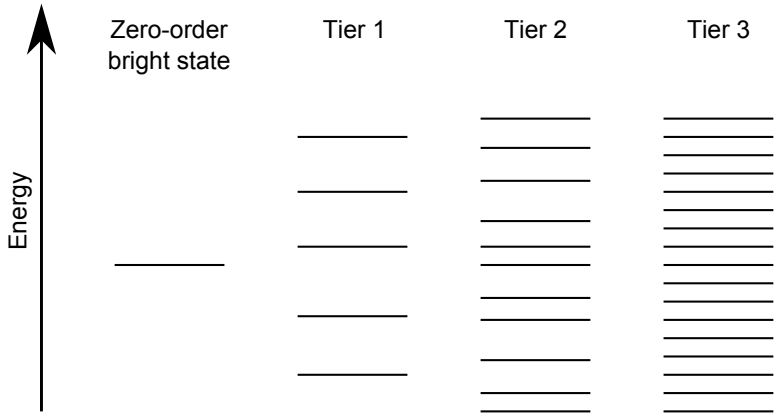

Fig. 2.2. The tier model of IVR. In this picture the strength of coupling to the zero-order bright state decreases rapidly with increasing tier number. However the average coupling between the bright state and the states of tier 1 is comparable with the average couplings between tiers 1 and 2, 2 and 3 etc. Each tier contains more states than the previous one. (This diagram is based upon Fig. 3 of Ref. 12.)

Since we do not know the form of the eigenstates of the vibrational Hamiltonian, our choice of the harmonic oscillator eigenstates as our basis set is somewhat arbitrary. We could equally well have used any other set of orthogonal basis functions, such as the localised bond vibrations that arise from an internal coordinate analysis. One might therefore question whether or not the division of the zero-order states into tiers is physically meaningful. In many cases, however, spectroscopy provides direct evidence that the tiers are in some sense real [12]. At low resolution, an absorption spectrum will show a single peak which corresponds to the zero-order bright state. As the resolution is gradually increased, the peak first splits into a series of lines which correspond to the doorway states of tier 1. These then split further to reveal the states of tier 2 and so on,

[1] Note that this usage of the term "doorway state" differs from that favoured by Felker and Zewail [27–32]. In their work, zero-order bright states are referred to as "absorption doorway states"; similarly any state which exhibits fluorescence is called a "fluorescence doorway state".

becoming progressively weaker as the coupling to the bright state becomes smaller from one tier to the next.

In situations where it is possible to estimate the strength of the couplings, a tier model can be constructed in quantitative terms. One example can be found in the work of Stuchebrukhov and Marcus [73], who developed a computer model to describe IVR in a family of terminal acetylenes of the form $(CX_3)_3Y{-}C{\equiv}CH$. Here X represents H or D and Y is C or Si. These authors were able to calculate the absorption line widths of the C−H stretches, which are equivalent to IVR lifetimes, with a high degree of success. However, the details of the computations are beyond the scope of the present work.

2.7. Influence of methyl rotors

As discussed in Section 1.5.1, the chemical timing experiments of Parmenter and co-workers have revealed that IVR proceeds very much faster in *para*-fluorotoluene than in its close relative *para*-difluorobenzene [21, 22]. The difference was attributed to the fact that the methyl group in *para*-fluorotoluene is free to rotate [22, 23, 74, 75]. In this section, an outline will be given of the quantum mechanical treatment of methyl rotors and their possible implications for IVR dynamics. The rotation of the methyl group is also called *torsion*.

2.7.1. Unhindered rigid rotor model

The simplest model for the methyl torsion assumes that there is no energy barrier to rotation and that the torsion is independent of all other motions. We also neglect the possibility of centrifugal distortion. In this case, the Schrödinger equation for the rotor is equivalent to that of a particle on a ring:

$$-B\frac{\partial^2\psi(\phi)}{\partial\phi^2} = E\psi(\phi), \tag{2.4}$$

where $B = \hbar/2I$ is the reduced[2] rotational constant, I is the moment of inertia and ϕ is the angle between one of the C−H bonds and the benzene ring. Equation (2.4) has an analytic solution [77] of the form:

$$\psi_m(\phi) = \frac{1}{\sqrt{2\pi}}e^{im\phi}, \tag{2.5}$$

[2] A *reduced* rotational constant is needed because the methyl and phenyl groups are rotating in opposite directions about a common axis [76].

where the torsional quantum number m can have any positive or negative integer value (including zero). The corresponding energy eigenvalues are:

$$E_m = m^2 B. \tag{2.6}$$

2.7.2. Hindered rotors

In real molecules there will always be some resistance to internal rotation. The potential energy function can be expressed as a sum of cosines of the torsional angle:

$$V(\phi) = \frac{1}{2} \sum_n V_n \left(1 - \cos n\phi\right), \tag{2.7}$$

in which the contributing values of n are determined by the symmetry of the molecule. In the case of toluene (or a *para*-substituted derivative) there are six equivalent possible orientations of the methyl group; for example any one of the three C−H bonds could be oriented perpendicular to the benzene ring and pointing either up or down. For this reason, only $n = 6$ appears in the sum and the potential simplifies down to [77]:

$$V(\phi) = \frac{V_6}{2} \left(1 - \cos 6\phi\right). \tag{2.8}$$

In *ortho*- and *meta*-substituted toluenes, orientations of the methyl group in which a given hydrogen points "left" or "right" in the plane of the ring are no longer equivalent. The torsional potential therefore has threefold symmetry, and terms appear in Equation (2.7) for both $n = 6$ and $n = 3$.

Equation (2.8) is plotted as a function of torsional angle for the S_0 electronic state of toluene in Fig. 2.3. The barrier height $V_6 = -4.874\,\mathrm{cm}^{-1}$ is the value reported by Borst and Pratt [17], which is based upon a fit to a microwave absorption spectrum [78]. From the plot, it can be seen that the sign of V_6 determines the most stable orientation of the methyl group. In toluene, V_6 is negative and so the eclipsed conformations with a C−H bond parallel to the benzene ring ($\phi = 0^\circ, 60^\circ, 120^\circ, 180^\circ, 240^\circ, 300^\circ$) are energy maxima.

Unfortunately the Schrödinger equation cannot be solved analytically for a hindered rotor, and it is not possible to write down an expression for the torsional energy in a closed form. Instead the energy levels are usually found using a procedure developed by Lewis *et al.* [79] which involves constructing the Hamiltonian matrix in a basis set of free rotor eigenfunctions, and then using a computer to find the eigenvalues by numerical methods.

For a sixfold-symmetric hindered rotor, as found in toluene, the energy levels for

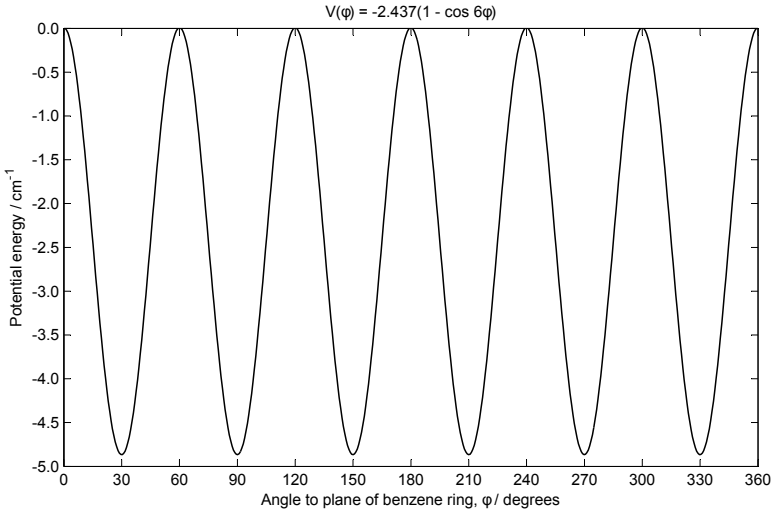

Fig. 2.3. Torsional potential function for toluene in the S_0 electronic state. An angle of $\phi = 0°$ corresponds to an eclipsed conformation of the methyl group, *i.e.* one C−H bond parallel to the benzene ring.

$m = \pm 3$ become non-degenerate. In principle, a similar lifting of degeneracy should also occur for $m = \pm 6$, $m = \pm 9$ etc.; however a fluorescence excitation study of *para*-fluorotoluene by Zhao *et al.* [76] showed that only the $m = \pm 3$ splitting was large enough to be observed. Using perturbation theory, these authors derived an approximate expression relating the magnitude of the splitting to the barrier height V_6:

$$\Delta E_3 = \left| \frac{V_6}{2} \right|. \tag{2.9}$$

2.7.3. Symmetry considerations

As discussed in Section 2.2.2, it is often convenient to approximate the symmetry of the toluene molecule as C_{2v}. However this classification neglects the structure of the methyl group, and strictly speaking point group symmetry is not appropriate for non-rigid molecules.

Symmetry classifications can be assigned to the hindered rotor eigenfunctions through the use of the *molecular symmetry group*, which considers the permutations of identical nuclei that can be achieved without breaking any chemical bonds [80]. Under this scheme, the toluene molecule belongs to a group called G_{12}. Parmenter and co-workers [74] have identified a one-to-one correspondence between four of the irreducible representations of G_{12} and those of C_{2v}. However, examination of the character tables given by Bunker and Jensen [80], paying particular attention to the species of the three translation operations, suggests that the correlations of B_1 and B_2 may have been printed the wrong way around in Ref. 74. The relationships between G_{12} and C_{2v} are listed in Table 2.1, incorporating

this correction. It is notable that a Ph.D. thesis by one of Parmenter's students [81] gives a correlation between G_{12} and C_{2v} which agrees with Table 2.1 and not with Ref. 74.

Table 2.1. Symmetries of torsional levels in toluene.

m	0	±1	±2	+3	-3	±4	±5	+6	-6
G_{12} symmetry	A_1'	E''	E'	A_1''	A_2''	E'	E''	A_1'	A_2'
C_{2v} equivalent	A_1	—	—	B_2	B_1	—	—	A_1	A_2

The relative energies of the $3A_1''$ and $3A_2''$ torsional levels depend upon the sign of V_6. Experimentally, the $3A_1''$ (or $m = +3$) level is seen to be the higher of the two in both the S_0 and S_1 electronic states of toluene. This indicates that V_6 is negative and therefore the molecule prefers a staggered orientation for the methyl group [17].

2.7.4. Torsion-vibration coupling and the acceleration of IVR

The observed acceleration of IVR by methyl rotors suggests that there is a coupling between the torsional and vibrational motions. Moss *et al.* [74] attributed the coupling (in *para*-fluorotoluene) to a van der Waals interaction between the methyl hydrogens and the adjacent carbon and hydrogen atoms. Based upon the correspondence between the G_{12} and C_{2v} irreducible representations shown in Table 2.1, these authors have derived the selection rules for torsion-vibration coupling in the approximate C_{2v} point group. Coupling is allowed between two states $|v_1, m_1\rangle$ and $|v_2, m_2\rangle$ if:

$$\Gamma(v_1) \otimes \Gamma(v_2) = \begin{cases} a_1 \text{ or } a_2 & \text{for } \Delta m = \pm 6, \\ b_1 \text{ or } b_2 & \text{for } \Delta m = \pm 3, \end{cases} \tag{2.10}$$

where $\Gamma(v_1)$ and $\Gamma(v_2)$ are the irreducible representations of vibrational states $|v_1\rangle$ and $|v_2\rangle$, and $\Delta m = m_2 - m_1$ is the difference in the number of torsional quanta.

Moss and Parmenter [22] invoked these coupling rules and the Fermi golden rule of Equation (2.3) to rationalise the much higher IVR rate in *para*-fluorotoluene compared with *para*-difluorobenzene. Although the mean square coupling matrix element, $\langle V^2 \rangle$, is expected to be of similar magnitude in both molecules [22], two factors combine to increase the density of effectively coupled states, ρ. The lowering of the symmetry from D_{2h} to C_{2v} leads to less restrictive selection rules for anharmonic coupling, approximately doubling the number of states that are allowed to couple. In addition to this, torsion-vibration interactions allow vibrations of different symmetries to couple to one another, provided that the conditions of Equation (2.10) are satisfied, further boosting ρ.

The further order-of-magnitude increase in the IVR rate on moving the methyl group

to the *meta* position [23] is not so easily explained. Partly it is due to the lowering of symmetry to C_s, which further relaxes the anharmonic coupling selection rules and increases the density of effectively coupled states by approximately a factor of two. There may also be an increased coupling between the methyl torsion and the overall rotation of the molecule, because the axis of the methyl group is no longer aligned with a principal axis of rotation in the *meta* isomer. Thirdly, a V_3 term is introduced which changes the shape of the torsional potential, and this may affect the average coupling matrix element. The relative importance of these factors remains uncertain.

More recently, Borst and Pratt [17] have proposed an alternative mechanism for torsion-rotation coupling in toluene, based upon the overlap of the methyl π orbitals with the phenyl π system. This orbital interaction, also known as *hyperconjugation*, causes the ring C−C bonds adjacent to the methyl group to shorten when they are eclipsed by a methyl C−H bond. Similarly, the bonds lengthen when the methyl group is in a staggered conformation. Thus, as the methyl group rotates, the phenyl ring is distorted, providing an efficient mechanism for IVR. Although this explanation for the coupling between torsion and rotation is fundamentally different from that of Moss *et al.*, the selection rules of Equation (2.10) remain valid.

2.7.5. Thermal population of torsional levels in toluene

In order to assess the effect the the rotation of the methyl group may have in the present experiments, it is important to know which excited torsional levels are populated. Prior to the absorption of the pump photon, the populations of the torsional levels can be calculated using the Boltzmann distribution:

$$\frac{N_i}{N} = \frac{g_i \exp\left(-E_i/k_B T\right)}{\sum_i g_i \exp\left(-E_i/k_B T\right)}, \tag{2.11}$$

where N is the total number of molecules, N_i is the population of the i^{th} quantum level, E_i is the energy, g_i is the degeneracy and k_B is the Boltzmann constant.

The torsional temperature T is assumed to be similar to the rotational temperature of the molecular beam used in this work, which is approximately 10 K (see Section 3.2), and the energies of the first seven torsional levels have been reported in a dispersed fluorescence study by Breen *et al.* [77]. No significant error is introduced by truncating the sum at $i = 7$, since $k_B T \approx 7\,\text{cm}^{-1}$, which is very much less than the energy of the seventh torsional level ($128.8\,\text{cm}^{-1}$). The resulting populations are expressed in percentage terms in Table 2.2. The two lowest levels, $0a_1'$ and $1e''$, are almost equally

populated and between them account for almost 95% of the molecules.

Table 2.2. Torsional levels in the S_0 state of toluene. Energy values determined by Breen *et al.* [77].

Level	$0A_1'$	$1E''$	$2E'$	$3A_2''$	$3A_1''$	$4E'$	$5E''$
Energy / cm^{-1}	0.00	5.19	20.78	45.56	48.06	83.23	128.80
Degeneracy	1	2	2	1	1	2	2
% population at 10 K	48.76	46.22	4.91	0.07	0.05	0.00	0.00

2.7.6. Torsional selection rules upon electronic excitation

In this work, IVR processes are studied following the excitation of toluene to a chosen vibrational level in the S_1 electronic state. It is therefore important to consider which torsional levels may become populated in the excitation step. In molecules of G_{12} symmetry, only transitions with $\Delta m = 0, \pm 6$ are formally allowed [17]. However, "forbidden" torsional excitations are often seen in absorption spectra. These arise due to coupling between the methyl torsion and overall rotation of the molecule, or a dependence of the transition dipole moment upon the orientation of the CH_3 group which causes the torsion to couple to the electronic motion [17]. Despite these effects the symmetry selection rule $a \nleftrightarrow e$, which arises from the nuclear spin, is *always* obeyed [82]. Based upon this minimal selection rule, excitation from levels with $m = 0$ in S_0 can produce $m = 0, 3, 6 \cdots$ in S_1, whereas excitation from $m = 1$ in S_0 leads to $m = 1, 2, 4, 5 \cdots$ in S_1. A further restriction is introduced by the requirement for conservation of energy: only those states which fall within the exciting laser bandwidth can be prepared. Consequently, the accessible torsional levels depend upon the frequency of the vibration being excited.

In practice, the fully allowed transitions $|S_1, m = 0\rangle \leftarrow |S_0, m = 0\rangle$ and $|S_1, m = 1\rangle \leftarrow |S_0, m = 1\rangle$ are usually by far the most intense [82]. *We can therefore expect approximately half of the molecules in S_1 to be prepared with $m = 0$ and half with $m = 1$.* This conclusion will be of crucial importance to the interpretation of the experimental results presented Chapters 7 and 9.

Part II.

Techniques

3. Time-resolved photoelectron spectroscopy: velocity map imaging

This chapter describes the techniques used to study IVR processes in the time domain. Preliminary studies carried out by our group at the Rutherford-Appleton laboratory [13, 56–58, 60] have shown that it is possible to observe IVR using picosecond time-resolved photoelectron spectroscopy; a review is given in Ref. 13. In those experiments, a picosecond laser pulse was used to prepare a selected vibrational level within the S_1 manifold. A second pulse then ionised the molecule and the evolution of the photoelectron spectrum was monitored as a function of the time delay between the two laser pulses.

Such experiments require a means of measuring the photoelectron spectrum which is both fast and sensitive. Although the ZEKE technique (Chapter 4) might seem attractive due to its very high resolution, it would be prohibitively time-consuming due to the need to scan the laser wavelength: the spectrum for each individual time delay would take several hours to complete. Instead we employ *velocity map imaging* (VMI), which will be described fully in Section 3.2. In essence, an electrostatic lens is used to focus the photoelectrons onto a phosphor screen which is photographed by a CCD camera. The lens is designed such that the electrons strike the screen at a position determined solely by their initial velocity. The image captured by the camera thus contains information about both the kinetic energies of the photoelectrons and their angular distribution. Since electrons with a range of different kinetic energies are detected simultaneously, it is not necessary to scan the laser wavelengths and a complete spectrum can be measured in just a few minutes. A further advantage of VMI is an electron collection efficiency of nearly 100%, due to the use of an electric field which accelerates the electrons towards the detector.

In the present work, a new "in-house" picosecond laser system has been used to build upon the preliminary studies. This laser system is able to provide more stable power output and a narrower, better-defined bandwidth than the one previously used at the Rutherford-Appleton Laboratory. It also has the key advantage that the wavelengths of the two laser beams used for the excitation and ionisation steps can be tuned independently of one another. By changing the wavelength of the ionisation laser, a technique known as *slow electron velocity map imaging* (SEVI) can be used to greatly improve the

resolution of the photoelectron spectra. This will be discussed in detail in Section 3.4. The experiments described in this chapter were carried out by, or under the supervision of, Dr Julia Davies.

3.1. Picosecond laser system

The time-resolved experiments were carried out using a bespoke laser system supplied and installed by Coherent (Fig. 3.1). This is designed to provide two independently-tunable beams, with a pulse duration of approximately one picosecond and spectral bandwidth of around $15\,\mathrm{cm}^{-1}$.

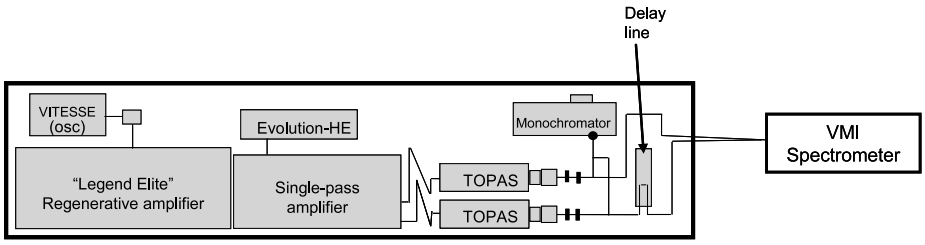

Fig. 3.1. A schematic view of the picosecond laser system. Diagram courtesy of Dr Julia Davies.

Initially the "Vitesse" mode-locked Ti:sapphire laser generates 100 fs pulses of light at a wavelength of 800 nm, with a spectral bandwidth of 10 nm and a repetition rate of 80 MHz. These pulses then pass into the "Legend Elite" unit, which contains a pulse stretcher and a neodymium:yttrium lithium fluoride (Nd:YLF) laser pumping a regenerative amplifier. The stretcher uses a diffraction grating to disperse the different wavelengths which make up the pulse, so that each wavelength travels a different optical path length. This results in an increase in the pulse's duration to around 200 ps, thus lowering the peak power and preventing damage to the optical components in subsequent stages of the system. A mask within the pulse stretcher blocks some of the wavelengths as they leave the diffraction grating, cutting down the spectral bandwidth.

The regenerative amplifier stage contains a Ti:sapphire crystal inside a resonant optical cavity. The crystal is pumped by the Nd:YLF laser so that the pulses from the Vitesse will be amplified as they pass through it. A pair of Pockels cells traps each pulse within the amplifier cavity for approximately 20 round trips, bringing about a millionfold increase in the pulse's energy, before allowing it to escape.

On entering the single pass amplifier unit, the beam is split into two and each half is further amplified by a Ti:sapphire crystal which is pumped by the "Evolution HE" Nd:YLF laser. The pulses are then compressed to 1 ps duration. On leaving the amplifier

unit, both beams have a wavelength of 800 nm, a repetition rate of 1 kHz and a power of 3.4 W. One of these beams will become the 'pump' which prepares a chosen vibrational level in the S_1 electronic state, and the other beam will be used as the 'probe' to ionise the molecule.

The wavelengths of the two beams can be independently tuned using a pair of optical parametric amplifiers ("TOPAS", Light Conversion). These produce infra-red light in the range 1100–2950 nm, which is then converted to ultraviolet light using sum-frequency and higher-harmonic generation.

A motorised delay stage (Standa) is used to alter the time delay between the pump and probe pulses. The probe beam is reflected off a pair of mirrors which can be moved using a stepper motor in order to vary the optical path length (see Fig. 3.2). The stepper motor is controlled *via* a USB interface using custom software which was developed using *LabVIEW* [83].

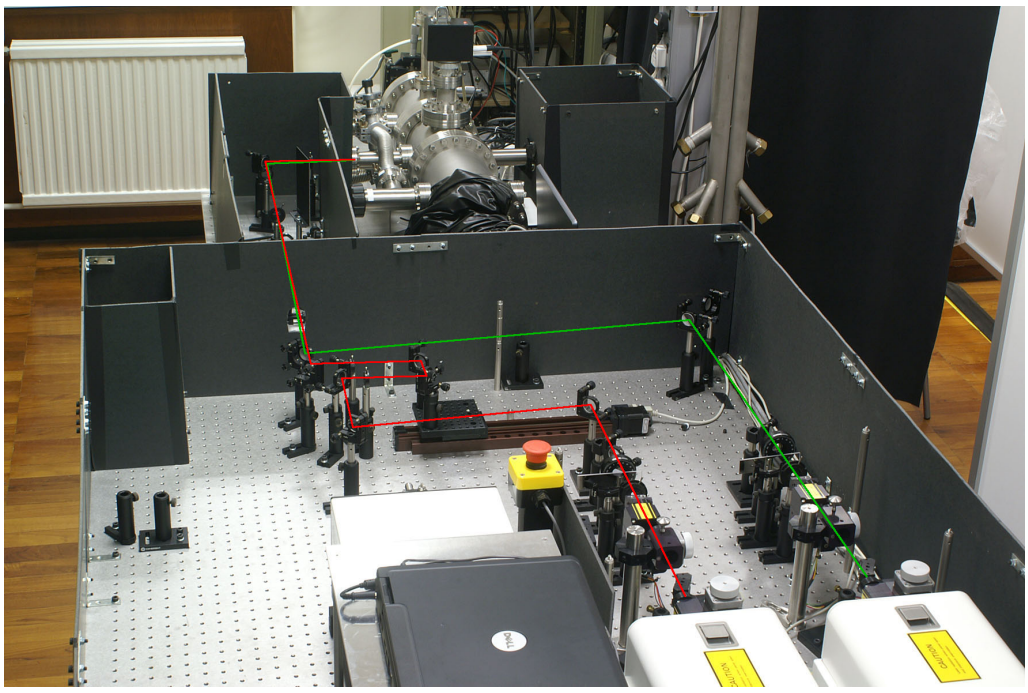

Fig. 3.2. Optical delay line and beam path into the VMI chamber. The pump beam is shown in green and the probe beam in red.

The two beams are then focussed into the VMI spectrometer, in a co-propagating arrangement, using a 1.0 m focal length lens. The final intensities are typically 2×10^{10} and 1×10^{11} W cm^{-2} for the pump and probe respectively, and both beams are vertically polarised.

Using a flip mirror, the beams may instead be directed into a monochromator in order to measure their spectral profiles. These measurements indicate a bandwidth of approximately 12–15 cm^{-1}.

3.2. Velocity map imaging spectrometer

A photodissociation or photoionisation event will produce two fragments travelling in opposite directions, with equal momentum in the centre-of-mass reference frame. If we observe many of these events, we can plot the distributions of the fragments in velocity space and obtain a set of so-called *Newton spheres*, whose sizes are directly proportional to the speed of the fragments [84]. Imaging experiments provide a direct view of the Newton spheres by projecting them onto a screen.

The first such experiment was performed by Chandler and Houston [85] in 1987. These authors produced CH_3^+ ions by photodissociation of CH_3I with linearly polarised light, and then used a Wiley-Mclaren time-of-flight mass spectrometer to accelerate the methyl ions towards a position-sensitive microchannel plate detector. With this configuration, all of the CH_3^+ ions would have the same time of flight. However, due to their initial velocity imparted by the dissociation event, they would not simply travel parallel to the direction of the flight tube. Ions with a large velocity component perpendicular to the flight tube axis would strike the detector near the edge, whereas those with a smaller velocity would arrive closer to the centre.

A phosphor screen located behind the detector fluoresced to indicate the positions of the ion impacts, giving an image that could be recorded using either a Polaroid photographic film or a CCD array. Two crescent shapes were seen, indicating that the CH_3^+ fragments were travelling preferentially parallel, and not perpendicular, to the polarisation direction of the photolysis laser. The image was, however, blurred because of the finite size of the ionisation region: ions originating with the same velocity from different places would end up at different positions on the screen.

A decade later, Eppink and Parker [54, 84] introduced a new electrostatic lens design which dramatically improved the resolution of the images. This lens was able to focus all particles with a given velocity onto the same point on the screen, regardless of their starting position. The new technique was given the name *velocity map imaging* (VMI). Since that time, VMI has gained great popularity as a means of studying the velocity distributions of both ions and electrons.

The present study made use of an existing velocity map imaging spectrometer [86], which had also been employed in the previous time-resolved experiments [56–58, 60]. A schematic view of the instrument is shown in Fig. 3.3 on the next page.

The molecule to be studied is seeded in helium at approximately 3 bar and introduced into the source chamber (left hand side of Fig. 3.3) through a pulsed nozzle (General Valve) of 0.5 mm diameter, producing a supersonic jet. A commercial solenoid valve

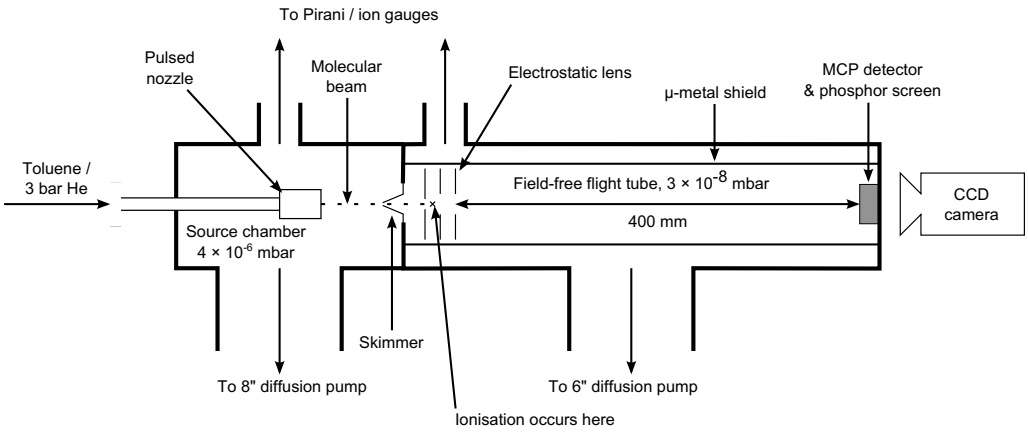

Fig. 3.3. Schematic of the velocity map imaging spectrometer. The directions of the molecular beam, laser beam propagation and laser polarisation are mutually perpendicular.

controller (Iota One, General Valve) drives the nozzle at 20 Hz, the highest frequency that can be maintained without causing overheating. The jet then passes through a skimmer (Beam Dynamics, 0.8 mm) and into the ionisation chamber, where it intersects with the laser beams. At this point the molecules are vibrationally cold and the rotational temperature is expected to be around 10 K.

The electrostatic lens (Fig. 3.4) closely follows Eppink and Parker's design [54] and consists of three circular stainless steel plates. The first plate, known as the *repeller*, is located behind the ionisation region and held at a constant voltage of between 200 and 1000 V, depending upon the experiment to be performed. It contains a 4 mm hole which allows the molecular beam to pass through. Beyond the ionisation region, the second plate (*extractor*) is held at a lower potential, typically $\sim$ 70% of the repeller voltage. The third and final plate is grounded, providing a 0 V reference.

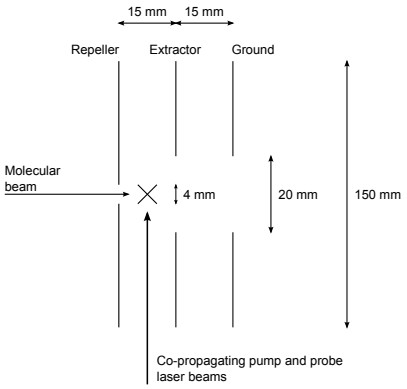

Fig. 3.4. Cross section view of the electrostatic lens used for velocity map imaging. The photoelectrons are produced at the point marked by the cross, where the molecular beam and laser beams intersect.

Focussing is achieved by adjusting the ratio of the repeller and extractor voltages until a sharp image is obtained. The 'magnification' of the image is determined by the absolute

values of these voltages: a lower extraction voltage leads to a longer time of flight for the electrons, so that they have more time to move off-axis and the image becomes larger. The extraction voltage is therefore usually set such that the outermost ring of the image, corresponding to the fastest electrons, is as large as possible without touching the edges of the detector.

After passing through the holes in the extractor and ground plates, the photoelectrons travel approximately 400 mm along a flight tube which is shielded with μ-metal to block any external magnetic fields. At the end of the tube is a 40 mm dual microchannel plate / phosphor screen detector (Photek). The microchannel plate (MCP) acts as an amplifier, so that the impact of each photoelectron releases a cascade of electrons into the phosphor screen. By stepping the voltage applied to the MCP, the detector is gated on for a period of about 500 ns as the electrons arrive, then deactivated until the next pulse of the molecular beam. A CCD camera (Basler A302f) captures images of the phosphor screen, which are then transferred to a computer using IFS32 software (Photek). The images are added together, producing a 2D histogram of electron count versus position on the detector, until an acceptable signal:noise ratio is achieved. The final image is saved as a *Flexible Image Transport System* (FITS) file, which is a format originally developed for use in astronomy [87, 88].

3.3. Image analysis

3.3.1. Recovery of the photoelectron spectrum

As discussed in Section 3.2, the image recorded by the CCD camera is a 2D projection of the three-dimensional photoelectron velocity distribution. As the polarisations of the pump and probe laser beams are parallel, the 3D distribution is guaranteed to be cylindrically symmetric about the polarisation axis, which is parallel to the plane of the detector. This symmetry means that the 2D image contains sufficient information to reconstruct a slice through the original 3D distribution, in a process referred to by some authors as *inversion*. From that slice the photoelectron intensity can be measured as as function of the radius from the centre of the image and the angle with respect to the laser polarisation.

The so-called *inverse Abel transform* provides an analytic solution to the reconstruction problem, but is not ideal in practice as it tends to amplify any noise present in the image. For this reason, a number of alternative methods have been proposed [89]. Among these is *basis set expansion* (BASEX), in which the image is fitted to a set of functions which

are the analytical 2D projections of known 3D basis functions. The *pBasex* computer program of Garcia *et al.* [90], which is used in this work, implements a refinement of BASEX using polar rather than Cartesian coordinates for the basis functions. Modelling the kinetic energy distribution of the photoelectrons as a series of Gaussian functions with width σ, the 3D velocity distribution is given by:

$$F(R,\theta) = \sum_{k=0}^{k_{\max}} \sum_{l=0}^{l_{\max}} c_{kl} e^{-(R-R_k)^2/\sigma} P_l(\cos\theta) \tag{3.1}$$

where R is the radius from the centre of the image, R_k is the centre of the k^{th} Gaussian, θ is the angle with respect to the polarisation vector of the laser light and P_l is the Legendre polynomial of order l. The job of the *pBasex* program is to find the coefficients c_{kl} such that the 2D projection of $F(R,\theta)$ matches the recorded image.

The value of $l_{\max}$ must be specified by the user, and is equal to twice the number of photons involved in the ionisation process [90]; hence in the present work $l_{\max} = 4$. A further simplification arises from the use of linearly, as opposed to circularly polarised light: the odd-l terms disappear from Equation (3.1). *pBasex* therefore considers only the terms for $l = 0$, 2 and 4. For a given electron kinetic energy, the angular distribution of the electrons can then be described in terms of two *anisotropy parameters*, β_2 and β_4:

$$I(\theta) \propto 1 + \beta_2 P_2(\cos\theta) + \beta_4 P_4(\cos\theta) \tag{3.2}$$

Three output files are produced, giving the photoelectron intensity and anisotropy parameters as a function of the distance in pixels from the centre of the image. In this work the anisotropy parameters were found to provide little useful information, since they did not show a clear time dependence. The following discussion therefore concentrates on the analysis of the photoelectron intensity data, which is carried out using the *Matlab* software package [91].

3.3.2. Background subtraction

The desired photoelectron spectrum in these experiments results from "two-colour" ionisation, *i.e.* the absorption of one photon from the pump laser, followed by one photon from the probe. It is, however, possible for ionisation to be effected by two pump photons, or in some cases by multiple probe photons. These undesired "one-colour" processes will produce a background signal which must be removed, since it does not correspond to the required time delay. To this end, background images are recorded in which the probe

laser pulse arrives 5 ps before the pump. The spectra obtained from these images are due solely to one-colour ionisation.

For each positive time delay, the background spectrum is renormalised to match the intensity of part of the baseline, and then subtracted to leave just the two-colour signal. An example is shown in Fig. 3.5: the peak at 235 pixels is purely due to one-colour ionisation and disappears after subtraction.

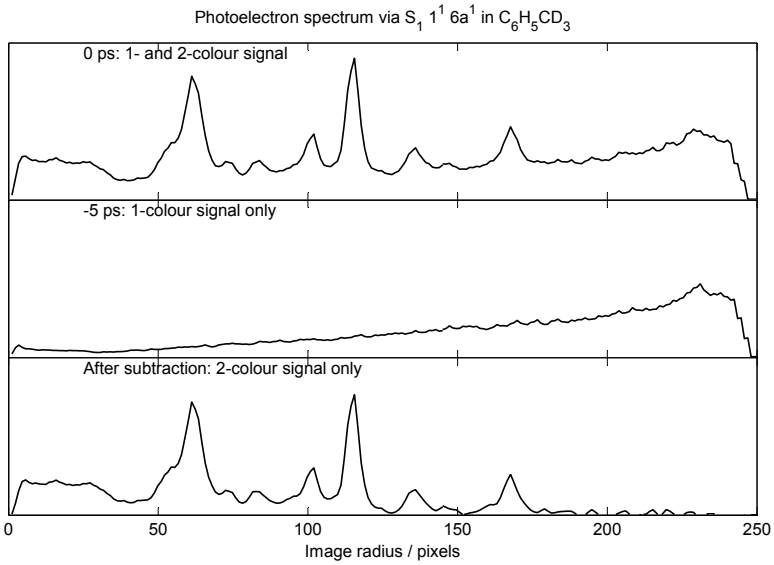

Fig. 3.5. Example of background subtraction. The −5 ps spectrum has been normalised to match the intensity of the 0 ps spectrum over the radius range 200–240 pixels.

3.3.3. Calibration

The *pBasex* software outputs the photoelectron spectrum in terms of the distance, R, in pixels from the centre of the image. This distance is proportional to the speed of the photoelectrons, and so their kinetic energy depends upon R^2. The spectrum is effectively a histogram with a constant bin width in radius. If, however, we plot the spectrum as a function of R^2 (or kinetic energy) then the bin widths will become unequal and so an adjustment to the intensity values is needed. If the radius bin width is $2\delta R$, then the width of the R^2 bin centred on radius value R is given by:

$$\begin{aligned} W &= (R+\delta R)^2 - (R-\delta R)^2 \\ &= R^2 + 2R\delta R + \delta R^2 - \left(R^2 - 2R\delta R + \delta R^2\right) \\ &= 4R\delta R \end{aligned}$$

Consequently the intensity values should be divided by $2R$ to preserve the same integral for each bin when the spectrum is plotted on an R^2 scale. However, since the photoelectron intensity is given in arbitrary units, the factor of two is not important and so the intensity values are simply divided by R.

Next we need to find the constant of proportionality which relates the kinetic energy of the electrons to R^2. This value shall hereafter be referred to as the *calibration factor*, k. The cation internal energy scale is given by:

$$E_{\text{int}} = h\nu_{\text{pump}} + h\nu_{\text{probe}} - I - kR^2, \tag{3.3}$$

where $h\nu_{\text{pump}}$ and $h\nu_{\text{probe}}$ are the photon energies of the the two laser beams, and I is the ionisation potential of the molecule. For toluene, $I = 8.8276$ eV $= 71\,199\,\text{cm}^{-1}$ [92]. If the spectrum shows a clear vibrational origin peak then the determination of k is straightforward, since we know the pixel radius for which $E_{\text{int}} = 0$. This radius value is taken from the centre of the origin peak, measured by plotting the photoelectron intensity against R^2 and fitting the peak to a Gaussian function.

As the calibration factor is sensitive to the exact voltages applied to the extractor and repeller plates, it may vary slightly over time. For this reason, k has been determined separately for each set of photoelectron images recorded.

3.3.4. Distortion correction

Under ideal conditions, the rings in the photoelectron image should be perfectly circular. Unfortunately, due to imperfections in the electrostatic optics the images were in fact slightly distorted, leading to a broadening of the peaks in the photoelectron spectrum produced by *pBasex*. An additional problem was the presence in some cases of 'hot' pixels with anomalously high photoelectron intensity.

A computer program was developed using the C programming language in order to correct the images. The CFITSIO library [93], which has been made freely available by NASA, was employed to read and write the FITS format image files. 'Hot' pixels are identified by comparing the brightness of each pixel in the image with the mean brightness of the eight adjacent pixels. Any pixel which exceeds this mean value by more than a specified amount (by default, a factor of ten) is replaced by that mean value.

Having removed the 'hot' pixels, the distortion is corrected by stretching the image horizontally. A quadratic interpolation scheme [94] is used to resize the image to the pixel dimensions specified by the user. The correct dimensions for each set of images are found

by trial and error in order to give the narrowest possible peaks in the spectrum returned by *pBasex*. Examples of unprocessed and corrected images are shown in Fig. 3.6.

3.4. Improving resolution: the SEVI technique

In a VMI experiment, the outermost ring of the image corresponds to the fastest-moving electrons and thus the lowest level of vibrational excitation in the cation. Ionisation to a higher internal energy level will produce slower electrons, which strike closer to the middle of the detector. Since the electron kinetic energy is proportional to the square of the radius, the best resolution is achieved close to the centre of the image, corresponding to the highest accessible vibrational levels in the cation.

With a long probe laser wavelength (low photon energy in the ionisation step), only a few cation vibrational levels will be accessible and the photoelectrons will be travelling relatively slowly, so that even the ion origin peak is close to the centre of the image and thus well-resolved. If a shorter probe wavelength is used, then the innermost rings will correspond to higher vibrational levels in the cation, extending the range of the spectrum. However ionisation to lower cation vibrational levels will now produce fast electrons, which strike further from the centre of the detector. Consequently the resolution for low vibrational levels in the ion is poor. In some cases, the ion origin peak may be lost altogether as the fastest photoelectrons fall off the edge of the detector.

Neumark and co-workers [59] were the first to realise that the choice of probe wavelength need not be a compromise. By recording a series of photoelectron images with different probe wavelengths and splicing the resulting spectra together, they were able to achieve good resolution over a wide internal energy range. These authors dubbed the technique *slow electron velocity map imaging* (SEVI).

As the probe wavelength is increased, the image becomes smaller. In principle, the extraction voltage could then be lowered so that the image expands to fill the detector once more. Although the increased magnification should lead to better energy resolution, it would then be necessary to re-calibrate the ion internal energy scale for each extraction voltage. For this reason, in the present work a constant extraction voltage has been used for all probe wavelengths, allowing a single calibration factor to be used for all of the images.

Fig. 3.7 illustrates the benefits of SEVI in the present work. Spectra *via* the S_1 origin in toluene are shown for five different probe wavelengths. In order to match the intensities, the spectra have been normalised according to the integral over the ion origin peak,

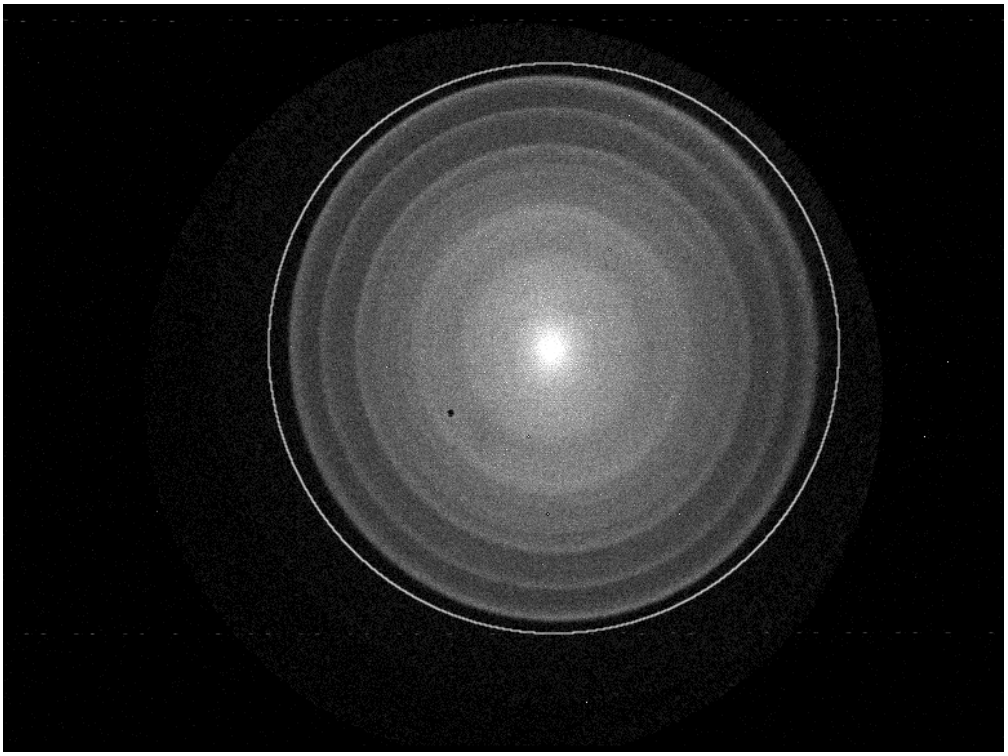

(a) Original image: 776 × 580 pixels.

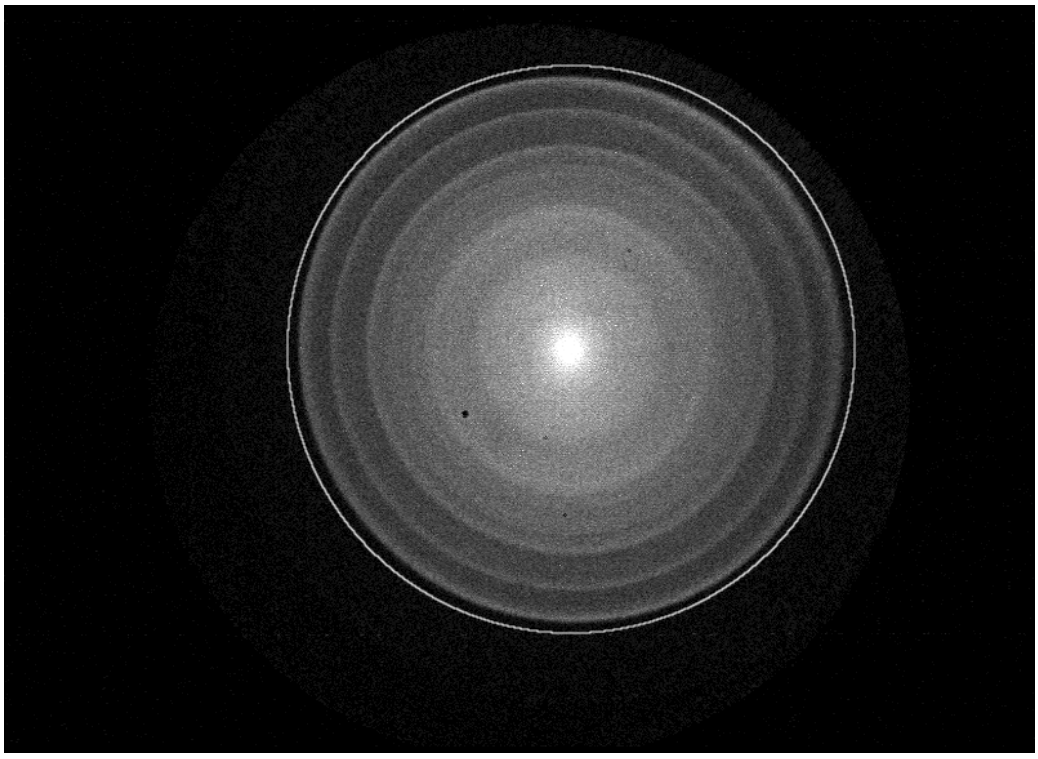

(b) Corrected image: 800 × 580 pixels, with 'hot' pixels removed.

Fig. 3.6. Example of distortion correction. These images were produced by ionisation from the S_1 vibrational origin in deuterated toluene ($C_6H_5CD_3$). Perfect circles have been superimposed so that the distortion can be seen more clearly.

from -200 to 200 cm^{-1}, determined by the Trapezium Rule. As the probe wavelength is decreased, it can be seen that the origin peak becomes broader but a greater range of cation internal energies is covered. After splicing, good resolution is achieved across the entire spectrum.

The calibration factor used is an average of the values determined from the ion origin peak for each of the five probe wavelengths. The probe photon energies used in Equation (3.3) were then adjusted to ensure that the origin peaks would remain centred on 0 cm^{-1}.

3.5. Characterisation of the S_1 electronic state: REMPI

The time-resolved experiments require the pump laser to prepare a chosen vibrational level within the S_1 excited electronic state. In order to select the correct pump wavelength, we need to determine the exact frequencies of those S_1 vibrational levels. This can be done using the *resonance-enhanced multi-photon ionisation* (REMPI) spectrum, which provides similar information to a UV absorption spectrum.

For REMPI spectroscopy the polarities of the MCP detector and electrostatic lens are reversed, so that ions are detected rather than electrons. The probe laser beam is blocked and the total ion count rate is recorded as the pump wavelength is scanned. This is a so-called "$(1+1)$ REMPI" process in which the first photon excites the molecule to the S_1 electronic state, and absorption of a second photon of the same wavelength leads to ionisation. When the laser wavelength is resonant with the transition to one of the vibrational levels in S_1, the probability of the absorption step is increased and so a higher ion count rate is seen.

The laser power is simultaneously measured by a meter placed beyond the exit window of the vacuum chamber. This measurement confirms that there is only a small variation in power across the required wavelength range, and hence the intensities of the REMPI peaks closely reflect the transition probabilities for the excitation of the different S_1 vibrational levels.

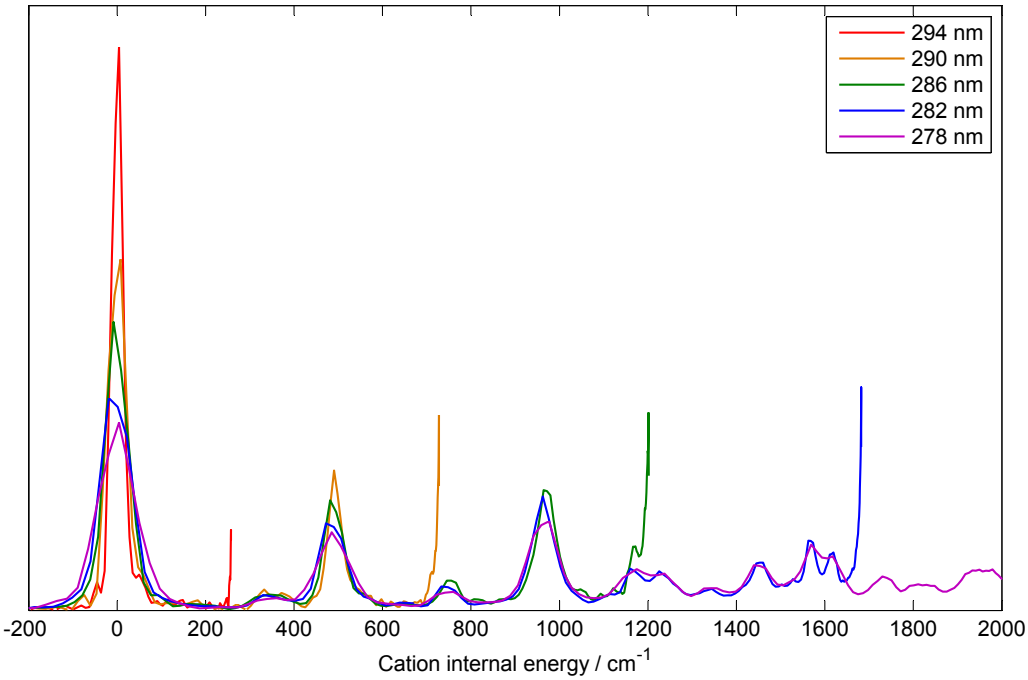

(a) Spectra for different probe laser wavelengths.

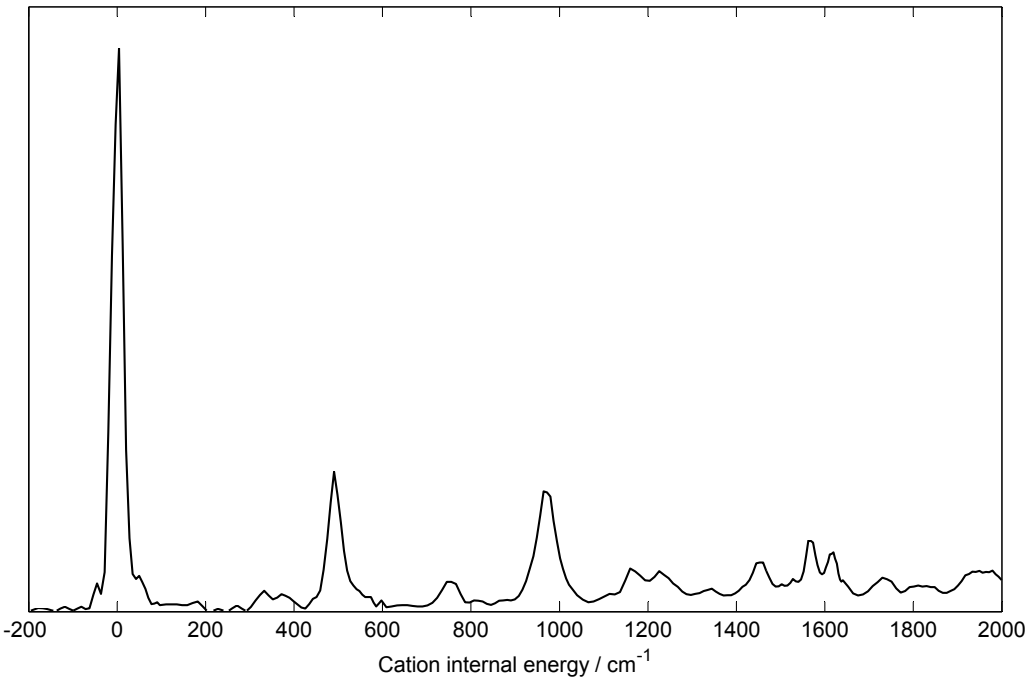

(b) SEVI spectrum after splicing.

Fig. 3.7. SEVI spectrum *via* the S_1 vibrational origin in toluene.

4. High resolution photoelectron spectroscopy: ZEKE

The time-resolved experiments described in Chapter 3 used laser pulses of 1 ps duration and 12–15 cm^{-1} bandwidth. The energy spacing of the vibrational eigenstates in the S_1 manifold is often smaller than this, so that the pump laser excites a coherent superposition. Such a superposition is a necessary condition if time dependence is to be observed; however we can also gain complementary information by performing an experiment in which the excitation bandwidth is sufficiently narrow to prepare just one vibrational level at a time.

The well-known time-energy uncertainty relation, $\Delta E \Delta t \geq \hbar$ [14], implies the need for a longer laser pulse duration in order to achieve a narrower excitation bandwidth. The experiments described in this chapter therefore employed a laser system with approximately 5 ns pulse duration and a bandwidth of $\sim 0.3\,cm^{-1}$. In order to take full advantage of this reduced bandwidth, we require a means of obtaining a photoelectron spectrum with similarly high resolution.

4.1. Principle of ZEKE spectroscopy

In conventional photoelectron spectroscopy the sample is irradiated with photons of a fixed wavelength and the kinetic energy distribution of the photoelectrons is measured. The precision to which these kinetic energies can be measured is often the limiting factor which determines the resolution of the spectrum. *Zero electron kinetic energy*, or ZEKE, spectroscopy [95] takes a fundamentally different approach: the ionising wavelength is scanned and we seek to detect only those electrons produced at the ionisation threshold. These are termed the "ZEKE" electrons, since they have no kinetic energy. Fig. 4.1 illustrates how this works. First, a pump laser of fixed wavelength excites a chosen vi-

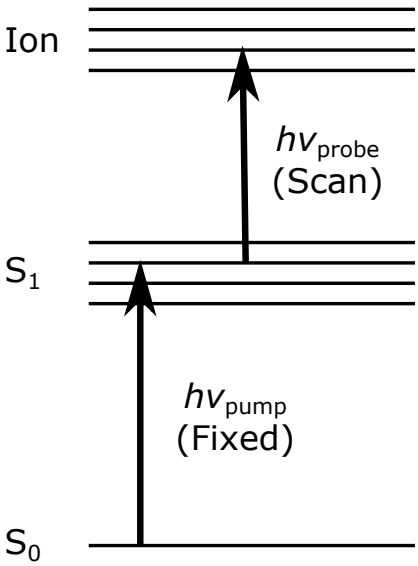

Fig. 4.1. Principle of the ZEKE experiment.

brational eigenstate within the S_1 electronic state. The excited molecule is then ionised by a second, probe laser, whose wavelength is scanned. A ZEKE signal will be seen only when the wavelength of the probe laser closely matches the energy of the transition to an eigenstate in the cation.

The key to the detection of the ZEKE electrons is the existence of surprisingly long-lived Rydberg states just below the ionisation continuum. These are highly excited electronic states in which an electron occupies a hydrogen-like orbital of high principal quantum number (n), orbiting some distance away from the rest of the molecule. Most Rydberg states decay within a few nanoseconds or less. However for sufficiently high Rydberg levels ($n \approx 100$ to 300) the lifetime can become many orders of magnitude longer, up to tens of microseconds. Schlag [95] explains this behaviour in terms of the penetration of the Rydberg electron close to the ionic core. When the Rydberg state is first prepared, the electron's orbital angular momentum quantum number, ℓ, is small. Since the closest approach to the core varies as $\frac{1}{2}\ell\,(\ell+1)$, the electron can get close enough to interact with the core and this would usually cause the Rydberg state to decay. However, when the principal quantum number is large enough, the density of states becomes very high. Due to the presence of small residual electric fields, states of different ℓ begin to mix so that high-ℓ states become populated. Once in a high-ℓ orbital, the electron stays well away from the core and can no longer interact with it. This is the so-called "ZEKE state" that we wish to detect.

Following the probe laser pulse, we simply wait for around 10 to 20 µs. During this time, any electrons which have been produced with some kinetic energy (the so-called "prompt electrons") will escape from the detection region, and any low-n Rydberg states will decay. Eventually only the ZEKE states remain. A pulsed electric field is then applied, which ionises the ZEKE states and accelerates the electrons towards a detector. In our experiments, this process is typically repeated for ten laser shots and the ZEKE signal is averaged before stepping to the next probe wavelength.

Although ZEKE offers the highest resolution of any photoelectron spectroscopy technique, it is not without its disadvantages. Due to the requirement to scan the laser wavelength, it is far more time-consuming than velocity map imaging. The inherent sensitivity of ZEKE is also rather low because the majority of the photoelectrons are produced with some kinetic energy, and hence are rejected. In the present ZEKE studies of toluene, which has a relatively small ionisation cross section, this low sensitivity meant that an average of three or four scans was typically needed in order to achieve an acceptable signal:noise ratio. Consequently each spectrum took several hours to complete,

compared with just a few minutes for VMI. The cation internal energy range covered was also smaller, as it was restricted by the tuning range of the probe laser. Variations in the laser power across the wavelength range affected the apparent intensities of the ZEKE peaks, which therefore did not accurately reflect the true transition probabilities.

4.2. ZEKE apparatus

The ZEKE experiments were carried out in collaboration with Adrian Gardner in Professor Tim Wright's laboratory at Nottingham. The equipment used was similar to that employed in previous ZEKE studies of *para*-fluorotoluene [96–98], being based upon a modified REMPI spectrometer [99]. The set-up is illustrated in Fig. 4.2.

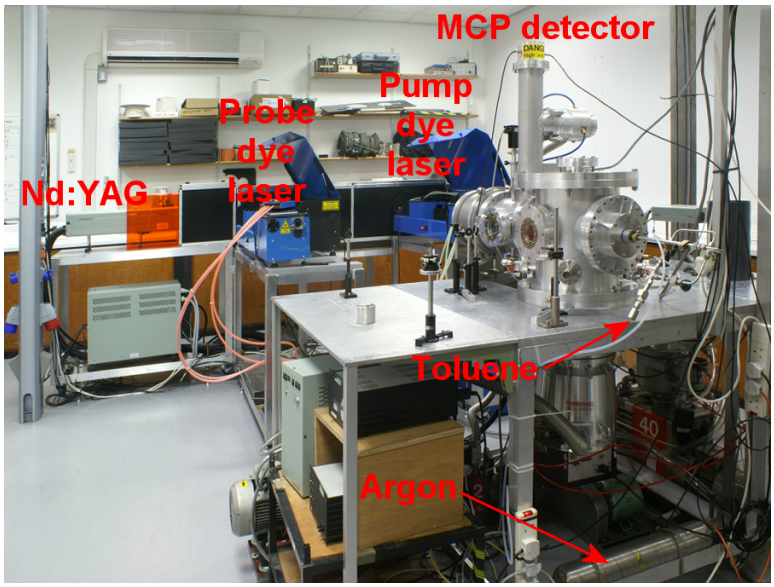

Fig. 4.2. Apparatus used for nanosecond REMPI and ZEKE experiments. The MCP detector visible here was used for ion detection in the REMPI spectra. Electron detection for ZEKE was achieved using a second set of MCPs located underneath the table (not visible).

A single Nd:YAG laser (Continuum Surelite III, 10 Hz, 5 ns pulse duration) is used to pump two dye lasers (Sirah Cobra Stretch, 1800 lines/mm grating). The first dye laser, used for the $S_1 \leftarrow S_0$ excitation step, is pumped with the third harmonic of the YAG (355 nm) and contains Coumarin 307 dye. For the ionisation step, the second laser is pumped with the second harmonic of the YAG (532 nm) and operates on Pyrromethene 597 dye. Both dyes are supplied by Exciton and dissolved in methanol. The frequency-doubled output from each dye laser is focussed with a quartz lens (250 mm focal length) and directed into the vacuum chamber in a coaxial and counter-propagating arrangement. The pump beam is slightly defocussed so that two-colour overlap can be achieved more easily.

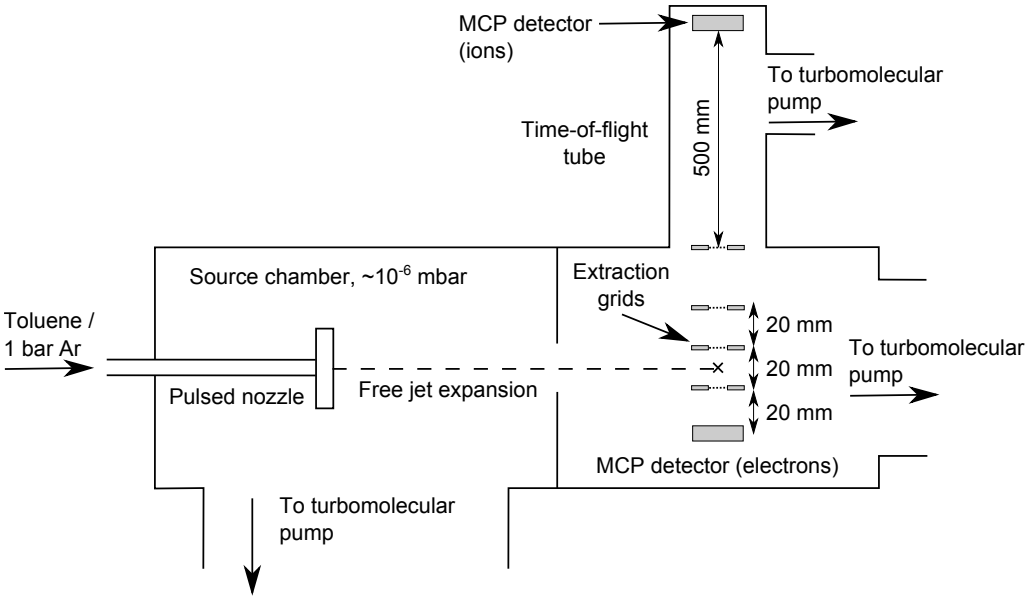

Fig. 4.3. Schematic of the combined REMPI / ZEKE spectrometer used in the nanosecond experiments. Ionisation occurs at the point marked by the cross; the laser beams are counter-propagating and perpendicular to the plane of the paper.

A schematic diagram of the spectrometer is shown in Fig. 4.3. The vacuum system comprises two connected chambers, each evacuated by a turbomolecular pump backed by a rotary pump. In the source chamber, a pulsed valve (Parker / General Valve, 750 µm orifice, 10 Hz) creates a free jet expansion of toluene seeded in $\sim$ 1 bar of argon. This beam passes unskimmed into the second chamber, where it intersects with the two laser beams.

In the second chamber, a set of three extraction grids can be used in two different ways. For REMPI spectroscopy the grids act as a standard Wiley-Mclaren mass spectrometer, directing ions upwards into a 500 mm time-of-flight tube terminated by an MCP detector. By appropriate gating of the signal from the MCP, ions with a chosen mass (in this case, the toluene monomer) can be detected selectively. In this work, a one-colour $(1 + 1)$ REMPI scheme was employed and so the probe laser beam was blocked when recording REMPI spectra.

In ZEKE mode, the two upper grids are grounded and a fast-rising pulsed voltage is applied to the bottom grid in order to achieve the field ionisation of the Rydberg states. The ZEKE electrons are directed downwards onto a second MCP detector. Each flight tube is evacuated by its own small turbomolecular pump (Leybold Turbovac 151, $150\,\mathrm{l\,s^{-1}}$ pumping speed). Both of the Turbovac 151 units are backed by a single rotary pump (Leybold Trivac D10E).

The signal from the appropriate MCP detector is passed to an oscilloscope (LeCroy

LT342 Waverunner) for monitoring, and also to a boxcar integrator (SRS SR250) which calculates 10-shot averages over two timing gates. One of these gates contains the ZEKE or REMPI signal, and the other is used as a background to account for any changes in the overall signal intensity. The boxcar is interfaced to a personal computer, which records the spectrum.

4.3. Laser wavelength calibration

In both REMPI and ZEKE spectroscopy, it is essential to have an accurate knowledge of the photon energies used in order to produce a spectrum with an accurate energy scale. In this work, the pump dye laser was calibrated by comparing the line positions in the REMPI spectrum with a fluorescence excitation spectrum of toluene published by Hickman *et al.* [63]. Prior to embarking on the ZEKE studies of toluene, a set of ZEKE spectra were recorded from *para*-fluorotoluene (pFT). The vibrational frequencies of the pFT cation were already known from a previous ZEKE study [97], enabling the determination of an accurate calibration for the wavelength of the probe laser.

5. Computational methods

Theoretical and computational methods have an important role to play in the interpretation of the present experimental results. We begin by calculating the vibrational frequencies of toluene in each of the relevant electronic states (Section 5.1), which can aid the assignment of features seen in the photoelectron spectra. In Section 5.2, these calculated normal modes are used to simulate the appearance of the photoelectron spectra from different vibrational levels in the intermediate S_1 electronic state. Such simulations are valuable for the identification of "dark" vibrational states which appear in the picosecond spectra for time delays > 0 ps.

The calculated frequencies are also useful for rationalising the differences in the IVR behaviour of various initially prepared S_1 vibrational levels. Section 5.3 describes the method used to calculate the density of states over a given range of internal energies, which is one of the important factors influencing the rate of IVR.

5.1. Vibrational frequencies

The vibrational frequency calculations were carried out using the *Gaussian 09* quantum chemistry package [100], running on a high performance computing cluster provided by the National Service for Computational Chemistry Software [101]. Default parameters were used in all cases, and in order to obtain a complete set of real vibrational frequencies it was found that the methyl group had to be oriented in a 'staggered' conformation, with one of the C−H bonds perpendicular to the plane of the benzene ring. This result is consistent with the experimental findings of Borst and Pratt [17], who deduced from a fluorescence-excitation spectrum that the methyl group prefers a staggered conformation in both the S_0 and S_1 electronic states.

5.1.1. Neutral and ion ground states

Density functional theory (DFT) was employed for the frequency calculations in the ground electronic states of both neutral toluene and the cation, using the popular B3LYP hybrid density functional and the Dunning aug-cc-pVTZ basis set.

In this notation, 'TZ' (Triple-Zeta) denotes the use of three contracted basis functions to represent each valence orbital. Each contracted function is constructed from a set of

primitive functions, the coefficients of which have been variationally optimised. The 'cc' (correlation consistent) indicates that the optimisation employed levels of theory which include some electron correlation.

The 'p' denotes the presence of polarisation functions, which have higher angular momentum quantum numbers than the occupied atomic orbitals. These can be used to approximate the distortion of the atomic orbitals within a molecule caused by interactions with other nearby atoms. One set of d and two sets of p functions are added to each hydrogen atom, whereas one set of f and two sets of d functions are added to the carbons.

Accurate modelling of the aromatic ring requires a high degree of delocalisation of electron density. This is made possible by adding a set of diffuse functions to each angular momentum function in the basis set, denoted by the prefix 'aug' (augmented).

At this level of theory, *Gaussian 09* is able to calculate the first and second derivatives of the energy analytically. Geometry optimisation and the calculation of the harmonic vibrational frequencies were therefore straightforward. It was also possible to obtain a first-order anharmonic correction to the frequencies, using a numerical approximation to the third derivatives. In the S_0 state, for which all 38 vibrational frequencies have been determined experimentally [63, 65], the anharmonic correction reduced the root mean square error from 69 to 39 cm^{-1} (see Table 5.1 on the following page). The calculated frequencies for the cation are listed in Table 5.2 on page 61.

The calculated normal modes were assigned labels in Varsányi notation [65] by examination of the atomic motions and comparison of the energies with the experimental values listed by Hickman *et al.* [63]. As noted in Section 2.1, a variety of different naming schemes exist in the literature, leading to some confusion over the meaning of the assignments. Table 1 of Ref. 63 lists the fundamental frequencies of S_0 toluene and the conversions between the notation schemes of Varsányi [65] and three other authors [102–104]. However, examination of the diagrams given in these references reveals some inconsistencies which appear to have been overlooked. The mode at 1605 cm^{-1} is described as "8a" in all four cases; however the diagram for "8a" in Ref. 102 appears to match the motion labelled as "9a" in Refs. 65 and 103 and vice-versa. Similar confusion exists for modes 8b/9b and 18a/19a.

For convenience, the labels used in the present work are chosen to match the energies listed for the corresponding Varsányi modes given in Table 1 of Ref. 63. The atomic motions for each normal mode are illustrated in Appendix A. It should be noted that the labels 8a/9a, 8b/9b and 18a/19a are reversed with respect to the atomic displacement diagrams (but not the assigned frequencies) given by Varsányi [65]. This difference may

Table 5.1. Calculated frequencies for toluene in the S_0 electronic state (this work, B3LYP/aug-cc-pVTZ), compared with experiment (Table 1 of Ref. 63).

	Mode label:		Wavenumber (cm^{-1})		
Symmetry	Mulliken	Varsányi	Harmonic	Anharmonic	Experiment
A_1	1	20a	3154	2999	3087
	2	2	3189	3045	3063
	3	$7a$	3168	3036	3055
	4	ν_s	3022	2908	2921
	5	$8a$	1645	1604	1605
	6	$19a$	1532	1499	1494
	7	δ_s	1415	1405	1379
	8	13	1230	1202	1210
	9	$9a$	1204	1191	1175
	10	$18a$	1053	1035	1030
	11	12	1022	1008	1003
	12	1	800	786	785
	13	$6a$	529	525	521
A_2	14	$17a$	994	976	964
	15	$10a$	863	848	843
	16	$16a$	417	409	407
B_1	17	ν_{as}	3100	2940	2979
	18	δ^+_{as}	1490	1476	1450
	19	δ^-_{as}	1067	1044	1040
	20	5	1013	995	978
	21	$17b$	921	902	895
	22	11	750	740	728
	23	4	717	705	695
	24	$16b$	478	474	464
	25	$10b$	210	210	216
B_2	26	$7b$	3155	3016	3039
	27	$20b$	3176	3033	3029
	28	ν_{as}	3073	2928	2952
	29	$8b$	1624	1584	1586
	30	δ^+_{as}	1504	1486	1463
	31	$19b$	1472	1441	1445
	32	14	1181	1168	1312
	33	3	1362	1343	1280
	34	$9b$	1327	1286	1155
	35	$18b$	1112	1092	1080
	36	δ^-_{as}	1002	998	967
	37	$6b$	638	633	623
	38	15	343	364	342

Table 5.2. Calculated (B3LYP/aug-cc-pVTZ) and measured frequencies for the toluene cation. Experimental values are from the ZEKE experiments carried out as part of the present work (see Chapter 6.)

	Mode label:		Wavenumber (cm^{-1})		
Symmetry	Mulliken	Varsányi	Harmonic	Anharmonic	Experiment
A_1	1	$20a$	3191	3074	
	2	2	3213	3082	
	3	$7a$	3198	3059	
	4	ν_{s}	2938	2873	
	5	$8a$	1674	1540	
	6	$19a$	1475	1439	
	7	δ_{s}	1357	1332	
	8	13	1257	1226	1235
	9	$9a$	1217	1190	
	10	$18a$	986	976	
	11	12	999	991	
	12	1	781	750	
	13	$6a$	514	508	494
A_2	14	$17a$	1026	1008	
	15	$10a$	804	783	
	16	$16a$	355	336	336
B_1	17	ν_{as}	3129	2917	
	18	δ^{+}_{as}	1485	1428	
	19	δ^{-}_{as}	1011	990	
	20	5	1039	1035	
	21	$17b$	943	934	
	22	11	748	748	
	23	4	581	566	
	24	$16b$	387	376	
	25	$10b$	150	130	
B_2	26	$7b$	3194	3070	
	27	$20b$	3209	3097	
	28	ν_{as}	3070	2922	
	29	$8b$	1300	1270	
	30	δ^{+}_{as}	1425	1373	
	31	$19b$	1538	1502	
	32	14	1167	1136	
	33	3	1406	1373	
	34	$9b$	1389	1358	
	35	$18b$	1085	1071	
	36	δ^{-}_{as}	981	954	
	37	$6b$	503	498	485
	38	15	346	349	

be simply due to the fact that Ref. 65 pre-dates the availability of a full calculation of the normal coordinates for toluene.

5.1.2. Neutral S_1 excited state

Within the DFT calculations described in Section 5.1.1 the electron density is variationally optimised, *i.e.* the Kohn-Sham orbitals are constructed in such a way as to minimise the total energy. Consequently, the calculations inherently tend to converge on the ground electronic state of the molecule. For this reason, a number of specialised methods exist for performing calculations on excited electronic states [105].

One of the simplest approaches is *Configuration Interaction Singles* (CIS), in which the orbitals are optimised for the ground electronic state and the wavefunction is expressed as a superposition of all the possible electron configurations where one electron has been promoted into a higher orbital. The resulting excited state wavefunctions are relatively crude, with an accuracy on a par with Hartree-Fock theory for the ground state [105]. However, the procedure does at least ensure that the wavefunctions for the different excited states are orthogonal to one another.

Gaussian 09 supports analytic first and second derivatives of the energy for a CIS calculation. Attempts to perform a geometry optimisation with a Dunning basis set (aug-cc-pVTZ or aug-cc-pVDZ) were unsuccessful, apparently due to technical issues within *Gaussian*. However it was possible to obtain harmonic frequencies by changing the basis set to 6-311++G**. Like aug-cc-pVTZ this is a "valence triple-ζ" basis set in the sense that three functions are used to represent each valence orbital. One of these is a contracted function composed of three Gaussian primitives, and the other two are individual Gaussian functions. The core orbitals are each represented by a single contracted function which is a weighted sum of six Gaussian primitives. Polarisation is achieved by adding a set of d angular momentum functions to each second-row atom (in this case, carbon), and adding p functions to the hydrogens (denoted by '**'). Diffuse functions are also included on both the hydrogens and the heavier atoms (denoted by '++').

Although anharmonic frequencies are in principle available for CIS calculations in *Gaussian 09*, attempts to find these resulted in several imaginary frequencies. The reasons for this remain unclear and so only the harmonic frequencies, which are all real, have been used in this work.

An alternative approach is *time-dependent density functional theory* (TD-DFT), which examines the effect on the electron density of a time-dependent external electric field of

the form $\vec{E} = \vec{r}\cos(\omega t)$. To a good approximation, the polarisability of the molecule varies with the frequency according to:

$$\langle\alpha\rangle_\omega = \sum_{i\neq 0}^{\text{States}} \frac{|\langle\Psi_0|\vec{r}|\Psi_i\rangle|^2}{\omega - (E_i - E_0)} \tag{5.1}$$

and so the frequencies where the polarisability goes to infinity correspond to the energies of the excited states [105].

With this method, *Gaussian 09* is able to calculate the first derivatives of the energy analytically in order to perform a geometry optimisation. The frequencies (second derivatives) must then be evaluated numerically. Although the high computational cost of the numerical differentiation precludes any correction for anharmonicity, it was nonetheless possible to obtain harmonic frequencies for S_1 toluene at the TD-B3LYP/aug-cc-pVTZ level of theory.

As a result of the Duschinsky mixing effect that was discussed in Section 2.3, some of the normal modes of the S_1 excited state differ significantly from those of the S_0 ground state (see Appendix A). Since the Varsányi mode labelling scheme is based upon the ground state, the task of assigning these labels to the S_1 normal modes presents some difficulties. A systematic approach was taken based upon the Duschinsky transformation which relates the modes of S_1 to those of S_0. Since the mixing is determined by the off-diagonal elements of the **S** matrix defined in Equation (2.1), the largest elements in each row and column show objectively which S_1 mode is most similar to each S_0 mode. (Details of the calculation of **S** will be given below, in Section 5.2.)

The two S_1 frequency calculations are compared in Table 5.3. Although only eleven[1] of the frequencies are known experimentally [63], it appears that the TD-B3LYP calculation is more accurate than the CIS. The root mean square error in the calculated values for these twelve frequencies is $78\,\text{cm}^{-1}$ for CIS, versus $21\,\text{cm}^{-1}$ for the TD-B3LYP. Part of this difference may be attributed to the use of a larger basis set in the DFT calculation.

It is possible to improve the accuracy of the calculated frequencies by applying a constant scaling factor. Based upon a survey of 1066 calculated frequencies for 122 different molecules, Merrick *et al.* [106] recommend that frequencies obtained from B3LYP / aug-cc-pVTZ calculations should be scaled by a factor of 0.9687 in order to achieve optimum agreement with experiment. In the present work, a least-squares fit of the TD-B3LYP S_1 frequencies to the experimental values of Hickman *et al.* [63] suggests a scaling factor of 0.972. A scaling factor of 0.97 is therefore employed, lowering the root mean square error

[1] Hickman *et al.* [63] give assignments for twelve S_1 frequencies, but their assignment for $9a^1$ is tentative and does not agree well with the calculations performed in this work. Mode $9a$ is therefore excluded from the assessment of the errors in the calculated S_1 frequencies.

Table 5.3. Calculated frequencies for S_1 toluene (this work), compared with experiment.

	Mode label:		Wavenumber (cm^{-1}):				
Symmetry	Mulliken	Varsányi	CIS[a]	Scaled[b]	TD-B3LYP[c]	Scaled[d]	Expt.[e]
A_1	1	$20a$	3342	3008	3183	3094	
	2	2	3375	3037	3213	3123	
	3	$7a$	3353	3018	3191	3102	
	4	ν_s	3124	2811	2936	2854	
	5	$8a$	1724	1551	1578	1534	
	6	$19a$	1584	1426	1458	1417	
	7	δ_s	1521	1369	1387	1348	
	8	13	1301	1171	1221	1187	1193
	9	$9a$	1264	1137	1177	1145	1021?
	10	$18a$	1071	963	974	946	935
	11	12	1045	941	990	963	966
	12	1	810	729	768	747	
	13	$6a$	500	450	466	453	457[f]
A_2	14	17a	825	742	719	699	687?
	15	$10a$	691	622	579	563	
	16	$16a$	185	167	217	211	228
B_1	17	ν_{as}	3234	2910	3079	2993	
	18	δ^+_{as}	1599	1439	1471	1430	
	19	δ^-_{as}	1102	992	997	970	
	20	5	911	820	822	799	
	21	$17b$	818	737	716	696	
	22	11	678	610	599	582	
	23	4	487	438	450	438	423
	24	$16b$	343	309	322	313	320
	25	$10b$	166	149	150	146	157
B_2	26	$7b$	3344	3010	3185	3096	
	27	$20b$	3365	3028	3204	3115	
	28	ν_{as}	3193	2874	3029	2945	
	29	$8b$	1619	1457	1539	1496	
	30	δ^+_{as}	1587	1428	1470	1429	
	31	$19b$	1534	1381	1415	1376	
	32	14	1258	1132	1175	1142	
	33	3	1431	1288	1331	1294	
	34	$9b$	1823	1641	1441	1401	
	35	$18b$	1147	1032	1059	1029	
	36	δ^-_{as}	1046	941	956	929	
	37	$6b$	579	521	538	523	532
	38	15	362	325	339	329	332

[a]Basis set: 6-311++G**.
[b]Scaling factor of 0.9.
[c]Basis set: aug-cc-pVTZ
[d]Scaling factor of 0.97.
[e]Fluorescence excitation spectrum by Hickman *et al*. See Table VIII of Ref. 63.
[f]Frequency of the eigenstate which has the largest contribution from the $6a^1$ zero-order state. $6a^1$ is strongly coupled to $10b^1 16b^1$ and weakly coupled to $16a^2$, both of which also make contributions to the eigenstate. See Chapter 7.

from 21 to 10 cm^{-1}. For the CIS calculation the least-squares fit to the experimental frequencies gives a scaling factor of 0.90, bringing the RMS error down to 29 cm^{-1}.

5.1.3. Deuterated toluene

All of the frequency calculations detailed above were repeated for the deuterated isotopomer $C_6H_5CD_3$, using the normal coordinates and force constants previously calculated for $C_6H_5CH_3$. Although the resulting harmonic frequencies were entirely real, the anharmonic calculations for the S_0 ground state and the $C_6H_5CD_3^+$ cation gave several imaginary frequencies. Consequently only the harmonic frequencies were used for this isotopomer. As for the S_1 frequency calculation in toluene-H_8, a scaling factor of 0.97 can be applied to improve the agreement between the B3LYP / aug-cc-pVTZ frequencies and experimental values [106]. The calculated frequencies, before and after scaling, are listed in Tables 5.4 to 5.6 on pages 66–68.

Table 5.4. Calculated and measured frequencies for deuterated toluene ($C_6H_5CD_3$) in the S_0 electronic state. The Mulliken mode numbers are appropriate for $C_6H_5CH_3$.

	Mode label:		Wavenumber (cm^{-1}):		
Symmetry	Mulliken	Varsányi	Calculation[a]	Scaled[b]	Experiment[c]
A_1	1	$20a$	3154	3059	3063
	2	2	3189	3093	3056
	3	$7a$	3168	3073	3005
	4	ν_s	2174	2109	2130
	5	$8a$	1645	1596	1606
	6	$19a$	1532	1486	1495
	7	δ_s	1070	1038	1045
	8	13	1249	1212	1225
	9	$9a$	1204	1168	1180
	10	$18a$	1049	1018	1026
	11	12	1022	991	1003
	12	1	773	750	758
	13	$6a$	506	491	498
A_2	14	$17a$	994	964	966
	15	$10a$	863	837	840
	16	$16a$	417	404	361
B_1	17	ν_{as}	2297	2228	2230
	18	δ^+_{as}	1077	1045	—
	19	δ^-_{as}	863	837	—
	20	5	1014	984	980
	21	$17b$	954	925	927
	22	11	726	704	709
	23	4	704	683	687
	24	$16b$	460	446	446
	25	$10b$	196	190	206
B_2	26	$7b$	3155	3060	3038
	27	$20b$	3176	3081	3029
	28	ν_{as}	2272	2204	2209
	29	$8b$	1620	1571	1586
	30	δ^+_{as}	1073	1041	1050
	31	$19b$	1482	1438	1448
	32	14	1181	1146	1261
	33	3	1360	1319	1300
	34	$9b$	1321	1281	1154
	35	$18b$	1104	1071	1073
	36	δ^-_{as}	804	780	—
	37	$6b$	637	618	623
	38	15	306	297	307

[a] Harmonic B3LYP / aug-cc-pVTZ
[b] Scaling factor of 0.97.
[c] Frequencies given by Varsányi [65].

Table 5.5. Calculated and measured frequencies for S_1 deuterated toluene ($C_6H_5CD_3$). The Mulliken mode numbers are appropriate for $C_6H_5CH_3$.

	Mode label:		Wavenumber (cm^{-1}):				
Symmetry	Mulliken	Varsányi	CIS[a]	Scaled[b]	TD-B3LYP[c]	Scaled[d]	Expt.[e]
A_1	1	$20a$	3315	2984	3183	3088	
	2	2	3419	3077	3213	3117	
	3	$7a$	3389	3050	3191	3095	
	4	ν_s	2254	2029	2126	2062	
	5	$8a$	1723	1551	1578	1531	
	6	$19a$	1587	1428	1459	1415	
	7	δ_s	1133	1020	1037	1006	
	8	13	1338	1204	1247	1210	
	9	$9a$	1265	1139	1178	1143	
	10	$18a$	1044	940	992	962	932
	11	12	1071	964	973	944	972
	12	1	786	707	740	718	713
	13	$6a$	480	432	449	436	438[f]
A_2	14	$17a$	834	751	719	697	
	15	$10a$	686	617	579	562	
	16	$16a$	185	167	217	210	227
B_1	17	ν_{as}	2398	2158	2281	2213	
	18	δ^+_{as}	1150	1035	1062	1030	
	19	δ^-_{as}	915	824	696	675	
	20	5	904	814	821	796	
	21	$17b$	777	699	831	806	
	22	11	671	604	594	576	
	23	4	461	415	430	417	
	24	$16b$	331	298	318	308	
	25	$10b$	152	137	142	138	
B_2	26	$7b$	3313	2982	3185	3089	
	27	$20b$	3385	3047	3204	3108	
	28	ν_{as}	2354	2119	2219	2152	
	29	$8b$	1610	1449	1534	1488	
	30	δ^+_{as}	1139	1025	1042	1011	
	31	$19b$	1536	1382	1421	1378	
	32	14	1253	1128	1175	1140	
	33	3	1416	1274	1327	1287	
	34	$9b$	1821	1639	1450	1407	
	35	$18b$	1119	1007	1026	995	
	36	δ^-_{as}	854	769	789	765	
	37	$6b$	576	518	536	520	529
	38	15	323	291	302	293	295

[a]Basis set: 6-311++G**
[b]Scaling factor of 0.9.
[c]Basis set: aug-cc-pVTZ
[d]Scaling factor of 0.97.
[e]Present work, nanosecond REMPI.
[f]Frequency of the eigenstate which has the largest contribution from the $6a^1$ zero-order state. $6a^1$ is strongly coupled to $10b^1 16b^1$ and weakly coupled to $16a^2$, both of which also make contributions to the eigenstate. See Chapter 7.

Table 5.6. Calculated and measured frequencies for $C_6H_5CD_3^+$. The Mulliken mode numbers are appropriate for $C_6H_5CH_3$.

	Mode label:		Wavenumber (cm^{-1}):		
Symmetry	Mulliken	Varsányi	Calculation[a]	Scaled[b]	Experiment[c]
A_1	1	$20a$	3191	3095	
	2	2	3213	3117	
	3	$7a$	3198	3102	
	4	ν_s	2130	2066	
	5	$8a$	1674	1624	
	6	$19a$	1475	1431	
	7	δ_s	1008	978	
	8	13	1282	1244	1225
	9	$9a$	1222	1185	
	10	$18a$	985	955	968
	11	12	1004	974	980
	12	1	756	733	738
	13	$6a$	491	476	474
A_2	14	17a	1027	996	
	15	$10a$	878	786	
	16	$16a$	352	341	332
B_1	17	ν_{as}	2322	2252	
	18	δ_{as}^+	1075	1043	
	19	δ_{as}^-	810	786	
	20	5	1039	1008	
	21	$17b$	980	951	
	22	11	697	676	
	23	4	538	522	~ 525
	24	$16b$	377	366	~ 367
	25	$10b$	142	138	~ 138
B_2	26	$7b$	3194	3098	
	27	$20b$	3209	3113	
	28	ν_{as}	2244	2177	
	29	$8b$	1405	1363	
	30	δ_{as}^+	1006	976	
	31	$19b$	1537	1491	
	32	14	1155	1120	
	33	3	1294	1255	
	34	$9b$	1392	1350	
	35	$18b$	1085	1052	
	36	δ_{as}^-	794	770	
	37	$6b$	501	486	476
	38	15	310	301	302

[a] Harmonic B3LYP / aug-cc-pVTZ
[b] Scaling factor of 0.97.
[c] ZEKE, this work. See Chapter 6.

5.2. Simulation of photoelectron spectra

A simulation of the photoelectron spectrum from a given vibrational level in the S_1 intermediate state requires not only knowledge of the vibrational frequencies in the S_1 state and the ion, but also a means of predicting the transition probabilities for ionisation into each of the possible final vibrational states. If the possibility of vibronic coupling is neglected then these probabilities are given by the *Franck-Condon factors*, which are the squares of the overlap integrals of the S_1 and ion vibrational wavefunctions. Several different methods have been proposed for the calculation of Franck-Condon factors, with varying levels of approximation and degrees of success [107].

In this work, Franck-Condon factors were calculated using the *FC-Lab II* software package developed by Pugliesi *et al.* [108, 109]. This code makes use of a recurrence formula, based upon the properties of harmonic oscillator wavefunctions, which allows for the rapid and efficient evaluation of large numbers of overlap integrals. A Duschinsky transformation is included to take into account the difference between the normal modes of the two electronic states (see Section 2.3). Full details of the algorithm can be found in Ref. 109 and references therein.

FC-Lab II is able to read the vibrational normal coordinates directly from the output file of a *Gaussian 09* frequency calculation. If necessary, the molecule is automatically rotated to ensure that the orientation is the same for both electronic states. The Duschinsky mixing matrix $\mathbf{S}$ and offset vector $\vec{d}$ are then calculated and output into separate data files. These quantities are defined in Equation (2.1), and as mentioned above in Section 5.1.2 the $\mathbf{S}$ matrix is helpful for defining the correspondence between the calculated normal modes in the S_0 and S_1 electronic states.

In the calculation of the Franck-Condon factors, only a single (user-specified) initial S_1 vibrational state is considered. Up to three normal modes are allowed to be simultaneously excited in the ion, with a maximum of five quanta in each. The highest cation internal energy to be considered can be adjusted by the user; in this work $2500\,\mathrm{cm}^{-1}$ was typically sufficient to cover the entire range of the spectrum seen in the experiments.

Three important caveats must be borne in mind when interpreting the results of the Franck-Condon simulations. Firstly, no allowance is made for vibronic (Herzberg-Teller) coupling. Hence a transition will only be predicted to have non-zero intensity if it adheres to a strict symmetry selection rule: the direct product of the irreducible representations of the initial and final vibrational states must contain the totally symmetric representation. In reality, vibronic coupling may relax this rule so that some "symmetry-forbidden" transitions are observed. Secondly, the calculation relies upon the properties of harmonic

oscillator eigenfunctions and so it is not possible to account for the effects of anharmonicity. It follows that the vibrational couplings which we are seeking to investigate in the real molecule cannot be reproduced in the simulation. Thirdly, the computed Franck-Condon factors can be very sensitive to the level of theory used to calculate the geometry and vibrational normal coordinates of the molecule in the two electronic states [109].

In order to produce a Franck-Condon simulation of a photoelectron spectrum, vibrational frequencies and normal coordinates must be provided for both the S_1 electronic state and the cation. In the case of the ion, the normal coordinates were taken from the B3LYP/aug-cc-pVTZ calculations. The harmonic frequencies were replaced by anharmonic values, since this procedure was found to give more accurate line positions without significantly altering the line intensities.

As discussed above in Section 5.1.2, there is a choice of two frequency calculations to use for the S_1 electronic state. Although the frequencies given by TD-B3LYP/aug-cc-pVTZ appear to be more accurate than those obtained from a CIS/6-311++G** calculation, they do not necessarily result in a better prediction of the Franck-Condon factors. In many cases, the intensities of minor features in the photoelectron spectrum are found to be seriously over-estimated when the TD-B3LYP calculation is used. Conversely, Franck-Condon simulations based on the CIS calculation for the S_1 state do not always reproduce the higher-energy ion vibrational peaks which are observed experimentally; however there are fewer spurious intense transitions compared with the predictions from TD-B3LYP. For this reason the calculations using CIS frequencies are preferred overall, although there is still considerable room for improvement. An example of the different results from the two methods is shown in Fig. 5.1 on the following page.

Regardless of which model is used for the S_1 state, the simulations often produce long spurious progressions of the methyl torsion in the ion. This error can be attributed to the incorrect assumption of an harmonic potential for the torsion, which the simulation treats like any other normal mode even though it is not a true vibration. As there is no way to exclude this mode from the Franck-Condon calculation, the simulated spectra are filtered afterwards to remove any transitions involving torsional excitation. This procedure has been applied to the examples shown in Fig. 5.1.

5.3. Density of vibrational states

The *density of states*, $\rho(E)\,\mathrm{d}E$, is defined as the number of vibrational levels which exist within an energy range E to $E + \mathrm{d}E$. Knowledge of this parameter is important

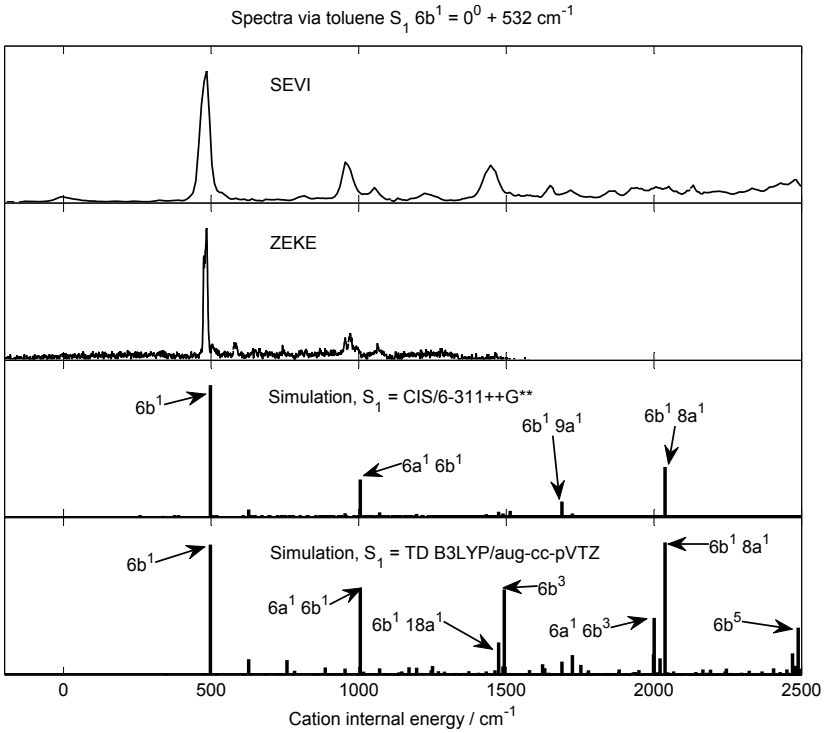

Fig. 5.1. Example of simulated photoelectron spectra using CIS and TD-B3LYP methods for the S_1 normal mode analysis. While the CIS simulation does not reproduce every peak, the TD-B3LYP gives several peaks which are significantly too intense.

for rationalising the differences in IVR behaviour from the various initially-prepared vibrational levels. Although ρ cannot easily be measured directly, it can be calculated based upon a knowledge of the vibrational frequencies of the molecule.

5.3.1. Total density of states: the Beyer-Swinehart Algorithm

If the molecule is regarded as a collection of harmonic oscillators, then the calculation of $\rho(E)$ is analogous to working out how many different combinations of coins could be used to pay a given sum of money. Instead of coins we have fundamental harmonic frequencies, and instead of a price we have a specified energy range E to $E + \delta E$, where δE is known as the *grain size*. The *Beyer-Swinehart algorithm* is a remarkably simple and efficient solution based upon direct counting of the combinations [110]. Tutorial explanations of the algorithm can be found in, for example, textbooks by Gilbert and Smith [4] and Baer and Hase [5].

In the simplest case, for which the algorithm is exact, the normal mode frequencies are specified to the nearest $1\,\mathrm{cm}^{-1}$ and $\delta E = 1\ \mathrm{cm}^{-1}$. Let $E_{\max}$ be the highest energy at which we need to know the density of states. It is essential that $E_{\max}$ is greater than the highest fundamental frequency.

Define a vector (or, in computing terminology, an array) ρ, with elements $\rho(0) \cdots \rho(E_{\max})$.

Each element $\rho(i)$ will correspond to the density of states over the energy range $i \leq E < (i+1)\,\mathrm{cm}^{-1}$. Clearly $\rho(0) = 1$, since there is only one vibrational ground state. All other elements of ρ are initialised to zero.

We then examine each normal mode frequency ν in turn. Notice that if a state exists with energy $(E - \nu)$ then it can combine with one quantum of ν to make a state with energy E. This relation will find not just the combination bands, but also the fundamentals (= combination of ν with the ground state) and overtones (= combinations of ν with itself). Therefore the complete density of states array is simply calculated via the procedure of Algorithm 1, which requires only two nested loops to deal with any number of normal modes. No restrictions are placed upon the number of quanta in each mode, or the number of modes excited simultaneously.

Algorithm 1: Beyer-Swinehart algorithm for the total density of harmonic vibrational states.

```
ρ(0) ← 1
ρ(1 ··· E_max) ← 0
foreach fundamental frequency ν do
    for E = ν to E_max do
        ρ(E) ← ρ(E) + ρ(E − ν)
    end for
end foreach
```

Larger grain sizes δE may be accommodated by expressing ν and E as multiples of δE, and reducing the number of elements in ρ accordingly. Increasing the grain size to $10\,\mathrm{cm}^{-1}$, for example, will reduce the required computer time by a factor of ten. With modern computers this increase in speed is inconsequential, since even with $\delta E = 1\ \mathrm{cm}^{-1}$ the calculation would usually take only a fraction of a second. However, increasing the grain size does have the advantage of giving a smooth curve when ρ is plotted as a function of E, since each data point is then an average over a wider energy range.

The simple algorithm presented above is appropriate for a rigid molecule, where all of the vibrations can be regarded as harmonic. Toluene, however, is more complicated since the torsional levels of the methyl rotor must also be taken into account. An extended version of the algorithm due to Stein and Rabinovitch [111] may be used to combine different degrees of freedom in a density of states calculation. The key difference from the original Beyer-Swinehart algorithm is that the energy levels for each degree of freedom are listed explicitly, rather than being assumed to be integer multiples of a given fundamental frequency.

An implementation of the Stein-Rabinovitch algorithm is provided by the *Densum* computer program, which is part of the *MultiWell* suite developed by Barker and co-

workers [112] for chemical kinetics simulations. This software has been made available free of charge, along with its Fortran source code, and was used to carry out the density of states calculations in the present work. A useful feature of *Densum* is the ability to compute the energy levels for the methyl torsion, given the reduced rotational constant of the CH_3 group and the magnitude of the barrier to its rotation. In the S_1 electronic state, these parameters have been measured from a fluorescence excitation spectrum [17] for both toluene and $C_6H_5CD_3$ (see Table 5.7).

Table 5.7. Parameters used to find torsional levels in the S_1 electronic state for the density of states calculations. Values are taken from Tables I and II of Ref. 17. The negative sign of V_6 indicates that a staggered conformation of the methyl group is more stable than the eclipsed conformation.

Molecule	Reduced rotational constant (cm^{-1})	Torsional barrier, V_6 (cm^{-1})
$C_6H_5CH_3$	5.298	-26.376
$C_6H_5CD_3$	2.74	-24.5

The harmonic frequencies for the S_1 state were taken from the TD-B3LYP/aug-cc-pVTZ calculations, and a grain size of $1\,cm^{-1}$ was used in the Stein-Rabinovitch algorithm. Fig. 5.2 on the following page shows the calculated density of states as a function of internal energy for S_1 toluene and for the deuterated isotopomer $C_6H_5CD_3$. For both of these molecules, the density of states increases rapidly above $\sim 1000\,cm^{-1}$. Due to the smaller rotational constant of the CD_3 group compared with CH_3, the deuterated molecule has more closely-spaced torsional levels and hence a significantly higher density of states than non-deuterated toluene.

The significance of these results will be discussed further in Chapter 8, which examines the dissipative IVR behaviour that occurs when the density of states is high.

5.3.2. Density of states with symmetry restrictions

Although a knowledge of the total density of states is useful for rationalising IVR behaviour, it is not the full story because only a subset of the vibrational states are able to couple to the zero-order bright state. If the coupling arises mainly through anharmonicity, then only dark states which share the same symmetry irreducible representation as the bright state can take part in IVR. For this reason, it is helpful to identify the vibrational states *with a given symmetry* that exist within a specified energy range around the bright state.

The Beyer-Swinehart and Stein-Rabinovitch algorithms described in the preceding section achieve their efficiency by counting vibrational states without listing them explicitly, and so cannot provide any information about the symmetries of the states. An alterna-

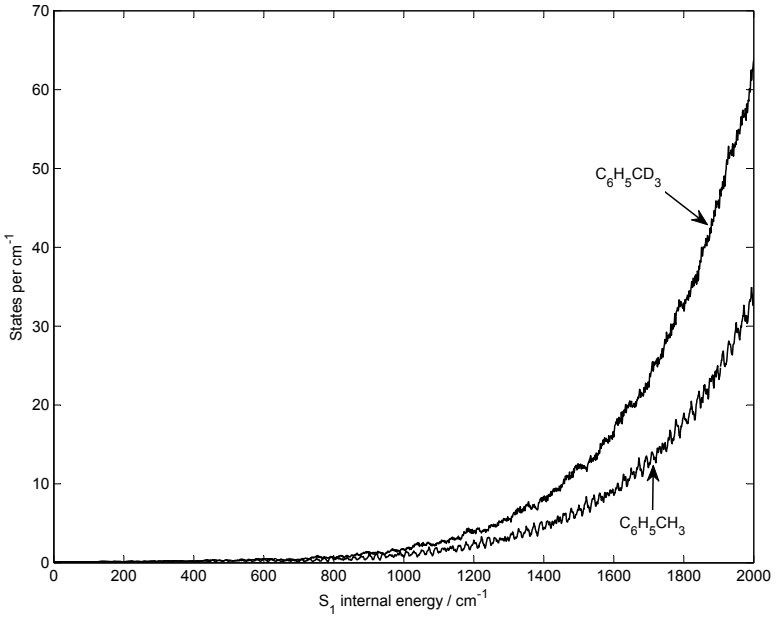

Fig. 5.2. Calculated density of states for S_1 toluene and deuterated toluene. For display purposes, the lines have been smoothed using a 10-point moving average filter.

tive approach, which does give assignments and therefore symmetries for the states, is the *backtracking algorithm* [113]. This is essentially an efficient way to search through all of the possible combinations of numbers of quanta in each degree of freedom, up to a specified energy limit $E_{\max}$. The procedure is shown in Algorithm 2. We begin with a single quantum of excitation in the first degree of freedom and calculate the energy and symmetry of this state. If the energy falls within a specified range and the symmetry is of the desired type, then a note is made of this energy level. The number of quanta is incremented, checking the energy and symmetry each time, until the energy exceeds $E_{\max}$. At this point the number of quanta is reduced by one, taking the energy back below $E_{\max}$, and we begin to increment the quanta of the next mode. On reaching the maximum number of quanta in the last degree of freedom, we go back to the next-highest occupied mode and decrease the number of quanta by one. In all of the modes above that the number of quanta is set to zero, and the count restarts. The algorithm terminates when only the last degree of freedom has a non-zero number of quanta.

In the present work, Algorithm 2 has been implemented using the C programming language. Excitations of the methyl torsion are considered according to the torsion-rotation coupling selection rules described in Section 2.7.4, which make use of the one-to-one correspondence between some of the irreducible representations of the full G_{12} molecular symmetry group and those of the C_{2v} point group (see Section 2.7.3). Coupling is permitted between two vibrational levels if their overall symmetries (including torsion)

Algorithm 2: The backtracking algorithm.

```
Let N be the number of degrees of freedom.
quanta (1 ··· N) ← 0
n ← 1
a ← 1
repeat
    while energy < E_max do
        quanta (n) ← quanta (n) + 1
        Calculate energy and symmetry.
        if energy in range and symmetry OK then Output: quanta array
    end while
    // Back off by one quantum and move to next degree of freedom.
    quanta (n) ← quanta (n) − 1
    n ← n + 1
    if n > N then we have reached maximum quanta in the last mode.
        if all elements of quanta (1 ··· N − 1) are zero then a ← 0
        else a ← largest integer < N for which quanta (a) ≠ 0
        if a > 0 then
            quanta (a) ← quanta (a) − 1
            n ← a + 1
            quanta (n ··· N) ← 0
        end if
    end if
until a = 0
```

are the same and their torsional quantum numbers differ by 0, ±3 or ±6. It is assumed that the bright state has a torsional level of $m = 0$ or 1, and so in searching for states which can couple to a given bright state it is necessary to consider m values of 0, 1, ±3, ±6 and ±7. The energy levels associated with these torsional quantum numbers are calculated using a free rotor model, with the reduced rotational constant taken from Table 5.7.

Uses of this program will be discussed in Chapter 8, in which rates of dissipative IVR are compared for different initially-prepared bright states, and in Chapter 9 where the backtracking method is employed to identify possible "doorway" states that could be coupled to the 13^1 C−CH_3 stretching vibration. If normal mode frequencies are supplied for the ion rather than the S_1 state, the same program can also be used as an aid to the assignment of peaks seen in the SEVI and ZEKE photoelectron spectra.

Part III.

Results and Discussion

6. Nano- and picosecond photoelectron spectroscopy of toluene

Toluene has 39 normal modes, of which 38 are true vibrations and one is more properly considered as an internal rotation, or 'torsion', of the methyl group. These have been well characterised for the neutral molecule, and in the ground electronic state all 38 vibrational frequencies are known. Hickman *et al.* [63] have surveyed the results of nine previous infrared and Raman studies [65, 102–104, 114–118] and used these to compile a full set of reliable assignments. In order to study the vibrational levels of the S_1 excited electronic state, Hickman *et al.* also recorded a fluorescence excitation spectrum in a jet-cooled molecular beam, extending to $\sim$2000 cm^{-1} of internal energy. The majority of the observed absorption features were identified using dispersed fluorescence, making use of the known S_0 frequencies to provide definitive assignments. These measurements yielded frequencies for thirteen normal modes in the S_1 excited state. Independent confirmation of some of the assignments is provided by Balfour and co-workers, who obtained infrared [119] and ultra-violet [120] absorption spectra for liquid toluene and seven deuterated isomers.

By contrast, only a few of the vibrational frequencies are known for the toluene cation. In the first ever application of laser two-photon ionisation to the photoelectron spectroscopy of a polyatomic molecule, Meek *et al.* [121] excited *via* the S_1 origin, $6b^1$ and 12^1 levels of toluene and examined the kinetic energy distribution of the photoelectrons by time-of-flight measurements. They observed progressions corresponding to the vibrational frequencies of the cation, but were only able to give tentative assignments. More recently, using a combination of time-of-flight and velocity map imaging techniques, Whiteside *et al.* [52, 53, 122] recorded photoelectron spectra *via* a series of S_1 vibrational levels and were able to assign seven cation frequencies. However the vibrational peaks were only partially resolved, and the spectra recorded from intermediate levels > 750 cm^{-1} above the S_1 origin were seen to be unstructured.

Zero electron kinetic energy (ZEKE) spectroscopy, described in Chapter 4, offers far higher resolution than the time-of-flight method. Lu *et al.* [92] were the first to study toluene with ZEKE, obtaining detailed information about the torsional levels in the cation. Using the closely related *mass analysed threshold ionisation* (MATI) technique,

in which ions rather than electrons are detected, Gunzer and Grotemeyer [123] were able to measure well-resolved spectra from two excited S_1 vibrational levels (460 and 528 cm^{-1}), as well as an excited torsional level.

In the present work, ZEKE spectra *via* a series of excited vibrational levels in S_1 toluene and $C_6H_5CD_3$ have been obtained for the first time [124]. These are complemented by picosecond SEVI spectra, which have lower resolution but are able to cover a wider range of cation internal energies and give more reliable peak intensities. This chapter will focus upon the vibrational levels which showed no time dependence in the SEVI studies, and a number of assignments will be made for previously-unknown frequencies in the toluene cation.

6.1. REMPI spectra via S_1

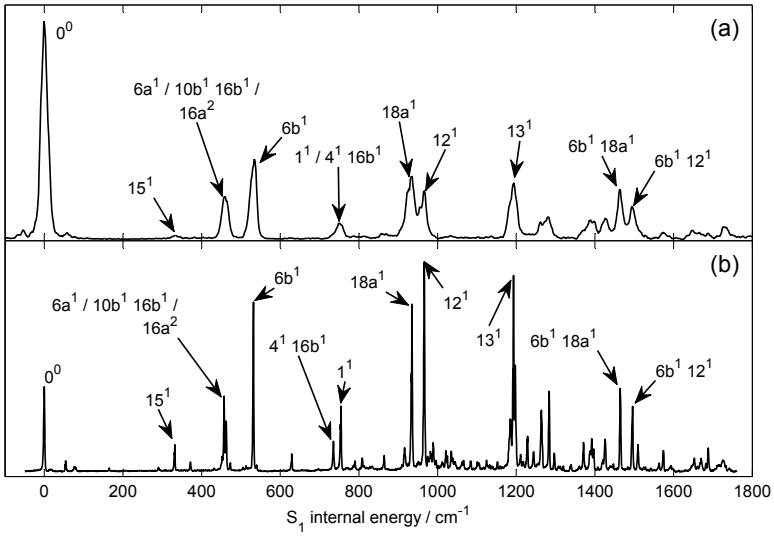

Fig. 6.1. REMPI spectra of toluene recorded in this work *via* the S_1 electronic state, using: (a) a solid state laser with 1 ps pulse duration and ∼15 cm^{-1} bandwidth; (b) a dye laser with 5 ns pulse duration and ∼0.3 cm^{-1} bandwidth. Energy scale is given relative to the S_1 origin at 37 477.4 cm^{-1} [63]. Peak intensities are affected by variations in laser power across the wavelength range.

Fig. 6.1 shows two REMPI spectra which were recorded in this work, using picosecond and nanosecond lasers, in order to characterise the vibrational levels in the S_1 electronic state of toluene. They provide similar information to a fluorescence excitation spectrum published by Hickman *et al.* [63], which was used to calibrate the energy scales of the REMPI spectra and to supply the assignments for the S_1 vibrational levels. The narrower bandwidth of the nanosecond laser enables a greater number of individual vibrational levels to be resolved compared with the picosecond REMPI spectrum. However the power

output of the nanosecond dye laser varied significantly across the range of wavelengths studied, and this affects the apparent intensity of the REMPI peaks. The picosecond laser gave a more consistent power output, and hence more reliable absorption intensities. One obvious example is the origin peak, which is expected to correspond to the strongest transition. In the picosecond REMPI spectrum the origin is the strongest peak, whereas in the nanosecond spectrum it appears weaker than 12^1 because the dye lases less efficiently at the wavelength of the origin.

6.2. Photoelectron spectra via the S_1 origin

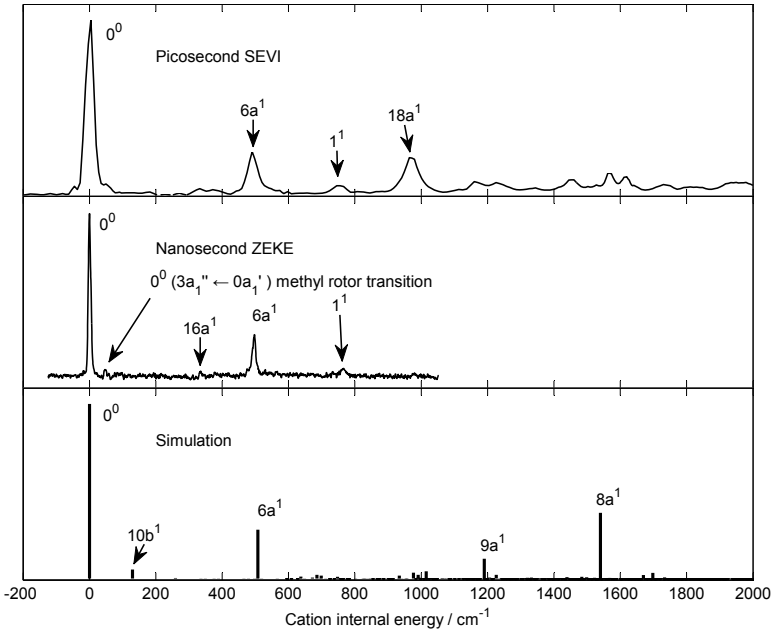

Fig. 6.2. Photoelectron spectra and Franck-Condon simulation *via* the S_1 origin in toluene.

The SEVI and ZEKE spectra recorded *via* the S_1 origin are shown in Fig. 6.2. This transition occurs at a pump photon energy of $37\,477.4\,\mathrm{cm}^{-1}$ [63]. As expected, the spectrum is dominated by cation vibrational levels of A_1 symmetry, with the origin being the most intense. This strong $\Delta v = 0$ transition suggests that the change in geometry between the S_1 electronic state and the cation is relatively small.

The very weak ZEKE feature at $\sim 332\,\mathrm{cm}^{-1}$ has previously been observed in a MATI spectrum by Gunzer and Grotemeyer [123], who identified it as the cation 15^1 level. This assignment is at odds with the frequency of $340\,\mathrm{cm}^{-1}$ for the cation 15^1 level measured in the present work (see Section 6.3). It therefore seems more likely that the $332\,\mathrm{cm}^{-1}$ peak is in fact the cation $16a^1$ level. The low intensity of the transition can be explained by the symmetry selection rule: the S_1 origin has a totally symmetric vibrational wavefunction,

but $16a^1$ transforms as A_2 in the approximate C_{2v} point group.

A weak methyl rotor transition, $0^0\,(3a_1'' \leftarrow 0a_1')$, appears at $46\,\mathrm{cm}^{-1}$ in the ZEKE spectrum. This frequency is in excellent agreement with the values reported by Lu *et al.* [92] and Gunzer and Grotemeyer [123] of 45 and $46\,\mathrm{cm}^{-1}$ respectively.

The probe wavenumber of the origin peak in the ZEKE spectrum indicates an adiabatic ionisation energy of $71201 \pm 5\,\mathrm{cm}^{-1}$, which is in excellent agreement with the previously published values of $71199 \pm 5\,\mathrm{cm}^{-1}$ [92] and $71198 \pm 7\,\mathrm{cm}^{-1}$ [123]. The error bar in this measurement is taken as being equal to half of the width at half-maximum of the ZEKE peak.

Fig. 6.3 shows the effect of deuteration of the methyl group on the ZEKE spectrum *via* the S_1 origin. The peak corresponding to $6a^1$ in the ion is shifted to the red by $22\,\mathrm{cm}^{-1}$. Unfortunately the signal-to-noise ratio is not sufficient to discern the weak $16a^1$ and methyl rotor transitions. The probe wavenumber corresponding to the origin peak indicates that the ionisation potential of $C_6H_5CD_3$ is 71247 ± 5 cm^{-1}. No other measurements of this quantity could be found in the literature for comparison.

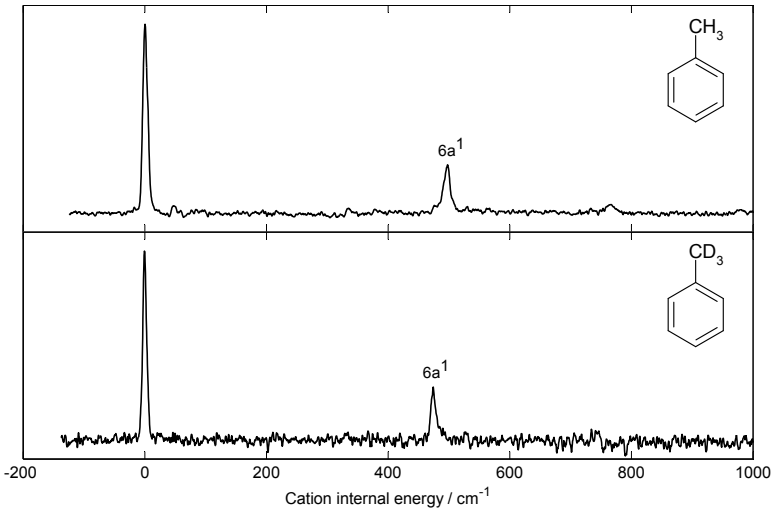

Fig. 6.3. Comparison of ZEKE spectra *via* the S_1 origin in the two isotopomers.

6.3. Photoelectron spectra via S_1 15^1 (0^0 + 332 cm^{-1})

Mode 15 is an in-plane wagging motion of the methyl group, which has B_2 symmetry in the C_{2v} point group. In Fig. 6.4 the ZEKE spectrum *via* S_1 15^1 is compared with a picosecond two-colour VMI spectrum, which was recorded with a single probe wavelength of 286 nm. The $\Delta v = 0$ transition is again dominant, and a combination band of B_2 symmetry, $6a^1 15^1$, is also seen. A third feature at $\sim$1311 cm^{-1} is observed in the VMI spectrum, but is absent from the ZEKE due to the fall-off in laser power towards the end

of the dye range. This peak is too broad to be assigned definitively, and is unfortunately overlooked by the Franck-Condon simulation. Plausible candidates could be $15^1 6a^2$ and / or $15^1 6b^2$, which have the correct energy and B_2 symmetry.

On deuteration of the methyl group, the 15^1 peak is red-shifted by 42 cm^{-1} and the $6a^1 15^1$ peak by 62 cm^{-1} (see Fig. 6.5).

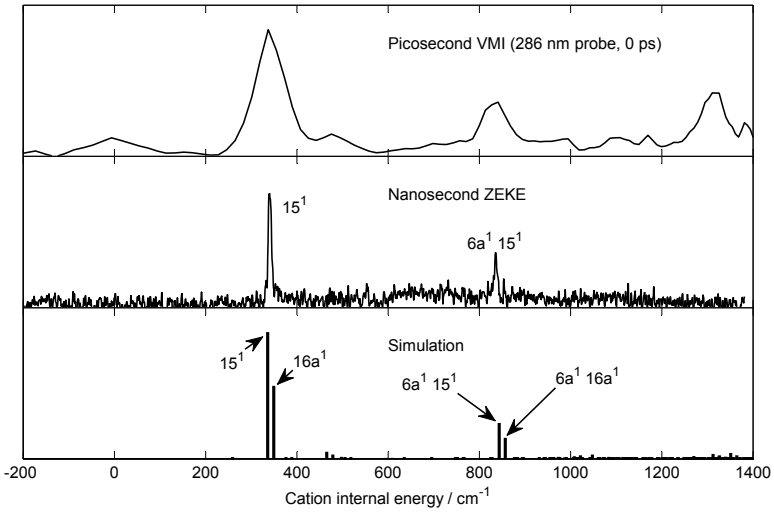

Fig. 6.4. Photoelectron spectra and Franck-Condon simulation via S_1 15^1.

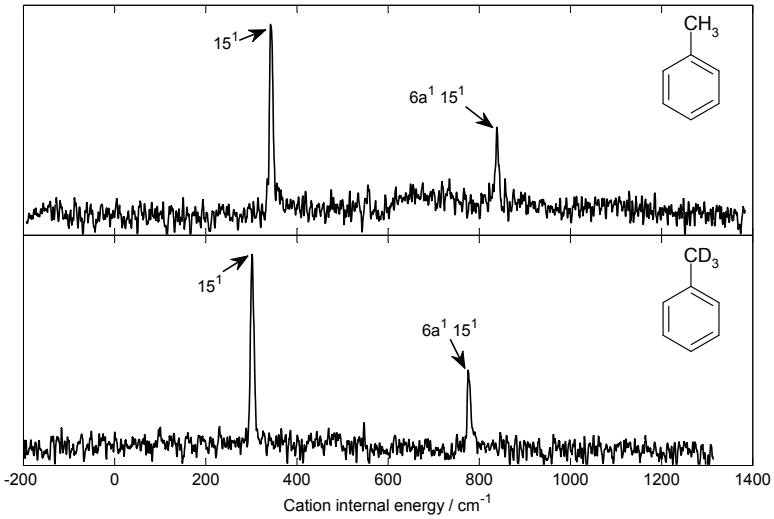

Fig. 6.5. ZEKE spectra *via* S_1 15^1 for the two isotopomers.

6.4. Photoelectron spectra via S_1 $6b^1$ (0^0 + 532 cm^{-1})

Mode $6b$ is an in-plane 'shearing' motion of the benzene ring with B_2 symmetry. The SEVI and ZEKE spectra *via* S_1 $6b^1$ are plotted in Fig. 6.6, along with a Franck-Condon simulation. Once again the $\Delta v = 0$ transition dominates, and a combination with $6a^1$ also appears. A weak feature at 485 cm^{-1} in the ZEKE spectrum is tentatively assigned

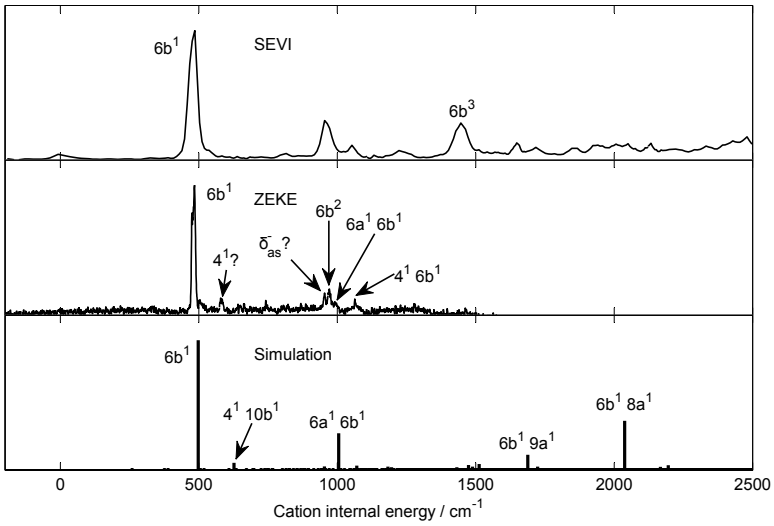

Fig. 6.6. Photoelectron spectra and Franck-Condon simulation *via* S_1 $6b^1$.

as a methyl C−H bending mode of B_2 symmetry ($\delta_{\rm as}^-$), as its frequency coincides with that predicted by the anharmonic B3LYP calculation (see Table 5.2). Three additional ZEKE features, assigned as 4^1, $6b^2$ and $4^1 6b^1$, do not have B_2 symmetry and are therefore weak.

On deuteration of the methyl group, the ion $6b^1$ frequency is red-shifted by 19 $\rm cm^{-1}$ (see Fig. 6.7). A weak (A_1 symmetry) $18a^1$ peak is revealed, which cannot be seen in non-deuterated toluene as it would be overlapped with the $6b^2$ transition. Two other features, at 703 and 937 $\rm cm^{-1}$, remain unassigned.

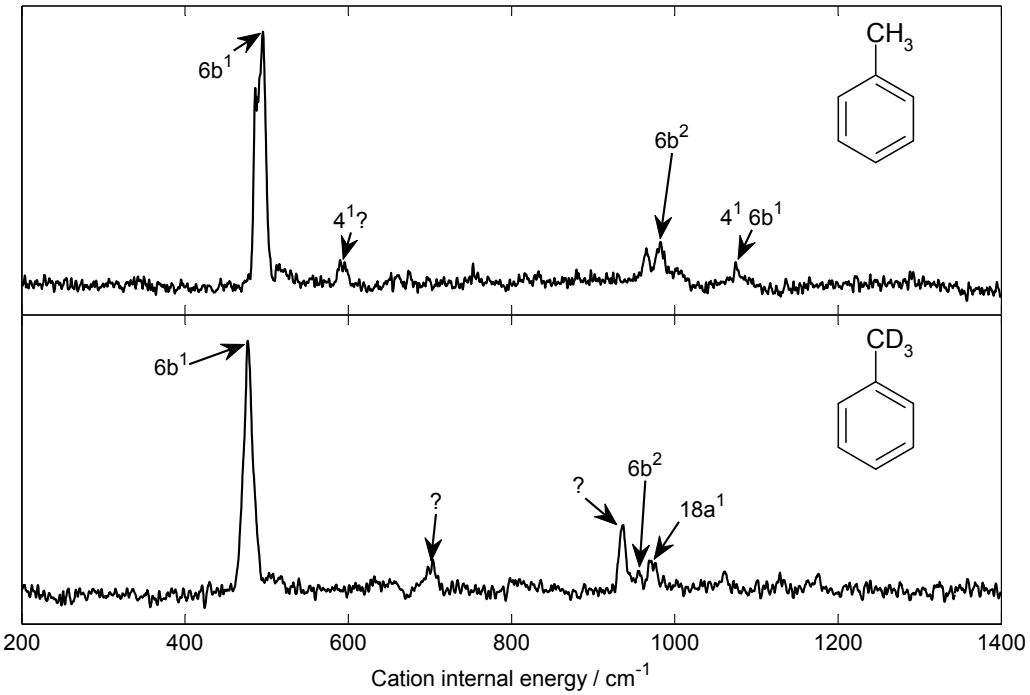

Fig. 6.7. ZEKE spectra *via* S_1 $6b^1$ in the two isotopomers.

6.5. Photoelectron spectra via S_1 1^1 / 4^1 $16b^1$ Fermi resonance (754 / 736 cm^{-1})

Hickman *et al.* [63] diagnosed a pair of lines at 736 and 754 cm^{-1} in the fluorescence excitation spectrum of toluene as the result of a Fermi resonance. Dispersed fluorescence spectra from these levels confirmed that the contributing zero-order states were 1^1 and $4^1 16b^1$, whose unperturbed harmonic frequencies would be 748 and 743 cm^{-1} respectively. The dispersed fluorescence from the vibrational level at 754 cm^{-1} also contained several bands that could not be explained by the Fermi resonance model, suggesting the involvement of a third, unidentified coupled zero-order state. Evidence of IVR was seen following excitation of both Fermi resonance components, with the sharp lines in the dispersed fluorescence spectra being superimposed upon a broad, unstructured "hump"; by contrast the dispersed fluorescence spectra from lower-lying S_1 vibrational levels had shown a flat baseline.

In this work, picosecond SEVI and nanosecond ZEKE photoelectron spectra were recorded *via* both levels of the Fermi resonance (see Fig. 6.8). Although the two vibrational levels were not fully resolved in the picosecond REMPI spectrum, they were found to be too far apart to prepare a coherent superposition and so no clear time dependence could be observed. Instead, two sets of picosecond SEVI spectra were recorded with the pump laser tuned to either side of the absorption maximum in order to excite each Fermi resonance component separately. The spectra shown here are the result of combining images with probe wavelengths of 282, 286, 290 and 294 nm.

The Franck-Condon simulations plotted in Fig. 6.8 predict that ionisation from each zero-order state should give a photoelectron spectrum dominated by the $\Delta v = 0$ transition. However, due to the Fermi resonance coupling, the experimental spectra *via* the two S_1 levels show features corresponding to both 1^1 and $4^1 16b^1$ in the cation. The spectrum from the upper component of the Fermi resonance shows a stronger 1^1 peak than the spectrum from the lower component, suggesting that the frequency ordering of the zero-order states in S_1 proposed by Hickman *et al.* is correct. In the ZEKE spectra the peaks are superimposed upon a broad "hump", reminiscent of the signature of IVR seen by Hickman *et al.* in the dispersed fluorescence.

In S_1 toluene-D_3 the 1^1 / $4^1 16b^1$ Fermi resonance produces vibrational energy levels at 713 and 731 cm^{-1}. ZEKE spectra recorded *via* these levels are shown in Fig. 6.9. The DFT calculations described in Section 5.1 predict that the 1^1 zero-order state should have a lower frequency than $4^1 16b^1$ in both the S_1 state and in the cation. As would be expected, excitation *via* the lower vibrational level gives a more intense 1^1 peak, whereas

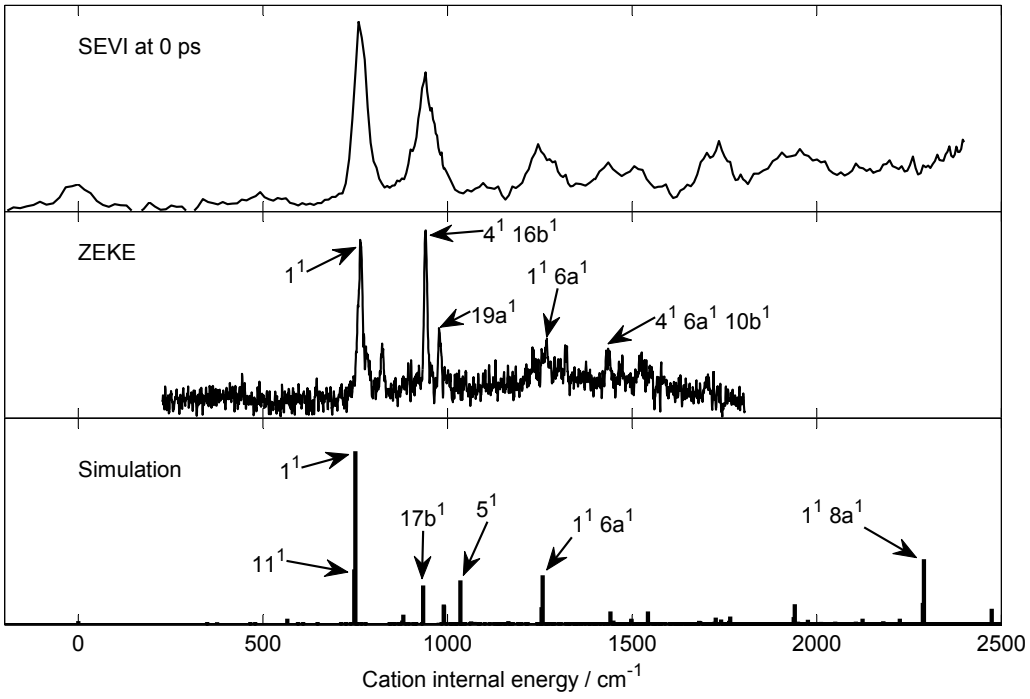

(a) Upper Fermi resonance component, "1^1" (754 cm^{-1})

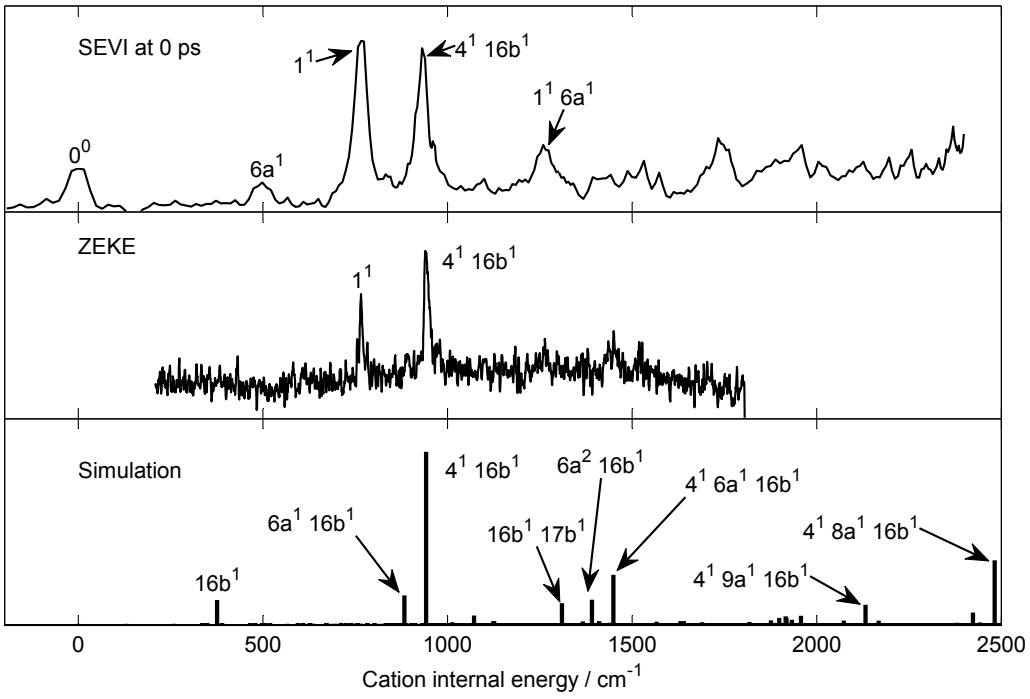

(b) Lower Fermi resonance component, "$4^1 16b^1$" (736 cm^{-1})

Fig. 6.8. SEVI and ZEKE spectra and Franck-Condon simulations *via* the S_1 1^1 / $4^1 16b^1$ Fermi resonance.

excitation *via* the upper level produces a ZEKE spectrum in which $4^1 16b^1$ is the strongest feature. It therefore appears that the energy ordering in S_1 of the 1^1 and $4^1 16b^1$ levels is reversed with respect to toluene-H_8.

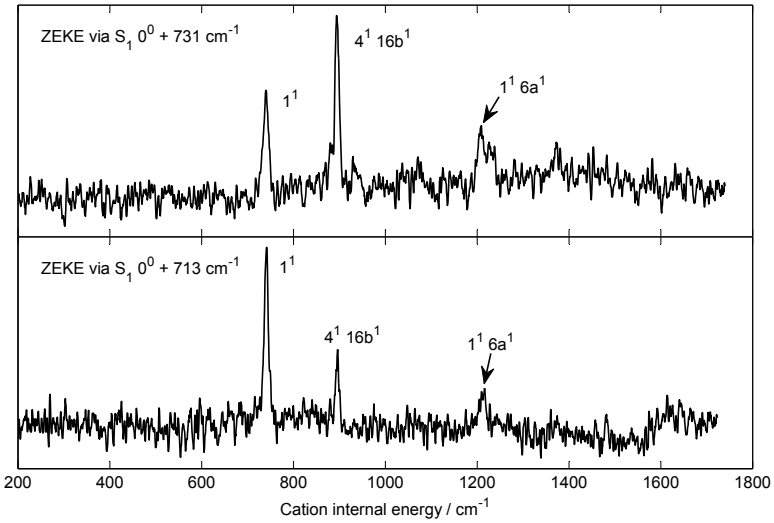

Fig. 6.9. ZEKE spectra *via* the two components of the 1^1 / $4^1 16b^1$ Fermi resonance in S_1 $C_6H_5CD_3$.

6.6. Photoelectron spectra via S_1 $18a^1$ (0^0 + 935 cm^{-1}) and 12^1 (0^0 + 966 cm^{-1})

The dispersed fluorescence spectra recorded by Hickman *et al.* [63] from the S_1 vibrational levels at 935 and 966 cm^{-1} showed no evidence of coupling between the zero-order states 12^1 and $18a^1$, since the two spectra had no bands in common. However, both spectra contained several lines that could be assigned to combinations involving modes 12 and $18a$ in the ground electronic state. This observation was taken as evidence of Duschinsky mixing: normal modes 12 and $18a$ in S_1 were hypothesised to differ significantly from their counterparts in S_0, each having some character from both.

The normal mode calculations described in Section 5.1 of the present work suggest that extensive mixing does indeed take place (see Fig. 6.10). In the electronic ground state, mode 12 is a pure ring breathing motion and mode $18a$ is an in-plane C−H wagging motion. However, in both S_1 and the cation, mode 12 involves significant C−H wagging; indeed its relationship to mode 12 of the S_0 state is only apparent on examination of the calculated Duschinsky mode mixing matrix (see Section 5.1.2). Throughout the following discussion, the S_1 vibrational level at 935 cm^{-1} will be referred to as "$18a^1$" and the level at 935 cm^{-1} as "12^1", but it should be borne in mind that in this case it is rather misleading to use the same naming convention for the normal modes of all three electronic states.

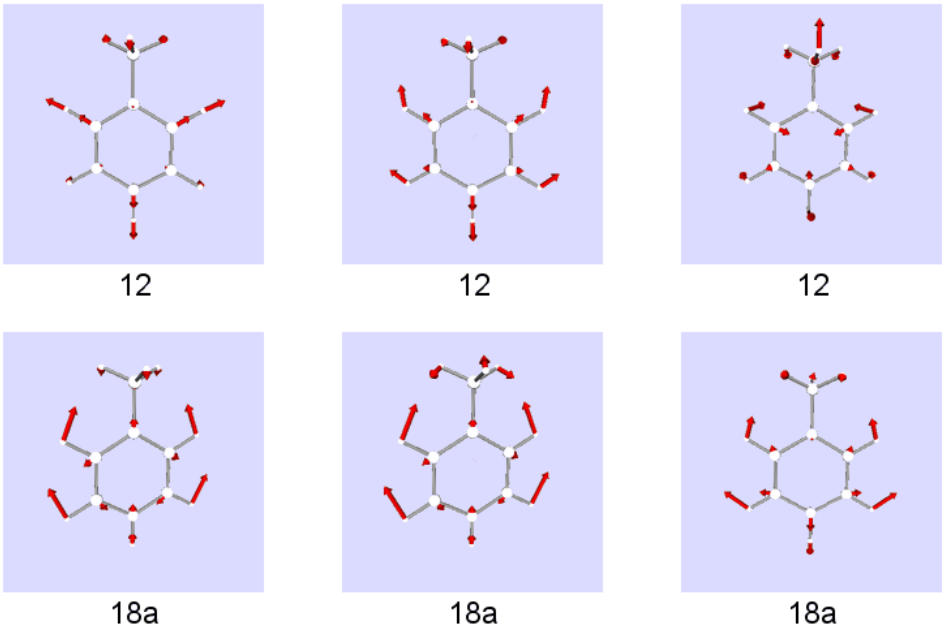

(a) Neutral S_0. **(b)** Neutral S_1. **(c)** Cation D_0.

Fig. 6.10. Comparison of modes 12 and 18a in the three electronic states.

In view of the mixing, it is no surprise that the SEVI and ZEKE photoelectron spectra recorded *via* the S_1 $18a^1$ and 12^1 vibrational levels are very similar (see Fig. 6.11). As for the other vibrational levels of A_1 symmetry examined in this work, peaks are seen corresponding to the $6a^1$ and $(\Delta v = 0) + 6a^1$ vibrational levels in the cation. In the Franck-Condon simulations, which are also plotted in Fig. 6.11, ionisation from S_1 12^1 is predicted to lead mainly to $18a^1$ in the ion and *vice-versa*.

The situation is more complicated for the deuterated isotopomer $C_6H_5CD_3$, as the REMPI spectrum reveals the presence of a third vibrational level (see Fig. 6.12). The S_1 $18a^1$ level occurs at 933 cm^{-1} above the origin, and the ZEKE spectrum recorded following excitation to this level is very similar to that seen for non-deuterated toluene (Fig. 6.13). However the ZEKE spectra *via* the other two levels, at 957 and 973 cm^{-1}, suggest that they are the result of a coupling between 12^1 and another zero-order state (see Fig. 6.14). Peaks corresponding to 12^1 and $6a^1 12^1$ in the ion occur in both of these spectra; the approximate label "12^1" is assigned to the S_1 level at 973 cm^{-1} as it gives the more intense 12^1 peak. However, the identity of the other zero-order state coupled to 12^1 remains unclear.

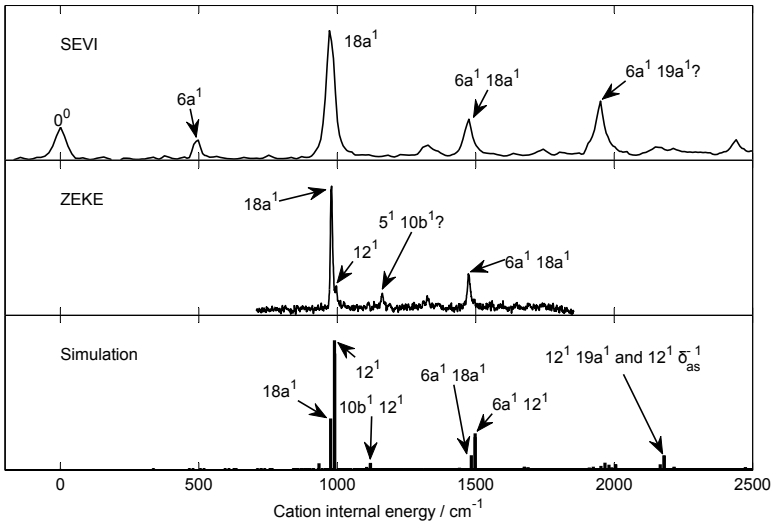

(a) *Via* $18a^1$ ($0^0 + 935$ cm^{-1})

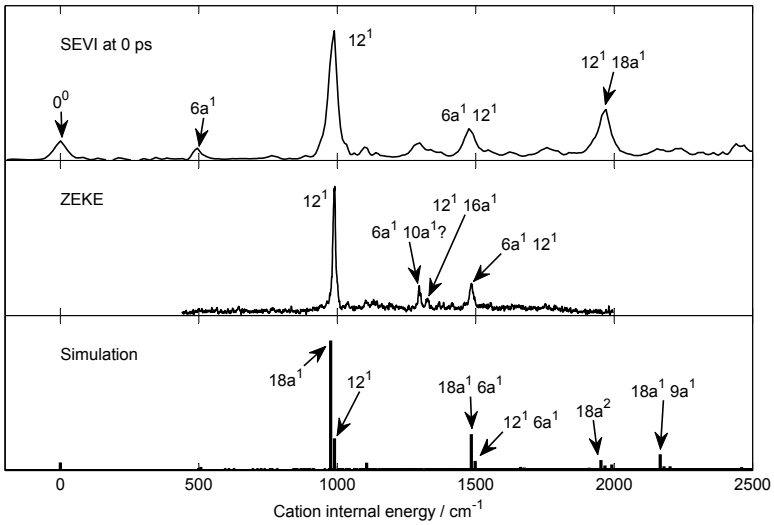

(b) *Via* 12^1 ($0^0 + 966$ cm^{-1})

Fig. 6.11. Photoelectron spectra and Franck-Condon simulations *via* the S_1 "$18a^1$" and "12^1" vibrational levels.

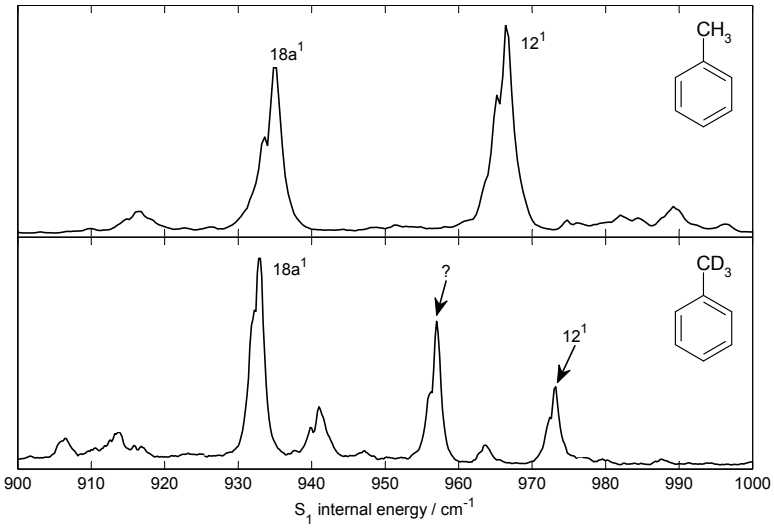

Fig. 6.12. Nanosecond REMPI spectra in the vicinity of $18a^1$ and 12^1 for the two isotopomers.

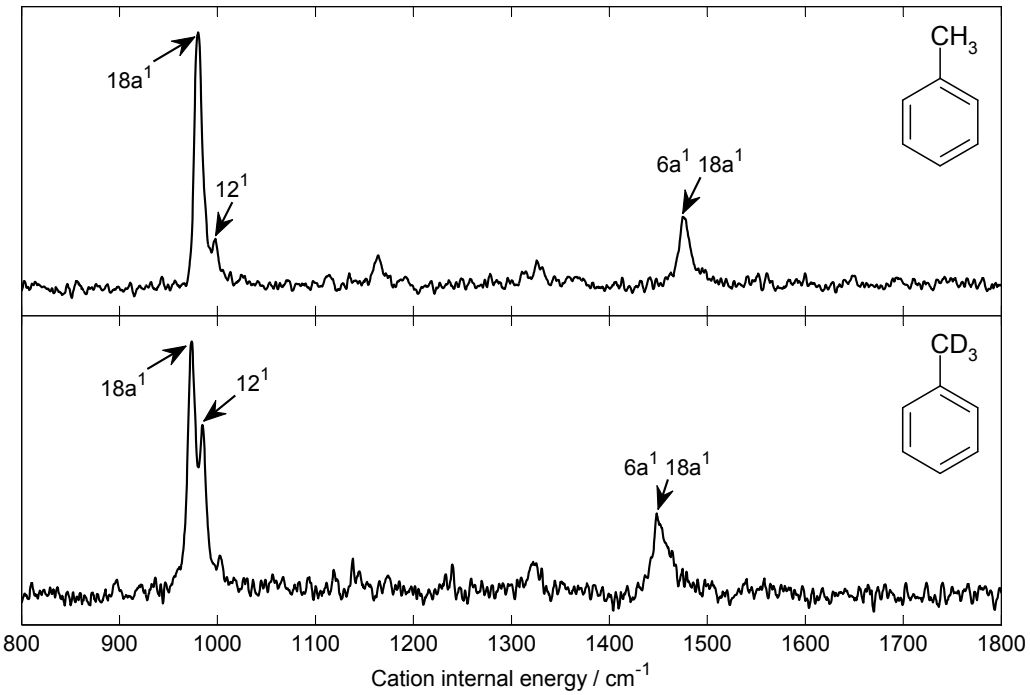

Fig. 6.13. ZEKE spectra *via* S_1 $18a^1$ in the two isotopomers.

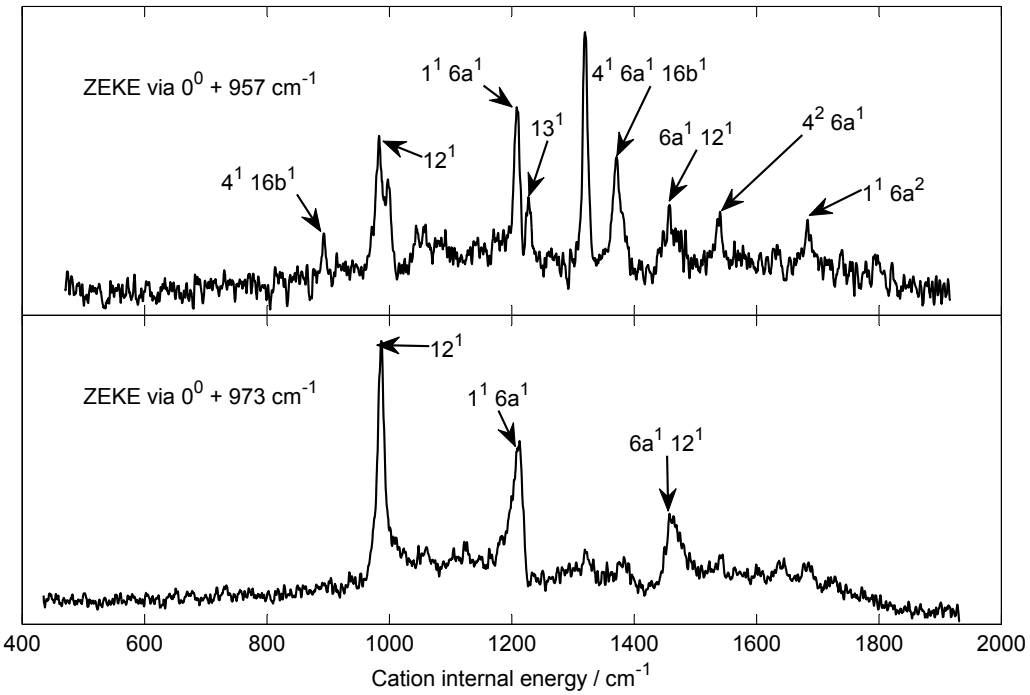

Fig. 6.14. ZEKE spectra *via* the S_1 vibrational levels at 957 and 973 cm^{-1} in $C_6H_5CD_3$.

6.7. Summary

In order to characterise the vibrational levels in the S_1 electronic state, REMPI spectra of toluene and the deuterated isotopologue $C_6H_5CD_3$ have been recorded using both picosecond and nanosecond lasers. The S_1 vibrational assignments for toluene-H_8 were drawn from dispersed fluorescence studies by Hickman *et al.* [63]. Assignments for the S_1 state of toluene-D_3 were then obtained by comparing the REMPI spectra of the two isotopomers.

Picosecond SEVI and nanosecond ZEKE photoelectron spectra have been recorded following excitation of the main features seen in the REMPI spectra. The results presented in this chapter pertain to the S_1 origin and seven excited vibrational levels which showed no time dependence in the picosecond experiments. Using these, and additional spectra which will be discussed in Chapters 7 and 9, it has been possible to establish the fundamental vibrational frequencies for eight normal modes in $C_6H_5CH_3^+$ and $C_6H_5CD_3^+$ (see Table 6.1). The ZEKE spectrum *via* the S_1 origin in toluene-D_3 has enabled the ionisation potential of this molecule to be determined for the first time (71247 ± 5 cm^{-1}).

Table 6.1. Cation vibrational frequencies determined in this work, with comparisons to a previous time-of-flight study of toluene-H_8.

	$C_6H_5CH_3$			$C_6H_5CD_3$	
Mode[a]	S_1[b]	Ion (ZEKE)	Ion (TOF)[c]	S_1[d]	Ion (ZEKE)
1	754	763	783	713	742
6*a*	457	494	529	439	472
6*b*	532	496	530	529	477
12	966	991	—	972	988
13	1193	1235	1209	1241	—
15	332	344	355	295	302
16*a*	228	333	—	227	333
18*a*	935	981	—	933	974

[a] Varsányi notation; see Appendix A and Ref. 65.
[b] From fluorescence excitation spectrum by Hickman *et al.* [63].
[c] Published by Whiteside *et al.* [122]. Nominal precision of ± 20 cm^{-1}.
[d] From nanosecond REMPI, present work.

The frequency-resolved spectra *via* the two components of the 1^1 / $4^1 16b^1$ Fermi resonance showed a signature of vibrational coupling, with peaks being seen corresponding to ionisation from both of the coupled zero-order states. This example illustrates that a lack of time dependence does not necessarily imply the absence of IVR; instead the vibrational eigenstates in S_1 were simply too far apart to be excited coherently by the 1 ps pump laser pulses. The following three chapters will examine cases where the eigenstates are closer together in energy, so that picosecond SEVI experiments can give a direct view of the progress of IVR in the time domain.

7. Restricted IVR: a "Fermi resonance"

The simplest prototype for intramolecular vibrational energy redistribution is the case where just two zero-order vibrational states are coupled together, producing a pair of eigenstates. As we saw in Section 1.2, this situation is often seen in the form of a *Fermi resonance*, where a fundamental harmonic vibration couples to an overtone or a combination which coincidentally has a similar frequency. If the two components of the resonance are coherently excited, then a time-resolved experiment should reveal quantum beats whose frequency corresponds to the energy spacing between the eigenstates. The effects of the coupling can also be seen in a frequency-resolved experiment, with the spectral line positions being shifted and their intensities altered from what we would expect in the absence of coupling. In this chapter, a Fermi resonance in the S_1 electronic state of toluene is studied using both picosecond time-resolved SEVI and nanosecond ZEKE techniques.

7.1. A Fermi resonance in toluene

Hickman *et al.* [63] have carried out a detailed investigation into the vibrational spectroscopy of toluene in the S_1 excited electronic state, using a combination of fluorescence-excitation and dispersed fluorescence techniques. Amongst the transitions observed were a pair of absorption features at 457 and 462 cm^{-1} above the S_1 origin, which these authors assigned as a Fermi resonance. A stretching motion of the ring ($6a^1$ in Varsányi notation[1]) is apparently coupled to a combination of ring bends ($10b^1 16b^1$), as shown in Fig. 7.1.

This system is well suited to a time-resolved photoelectron spectroscopy study. The two eigenstates are close enough in energy to be coherently excited by a 1 ps laser pulse, but are in an uncongested region of the absorption spectrum. It should therefore be possible to excite the Fermi resonance without any interference from other, uncoupled vibrational states.

Hammond *et al.* [57, 58] were the first to attempt this experiment, working in the Lasers for Science facility at the Rutherford-Appleton Laboratory. A 1 ps 'pump' laser

[1] Ref. 63 uses a different notation scheme for the normal modes, based upon the Mulliken convention [62]. The modes are first sorted by their symmetry, approximating the point group as C_{2v}, and then numbered in order of decreasing frequency. In this scheme modes 13, 24 and 25 correspond to Varsányi $6a$, $16b$ and $10b$ respectively.

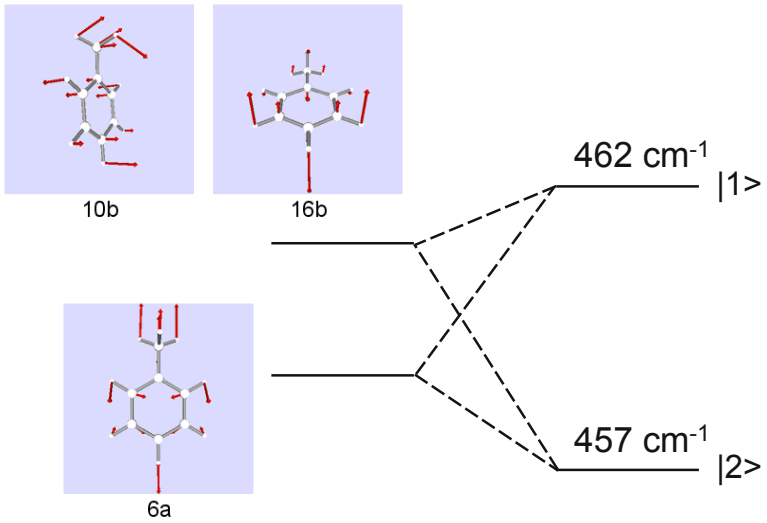

Fig. 7.1. Coupling of ring stretch and bends in a Fermi resonance of S_1 toluene. Zero-order states are shown on the left, and true eigenstates on the right.

pulse of ∼264 nm wavelength, which is approximately 460 cm^{-1} above the S_1 origin, was used to excite the two Fermi resonance components coherently. A second 'probe' pulse of the same wavelength ionised the molecule, and a photoelectron spectrum was obtained using velocity map imaging. Spectra were recorded for pump-probe time delays of 0, 2, 3.5, 5, 6, 7, 8.5, 10 and 20 ps.

Although the vibrational structure within the photoelectron spectra was only partially resolved, a clear time dependence was nonetheless visible. The vibrational origin peak was seen to oscillate out of phase with a peak at ∼500 cm^{-1}, and the ratio of the integrals of these two peaks could be successfully modelled as:

$$R(t) = B + A\cos\left(\frac{2\pi t}{T} + \phi\right), \tag{7.1}$$

with an oscillation period $T = 6 \pm 1$ ps. This result is consistent with Equation (1.18) and the previously observed energy separation between the eigenstates of 4.8 ± 0.5 cm^{-1}[57].

In the present work, the $6a^1$ / $10b^1 16b^1$ Fermi resonance has been re-visited with the benefit of the in-house picosecond laser system described in Section 3.1. Thanks to the ability to tune the wavelengths of the pump and probe laser beams independently of one another, it has been possible to achieve greatly improved resolution using the SEVI technique (see Section 3.4). Spectra have also been measured for a greater range of pump-probe time delays, revealing more complicated behaviour that could not be seen over the short time-scale of the previous study. The results indicate that this so-called "Fermi resonance" is not the simple two-level system that was expected. Furthermore, by detailed examination of the quantum beat patterns it has been possible to obtain

quantitative information about the strength of the coupling of the zero-order vibrational states. These findings have been published in the journal *Physical Chemistry, Chemical Physics* [61].

This data will be presented below, along with the results of complementary nanosecond ZEKE experiments. The nanosecond work was performed after the publication of Ref. 61, and provides further evidence in support of its conclusions.

7.2. Nanosecond REMPI and ZEKE studies

Fig. 7.2 shows an enlarged portion of each of the REMPI spectra in the vicinity of the $6a^1$ / $10b^1 16b^1$ Fermi resonance, recorded using the picosecond and nanosecond lasers. Due to the relatively large bandwidth ($\sim$15 cm^{-1}), the picosecond spectrum shows a single broad absorption feature. The nanosecond spectrum, by contrast, shows three separate peaks. These are labelled according to the zero-order vibrational state which they are believed to resemble most closely, although it should be noted that due to the coupling each is actually best described as a mixture of zero-order states. In addition to the two expected Fermi resonance components, we can identify a feature at 452 cm^{-1} as the ring-twisting overtone $16a^2$. This assignment is based upon the fundamental frequency for $16a$ in S_1 given by Hickman *et al.* [63], although those authors did not observe a $16a_0^2$ transition in their fluorescence excitation spectrum.

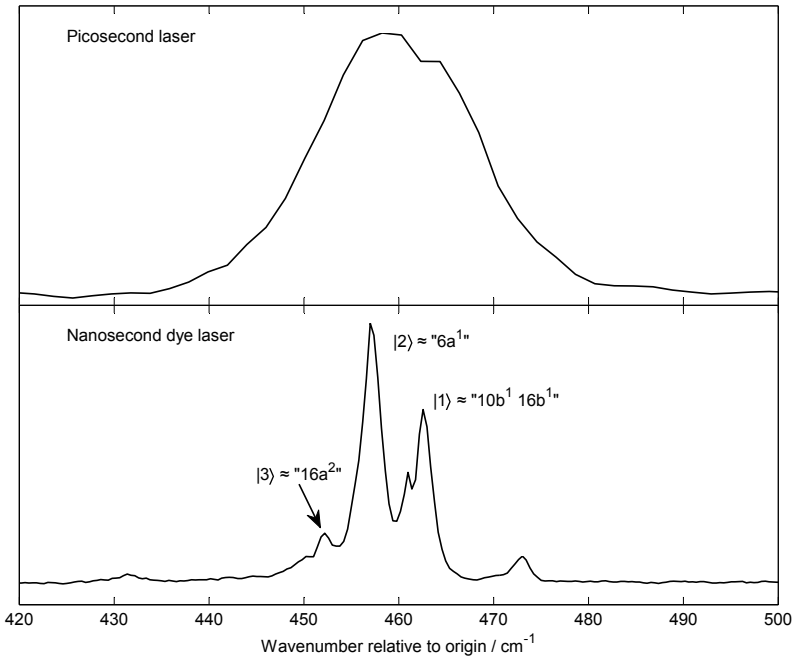

Fig. 7.2. Portion of the REMPI spectra of toluene in the vicinity of the S_1 $6a^1$ / $10b^1 16b^1$ Fermi resonance.

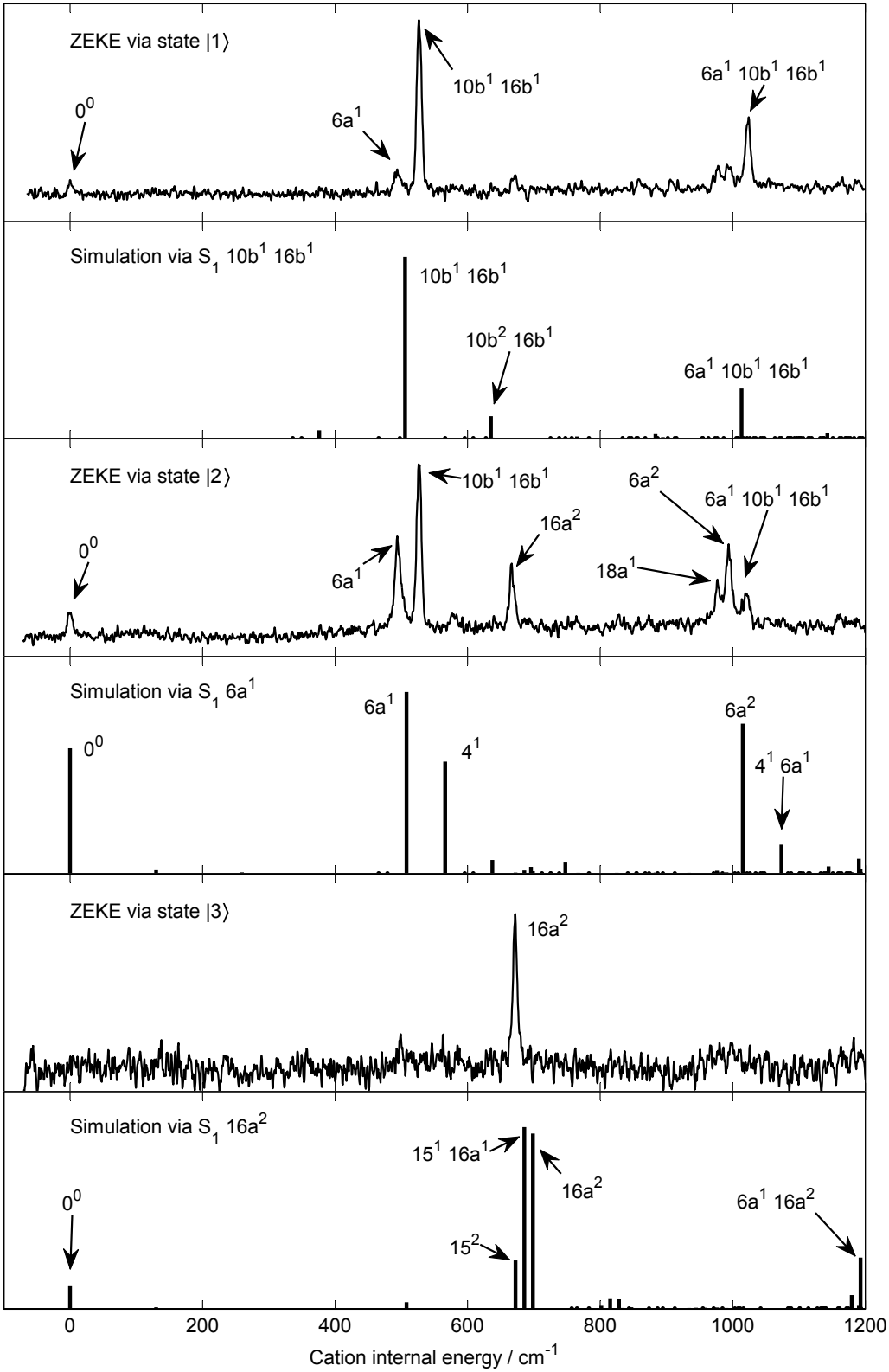

Fig. 7.3. ZEKE spectra via the three S_1 vibrational levels, compared with simulations via the zero-order states.

In Fig. 7.3 the ZEKE spectra recorded *via* each of the three REMPI peaks are compared with Franck-Condon simulations for ionisation from the corresponding zero-order states, which were calculated using the methods described in Section 5.2. The ZEKE spectrum following ionisation from the highest vibrational level, state $|1\rangle$, is dominated by the features predicted for ionisation from S_1 $10b^1 16b^1$, although some minor features from S_1 $6a^1$ are also present. State $|3\rangle$ appears to be almost purely $16a^2$ in character, and its ZEKE spectrum is dominated by the $\Delta v = 0$ transition.

The ZEKE spectrum via state $|2\rangle$ is more interesting. This level is expected to have the largest contribution from the $6a^1$ zero-order state, and does indeed show the strongest ion $6a^1$ and $6a^2$ features as predicted by the simulation. However the most intense peak corresponds to the $10b^1 16b^1$ vibrational level in the ion, in violation of the usual $\Delta v = 0$ propensity rule. This would suggest that there is a strong coupling between $6a^1$ and $10b^1 16b^1$, allowing the latter to "steal" intensity from the former. It is also noteworthy that the DFT calculation predicts the ion $6a^1$ and $10b^1 16b^1$ levels to be just $4\,\mathrm{cm}^{-1}$ apart, whereas in reality the ZEKE spectrum shows the two eigenstates to be separated by some $32\,\mathrm{cm}^{-1}$. Just as in the CO_2 example discussed in the introduction to this chapter, the coupling pushes the two vibrational states further apart and we see two peaks centred around the position where the uncoupled levels 'should' have been.

There is also a clear ion $16a^2$ peak, which the simulations suggest must be due to coupling with the S_1 $16a^2$ zero-order state. Since no $6a^1$ feature appears in the ZEKE spectrum via level $|3\rangle$, it is likely that this coupling is fairly weak.

7.3. Time-resolved spectra

Using fixed pump and probe wavelengths of 263.6 and 290.3 nm respectively, photoelectron images were taken at pump-probe time delays of 0–100, 472–480 and 500–510 ps in 1 ps steps. The use of a two-colour ionisation scheme gave a considerable improvement in resolution compared with the earlier one-colour images of Hammond *et al.* [57, 58] (see Fig. 7.4).

A further improvement in resolution can be achieved through the use of the SEVI technique, in which images are recorded with different probe wavelengths and the resulting spectra are spliced together (see Section 3.4). Although this process is too time-consuming to be used at every time delay, SEVI spectra were obtained at 0, 1, 2, 3 and 6 ps, with probe wavelengths of 298.3, 294.8, 293.3, 290.3, 288.3, 286.3 and 282.3 nm. For all of these images the repeller and extractor voltages of the electrostatic lens were

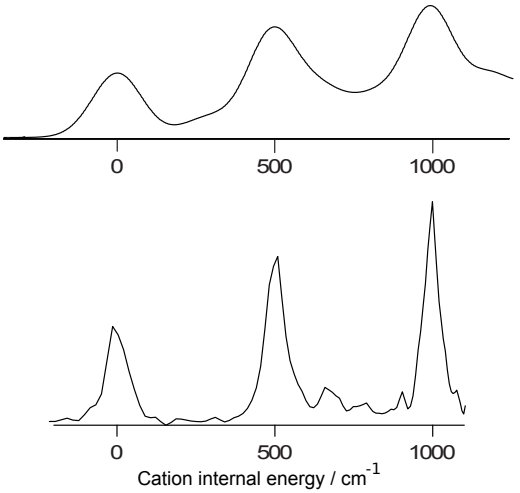

Fig. 7.4. Spectra at 0 ps from one-colour ionisation (Hammond *et al.*, top) and two-colour ionisation (this work, bottom).

-600 and −407 V respectively, ensuring that even the electrons with the highest possible kinetic energy would fall within the boundary of the detector.

At short time delays, the spectra show an oscillation with a period of ∼6 ps which is consistent with the results of Hammond *et al.* [57, 58]. Fig. 7.5 illustrates the spectra for 0–12 ps with a probe wavelength of 290.3 nm. It can be seen that the peaks at 0 and 1000 cm^{-1}, which are due mainly to ionisation from the bright state, have their maximum intensity at 0, 6 and 12 ps and minima at 3 and 9 ps. By contrast, the peak at ∼500 cm^{-1} has minima at 0 and 6, and maxima at 3 and 9 ps, indicating that it results mainly from ionisation out of the zero-order dark vibrational state.

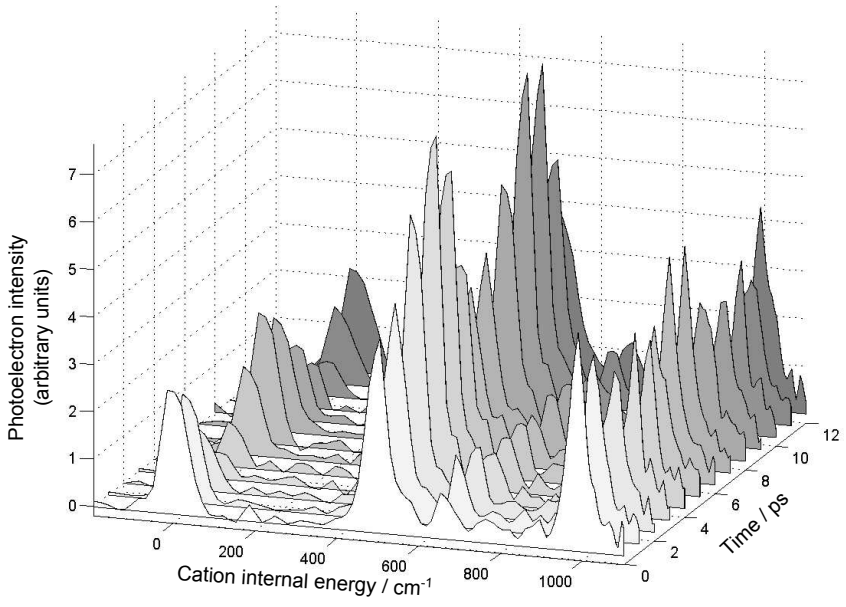

Fig. 7.5. Photoelectron spectra from the Fermi resonance for time delays of 0–12 ps.

The SEVI spectra taken at 0 and 3 ps provide signatures of the almost-pure bright and dark states respectively, with better resolution than the two-colour spectra plotted in Fig. 7.5. Even so, a comparison with the ZEKE spectra (Fig. 7.6) reveals that the peak at ∼500 ps is a composite of two features, and there are three unresolved ion states beneath the peak at ∼1000 cm^{-1}. These peaks shift from side to side over time, reflecting the change in the relative intensities of the features beneath them. At 0 ps, the $6a^1$ / $10b^1 16b^1$ peak is centred at 494 ± 10 cm^{-1}, coinciding exactly with the position of the $6a^1$ peak seen in the ZEKE spectrum. After 3 ps, the SEVI peak has moved to 515 ± 10 cm^{-1}, which is slightly to the left of the ZEKE $10b^1 16b^1$ peak (526 cm^{-1}). Presumably a small ion $6a^1$ feature is still present beneath the SEVI peak, due to a residual population of the originally prepared $6a^1$ bright state.

Further insights into the dynamics can be gained by measuring the integral of each ion vibrational peak as a function of pump-probe time delay. By fitting the spectrum to a sum of Gaussian functions, it is possible to estimate the relative contributions of the unresolved components beneath the peaks at ∼500 cm^{-1} and 1000 cm^{-1}. Each of the spectra taken with the 290.3 nm probe wavelength was modelled by optimising the amplitudes of six Gaussians, whose centre positions and widths were fixed to the values listed in Table 7.1; some example fits are shown in Fig. 7.7. The centres were determined from the SEVI spectra, with the composite peaks being represented by two functions in positions corresponding to the peak centre at 0 and 3 ps respectively. Appropriate widths were found by fitting a Gaussian function to each peak individually, allowing the centre, width and amplitude to vary, and then averaging the widths over all time delays.

Table 7.1. Gaussian functions used to fit the time-resolved spectra.

Ion vibrational level	0^0	$6a^1$	$10b^1 16b^1$	$16a^2$	$6a^2$	$6a^1 10b^1 16b^1$
Energy / cm^{-1}	0	494	515	663	985	1009
Gaussian FWHM / cm^{-1}	70	60	60	60	60	60

Plotting the amplitude of each fitted Gaussian as a function of time delay (Fig. 7.8), it becomes apparent that the behaviour of the time-resolved spectra is more complicated than the simple cosine oscillation predicted for a two-level system by Equation (1.18). We still see an oscillation with period ∼6 ps; however there is a sinusoidal modulation in intensity superimposed upon it with a period of ∼100 ps. This modulation was not visible on the 10 ps time-scale of the previous experiments by Hammond *et al.* [57, 58]. For five of the ion vibrational levels the amplitude of the oscillation is greatest at 0 and 100 ps, becoming very small at ∼50 ps. Surprisingly the ion $16a^2$ peak has a different modulation pattern, with minima at around 10 and 60 ps.

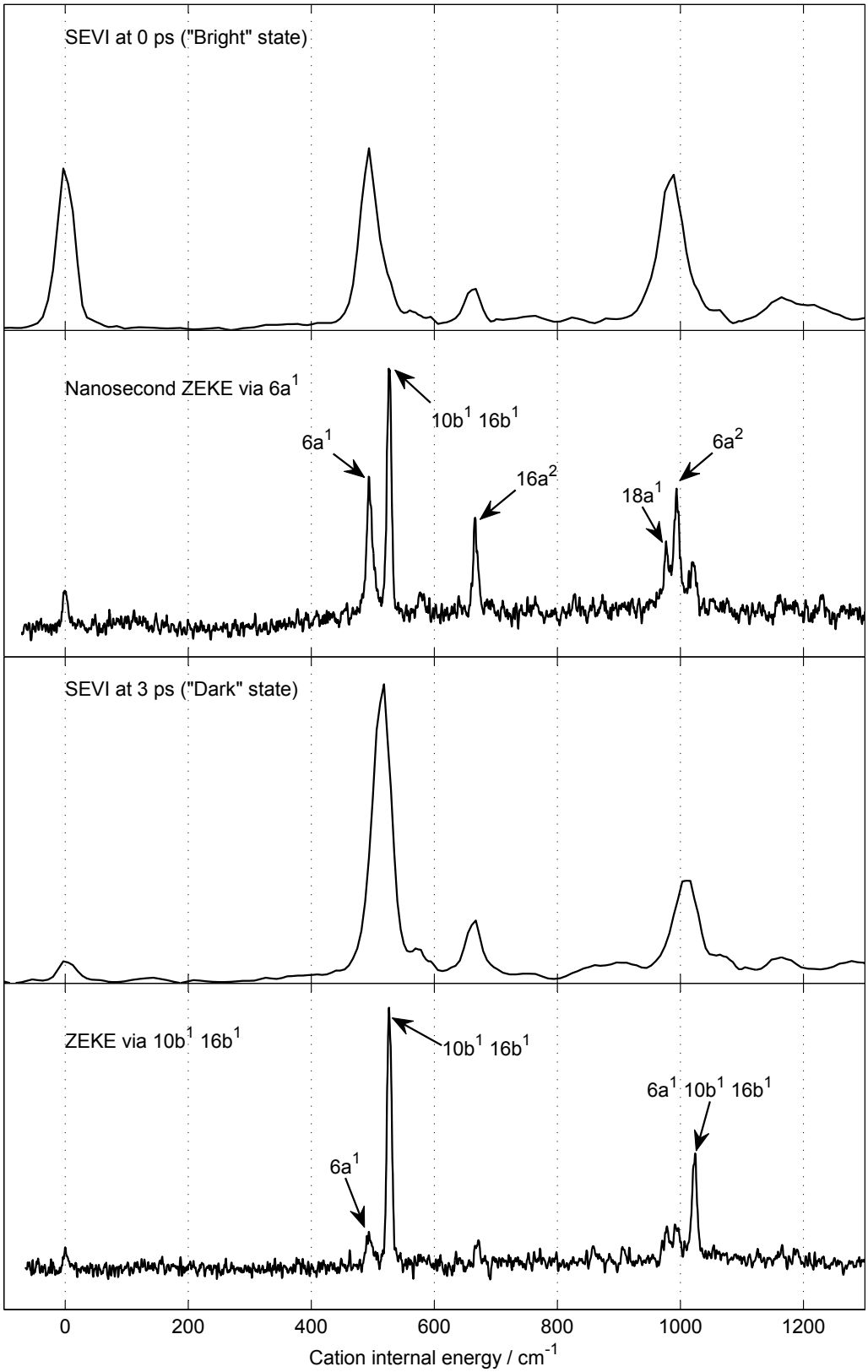

Fig. 7.6. Comparison of SEVI and ZEKE spectra via S_1 $6a^1$ / $10b^1 16b^1$. The apparent weakness of the origin peak in the ZEKE spectra is due to a fall-off in laser power at long wavelengths.

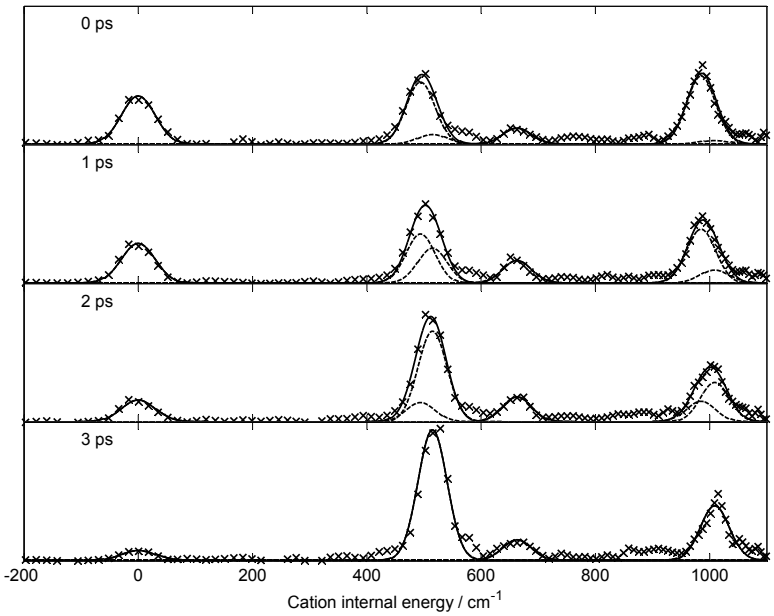

Fig. 7.7. Examples of Gaussian fits to time-resolved spectra. The dashed lines represent individual Gaussian functions and the solid line is the sum of all six Gaussians listed in Table 7.1.

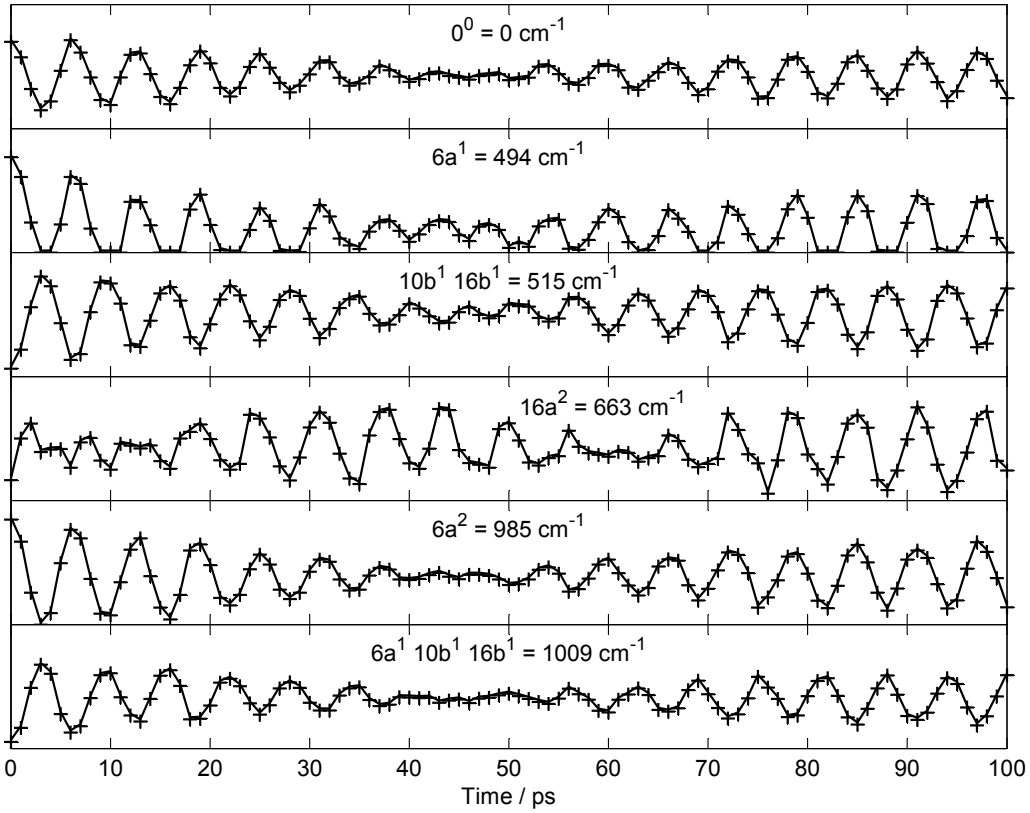

Fig. 7.8. Peak integrals as a function of time delay, determined from the Gaussian fit. In order to show the oscillation pattern more clearly, the points are connected by straight lines and a different intensity scale is used for each peak.

In order to confirm that this beating pattern continues at longer time delays, an additional experiment was performed in which the intensity of the ion origin peak was monitored as the delay stage was scanned from -20 to 400 ps in 0.2 ps steps. The probe laser wavelength was set to 300 nm, which is just above the ionisation threshold, so that the ion origin could be accessed but no vibrationally excited ions would be produced. In order to magnify the image, the electrostatic lens voltages were lowered to −61 V for the extractor and −42 V for the repeller. A cardboard mask was inserted between the CCD camera and phosphor screen, blocking the view of the edges of the detector so that only the ring corresponding to the ion origin could be seen and any higher-energy electrons would be excluded. In this way the intensity of the ion origin peak could be determined simply from the total electron count, without the need for the normal image analysis procedure described in Section 3.3.

The average of four scans is shown in Fig. 7.9. It is clear that the beating pattern does continue with the 100 ps modulation seen in the full spectra; however there is also an overall decay in the amplitude of the oscillations over time.

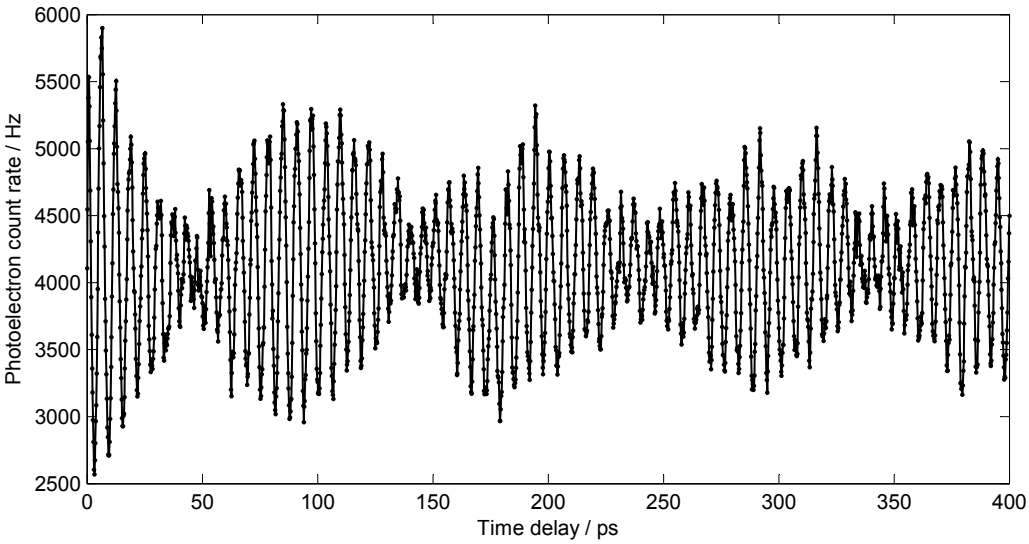

Fig. 7.9. Time-dependent intensity of the ion origin peak from 0 to 400 ps.

7.4. Interpretation

7.4.1. Fourier analysis

The observed oscillation pattern resembles the beats produced by interference of two or more cosine waves with different frequencies. In order to interpret these results it is necessary to find the number of cosine terms present, their frequencies and their relative phases. A similar problem arose in the work of Felker and Zewail [28], who used

fluorescence quantum beats to study IVR processes in anthracene (see Section 1.5.2). These authors were able to obtain the necessary information using Fourier analysis, and a similar technique has been applied to the present study.

Since the beat pattern consists of a series of evenly-spaced measured samples, rather than a continuous mathematical function, a *discrete Fourier transform* (DFT) must be employed. A number of efficient algorithms exist for the exact evaluation of the DFT using a computer, which are collectively known as the *Fast Fourier Transforms* (FFT) [125]. In this work the FFT is calculated with Matlab [91], which uses the open-source *FFTW* library [126].

Before carrying out a Fourier analysis, it is important to consider whether or not any information has been lost as a result of the sampling process. The *Nyquist sampling theorem* states that a set of discrete samples can provide enough information to reconstruct the underlying continuous waveform, provided that there are at least two samples within each oscillation period of the highest frequency component present. If this criterion is not met, then the Fourier transform will contain so-called "aliasing errors" in which the undetectable high-frequency components generate spurious components of lower frequency [125]. The highest detectable frequency, equal to half the sampling rate, is known as the *Nyquist frequency*. In these experiments, with samples at 1 ps intervals, the Nyquist frequency is π rad ps^{-1} or approximately 16.6 cm^{-1}.

The frequency components of the quantum beat pattern correspond to the energy spacings between coherently excited eigenstates. Consequently the highest beat frequency is not expected to exceed the spectral bandwidth of the excitation laser, which is approximately 12–15 cm^{-1}. As this is less than the Nyquist frequency, no aliasing errors are expected in the Fourier transform.

Given N discrete samples of a time-domain function $x(t)$, the discrete Fourier transform is given by [125]:

$$X\left(k\Delta f\right) = \Delta t \sum_{n=0}^{N-1} x\left(n\Delta t\right) e^{-i2\pi k\Delta f\, n\Delta t}, k = 0 \cdots (N-1), \tag{7.2}$$

where Δt is the time interval between samples, $\Delta f = 1/\left(N\Delta t\right)$ is the sample interval in the frequency domain and n and k are the sample indices in the time and frequency domains respectively. The number of data points in the frequency-domain output is equal to the number of data points in the time-domain input, spanning the range from zero to the sampling frequency. However, as mentioned above, we can only detect frequency components up to the Nyquist frequency, which is half of the sampling frequency. For

this reason, the output of the DFT is always symmetric about the Nyquist frequency.

The resolution obtained in the frequency domain, Δf, depends upon both the number of data points used and their spacing in time. For 101 data points (0–100 ps) at 1 ps intervals, $\Delta f \approx 0.0099$ ps^{-1} ≈ 0.33 cm^{-1}, which is too large to clearly discern the individual beat frequencies. This problem can be mitigated by padding the data with zeroes to increase the number of points in the transform [28]. A 10,000-point transform is used for the 0–100 ps data, whereas the 0–400 ps origin peak intensity measurements are zero-padded to $2^{16} = 65536$ points.[2] (In the latter case, a greater number of points is required due to the smaller sampling interval of 0.2 ps.) A further improvement is achieved by subtracting the mean intensity value from all of the data points prior to the Fourier transformation. By doing so, a large component at zero frequency is removed, allowing the other frequency components to be seen more clearly [125].

The results of the Fourier transforms are shown in Fig. 7.10. As in Felker and Zewail's work [28], only the real part of the complex Fourier transform is plotted. This corresponds to the cosine terms in the Fourier series. The imaginary part contains the sine terms, which are not expected to appear in the expression for the quantum beats [27].

Two major frequency components are clearly seen at ~ 5.1 and 5.5 cm^{-1} in all cases. As expected, these have positive phase (real part of Fourier transform > 0) for the ion vibrational features which correspond to ionisation from the 'bright' vibrational state in S_1. For ion vibrational levels accessed on ionisation out of the 'dark' state, these cosine terms have negative phase.

The oscillations of the ion $16a^2$ peak show three additional frequency components with negative phase, at 4.9, 5.7 and 10.4 cm^{-1}. Although the last of these is small, it is plausibly real since $10.4 = 4.9 + 5.5$.

Some small-amplitude, spurious oscillations are also present in the Fourier transforms. These can be attributed to the fact that the DFT inherently assumes a periodic signal, with the sampled data being repeated endlessly. As a result of the repetition there appears to be a discontinuity at the end of the sample window, leading to a so-called *leakage error* in which power is taken away from the genuine frequency components and added to frequency components that do not exist in the original signal [125]. Felker and Zewail [28] were able to substantially eliminate this effect by multiplying the data with the shaping function $(t_f - t)^{0.5}$ so that the signal would smoothly go to zero at $t = t_f$, t_f being the longest time delay studied. The drawback of such an approach is that the genuine frequency components become broadened [125]. In the present study the two

[2] This number is chosen because the FFT algorithm works most efficiently when the number of data points is an exact power of two [125].

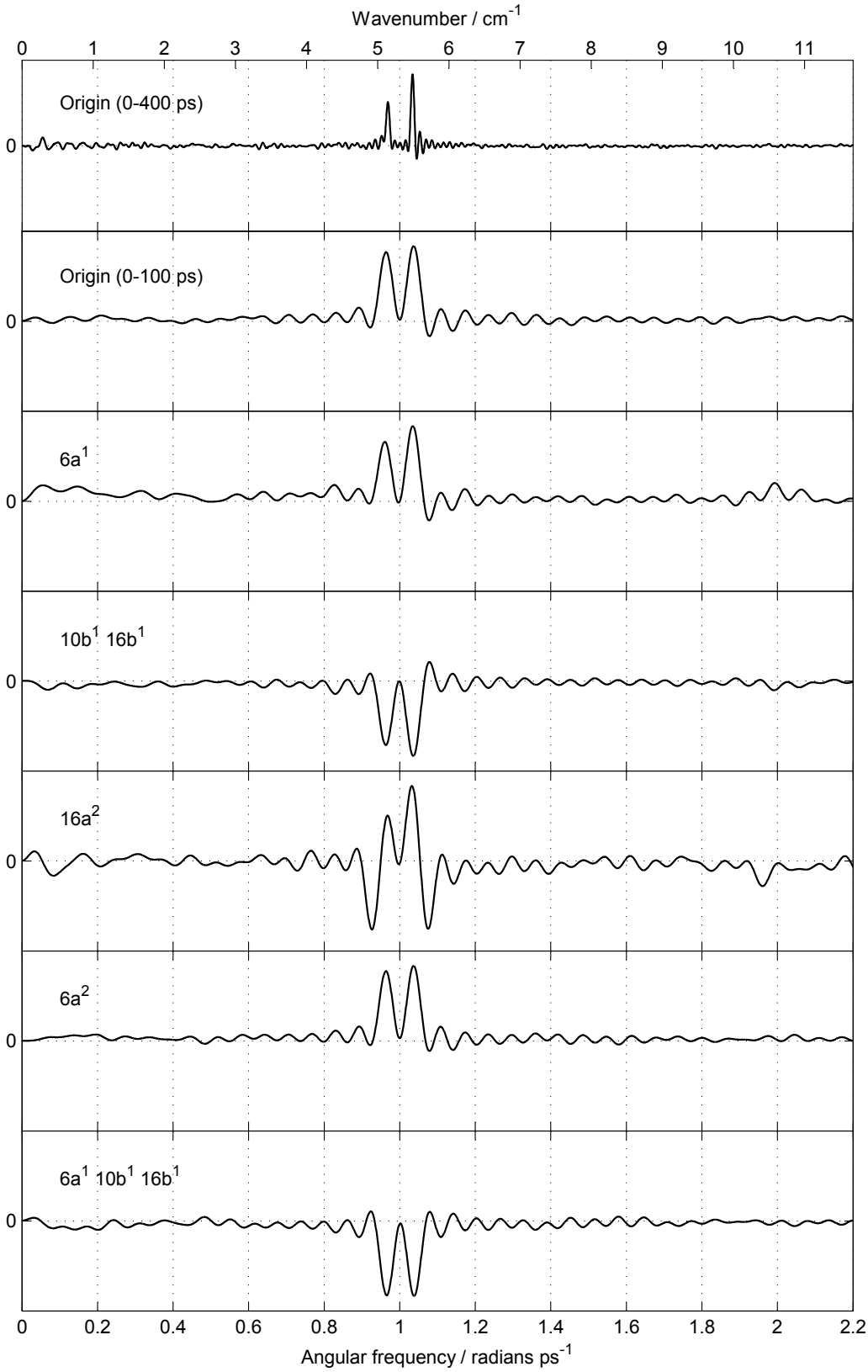

Fig. 7.10. Fourier transforms of the oscillations shown in Fig. 7.8 and Fig. 7.9.

major frequency components are very closely spaced, and a shaping function could not be used without causing them to merge together.

7.4.2. Empirical model for the quantum beats

Fig. 7.10 suggests that, for all peaks except $16a^2$, it should be possible to model the oscillations in time as a sum of two cosine waves. In practice an exponential decay term is also needed as the overall amplitude of the quantum beats decreases at longer time delays. The decay is far too rapid to be due to fluorescence, which has a lifetime of around 70 ns [63]. Instead, Felker and Zewail [29] have shown that the decay can be attributed to the dependence of the rotational constants of the molecule upon its vibrational state. Each vibrational level has underlying rotational structure, and a beat frequency will be present corresponding to the separation of each pair of rovibrational levels that share the same rotational quantum numbers. Since the rotational level spacings in the two vibrational levels are different, at finite rotational temperatures we observe a superposition of many frequencies which are all very close to some average value. The result resembles a cosine wave of that average frequency, modulated by an exponential decay.

Accordingly the time-resolved oscillations of the peaks are fitted to the function:

$$S(t) = \left[V\cos\left(\omega_v\left(t-t_0\right)\right) + W\cos\left(\omega_w\left(t-t_0\right)\right)\right] e^{-k(t-t_0)} + Z, \tag{7.3}$$

where t_0 is an offset to allow for any error in the delay line position taken as 0 ps. The fit is performed using a non-linear least squares optimisation routine in Matlab [91]. The frequency values given by the Fourier transform are taken as a starting point for ω_v and ω_w, and all of the parameters are optimised to produce the fit.

Fig. 7.11 and Table 7.2 show the fit of the origin peak intensity from 0–400 ps to Equation (7.3). The oscillation pattern is reproduced well, and the optimised values of the frequencies ω_v and ω_w are in excellent agreement with the Fourier transform.

Similar cosine fits were also performed to the peak oscillations shown in Fig. 7.8 for the time-resolved photoelectron spectra. The oscillations for the origin, $6a^1$, $10b^1 16b^1$, $6a^2$ and $6a^1 10b^1 16b^1$ peaks were simultaneously fitted to Equation (7.3), yielding a single averaged value for each of the parameters ω_v, ω_w, k and t_0. The $16a^2$ oscillations were then fitted to a sum of five exponentially decaying cosines, keeping ω_v, ω_w, k and t_0 fixed to those averaged values:

$$S(t) = Z + e^{-k(t-t_0)} \sum_{\gamma=U}^{Y} \gamma\cos\left(\omega_\gamma\left(t-t_0\right)\right) \tag{7.4}$$

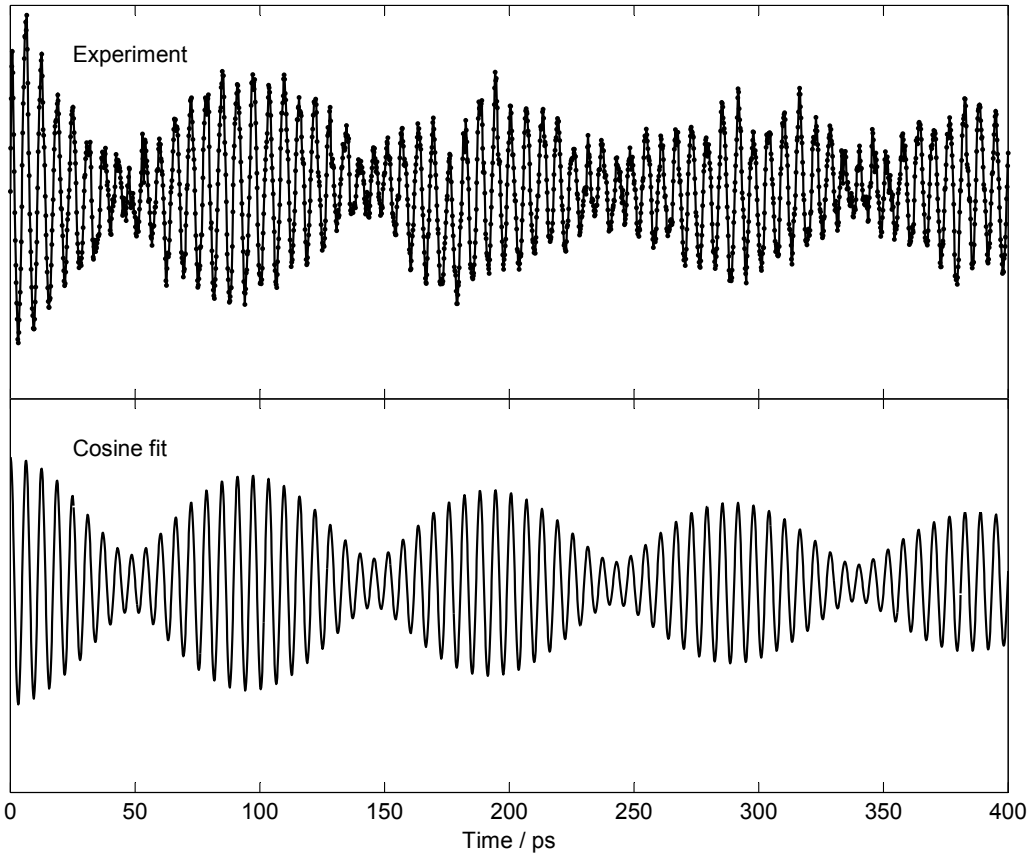

Fig. 7.11. Origin peak intensity from 0-400 ps, with fit to Equation (7.3).

Table 7.2. Parameters given by fit of origin peak intensity (0-400 ps) to Equation (7.3). $\tilde{\nu}_v$ and $\tilde{\nu}_w$ are the wavenumber equivalents of ω_v and ω_w.

Parameter	Fitted value
V	478
ω_v / rad ps^{-1}	0.969
$\tilde{\nu}_v$ / cm^{-1}	5.15
W	787
ω_w / rad ps^{-1}	1.034
$\tilde{\nu}_w$ / cm^{-1}	5.49
k / 10^{-3} ps^{-1}	1.50
t_0 / ps	0.10
Z	4129

All six cosine fits are plotted in Fig. 7.12 and the fitted parameters are listed in Table 7.3. Once again the optimised frequency values matched those obtained in the Fourier transform. It should be noted that, although Fig. 7.12 only shows the peak intensities from 0–100 ps, the spectra at 472–480 and 500–510 ps were also included in the fit. These longer time delays enabled an accurate determination of the decay constant, k.

Table 7.3. Parameters given by fit of time-resolved peak oscillations to Equation (7.3).

(a) Frequencies and globally-optimised parameters. $\tilde{\nu}_\gamma$ represents the wavenumber equivalent of angular frequency ω_γ.

Parameter	Fitted value
ω_u / rad ps^{-1}	0.926
$\tilde{\nu}_u$ / cm^{-1}	4.91
ω_v / rad ps^{-1}	0.969
$\tilde{\nu}_v$ / cm^{-1}	5.15
ω_w / rad ps^{-1}	1.034
$\tilde{\nu}_w$ / cm^{-1}	5.49
ω_x / rad ps^{-1}	1.078
$\tilde{\nu}_x$ / cm^{-1}	5.72
ω_y / rad ps^{-1}	1.962
$\tilde{\nu}_y$ / cm^{-1}	10.42
k / 10^{-3} ps^{-1}	1.30
t_0 / ps	0.16

(b) Coefficients of the frequency components.

Peak	U	V	W	X	Y	Z
Origin	—	33	39	—	—	125
$6a^1$	—	39	58	—	—	52
$10b^1 16b^1$	—	-86	-112	—	—	298
$16a^2$	-8	4	9	-7	-3	79
$6a^2$	—	47	54	—	—	114
$6a^1 10b^1 16b^1$	—	-35	-37	—	—	118

7.4.3. Three-level picture

Thus far the treatment of the observed oscillation patterns has been purely empirical. In order to obtain a physical justification for Equations 7.3 and 7.4, we need to modify the two-level picture of the Fermi resonance shown above in Fig. 7.1. What can the oscillation patterns tell us about the coupled vibrational states?

The nanosecond REMPI spectrum (Fig. 7.2) immediately suggests that a third vibrational state, $16a^2$, may have been excited. This state has the same symmetry as $6a^1$ and $10b^1 16b^1$ (A_1 in C_{2v}), and so could in principle be coupled to them through anharmonic-

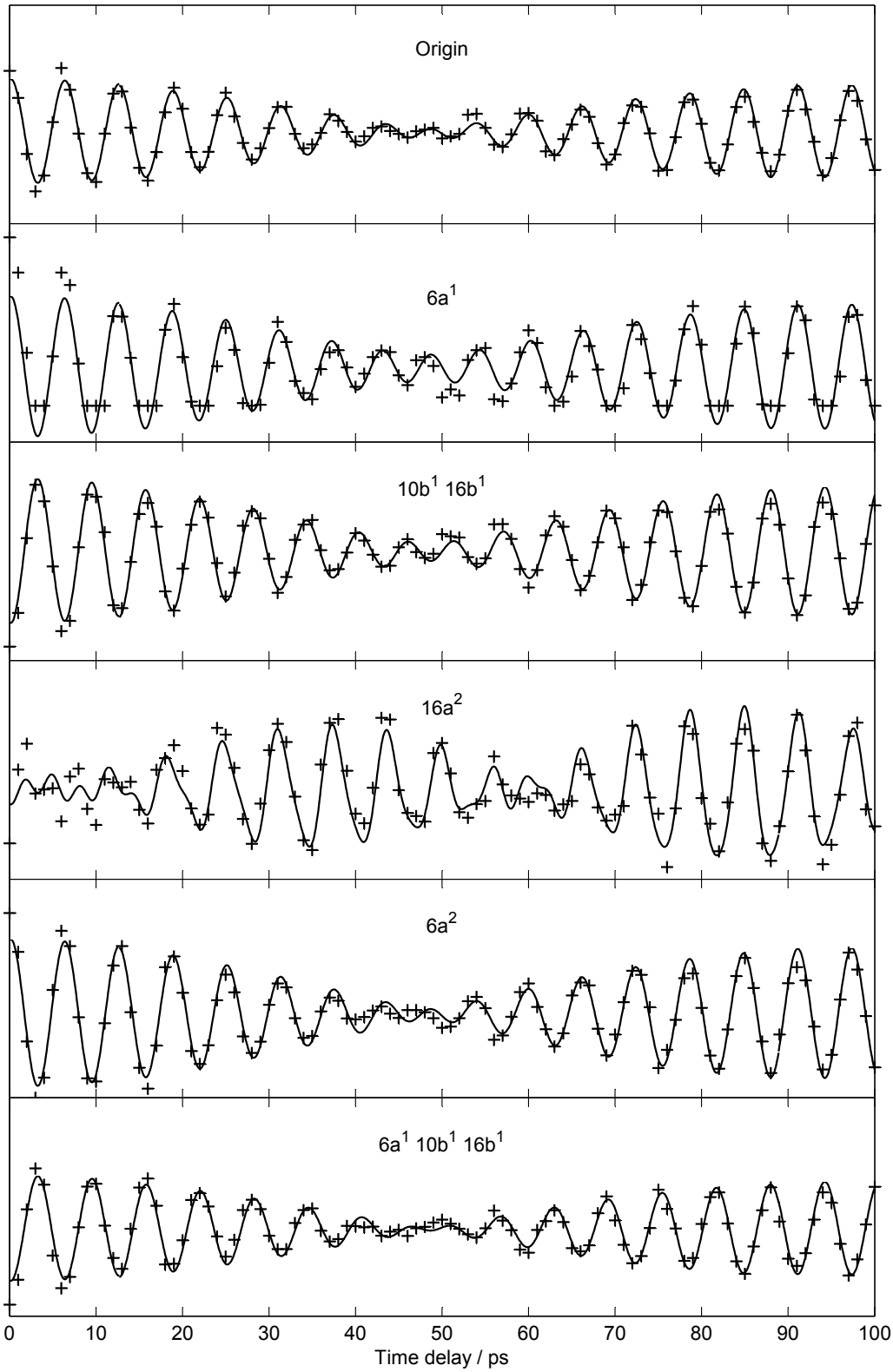

Fig. 7.12. Cosine fits to the peak oscillations in the time-resolved spectra. The $16a^2$ peak is modelled with Equation (7.4) and the others are fitted to Equation (7.3).

ity. At first sight, a coupling to $16a^2$ might seem to explain why there are two frequency components in the oscillation patterns of most of the photoelectron peaks: one of these would correspond to the energy separation between $16a^2$ and $6a^1$, and the other to the separation between $6a^1$ and $10b^1 16b^1$. In that case, however, we would also expect to see a third frequency component corresponding to the gap between $16a^2$ and $10b^1 16b^1$, at $5.15+5.49 = 10.64\,\mathrm{cm}^{-1}$. Although the experiment should be sensitive to any oscillations at that frequency (as discussed above in Section 7.4.1), none are observed. Moreover, this simple three-level picture cannot account for the more complicated behaviour of the $16a^2$ peak.

The presence of five frequency components in the $16a^2$ oscillation pattern might imply the involvement of a fourth coupled vibrational state. In order to be excited in these experiments, the fourth state would need to have an energy close to $459\,\mathrm{cm}^{-1}$. Examination of the known vibrational frequencies in S_1 (Table 5.3 on page 64) shows that the only remaining possibility is $10b^3 = 471\ \mathrm{cm}^{-1}$. However that level has B_1 symmetry, which prohibits anharmonic coupling to the Fermi resonance components. Instead the only possible coupling mechanism would be via the Coriolis effect, which arises due to the molecule's rotation (see Section 2.2.2). Such interactions are expected to be weak, and so it seems unlikely that there are more than three coupled levels.

We can gain a further insight into the reasons for the unexpected behaviour of the $16a^2$ peak by increasing the contribution of $16a^2$ to the wavepacket in the S_1 state. This is achieved by increasing the pump laser wavelength, thus lowering the photon energy and preferentially exciting the lowest-lying vibrational level.

7.4.4. Effect of pump wavelength

A series of images were recorded with a pump wavelength shifted by 0.05 nm to the red of the absorption maximum for the $S_1 \leftarrow S_0$ transition, corresponding to a reduction in the pump wavenumber of approximately $7\,\mathrm{cm}^{-1}$. The time delays examined ranged from 0–100 ps in 1 ps steps.

The resulting spectra show a stronger ion $16a^2$ peak than those taken 'on-resonance' (*i.e.* with a pump wavelength corresponding to the absorption maximum). Fig. 7.13 compares the oscillation patterns of the $16a^2$ peak for the two pump wavelengths, along with their associated Fourier transforms. When the pump wavelength is red-shifted, there is an increase in the relative amplitude of the two frequency components with negative phase, at 4.91 and $5.72\,\mathrm{cm}^{-1}$. We can therefore deduce that these frequency components must correspond to the energy spacing between $16a^2$ and the other coupled

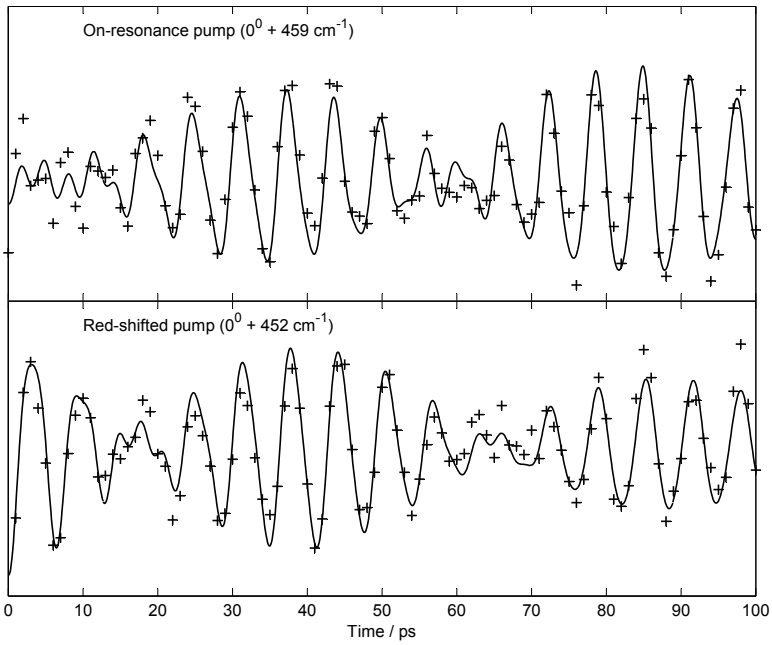

(a) Peak intensity as a function of time. The solid lines are fits to Equation (7.4).

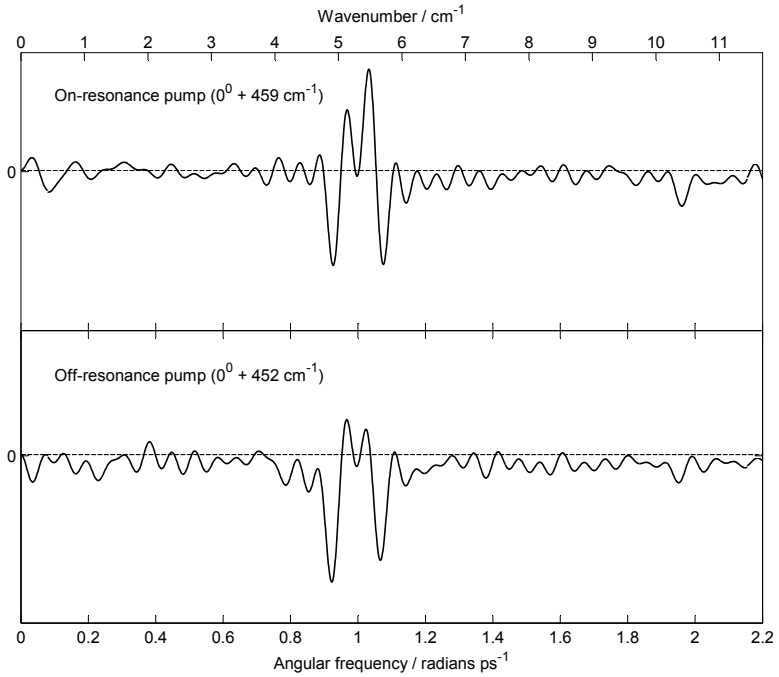

(b) Real parts of the Fourier transforms. The amplitude scale is the same for both plots.

Fig. 7.13. Effect of changing pump wavelengths on the oscillations of the ion $16a^2$ peak.

vibrational levels. Since they are seen only for the ion $16a^2$ peak, it follows that the other ion vibrational peaks must be relatively insensitive to the coupling to $16a^2$.

This result is rather puzzling. All of the peaks show two frequency components at 5.15 and 5.49 cm^{-1}, but apparently neither of these is related to the coupling to $16a^2$. How could the two remaining S_1 vibrational levels, $6a^1$ and $10b^1 16b^1$, give rise to two different beat frequencies? The answer is that the energy spacing between the two levels is not the same in all molecules. Instead, it seems to be influenced by another kind of motion that has not yet been taken into consideration: the internal rotation, or 'torsion', of the methyl group.

7.4.5. Role of the methyl group

In Section 2.7.5 it was demonstrated that, prior to absorption of a pump photon, approximately half of the toluene molecules in these experiments are in the $m = 0$ torsional level and half are in the torsinally excited state with $m = 1$. According to the selection rules laid down in Section 2.7.6, in the pump step excitation could occur from $|S_0, m = 0\rangle$ to $|S_1, m = 0, 3, 6 \cdots\rangle$, or from $|S_0, m = 1\rangle$ to $|S_1, m = 1, 2, 4, 5 \cdots\rangle$.

Next we must consider the implications of the conservation of energy. In order for a transition to be excited by the pump laser, the sum of the S_1 vibrational energy and the change in torsional energy must be close to 459 cm^{-1}. Table 7.4 lists the S_1 vibrational energies needed to meet this requirement for the allowed transitions with $\Delta m \neq 0$. Careful examination of the S_1 normal mode frequencies (Table 5.3) reveals that no vibrational levels exist at these energies. We can therefore conclude that *only $S_1 \leftarrow S_0$ transitions with $\Delta m = 0$ will be seen in these experiments.*

Table 7.4. Energies of the allowed torsional transitions on $S_1 \leftarrow S_0$ excitation (to nearest 1 cm^{-1}), and required final S_1 vibrational energies to achieve a total S_1 internal energy of 459 cm^{-1}. The energies of the torsional levels $m = 6$ and 7 have been estimated using the free rotor expression $E_m = m^2 B$, where the reduced rotational constant $B = 5.298$ cm^{-1} for toluene [17].

Change in $\lvert m \rvert$	Change in torsional energy / cm^{-1}	Required S_1 vibrational energy / cm^{-1}
$0 \rightarrow 3$	46 or 48	413 or 411
$0 \rightarrow 6$	190	269
$1 \rightarrow 2$	16	443
$1 \rightarrow 4$	78	381
$1 \rightarrow 5$	124	335
$1 \rightarrow 7$	254	205

Based upon the above arguments, we can expect roughly half of the molecules in the S_1 intermediate state to be in the $m = 0$ torsional level, and half in $m = 1$. There will

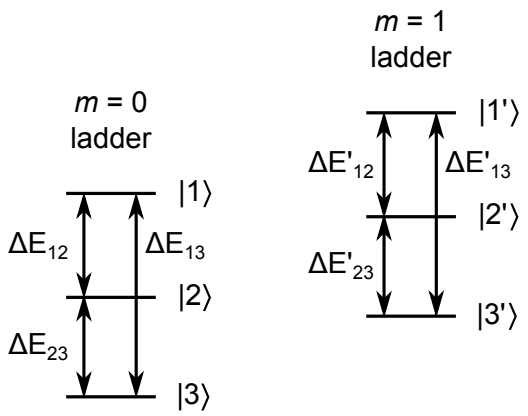

Fig. 7.14. Schematic representation of the two "torsional ladders" excited in the S_1 electronic state. There are three vibrational eigenstates associated with each of the torsional levels $m = 0$ and $m = 1$. Energy separations between eigenstates $|i\rangle$ and $|j\rangle$ are labelled ΔE_{ij}. (Based upon Fig. 10 of Ref. 61.)

therefore be two separate "torsional ladders" of vibrational eigenstates (see Fig. 7.14), and the pump laser excites these ladders incoherently. The first ladder results from the coupling of the zero-order states $|6a^1, m = 0\rangle$, $|10b^1 16b^1, m = 0\rangle$ and $|16a^2, m = 0\rangle$; similarly the second ladder is produced by the coupling of $|6a^1, m = 1\rangle$, $|10b^1 16b^1, m = 1\rangle$ and $|16a^2, m = 1\rangle$. Henceforth the eigenstates with $m = 0$ shall be denoted as $|1\rangle$, $|2\rangle$, $|3\rangle$ and the eigenstates with $m = 1$ as $|1'\rangle$, $|2'\rangle$, $|3'\rangle$.

The scheme of Fig. 7.14 can explain the observed quantum beat patterns if the eigenstate spacings in the two torsional ladders are slightly different, and if the coupling between $16a^2$ and the other two zero-order states is weak. The two frequency components seen at ~ 5.1 and $5.5\,\mathrm{cm}^{-1}$ in the Fourier transforms for all peaks would then correspond to the energy spacings ΔE_{12} and $\Delta E'_{12}$. Since eigenstate $|3\rangle$ consists mostly of the weakly-coupled $16a^2$ zero-order state, only the ion $16a^2$ peak is sensitive to ΔE_{23} and $\Delta E'_{23}$. The involvement of eigenstates $|3\rangle$ and $|3'\rangle$ thus accounts for the extra frequency components seen for this peak (see Fig. 7.15). In principle we might expect to see a sixth frequency component, since ΔE_{13} and $\Delta E'_{13}$ should appear separately, but this is not in fact observed. If the sixth component is weak, then it may have been obscured by an insufficient signal-to-noise ratio in these experiments.

Unfortunately it is not possible to determine which of the frequency components correspond to the $m = 0$ ladder, and which belong to $m = 1$. In future studies, this ambiguity could be resolved by changing the temperature of the molecular beam. Raising the rotational temperature would increase the population of $m = 1$ relative to that of $m = 0$, leading to a change in the relative intensities of the corresponding frequency components.

The "torsional ladder" model is nonetheless useful, as it enables us to obtain quantitative information about the strength of the couplings between the three zero-order

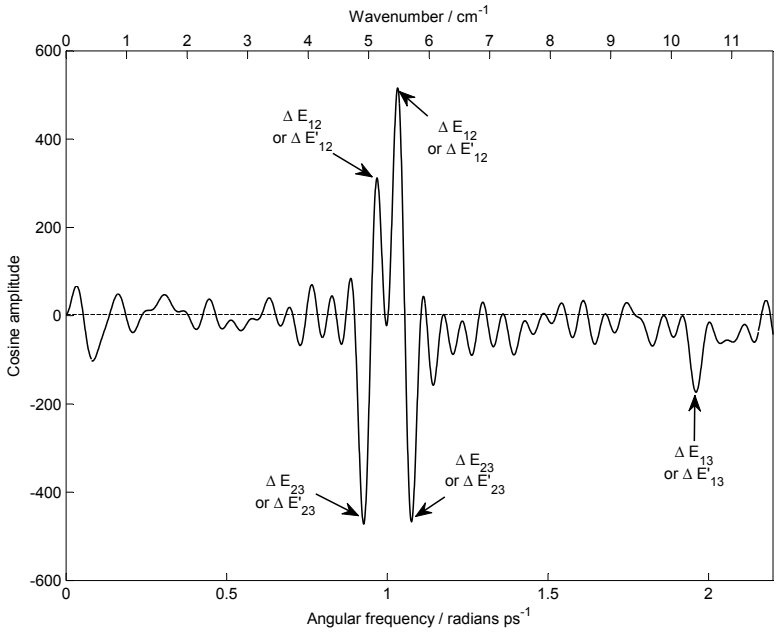

Fig. 7.15. Real part of Fourier transform for the $16a^2$ peak, with assignments of the frequency components to the energy spacings in the scheme of Fig. 7.14. It is not possible to determine which components belong to the $m = 0$ ladder and which belong to the $m = 1$ ladder.

states. In the following section the elements of the anharmonic coupling matrix will be deduced, and used to perform simulations of the quantum beat patterns which provide strong supporting evidence for the scheme shown in Fig. 7.14.

7.5. The eigenvector coupling matrix

Each of the vibrational eigenstates $|1\rangle$, $|2\rangle$, $|3\rangle$ consists of some mixture of the three zero-order states:

$$|n\rangle = \alpha_{na}|a\rangle + \alpha_{nb}|b\rangle + \alpha_{nc}|c\rangle,\ n = 1 \cdots 3, \tag{7.5}$$

where $|a\rangle$, $|b\rangle$ and $|c\rangle$ represent the zero-order states $6a^1$, $10b^1 16b^1$ and $16a^2$ respectively, and the coefficients $\alpha_{n\gamma}, \gamma = a, b, c$ are the elements of the eigenvector coupling matrix.[3] In this section, a formalism will be developed relating these matrix elements to the oscillation patterns of the photoelectron peaks. This will be adapted from equations which were originally developed by Felker and Zewail [27] to describe fluorescence quantum beats, and applied by those same authors to determine the coupling matrix for anthracene [28].

In this work, we excite the two torsional ladders incoherently. The total wavefunction,

[3] These should not be confused with the *Hamiltonian* coupling matrix elements, $H_{mn} \equiv \langle m|\,\hat{\mathrm{H}}_{\mathrm{vib}}\,|n\rangle$, where $|m\rangle$ and $|n\rangle$ are zero-order vibrational states and $\hat{\mathrm{H}}_{\mathrm{vib}}$ is the full (anharmonic) vibrational Hamiltonian operator.

Ψ, is therefore given by the sum of two separate wavepackets, $\phi(t)$ for the $m = 0$ ladder and $\phi'(t)$ for the $m = 1$ ladder. Within each ladder, we have a superposition of three eigenstates:

$$\Psi(t) = \phi(t) + \phi'(t) \tag{7.6a}$$

$$\phi(t) = a_1|1\rangle e^{iE_1 t/\hbar} + a_2|2\rangle e^{iE_2 t/\hbar} + a_3|3\rangle e^{iE_3 t/\hbar} \tag{7.6b}$$

$$\phi'(t) = a'_1|1'\rangle e^{iE'_1 t/\hbar} + a'_2|2'\rangle e^{iE'_2 t/\hbar} + a'_3|3'\rangle e^{iE'_3 t/\hbar} \tag{7.6c}$$

From this point onwards we need only consider $\phi(t)$, the $m = 0$ ladder, since the same arguments will apply equally to $\phi'(t)$. Three simplifying assumptions will be made:

1. The Born-Oppenheimer approximation is valid, so that Franck-Condon factors can be used to determine the transition probabilities into the different vibrational levels.

2. There is only one "bright" zero-order state, $|a\rangle \equiv |6a^1\rangle$.

3. Each ion vibrational state is produced by ionisation out of only one of the zero-order S_1 vibrational states. This assumption seems reasonable in the light of the Franck-Condon simulations shown in Fig. 7.3.

The coefficients a_n in Equation (7.6b) will depend upon the electronic transition dipole moment for the $S_1 \leftarrow S_0$ excitation, the Franck-Condon factor for the vibrational transition $|n\rangle \leftarrow |0\rangle$, and the square root of light intensity p_n at the appropriate wavelength:

$$a_n = p_n \langle S_0|\hat{\mu}_{\text{exc}}|S_1\rangle\langle 0|n\rangle. \tag{7.7}$$

It follows from Equation (7.5) that $\langle 0|n\rangle = \alpha_{na}\langle 0|a\rangle + \alpha_{nb}\langle 0|b\rangle + \alpha_{nc}\langle 0|c\rangle$. However, since $|b\rangle$ and $|c\rangle$ are 'dark' zero-order states, $\langle 0|b\rangle = \langle 0|c\rangle = 0$. Equation (7.7) therefore becomes:

$$a_n = p_n \alpha_{na} \langle S_0|\hat{\mu}_{\text{exc}}|S_1\rangle\langle 0|a\rangle \tag{7.8}$$

and substitution into Equation (7.6b) gives:

$$\begin{aligned}\phi(t) = {} & \langle S_0|\hat{\mu}_{\text{exc}}|S_1\rangle\langle 0|a\rangle \\ & \times \left(p_1\alpha_{1a}|1\rangle e^{iE_1 t/\hbar} + p_2\alpha_{2a}|2\rangle e^{iE_2 t/\hbar} + p_3\alpha_{3a}|3\rangle e^{iE_3 t/\hbar}\right).\end{aligned} \tag{7.9}$$

Now consider the intensity of the photoelectron peak corresponding to a vibrational

state $|\chi\rangle$ in the cation. The Franck-Condon factor for the ionisation process will be:

$$\begin{aligned}\langle\phi|\chi\rangle &= \langle \mathrm{S}_0|\hat{\mu}_{\mathrm{exc}}|\mathrm{S}_1\rangle\langle 0|a\rangle \\ &\times \left(p_1\alpha_{1a}e^{iE_1t/\hbar}\langle 1|\chi\rangle + p_2\alpha_{2a}e^{iE_2t/\hbar}\langle 2|\chi\rangle + p_2\alpha_{3a}e^{iE_3t/\hbar}\langle 3|\chi\rangle\right)\end{aligned} \tag{7.10}$$

and so the intensity of the photoelectron peak is given by:

$$S_\chi(t) = \mathrm{Re}\left\{|\langle \mathrm{S}_1|\hat{\mu}_{\mathrm{ion}}|\mathrm{D}_0\rangle|^2|\langle\phi|\chi\rangle|^2\right\} \tag{7.11a}$$

$$\begin{aligned}&= |\langle \mathrm{S}_1|\hat{\mu}_{\mathrm{ion}}|\mathrm{D}_0\rangle|^2|\langle \mathrm{S}_0|\hat{\mu}_{\mathrm{exc}}|\mathrm{S}_1\rangle|^2|\langle 0|a\rangle|^2 \\ &\times \{2p_1p_2\alpha_{1a}\alpha_{2a}\langle 1|\chi\rangle\langle 2|\chi\rangle\cos(\omega_{12}t) \\ &\quad + 2p_2p_3\alpha_{2a}\alpha_{3a}\langle 2|\chi\rangle\langle 3|\chi\rangle\cos(\omega_{23}t) \\ &\quad + 2p_1p_3\alpha_{1a}\alpha_{3a}\langle 1|\chi\rangle\langle 3|\chi\rangle\cos(\omega_{13}t) \\ &\quad + p_1^2\alpha_{1a}^2|\langle 1|\chi\rangle|^2 + p_2^2\alpha_{2a}^2|\langle 2|\chi\rangle|^2 + p_3^2\alpha_{3a}^2|\langle 3|\chi\rangle|^2\},\end{aligned} \tag{7.11b}$$

where $\omega_{nj} \equiv (E_n - E_j)/\hbar$. For brevity, let $K \equiv |\langle \mathrm{S}_1|\hat{\mu}_{\mathrm{ion}}|\mathrm{D}_0\rangle|^2|\langle \mathrm{S}_0|\hat{\mu}_{\mathrm{exc}}|\mathrm{S}_1\rangle|^2|\langle 0|a\rangle|^2$.

Equation (7.11b) contains the Franck-Condon factors for ionisation from each of the S_1 vibrational eigenstates into ion state $|\chi\rangle$. These can be expressed in terms of the zero-order states $|a\rangle$, $|b\rangle$ and $|c\rangle$:

$$\langle n|\chi\rangle = \alpha_{na}\langle a|\chi\rangle + \alpha_{nb}\langle b|\chi\rangle + \alpha_{nc}\langle c|\chi\rangle. \tag{7.12a}$$

However, since we assume that the ion peak is due to ionisation from only one of the zero-order states, which we shall call $|\gamma\rangle$, the expression simplifies down to:

$$\langle n|\chi\rangle = \alpha_{n\gamma}\langle\gamma|\chi\rangle. \tag{7.12b}$$

Substituting into Equation (7.11b),

$$\begin{aligned}S_\chi(t) &= K|\langle\gamma|\chi\rangle|^2\{2p_1p_2\alpha_{1a}\alpha_{2a}\alpha_{1\gamma}\alpha_{2\gamma}\cos(\omega_{12}t) \\ &\quad + 2p_2p_3\alpha_{2a}\alpha_{3a}\alpha_{2\gamma}\alpha_{3\gamma}\cos(\omega_{23}t) \\ &\quad + 2p_1p_3\alpha_{1a}\alpha_{3a}\alpha_{1\gamma}\alpha_{3\gamma}\cos(\omega_{13}t) \\ &\quad + p_1^2\alpha_{1a}^2\alpha_{1\gamma}^2 + p_2^2\alpha_{2a}^2\alpha_{2\gamma}^2 + p_3^2\alpha_{3a}^2\alpha_{3\gamma}^2\}\end{aligned} \tag{7.13a}$$

$$= K|\langle\gamma|\chi\rangle|^2\left\{2\sum_{n>j}^{3} p_np_j\alpha_{na}\alpha_{ja}\alpha_{n\gamma}\alpha_{j\gamma}\cos(\omega_{nj}t) + \sum_{n=1}^{3} p_n^2\alpha_{na}^2\alpha_{n\gamma}^2\right\} \tag{7.13b}$$

Two further modifications are needed in order to obtain an accurate model for the

intensity of the photoelectron peaks as a function of time. As discussed in Section 7.4.2, an exponential decay term must be added because of the finite rotational temperature of the molecular beam [29]. Secondly, we must add on the photoelectron signal generated from the $m = 1$ torsional ladder, which has the same form as Equation (7.13b). The total photoelectron signal is therefore:

$$\begin{aligned} S_{\chi,\chi'}(t) = {} & 2Ke^{-kt}|\langle\gamma|\chi\rangle|^2 \sum_{n>j}^{3} p_n p_j \alpha_{na}\alpha_{ja}\alpha_{n\gamma}\alpha_{j\gamma} \cos(\omega_{nj}t) \\ & + K|\langle\gamma|\chi\rangle|^2 \sum_{n=1}^{3} p_n^2 \alpha_{na}^2 \alpha_{n\gamma}^2 \\ & + 2K'e^{-k't}|\langle\gamma|\chi'\rangle|^2 \sum_{n>j}^{3} p'_n p'_j \alpha'_{na}\alpha'_{ja}\alpha'_{n\gamma}\alpha'_{j\gamma} \cos(\omega'_{nj}t) \\ & + K|\langle\gamma|\chi'\rangle \sum_{n=1}^{3} p'^2_n \alpha'^2_{na}\alpha'^2_{n\gamma}, \end{aligned} \tag{7.14}$$

where the primes denote quantities relating to the $m = 1$ torsional ladder. It is convenient to re-write this expression in a form which may be more easily compared with the empirical expressions for the quantum beats given in Equations 7.3 and 7.4:

$$\begin{aligned} S_{\chi,\chi'}(t) = {} & (A_{12}\cos\omega_{12}t + A_{23}\cos\omega_{23}t + A_{13}\cos\omega_{13}t)\, e^{-kt} \\ & + (A'_{12}\cos\omega'_{12}t + A'_{23}\cos\omega'_{23}t + A'_{13}\cos\omega'_{13}t)\, e^{-k't} + C, \end{aligned} \tag{7.15}$$

with $A_{nj} \equiv 2Kp_n p_j \alpha_{na}\alpha_{ja}\alpha_{n\gamma}\alpha_{j\gamma}|\langle\gamma|\chi\rangle|^2$, and A'_{nj} similarly defined for the $m = 1$ torsional ladder. All of the constant terms have been combined into a single parameter, C.

As mentioned above, the quantities p_1, p_2 and p_3 are proportional to the square root of the light intensity at the wavelengths resonant with absorption into the S_1 eigenstates $|1\rangle$, $|2\rangle$ and $|3\rangle$ respectively. These can be estimated by modelling the spectral profile of the excitation laser as a Gaussian function centred at $459\,\mathrm{cm}^{-1}$, with a full width at half maximum (FWHM) of $13\,\mathrm{cm}^{-1}$ and the intensity normalised to unity at $459\,\mathrm{cm}^{-1}$. With eigenstate energies of 462, 457 and $452\,\mathrm{cm}^{-1}$, this model gives:

$$\begin{pmatrix} p_1 & p_2 & p_3 \end{pmatrix} = \begin{pmatrix} 0.929 & 0.968 & 0.669 \end{pmatrix}. \tag{7.16}$$

Approximate values of the Franck-Condon factors $|\langle\gamma|\chi\rangle|^2$ can be obtained from the integrals of the photoelectron peaks at 0 ps (for $\langle 6a^1|\chi\rangle$) and 3 ps (for $\langle 10b^1 16b^1|\chi\rangle$). It is reasonable to assume that $\langle 16a^2|16a^2\rangle \approx \langle 10b^1 16b^1|10b^1 16b^1\rangle$, since both of these states are expected to show a strong $\Delta v = 0$ propensity for ionisation out of S_1. The

Franck-Condon factors used in this work are listed in Table 7.5.

Table 7.5. Franck-Condon factors, $|\langle\gamma|\chi\rangle|^2$, used in the calculation of the coupling matrix. These have been normalised to give $|\langle 6a^1|6a^1\rangle|^2 \equiv 1$.

Zero-order S_1 state	Zero-order ion state					
	0^0	$6a^1$	$10b^1 16b^1$	$16a^2$	$6a^2$	$6a^1 10b^1 16b^1$
$6a^1$	0.91	1.00	0.00	0.00	1.10	0.00
$10b^1 16b^1$	0.00	0.00	2.09	0.00	0.00	0.88
$16a^2$	0.00	0.00	0.00	2.09	0.00	0.00

In order to proceed with the calculation of the coupling matrix elements, each term in Equation (7.15) must be equated to one of the fitted parameters listed in Table 7.3. As mentioned in Section 7.4.5, it is not clear which of the fitted frequencies correspond to the $m = 0$ ladder, and which to $m = 1$. It does, however, seem likely that ω_u, ω_w and ω_y all belong to the same ladder since $\omega_u + \omega_w \approx \omega_y$. For the purposes of the calculation it will be assumed that this is the $m = 0$ ladder, and that ω_v, ω_x and $(\omega_v + \omega_x)$ belong to the $m = 1$ ladder.

It is also a good starting point to assume that all parameters apart from the beat frequencies are the same for both torsional ladders. The empirical cosine fits give $V \approx W$ and $U \approx X$ (see Table 7.3), implying that $A_{12} \approx A'_{12}$ and $A_{23} \approx A'_{23}$. A single averaged value can therefore be used for each of these amplitudes in both ladders. Equation (7.15) is thus reduced down to:

$$\begin{aligned} S_{\chi,\chi'}(t) = \{&\overline{A}_{12}(\cos\omega_{12}t + \cos\omega'_{12}t) + \overline{A}_{23}(\cos\omega_{23}t + \cos\omega'_{23}t) \\ &+ \overline{A}_{13}(\cos\omega_{13}t + \cos\omega'_{13}t)\}e^{-kt} + D, \end{aligned} \tag{7.17}$$

with the value of the decay constant taken from the empirical cosine fits, $k = 1.3 \times 10^{-9}$ s^{-1} (see Table 7.3).

The coupling matrix is found by an iterative fitting process. We begin by establishing approximate, trial values of the elements α_{na} which give the contributions of the zero-order bright state to each of the three eigenstates. These are reflected in the transition probabilities for absorption from S_0 into each S_1 vibrational level. A fluorescence excitation spectrum published by Doyle *et al.* [127], in which the eigenstates are clearly resolved, suggests that the ratio of the absorption cross sections for eigenstates $|1\rangle$, $|2\rangle$ and $|3\rangle$ is roughly $9 : 10 : 1$. Applying the normalisation condition $\sum_n \alpha_{na}^2 = 1$ and then taking the square roots gives:

$$\begin{pmatrix} \alpha_{1a} & \alpha_{2a} & \alpha_{3a} \end{pmatrix} \approx \begin{pmatrix} 0.671 & 0.707 & 0.224 \end{pmatrix}. \tag{7.18}$$

Next, the matrix elements associated with zero-order state $|c\rangle$ are found from the fit of the $16a^2$ peak oscillations to Equation (7.4) (see Table 7.2b). Taking the average of V and W gives $\overline{A}_{12} = 6.5$, the average of U and X gives $\overline{A}_{23} = -7.5$ and $\overline{A}_{13} = W = -3.1$. The elements α_{nc} can be determined by taking the ratios of these amplitudes:

$$\frac{\overline{A}_{12}}{\overline{A}_{23}} = \frac{p_1 p_2 \alpha_{1a}\alpha_{2a}\alpha_{1c}\alpha_{2c}}{p_2 p_3 \alpha_{2a}\alpha_{3a}\alpha_{2c}\alpha_{3c}} = -0.864 \tag{7.19a}$$

$$\frac{\alpha_{1a}\alpha_{1c}}{\alpha_{3a}\alpha_{3c}}\left(\frac{p_1}{p_3}\right) = -0.864 \tag{7.19b}$$

$$\begin{aligned}\frac{\alpha_{1c}}{\alpha_{3c}} &= -0.864 \times \left(\frac{\alpha_{3a}}{\alpha_{1a}}\right)\left(\frac{p_3}{p_1}\right) \\ &= -0.226\end{aligned} \tag{7.19c}$$

and by similar logic the ratio $\overline{A}_{12}/\overline{A}_{13}$ yields $\alpha_{2c} = -0.364\alpha_{3c}$. Using this information and the normalisation condition $\sum_n \alpha_{nc}^2 = 1$ gives:

$$\begin{pmatrix}\alpha_{1c} & \alpha_{2c} & \alpha_{3c}\end{pmatrix} = \begin{pmatrix}0.186 & 0.406 & -0.895\end{pmatrix}. \tag{7.20}$$

The signs of these matrix elements are arbitrary, except that α_{3c} must have the opposite sign to α_{1c} and α_{2c}.

Finally the elements relating to zero-order state $|b\rangle$ are found using the normalisation condition $\sum_b \alpha_{nb}^2 = 1$. Since ionisation out of $|b\rangle$ is seen to give frequency components ω_{12} and ω'_{12} with negative phase, α_{1b} must have the opposite sign to α_{2b}. These considerations lead to the following approximate coupling matrix:

$$\begin{pmatrix}\alpha_{1a} & \alpha_{2a} & \alpha_{3a} \\ \alpha_{1b} & \alpha_{2b} & \alpha_{3b} \\ \alpha_{1c} & \alpha_{2c} & \alpha_{3c}\end{pmatrix} \approx \begin{pmatrix}0.671 & 0.707 & 0.224 \\ -0.718 & 0.579 & 0.386 \\ 0.186 & 0.406 & -0.895\end{pmatrix}. \tag{7.21}$$

The quantum beats for each photoelectron peak may then be simulated by substituting these values into Equation (7.17), and using an analytic linear least squares procedure to find the value for K which best fits the measured intensities. The constant term, C, is fixed to the mean intensity value for each peak. Having done this, adjustments can be made to the coupling matrix in an attempt to improve the fit further. Using Equation (7.19c) and the normalisation conditions, the complete matrix can be recalculated for different assumed values of α_{2a} and α_{3a}. A non-linear least squares optimisation routine in Matlab was used to adjust the values of these parameters in order to achieve the best match to the measured values for the intensity of the ion $16a^2$ peak. This procedure

yielded a more accurate coupling matrix:

$$\begin{pmatrix} \alpha_{1a} & \alpha_{2a} & \alpha_{3a} \\ \alpha_{1b} & \alpha_{2b} & \alpha_{3b} \\ \alpha_{1c} & \alpha_{2c} & \alpha_{3c} \end{pmatrix} = \begin{pmatrix} 0.643 & 0.754 & 0.132 \\ -0.756 & 0.611 & 0.236 \\ 0.123 & 0.241 & -0.963 \end{pmatrix}, \tag{7.22}$$

whose simulated quantum beats, shown in Fig. 7.16, are in good agreement with experiment. The corresponding modulation depths are listed in Table 7.6.

Table 7.6. Quantum beat modulation depths given by the fitted coupling matrix. Experimental values are given in brackets for comparison.

Ion peak	$\overline{A}_{12}$		$\overline{A}_{23}$		$\overline{A}_{13}$	
Origin	42.7	(35.8)	1.3		0.9	
$6a^1$	47.0	(48.3)	1.4		1.0	
$10b^1 16b^1$	-93.5	(-99.3)	4.3		-4.4	
$16a^2$	6.0	(6.5)	-6.9	(-7.5)	-2.9	(-3.1)
$6a^2$	51.6	(50.6)	1.6		1.1	
$6a^1 10b^1 16b^1$	-39.3	(-36.1)	1.8		-1.8	

Although the error bars of the fitted matrix elements are not easy to determine, an accuracy of ± 0.1 is a reasonable conservative estimate. Taking the squares of the matrix elements reveals the fractional contributions of each zero-order state to the three eigenstates (Table 7.7).

Table 7.7. Composition of the eigenstates, derived from the squares of the matrix elements given in Equation (7.22).

Eigenstate	% Contribution from:		
	$\|6a^1\rangle$	$\|10b^1 16b^1\rangle$	$\|16a^2\rangle$
$\|1\rangle$	41.4	56.9	1.7
$\|2\rangle$	57.1	37.3	5.6
$\|3\rangle$	1.5	5.8	92.7

7.6. Deuteration of the methyl group

In order to gain further insights into the effect of the methyl group on the IVR dynamics, nanosecond ZEKE and picosecond time-resolved studies were also carried out on the isotopologue $C_6H_5CD_3$, in which the methyl group was fully deuterated. Although the frequencies of the S_1 $6a^1$ and $10b^1 16b^1$ levels were shifted to the red by this change, the frequency of the $16a^2$ ring twist was unaffected. The nanosecond REMPI spectra over the Fermi resonance region are compared for the two isotopomers in Fig. 7.17. From the REMPI it can be seen that the eigenstate corresponding mostly to $16a^2$ has the *highest*

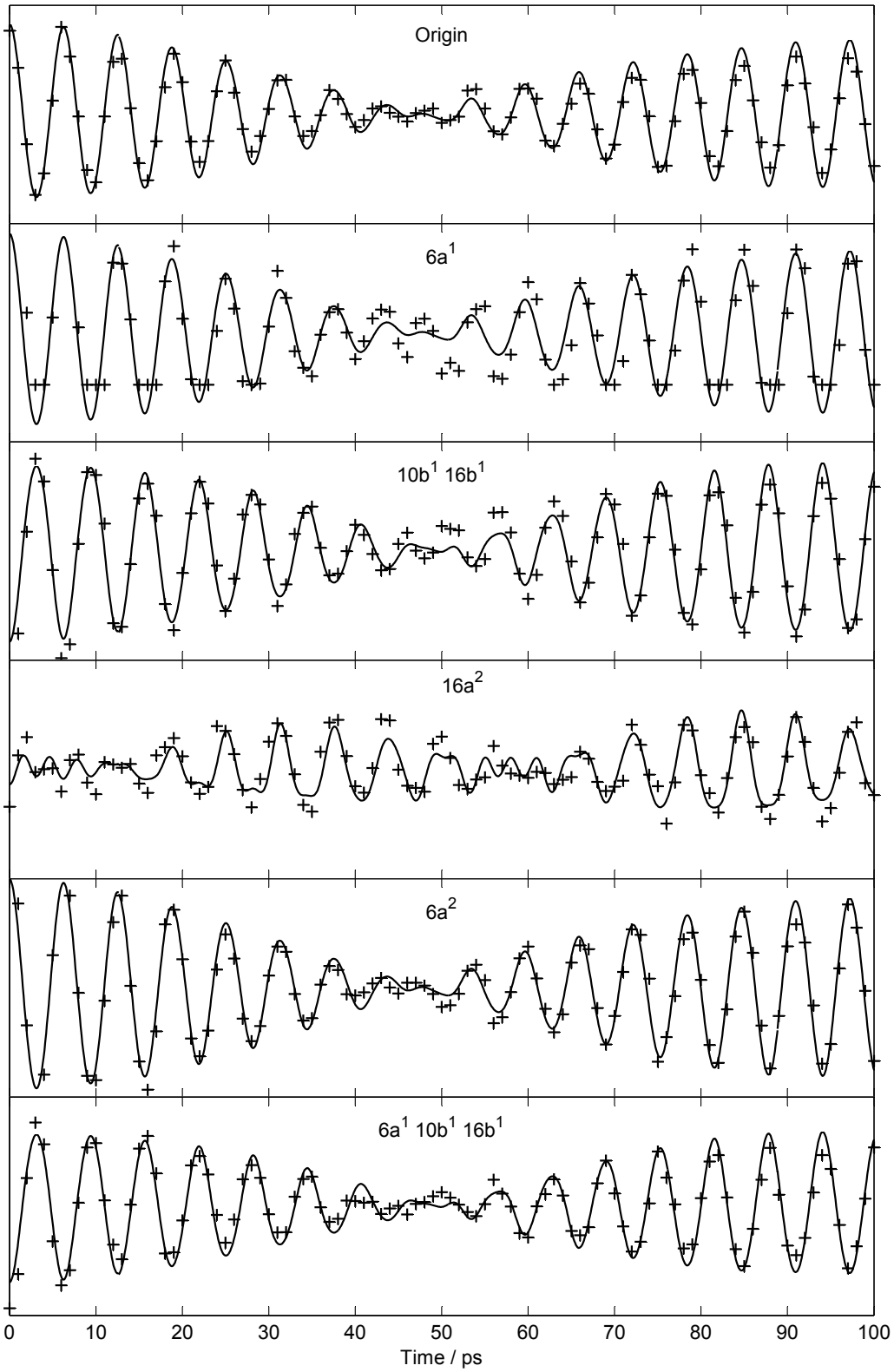

Fig. 7.16. Simulations of the peak oscillations for on-resonance pump wavelength, using Equation (7.17) and the fitted coupling matrix of Equation (7.22). The crosses represent the experimental values for the peak intensities.

frequency in $C_6H_5CD_3$. More surprisingly, two additional vibrational levels appear at 437 and 441 cm^{-1} in deuterated toluene.

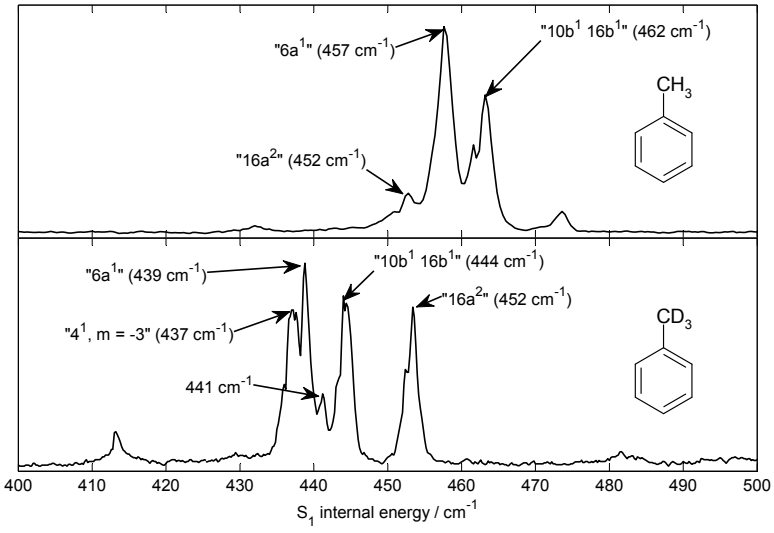

Fig. 7.17. Comparison of nanosecond REMPI spectra in the vicinity of S_1 $6a^1$ / $10b^1 16b^1$ / $16a^2$ for $C_6H_5CH_3$ and $C_6H_5CD_3$.

ZEKE spectra were recorded *via* each of the four most intense features seen in the REMPI, and these are plotted in Fig. 7.18. The spectrum from the S_1 vibrational level at 437 cm^{-1} shows a $\Delta v = 0$ peak at 541 cm^{-1}. A search using the backtracking algorithm (see Section 5.3.2) reveals only one zero-order state of overall A_1 symmetry that is consistent with the observed frequencies in the S_1 state and the cation. The REMPI peak at 437 cm^{-1} is therefore tentatively assigned as $|4^1, m = -3\rangle$, which has calculated frequencies of 448 and 547 cm^{-1} in the S_1 state and the cation respectively.[4] According to the selection rules discussed in Section 2.7.6, this state is accessible only through torsion-vibration coupling.

The ZEKE spectra *via* the S_1 vibrational levels at 437, 439 and 444 cm^{-1} all contain peaks corresponding to $|4^1, m = -3\rangle$, $|6a^1, m = 0\rangle$ and $|10b^1 16b^1, m = 0\rangle$ in the cation, suggesting that these three zero-order states may be coupled together. However the spectrum *via* "$16a^2$" is essentially the same as for non-deuterated toluene (Fig. 7.3), which would seem to imply that any coupling between $16a^2$ and the other zero-order states is probably weak.

A time-resolved series of picosecond two-colour VMI photoelectron spectra was also recorded, with pump-probe time delays ranging from 0–100 ps in 1 ps steps. For all

[4]The B3LYP calculations carried out in this work, with a scaling factor of 0.97, give frequencies for 4^1 of 417 cm^{-1} in the S_1 electronic state and 522 cm^{-1} in the cation (see Tables 5.5 and 5.6). The torsional energies were estimated using the free rotor expression of Equation (2.6), with a reduced rotational constant $B = 2.74\,cm^{-1}$ as given by Borst and Pratt [17]. In the S_1 electronic state, for which the torsional barrier height is known, a correction was made using Equation (2.9) with $V_6 = -24.5\,cm^{-1}$ [17]. Unfortunately no measurement of V_6 is available for the cation.

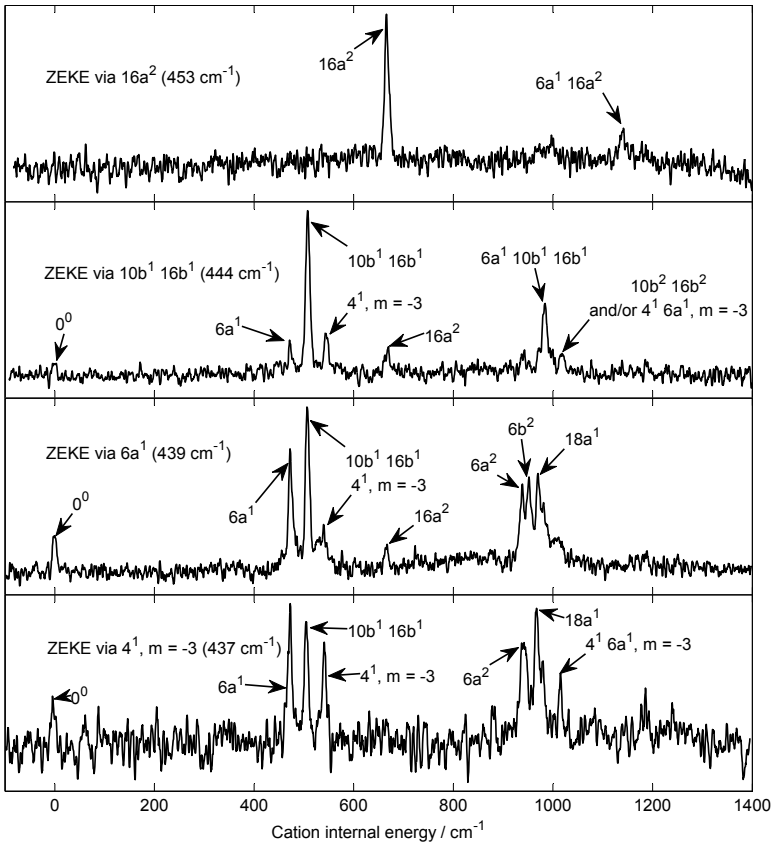

Fig. 7.18. Nanosecond ZEKE spectra recorded *via* the four vibrational levels in the vicinity of S_1 $6a^1$ in $C_6H_5CD_3$.

of these images the probe wavelength was 288 nm. The pump laser was tuned to the absorption maximum at $\sim$443 cm^{-1} above the S_1 origin, and its bandwidth is represented by the dashed line in Fig. 7.19. A comparison with the nanosecond REMPI spectrum (solid line in Fig. 7.19) shows that the absorption feature at 452 cm^{-1}, which is mainly "$16a^2$" in character, was only weakly excited. It is therefore possible that the initially prepared vibrational state may not have corresponded to the pure zero-order bright state ($6a^1$).

The photoelectron spectra for time delays of 0–12 ps are shown in Fig. 7.20. As in toluene-H_8, the intensities of some of the peaks show a clear oscillation in time. However, the analysis of this quantum beat pattern is complicated by the fact that the peaks at $\sim$ 500 and $\sim$1000 cm^{-1} are composites of three unresolved features (compare with the ZEKE spectra in Fig. 7.18). This increased congestion means that the Gaussian fitting procedure described in Section 7.3 can no longer be used to deconvolute the oscillations of the $6a^1$ and $10b^116b^1$ peaks. Unfortunately the $16a^2$ peak, which provided the most useful information in toluene-H_8, does not show a clear oscillation pattern. Nonetheless, some insight into the dynamics can be gained by studying the quantum beats of the origin peak.

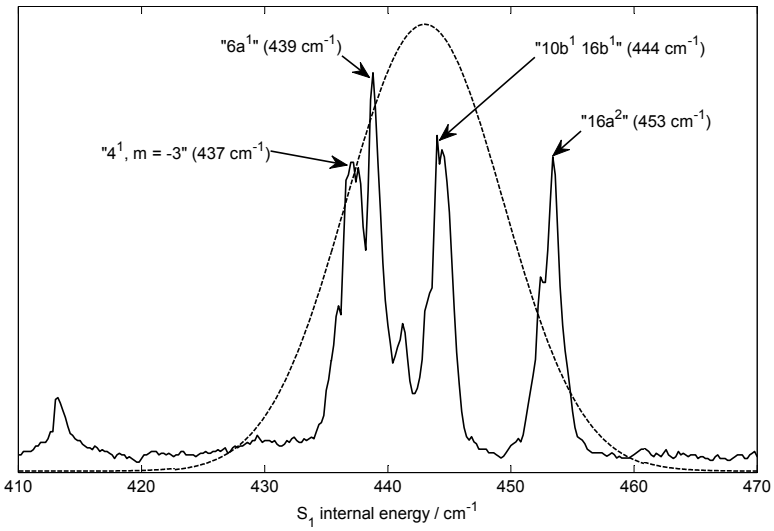

Fig. 7.19. Comparison of energy spacing of the "Fermi resonance" components in $C_6H_5CD_3$ with the bandwidth of the picosecond laser. The solid line is the nanosecond REMPI spectrum and the dashed line is a Gaussian function of $15\,\mathrm{cm}^{-1}$ FWHM centred at the pump wavelength used in the picosecond time-resolved experiments.

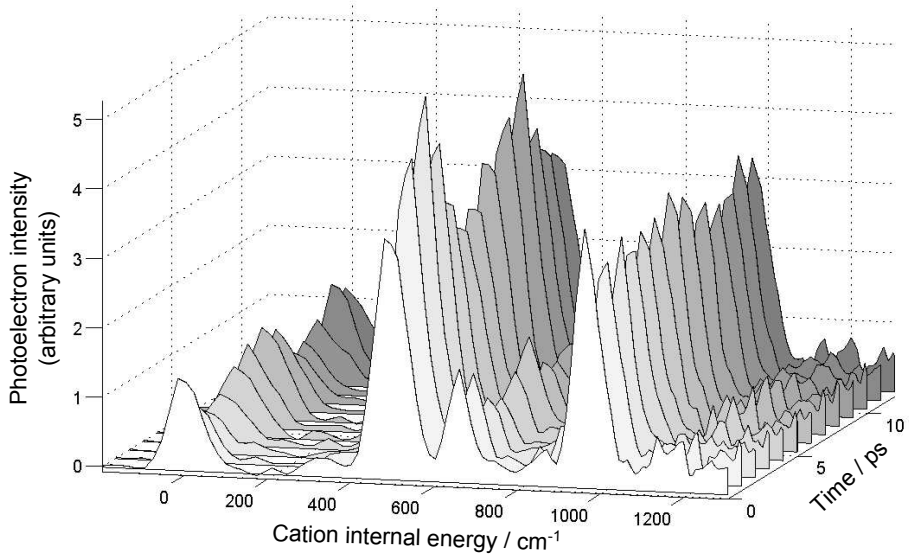

Fig. 7.20. Picosecond two-colour VMI photoelectron spectra *via* the Fermi resonance in S_1 $C_6H_5CD_3$ for time delays of 0–12 ps. The images were recorded with a probe wavelength of 288 nm and the spectra are normalised by the integral from -200 to $1100\,\mathrm{cm}^{-1}$.

The integral of the origin peak was measured as a function of time by fitting it to a Gaussian function of $95\,\mathrm{cm}^{-1}$ FWHM centred at $0\,\mathrm{cm}^{-1}$, and the resulting oscillation pattern is plotted in Fig. 7.21. A Fourier transform (Fig. 7.22) reveals two frequency components of approximately 5.4 and $8.0\,\mathrm{cm}^{-1}$, suggesting that the quantum beats can be modelled empirically by fitting to Equation (7.3) (solid line in Fig. 7.21). The anomalously large integral at 0 ps was excluded from the fit, since the spectrum may have been influenced by strong field effects due to the high light intensity when the pump and probe pulses were overlapped in time. The fitted parameters are listed in Table 7.8, and the two frequency components correspond to the energy spacings between the "$|4^1, m = -3\rangle$", "$6a^1$" and "$10b^1 16b^1$" REMPI peaks shown in Fig. 7.17.

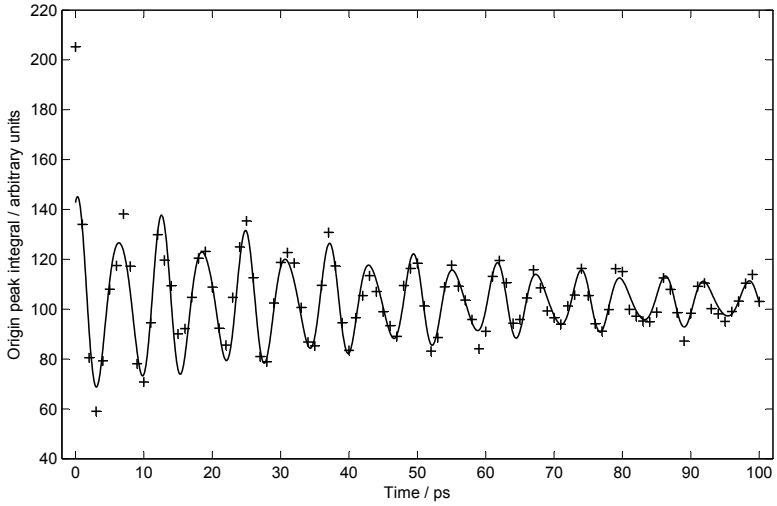

Fig. 7.21. Time-resolved oscillations of the origin peak for the Fermi resonance in $C_6H_5CD_3$, with fit to Equation (7.3). The anomalously large integral at 0 ps has been excluded from the fit.

Table 7.8. Parameters obtained from a fit of the origin peak oscillations for $C_6H_5CD_3$ to Equation (7.3).

Parameter	Fitted value
V	34
ω_v / $\mathrm{rad\,ps}^{-1}$	1.026
$\tilde{\nu}_v$ / cm^{-1}	5.45
W	8
ω_w / $\mathrm{rad\,ps}^{-1}$	1.525
$\tilde{\nu}_w$ / cm^{-1}	8.10
k / 10^{-2} ps^{-1}	1.56
t_0 / ps	0.31
Z	104

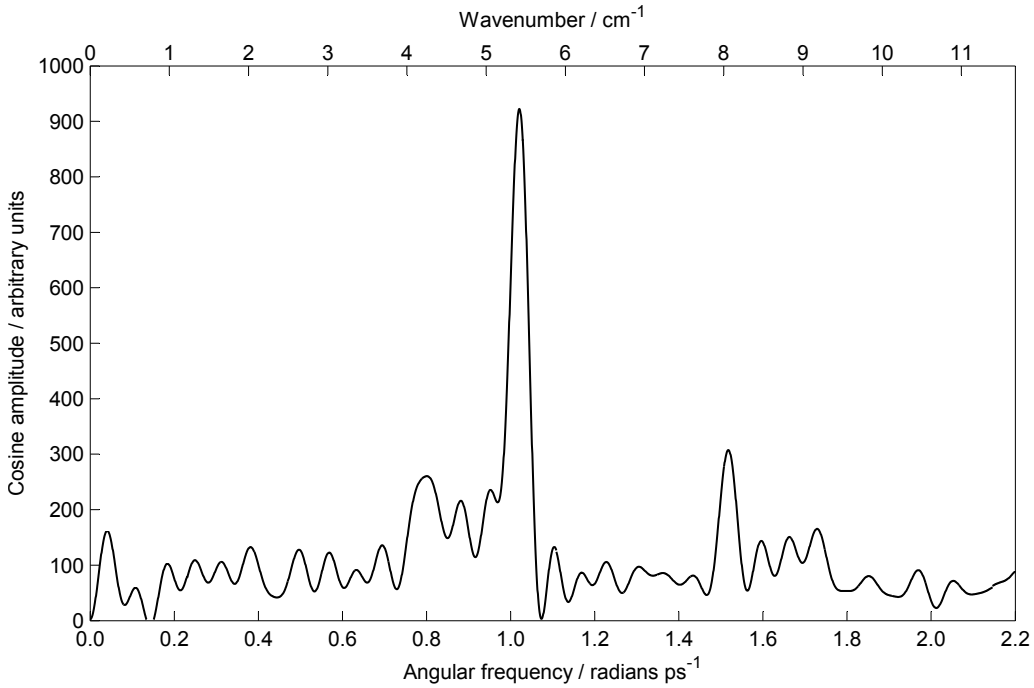

Fig. 7.22. Fourier transform of the time–resolved oscillations of the origin peak for the Fermi resonance in $C_6H_5CD_3$.

7.7. Conclusions

The work presented in this chapter shows the power of time-resolved experiments to reveal dynamical information that was not apparent in previous frequency-resolved studies. A system which was initially diagnosed as a Fermi resonance between the $6a^1$ ring stretch and $10b^1 16b^1$ ring bending combination has been shown also to involve a third coupled zero-order state, the $16a^2$ ring twist. Although Hickman *et al.* [63] were able to observe fluorescence from the Fermi resonance components into S_0 $16a^2$, amongst many other levels, that information alone was not sufficient to demonstrate that $16a^2$ is a coupled state rather than merely a spectator. By contrast the time-resolved results are much more sensitive to the very weak coupling, which is indicated by the definite phase relationship between the population of $16a^2$ and the other zero-order states.

For a system comprising three coupled vibrational levels, we would normally expect to see quantum beats with three frequency components, corresponding to the energy spacing between each pair of eigenstates. The observation of two different frequency components for each pair of eigenstates has led to the deduction that the torsional levels of the methyl group are also important. Although it is not yet clear why the torsional motion should affect the energy spacing between different vibrational levels of the ring, this effect will have to be taken into account in future studies of systems containing methyl rotors. It would be interesting to perform experiments in which the temperature of the molecular

beam is varied, in order to determine which frequency components correspond to the $m = 0$ torsional ladder and which to $m = 1$.

This work also demonstrates for the first time that time-resolved photoelectron spectra can provide *quantitative* information, in the form of the eigenvector coupling matrix, when a relatively simple vibrational wavepacket is prepared. The approach taken is similar to the method developed by Felker and Zewail [27, 28] for the analysis of fluorescence quantum beats. However photoelectron spectroscopy can be applied to a wider range of systems, as it is subject to less strict selection rules, and it avoids the need to deconvolute the beating pattern from an exponential decay.

Extremely high resolution would be required to obtain the eigenvector coupling matrix from a frequency-resolved experiment, and this would be very challenging to achieve in practice. Although the nanosecond ZEKE results cannot be used to calculate the eigenvector coupling matrix elements, they do nonetheless provide valuable information which is complementary to the time-resolved spectra. In combination with the Franck-Condon simulations, they give insights into the nature of the vibrational eigenstates which corroborate some of the conclusions reached from the time-resolved data.

It was initially hoped that a study of the $6a^1$ / $10b^1 16b^1$ / $16a^2$ system in toluene-D_3 might give further insights into the effect of the methyl group on the IVR dynamics. However, the nanosecond REMPI spectrum of $C_6H_5CD_3$ revealed the unexpected presence of a fourth S_1 vibrational level which leads to more complicated IVR behaviour. The most likely assignment for this fourth level is $|4^1, m = -3\rangle$, which would require torsion-vibration coupling to play a significant role. The nanosecond ZEKE spectra suggest that $|4^1, m = -3\rangle$ is coupled to both $6a^1$ and $10b^1 16b^1$. Further evidence for its involvement in the coupling is provided by the picosecond time-resolved experiments, as the time-resolved oscillations of the origin peak contain two frequency components: one at $\sim 5\,\mathrm{cm}^{-1}$, corresponding to the energy separation of $6a^1$ and $10b^1 16b^1$, and one at $\sim 8\,\mathrm{cm}^{-1}$, which can be identified with the separation of $|4^1, m = -3\rangle$ and $10b^1 16b^1$. Unfortunately, because the photoelectron spectra were more congested than those of $C_6H_5CH_3$ and the excitation laser bandwidth was not sufficient to ensure preparation of the pure bright state, it has not been possible to obtain the eigenvector coupling matrix for toluene-D_3.

8. Dissipative IVR following excitation to high vibrational levels

In Chapter 7 a case of restricted IVR was examined, in which quantum beats were observed in the time-resolved photoelectron spectra. These indicated that the molecule was oscillating between just three vibrational states. However, in cases where the number of coupled states is sufficiently large, we can expect vibrational energy to flow irreversibly out of the bright state and become distributed across many different modes of vibration. This behaviour is known as *dissipative* or *statistical IVR*.

Fig. 8.1 shows how the density of vibrational states in the S_1 electronic state of toluene rises sharply as a function of the vibrational energy. Dissipative IVR is not expected to occur when the density of states is low, since there will be only a few dark states sufficiently close in energy to couple to the bright state that is prepared by the pump laser pulse. This chapter will examine the vibrational levels that have been highlighted in bold in Fig. 8.1, from which dissipative IVR has been observed in this work. These are the highest-energy vibrational states that have been examined in the present time-resolved experiments. A key question to be addressed in this chapter is whether the IVR rate is affected by the type of motion excited in the bright state, or is simply determined by the total energy and density of states.

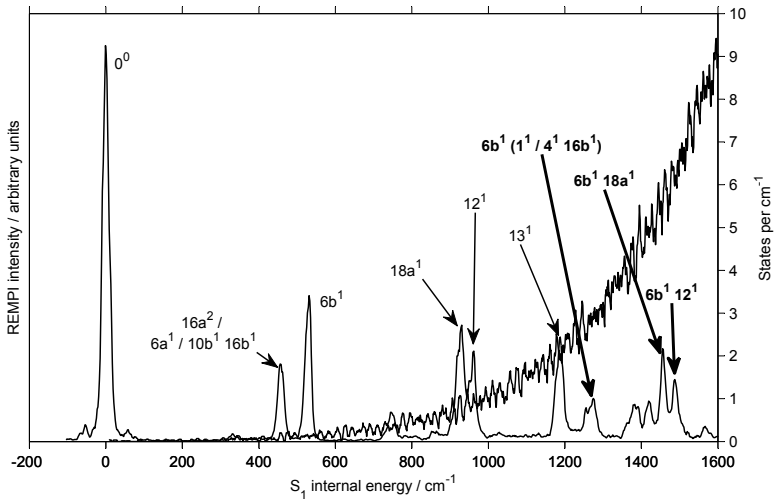

Fig. 8.1. Calculated density of vibrational states superimposed upon the picosecond REMPI spectrum of toluene. The S_1 vibrational levels to be examined in this chapter are highlighted in bold.

8.1. S_1 $6b^1$ (1^1 / 4^1 $16b^1$) Fermi resonance

8.1.1. Assignments

Hickman *et al.* [63] diagnosed a pair of features at 1263 and 1284 cm^{-1} in the fluorescence excitation spectrum of toluene as resulting from the combination of $6b^1$ (= 532 cm^{-1}) with the Fermi resonance couple 1^1 / $4^1 16b^1$ (= 736 / 754 cm^{-1}). However these authors found the corresponding dispersed fluorescence spectra to be unstructured, presumably due to rapid IVR, and were therefore unable to verify their assignments experimentally. For this reason, one of the first objectives in the present work was to confirm the identities of the vibrational states using photoelectron spectroscopy.

Fig. 8.2 shows an enlarged portion of the nanosecond REMPI spectrum recorded in this work. The two Fermi resonance components are clearly visible. Although it was not possible to record nanosecond ZEKE spectra *via* these vibrational levels, they were sufficiently well separated to be prepared separately by the picosecond laser. The dashed lines in Fig. 8.2 are Gaussian functions of 15 cm^{-1} FWHM, representing the bandwidth of the picosecond pulses. It can be seen that, with an excitation wavenumber centred on each absorption feature, the other Fermi resonance component will make only a small contribution to the prepared state. Consequently the pure $6b^1 1^1$ zero-order bright state was *not* prepared.

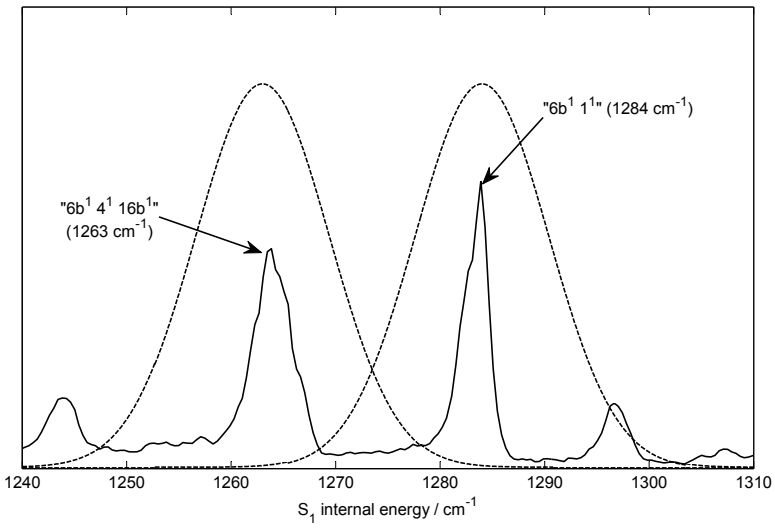

Fig. 8.2. Comparison of energy spacing of the $6b^1$ $\left(1^1/4^1 16b^1\right)$ Fermi resonance components with the bandwidth of the picosecond laser. The solid line is the nanosecond REMPI spectrum obtained in this work, and the dashed lines are Gaussian functions of 15 cm^{-1} FWHM centred at the two excitation wavenumbers used in the picosecond experiments.

A time-resolved series of two-colour VMI photoelectron spectra was recorded *via* each of the Fermi resonance components, using a single probe laser wavelength of 290 nm.

The spectra at 0 ps are plotted in Fig. 8.3, alongside the picosecond SEVI spectra from the $4^1 16b^1$ and 1^1 levels which were first presented in Section 6.5. For comparison purposes the spectra from the levels at 1263 and 1284 cm^{-1} have been shifted to the left by 485 cm^{-1}, which is the frequency of $6b^1$ in the cation (see Section 6.4). The close resemblance between the spectra provides supporting evidence for the assignments made by Hickman *et al.* In the following discussion, the lower Fermi resonance component at 1263 cm^{-1} level will be referred to as "$6b^1 4^1 16b^1$", and the upper component at 1284 cm^{-1} as "$6b^1 1^1$; however it should be noted that these labels are approximate due to the Fermi resonance coupling. In reality, each of the two eigenstates contains some character from both of these zero-order states.

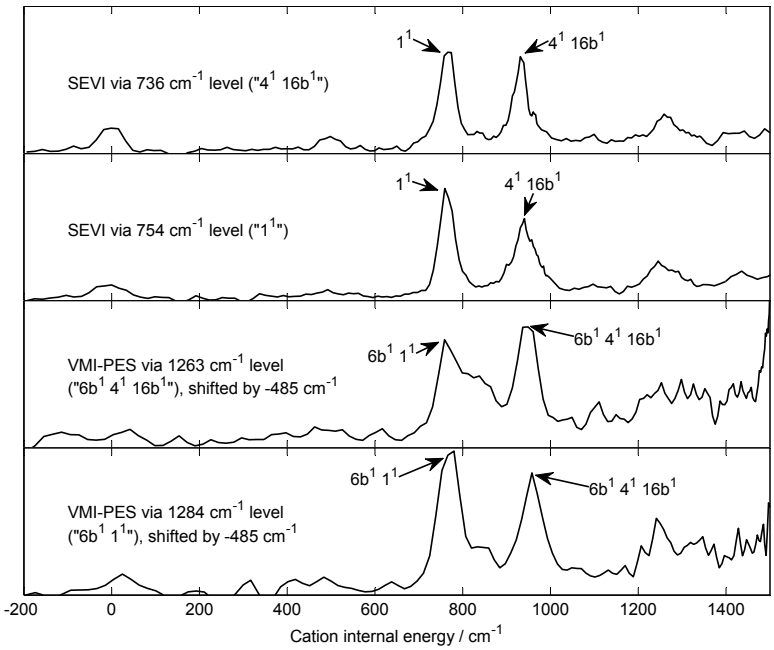

Fig. 8.3. Confirmation of the assignment of the S_1 vibrational levels at 1263 and 1284 cm^{-1}. The two-colour VMI photoelectron spectra from these levels were recorded at 0 ps time delay with a probe wavelength of 290 nm. For comparison purposes, they have been shifted to the left by 485 cm^{-1}, which is the frequency of $6b^1$ in the cation. The peaks are well aligned with those seen in the SEVI spectra at 0 ps from the 1^1 and $4^1 16b^1$ levels, which were first presented in Section 6.5.

8.1.2. Time-resolved spectra via S_1 "$6b^1$ 4^1 $16b^1$" level (0^0 + 1263 cm^{-1})

The time-resolved photoelectron spectra *via* the lower Fermi resonance component are plotted in Fig. 8.4. Surprisingly, the $\Delta v = 0$ peak at ~1440 cm^{-1} is considerably more intense at a pump-probe delay of 1 ps than at 0 ps. Beyond 1 ps the intensity of the peak falls off with increasing time delay as the $6b^1 4^1 16b^1$ bright state is irreversibly depopulated, and the spectrum becomes congested as many different dark states begin

to contribute. It is possible that the spectrum at 0 ps may have been influenced by strong field effects, due to the high light intensity when the pump and probe laser pulses were overlapped in time.

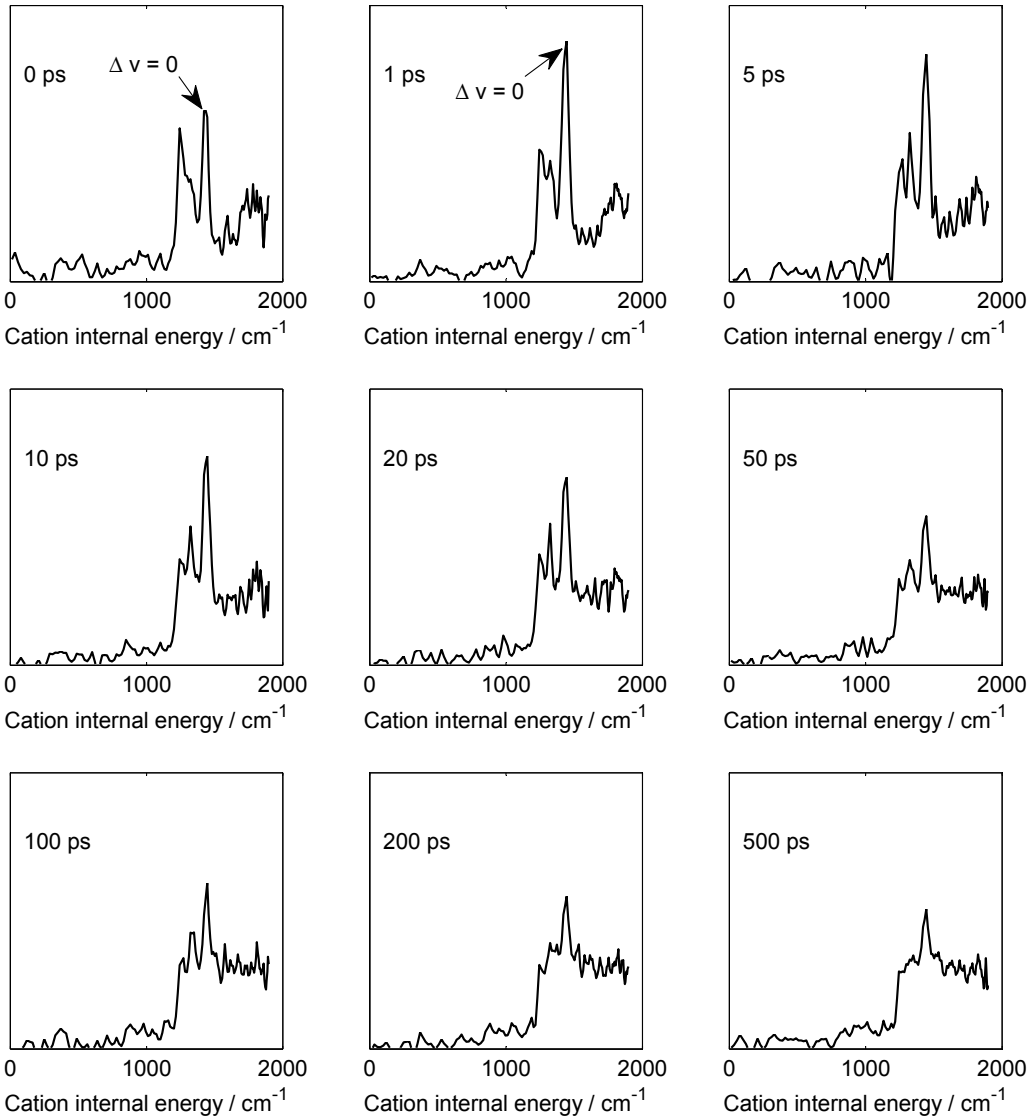

Fig. 8.4. Time-resolved two-colour VMI photoelectron spectra *via* S_1 $6b^1 4^1 16b^1$, taken with a probe wavelength of 290 nm. The spectra are normalised according to the integral from -200 to 1900 cm^{-1}.

An estimate of the bright state population was obtained as a function of time by integration of the $\Delta v = 0$ peak over the internal energy range 1400–1480 cm^{-1} using the Trapezium Rule (see Fig. 8.5). Since only one image was taken at each time delay, the error bars on these measurements are not easy to determine. As a crude estimate, it has been assumed that the change in the spectrum between 200 and 500 ps is not significant, so that the error bar can be taken as the difference between the measured integrals for these two time delays. The time dependence of the bright state population

can be modelled empirically using an exponential function of the form:

$$I(t) = A + B\exp(-t/\tau_{\mathrm{IVR}}), \tag{8.1}$$

where τ_{IVR} is the IVR lifetime in picoseconds. In order to assess the reliability of the fitted value of τ_{IVR}, two fits are shown in Fig. 8.5. Both of these exclude the anomalously low peak integral at 0 ps. The solid line is a fit taking into account the data points from 1 to 500 ps, giving an IVR lifetime of 25.0 ps. The dashed line is the result of a fit to the data points between 1 and 200 ps, with a shorter optimised lifetime of 22.8 ps.

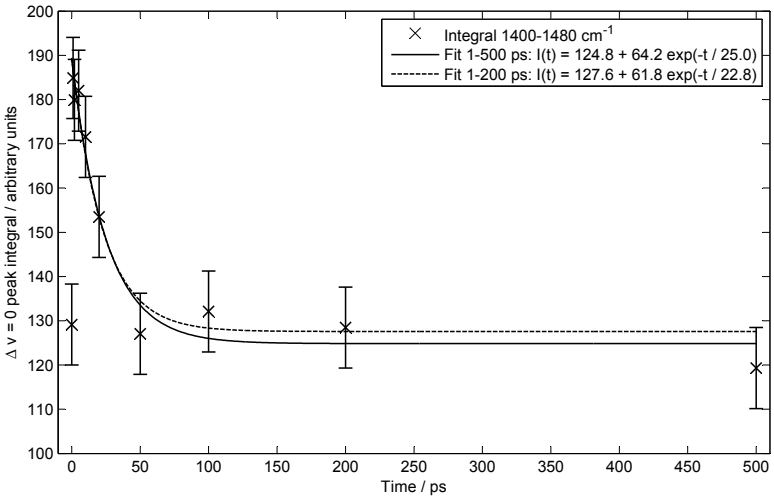

Fig. 8.5. Decay of bright state population following excitation to S_1 $6b^1 4^1 16b^1$, with fits to Equation (8.1). The anomalously low value at 0 ps has been excluded from the fits.

In the spectrum at 1 ps time delay there is a flat, featureless region immediately to the right of the $\Delta v = 0$ peak, between 1550 and 1700 ps (see Fig. 8.4). Since no peaks are present corresponding to ionisation from the bright state, the integral over this region can be used to obtain a rough estimate of the rate of increase of the population of the dark vibrational states. A plot of this integral as a function of time shows a growth consistent with Equation (8.1), with a negative value of B and an IVR lifetime of between 16 and 17 ps (Fig. 8.6).

Taking an average of the fitted values for the IVR lifetime from the bright and dark state populations suggests that $\tau_{\mathrm{IVR}} = 20.6 \pm 5$ ps. Using this averaged value, acceptable fits can be achieved for both the decay of the bright state and the rise of the dark states (Fig. 8.7).

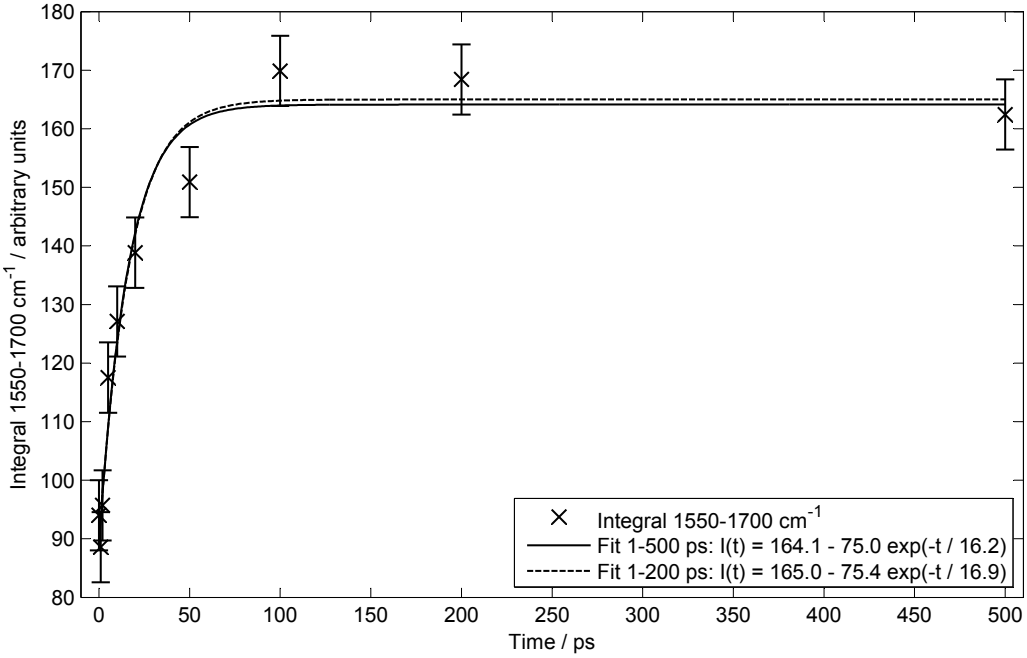

Fig. 8.6. Increase of dark state population following excitation to S_1 $6b^1 4^1 16b^1$.

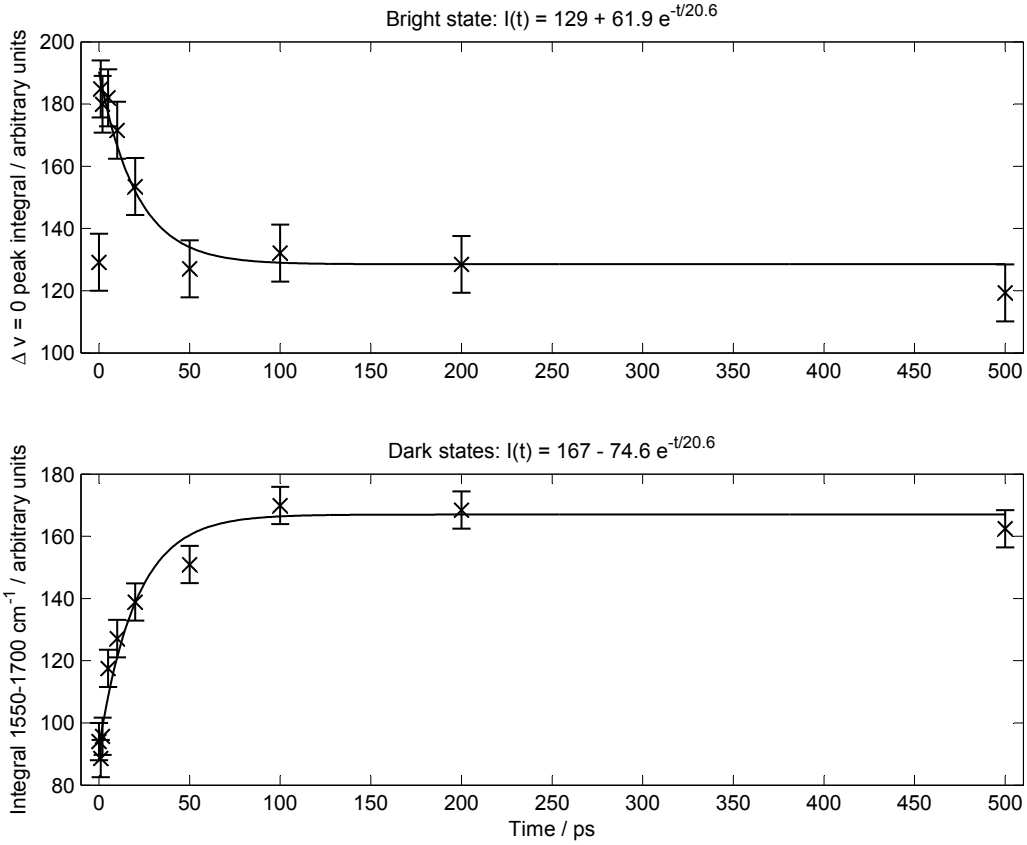

Fig. 8.7. Fit to bright and dark state populations as a function of time following excitation to S_1 $6b^1 4^1 16b^1$, using an averaged value for the IVR lifetime.

8.1.3. Time-resolved spectra via S_1 "$6b^1$ 1^1" level (0^0 + 1284 cm^{-1})

The time-resolved spectra obtained *via* the upper component of the Fermi resonance, "$6b^1 1^1$", are plotted in Fig. 8.8 and show a similar time dependence to that of $6b^1 4^1 16b^1$. Once again the intensity of the $\Delta v = 0$ peak ($\sim$1250 cm^{-1}) is anomalously low at 0 ps, possibly as a result of strong field effects.

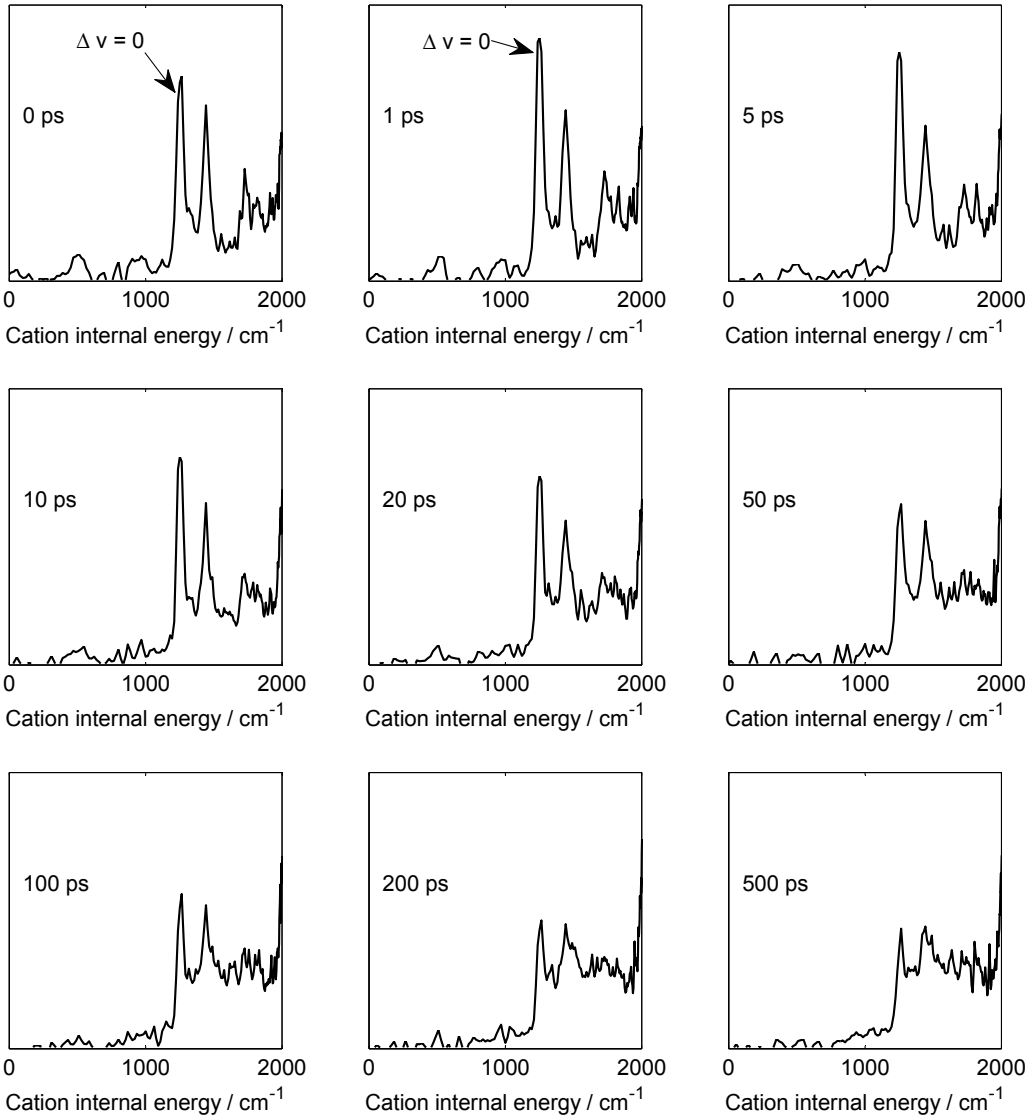

Fig. 8.8. Time-resolved two-colour VMI photoelectron spectra *via* S_1 $6b^1 1^1$, taken with a probe wavelength of 290 nm.

Trapezium rule integration of the $\Delta v = 0$ peak over the internal energy range 1200–1300 cm^{-1} gives an estimate of the population of the bright state as a function of time (see Fig. 8.9). As for $6a^1 4^1 16b^1$, the error bar is taken to be equal to the difference between the measured integrals at 200 and 500 ps. Two fits to Equation (8.1) are shown in Fig. 8.9, using the data points from 1–500 and 1–200 ps, giving IVR lifetimes of 44.7 and 32.4 ps respectively. The large difference between these two values indicates that the

fitted lifetime is very sensitive to the single data point at 500 ps, and so in future work it would be useful to repeat the experiment with measurements at several more time delays between 200 and 500 ps.

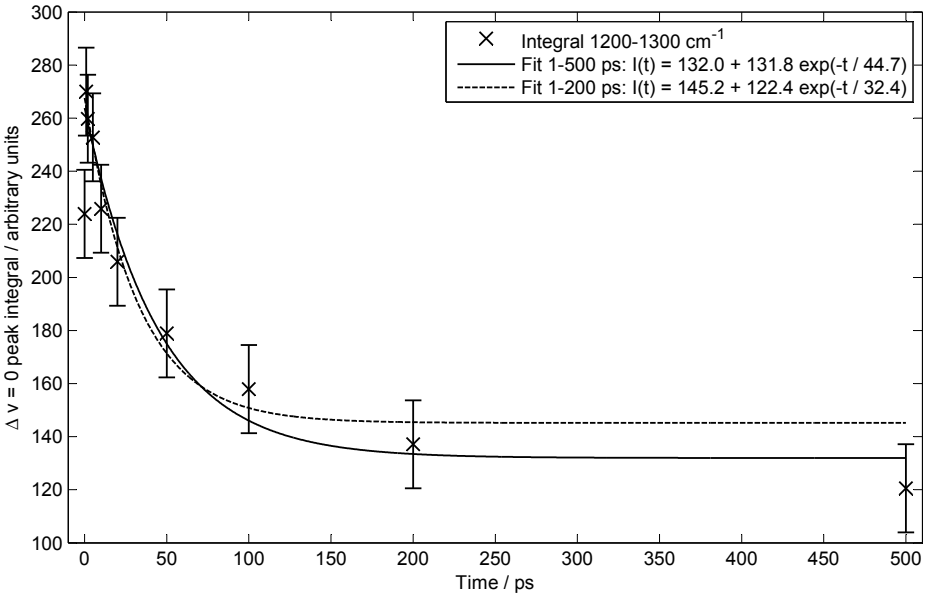

Fig. 8.9. Decay of bright state population following excitation to S_1 $6b^1 1^1$, with fits to Equation (8.1).

An estimate of the population of the dark states can be obtained from the integral over the internal energy range 1550–1670 cm^{-1}, where there are no peaks in the spectrum at 0 ps (see Fig. 8.8). The dark state population is plotted as a function of time in Fig. 8.10. Fitting the growth to Equation (8.1) yields an IVR lifetime of 34 ps, or 28 ps if the data point at 500 ps is excluded.

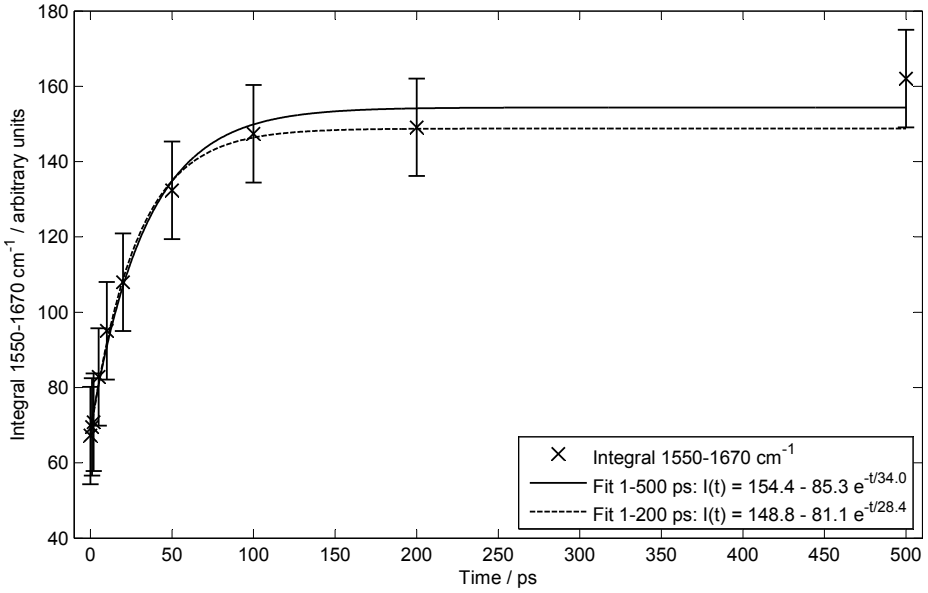

Fig. 8.10. Increase of dark state population following excitation to S_1 $6b^1 1^1$.

Taking the average of the values from the 0–500 ps fits to the bright and dark state populations, the best estimate that can be given for the IVR lifetime is 39 ± 11 ps. Using a fixed value of $\tau_{\mathrm{IVR}} = 39$ ps in Equation (8.1), acceptable fits to both the bright and dark state populations can be achieved (Fig. 8.11).

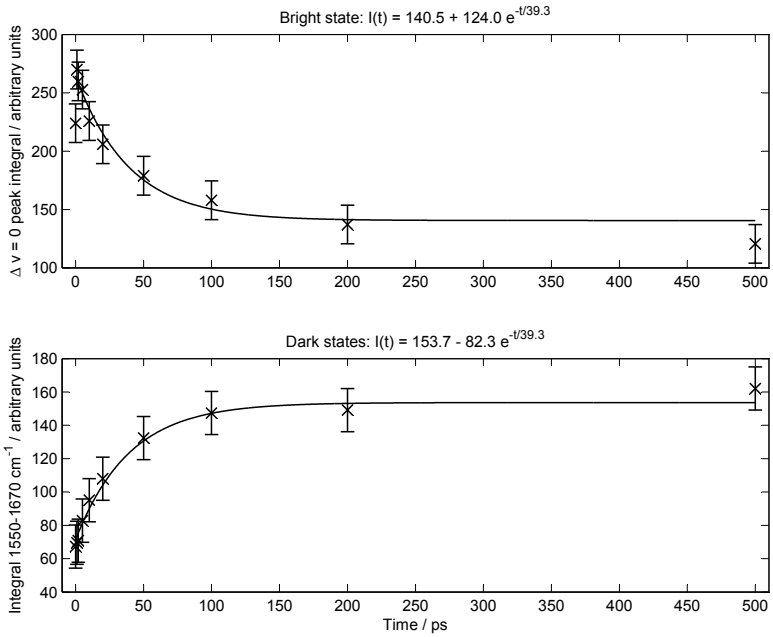

Fig. 8.11. Fit to bright and dark state populations as a function of time following excitation to S_1 $6b^1 1^1$, using an averaged value for the IVR lifetime.

8.2. S_1 $6b^1$ $18a^1$ level (0^0 + 1466 cm^{-1})

Fig. 8.12 shows a series of SEVI spectra recorded *via* S_1 $6b^1 18a^1$ in toluene at time delays of 0, 2, 5, 10, 20, 50, 100, 200 and 500 ps. These were produced by splicing together the spectra from images taken with probe wavelengths of 294, 290, 286 and 282 nm. Additionally, spectra were recorded with a single probe wavelength of 290 nm at 30 ps, 40 ps and 1–10 ps in 1 ps steps. As for the $6b^1$ $\left(1^1/4^1 16b^1\right)$ levels, the intensity of the $\Delta v = 0$ peak is weaker at 0 ps than at 2 ps, possibly due to strong field effects. Beyond 2 ps there is a gradual loss of structure and fall-off in the strength of the $\Delta v = 0$ peak due to dissipative IVR.

A series of images was also taken *via* the corresponding level in the deuterated isotopologue $C_6H_5CD_3$, with a fixed probe wavelength of 290 nm. Since modes $6b$ and $18a$ involve mainly motion of the benzene ring, deuteration of the methyl group does not alter the frequency of the $6b^1 18a^1$ level; nor is there any shift in the energies of the peaks in the photoelectron spectrum. Despite this, a difference is apparent in the rate of dissipative IVR. In Fig. 8.13 the intensity of the $\Delta v = 0$ peak, as measured by the Trapezium Rule

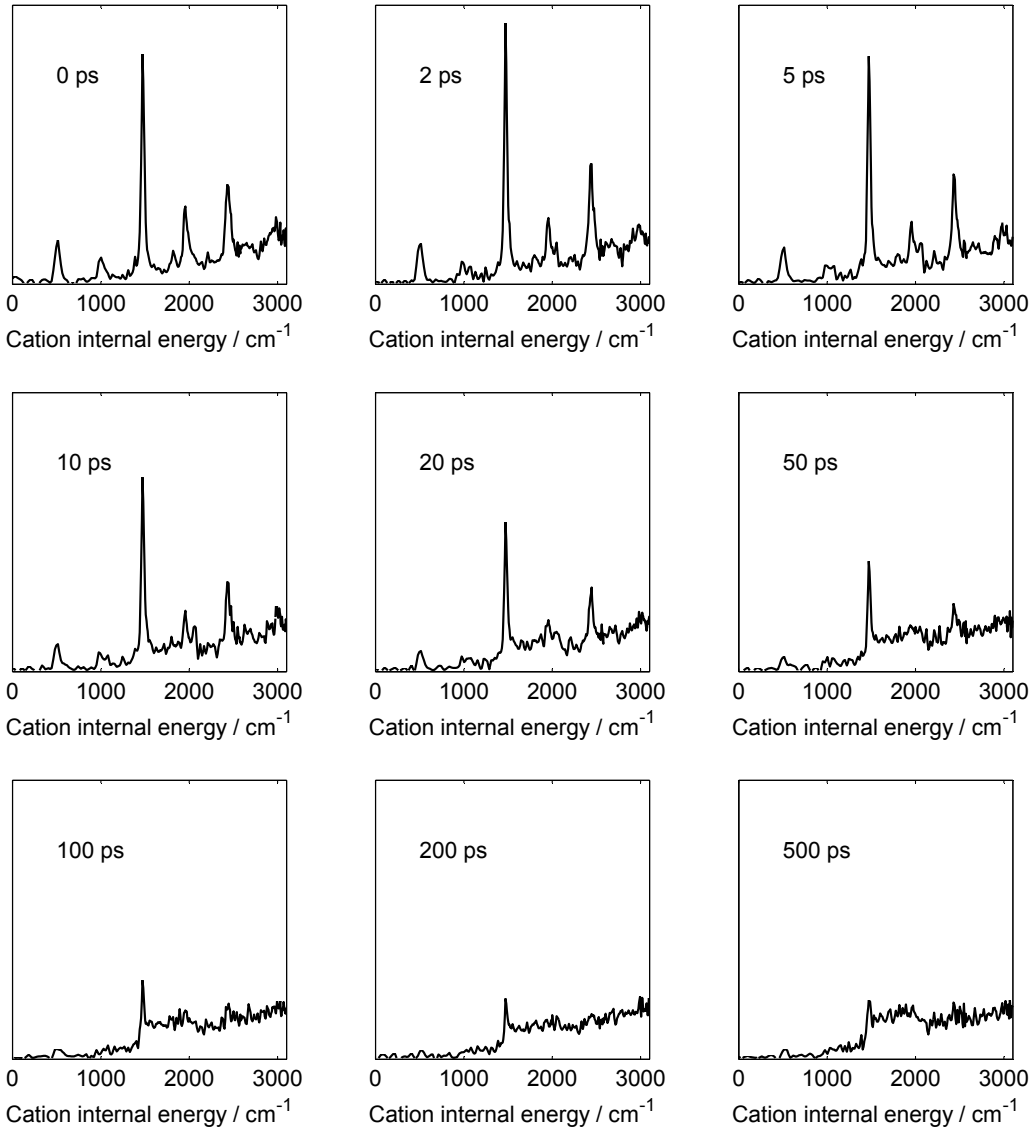

Fig. 8.12. Time-resolved SEVI spectra *via* S_1 $6b^1 18a^1$. These were produced by splicing together the spectra from images with probe wavelengths of 294, 290, 286 and 282 nm and have been normalised according to the integral from 0 to 3000 cm^{-1}.

integral over the internal energy range 1400–1550 cm^{-1}, is plotted as a function of time for the two isotopomers. Two separate images were recorded for $C_6H_5CD_3$ at 100 ps, and the difference between the measured integrals from these has been used to obtain an estimate for the size of the error bars. Fits to Equation (8.1) yield an IVR lifetime of 54 ps for $C_6H_5CD_3$, but only 38 ps for $C_6H_5CH_3$. Since more data points are available in the deuterated case, a fit was also performed using only those time delays at which spectra had been taken for $C_6H_5CH_3$. This is shown by the dotted line in Fig. 8.13b and gives $\tau_{IVR} \approx 48$ ps, suggesting that the fitted lifetimes are accurate to approximately ± 6 ps.

The SEVI spectrum at 0 ps contains a flat region adjacent to the $\Delta v = 0$ peak, between 1570 and 1870 cm^{-1} (see Fig. 8.12). Integration over this energy range gives an estimate of the rate of increase of the population of the dark vibrational states. Plots of the dark state population as a function of time are shown in Fig. 8.14, together with fits to Equation (8.1) which suggest IVR lifetimes of 32 and 50 ps for $C_6H_5CH_3$ and $C_6H_5CD_3$ respectively. Averaging these with the fitted values from the decay of the $\Delta v = 0$ peak gives best estimates for the IVR lifetimes of 35 ± 6 ps for $C_6H_5CH_3$, and 52 ± 6 ps for $C_6H_5CD_3$.

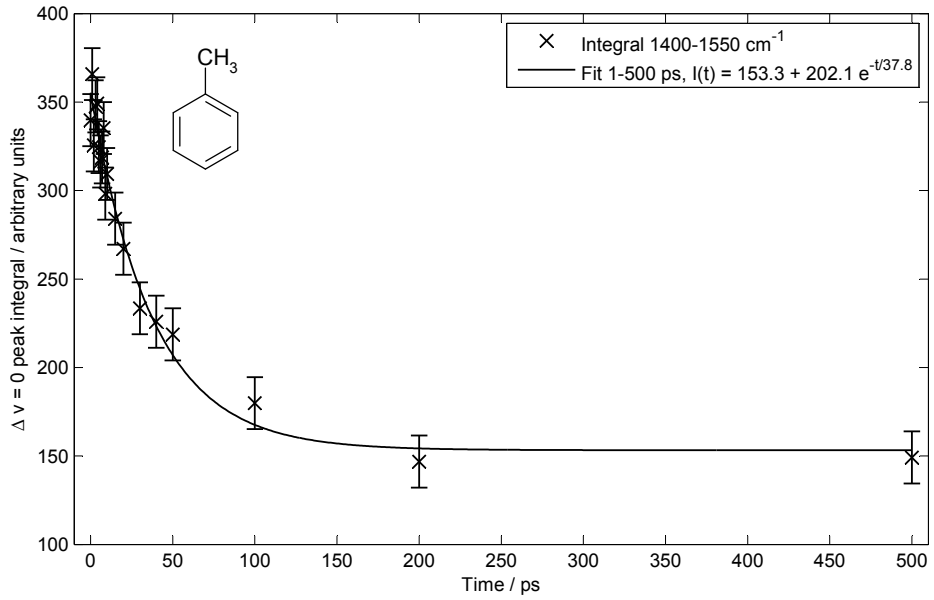

(a) $C_6H_5CH_3$.

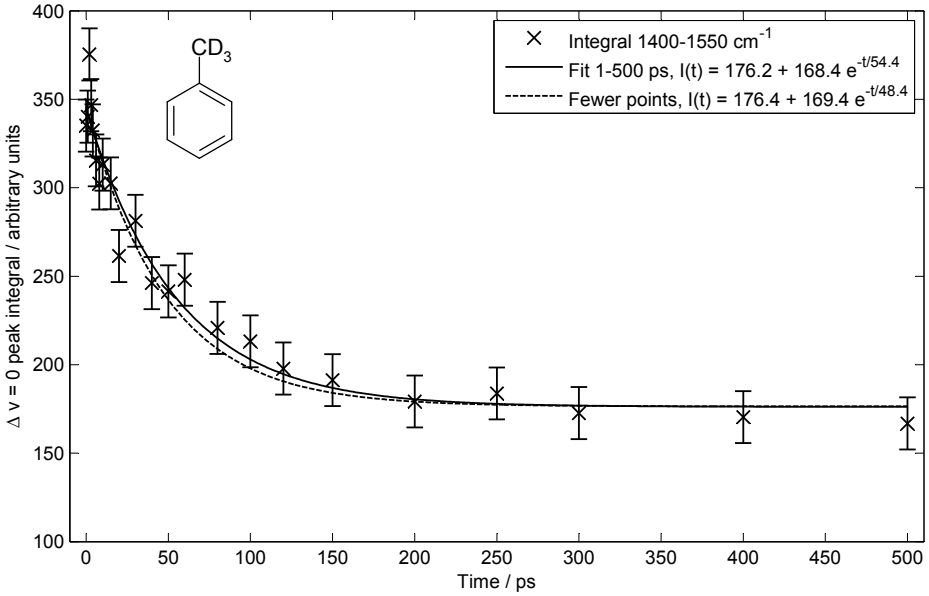

(b) $C_6H_5CD_3$. The solid line represents a fit using all data points except 0 ps. The dashed line is a fit using the same time delays as the fit for $C_6H_5CH_3$ shown above.

Fig. 8.13. Decay of bright state population following excitation to S_1 $6b^1 18a^1$, with fits to Equation (8.1). The integrals were measured from the spectra taken with a probe wavelength of 290 nm.

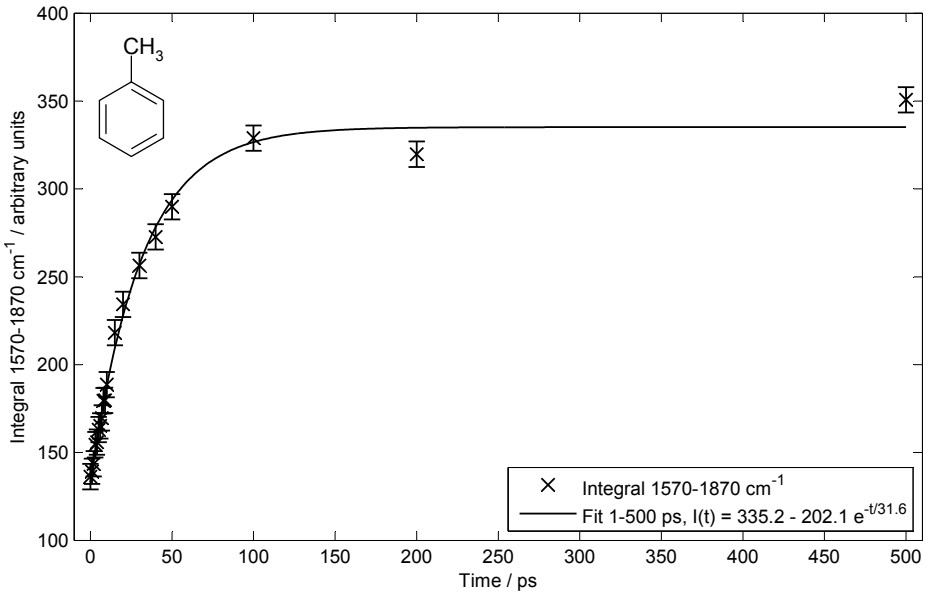

(a) $C_6H_5CH_3$.

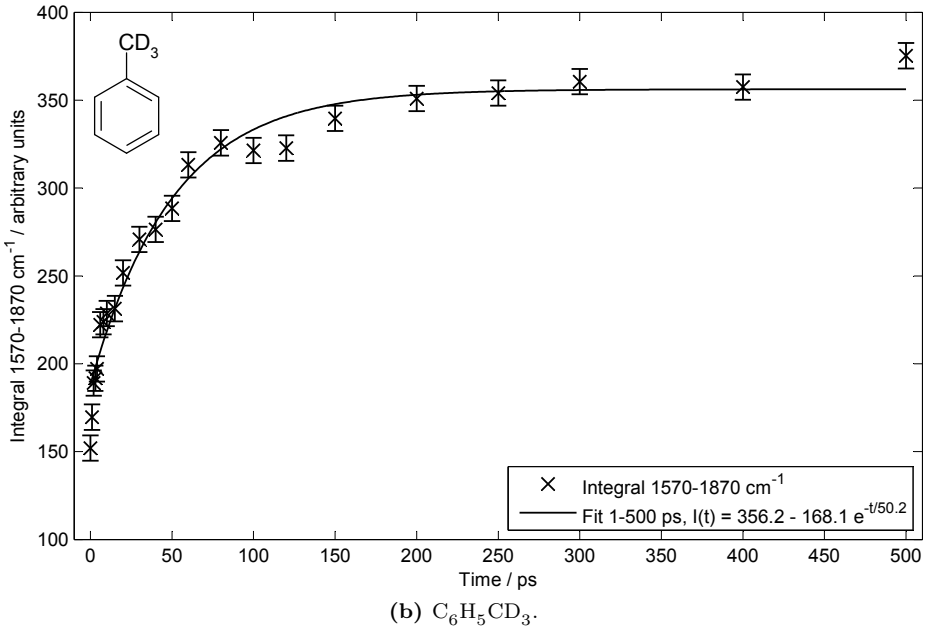

(b) $C_6H_5CD_3$.

Fig. 8.14. Increase of dark state population following excitation to S_1 $6b^1 18a^1$, with fits to Equation (8.1).

8.3. S_1 $6b^1$ 12^1 level (0^0 + 1494 cm^{-1})

Hickman *et al.* [63] tentatively assigned the S_1 vibrational level at 1494 cm^{-1} as a state resulting from a combination of ring-breathing modes, $6b^1 12^1$. However, they did not attempt to confirm this by dispersed fluorescence. All of the other levels above 1193 cm^{-1} had given unstructured fluorescence due to rapid IVR, suggesting that no useful information was likely to be gained from such an experiment.

In the present work, a series of time-resolved SEVI spectra has been obtained *via* the 1494 cm^{-1} level, using probe wavelengths of 294, 290, 286 and 282 nm. The SEVI spectrum at 0 ps is compared with a Franck-Condon simulation in Fig. 8.15. The simulation *via* $6b^1 12^1$ is reasonably consistent with the observed spectrum, although it is unable to account for the observed $(\Delta v = 0) + 18a^1$ peak at 2437 cm^{-1}. As discussed in Section 6.6 the calculated normal modes show extensive Duschinsky mixing of 12 and 18*a* between the S_1 electronic state and the ion, hence the dominance of the ion $18a^1$ peak in the Franck-Condon simulation.

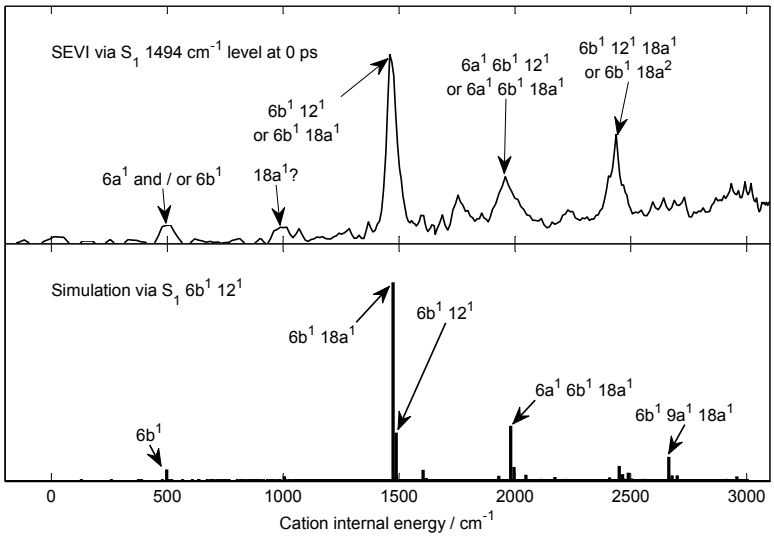

Fig. 8.15. Comparison of the SEVI spectrum at 0 ps with a Franck-Condon simulation via S_1 $6b^1 12^1$.

The time-resolved SEVI spectra are plotted in Fig. 8.16 and show behaviour characteristic of fairly rapid dissipative IVR, with no vibrational structure resolved beyond 100 ps. Fig. 8.17 shows the decay of the population of the bright state as a function of time, measured using the trapezium rule integral of the $\Delta v = 0$ peak over the range 1415–1530 cm^{-1}. Fits of the decay to Equation (8.1) indicate an IVR lifetime of approximately 18 ps, or 17 ps if the data point at 500 ps is excluded. Due to the dense vibrational structure present in the "bright state" spectrum at 0 ps, it is not straightforward to obtain an estimate of the rate of increase of dark state population for comparison. However, the

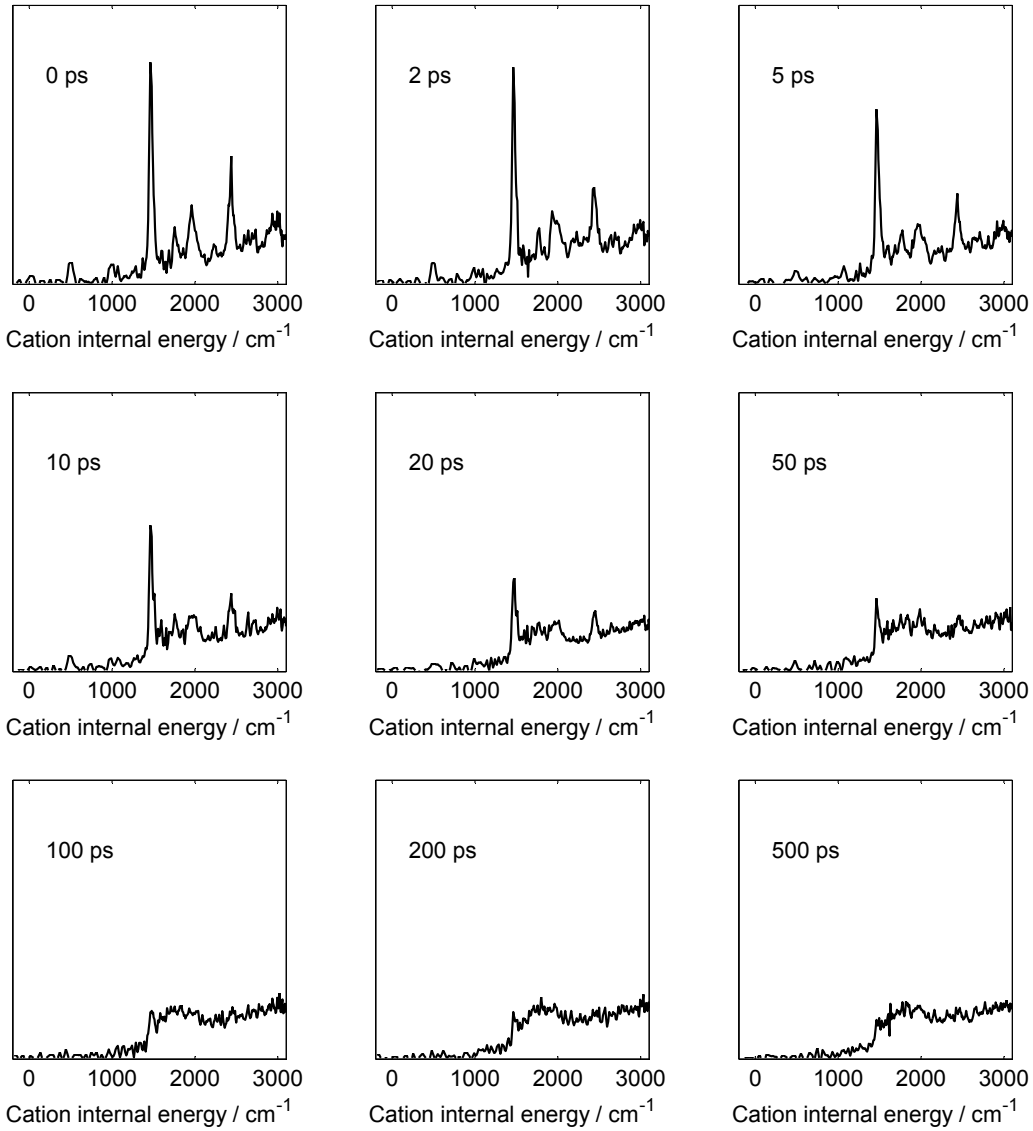

Fig. 8.16. Time-resolved SEVI spectra via the S_1 $6b^1 12^1$ level in toluene. These were produced by splicing together the spectra from images taken with probe wavelengths of 294, 290, 286 and 282 nm, and are normalised by the integral from 0 to 3000 cm^{-1}.

results from the other vibrational levels suggest that an error bar on the fitted lifetimes of roughly ±6 ps would be reasonable.

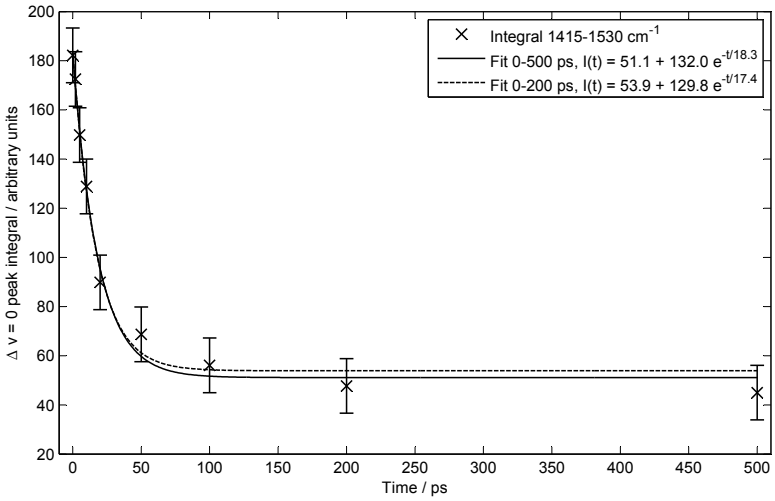

Fig. 8.17. Decay of bright state population following excitation to S_1 $6b^1 12^1$.

8.4. Discussion

In all of the time-resolved photoelectron spectra presented in this chapter, a loss of structure is seen as the pump-probe time delay is increased and the $\Delta v = 0$ peak, which corresponds to ionisation from the initially-prepared state, shows an exponential decay of intensity. This is indicative of irreversible, dissipative IVR and is the type of behaviour predicted in the statistical limit by Fermi's Golden Rule (see Section 2.5). A key question, then, is whether or not the different IVR lifetimes observed in this work can be simply rationalised by Equation (2.3). If the initially prepared states have roughly equal couplings to many different dark states, then we would expect the IVR rate constant to be directly proportional to the density of states. Conversely, if the IVR rate is not simply correlated with the density of states, then that would suggest a mechanism proceeding *via* a few particular doorway states that are strongly coupled to the initial state (see Section 2.6).

If an approximate C_{2v} point group is used, then all four vibrational levels examined in this chapter transform as B_2 and they should only be able to couple anharmonically to dark states which have the same symmetry. A search was therefore undertaken, using the backtracking algorithm described in Section 5.3.2, to find the number of states with B_2 symmetry that exist within ± 15 cm^{-1} of each of the initially prepared states (see Table 8.1). Since significant couplings are not expected between states with very different total numbers of vibrational quanta, Table 8.1 also lists separately the number

of B_2 states with three or fewer quanta for each energy range.

Table 8.1. Comparison of IVR rates with number of potential doorway states, *i.e.* the number of states with B_2 symmetry which lie within ± 15 cm^{-1} of the bright state. The rate constant is given by $k_{\mathrm{IVR}} \equiv 1/\tau_{\mathrm{IVR}}$.

State	Energy / cm^{-1}	Potential doorway states: Total	≤ 3 quanta	τ_{IVR} / ps	k_{IVR} / 10^{-2} ps^{-1}
$6b^1 4^1 16b^1$	1263	63	34	20 ± 5	5.3 ± 1.3
$6b^1 1^1$	1284	70	33	39 ± 11	2.8 ± 0.8
$6b^1 18a^1$ ($C_6H_5CH_3$)	1466	129	53	35 ± 6	2.9 ± 0.5
$6b^1 18a^1$ ($C_6H_5CD_3$)	1466	191	63	52 ± 6	1.9 ± 0.2
$6b^1 12^1$	1494	128	44	18 ± 6	6.3 ± 2.1

Examination of Table 8.1 does not reveal any simple relationship between the IVR rate constant and the calculated number of states available for coupling. It is therefore likely that only a subset of these candidate doorway states actually have a significant coupling strength to the bright state, and so the most important factor governing the IVR rate is the nature of the vibrational motion that is initially prepared.

The result for $6b^1 18a^1$ in $C_6H_5CD_3$ is especially interesting, since this level shows the slowest IVR rate despite having the highest density of states. In particular, the IVR lifetime appears to be longer than that of the same vibrational level in $C_6H_5CH_3$, even though the frequency of $6b^1 18a^1$ is the same in both isotopomers and the initially-prepared vibration is localised in the benzene ring. This suggests that the IVR mechanism might proceed *via* a doorway state which involves motion of the methyl group.

8.5. Conclusions

Picosecond time-resolved photoelectron spectra recorded *via* four different vibrational levels in S_1 toluene have shown evidence of dissipative IVR. Integration of the $\Delta v = 0$ peak in each spectrum gives an estimate of the population remaining in the bright state as a function of time. In each case, from 1 ps onwards the decay of the bright state population is exponential, with a time constant that serves as a measure of the rate of IVR. Anomalies were seen in the apparent bright state population at 0 ps, *i.e.* when the pump and probe pulses were overlapped in time. A possible explanation may lie in strong field effects brought about by the high light intensity. This hypothesis could in principle be tested by examining the effect on the spectrum of varying the probe laser power.

The observed IVR lifetimes do not show a regular dependence upon either the vibrational energy or the density of vibrational states. This result suggests that the initially-

prepared vibrational states do not have roughly equal couplings to a large number of dark states; instead IVR proceeds *via* particular doorway states which are strongly coupled to the bright state. Consequently, the most important factor determining the IVR rate is the nature of the vibrational motion that is excited by the pump laser. In the case of $6b^1 18a^1$, deuteration of the methyl group has been shown to slow the rate of IVR, even though the vibration initially involves motion mainly of the benzene ring. Motion of the methyl group must therefore be involved in the doorway state that leads to IVR. In future it would be interesting to examine the effect of deuteration on the rate of IVR from the $6b^1$ $\left(4^1 16b^1/1^1\right)$ and $6b^1 12^1$ levels.

The error bars on the fitted IVR lifetimes are unfortunately rather large (see Table 8.1). This uncertainty arises due to the small number of data points at long pump-probe time delays, and in future work it would be useful to obtain spectra at several more time delays between 100 and 500 ps. A further improvement would be to record more than one spectrum for each time delay, allowing the determination of more accurate values for the error bars on the measured bright and dark state populations.

9. IVR in the intermediate regime

The preceding two chapters have examined the limiting cases of IVR behaviour. In Chapter 7 a system of three coupled vibrational levels was investigated, displaying restricted IVR. Recurrences were seen in the time-resolved photoelectron spectra as the vibrational wavepacket oscillated amongst the coupled zero-order states, and the spectra retained well-defined vibrational structure even after 500 ps. At the other end of the scale, the S_1 vibrational levels studied in Chapter 8 exhibited dissipative IVR: population flowed irreversibly from the initially prepared bright state into many different dark states, leading to a progressive loss of structure in the photoelectron spectra over time.

An interesting intermediate case occurs when the zero-order bright state is coupled initially to a small number of dark states, but one or more of those then acts as a "doorway" allowing the molecule to access many more dark states. This chapter will examine two examples of *intermediate IVR* which have been encountered in the present work.

9.1. A C−CH_3 stretch in toluene: 13^1

The 13^1 vibrational level in S_1 toluene is mainly a stretch of the C−CH_3 bond, but also involves some in-plane distortion of the benzene ring (Fig. 9.1). In a study of the fluorescence excitation spectrum of toluene, Hickman *et al.* [63] assigned this level to an absorption feature at 1193 cm^{-1} above the S_1 origin.[1] These authors also obtained a dispersed fluorescence spectrum from 13^1 and found it to be congested, indicating that extensive IVR was taking place.

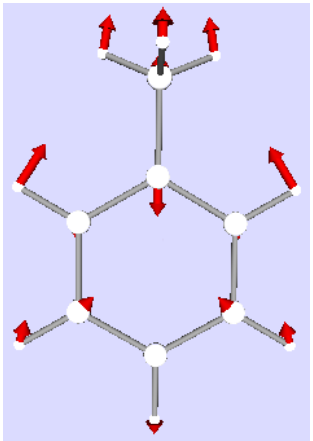

Fig. 9.1. S_1 mode 13.

Whiteside *et al.* [52, 53] were the first to obtain time-of-flight photoelectron spectra *via* the S_1 13^1 level. When nanosecond laser pulses were used to excite and ionise, no structure could be discerned in the spectrum. Some structure was recovered using picosecond pump and probe pulses overlapped in time, but this rapidly disappeared as the

[1] The assignment is given here in Varsányi notation [65], and corresponds to 8^1 in the Mulliken numbering scheme used by Hickman *et al.* [63].

time delay between the pump and probe pulses was increased. After 10 ps, no distinct peaks remained and so it appeared that complete dissipative IVR had taken place.

In a follow-up study, Hammond and Reid [13, 58] showed that vibrational structure could be partially resolved in the nanosecond photoelectron spectrum via 13^1 by using SEVI instead of time of flight detection. A series of time-resolved photoelectron images was also recorded, using picosecond laser pulses and a one-colour ionisation scheme. As in the earlier time-of-flight experiments, a rapid loss of structure was seen with increasing time delay. After just two picoseconds, no peaks could be discerned in the VMI spectra.

In the present work, the nano- and picosecond photoelectron spectra *via* 13^1 have been revisited with higher resolution techniques. By using SEVI instead of one-colour VMI, structure is retained in the picosecond spectra at much longer time delays than in the previous work, allowing quantum beats to be observed for the first time. With nanosecond laser pulses, ZEKE photoelectron spectroscopy is employed to achieve even greater resolution.

9.1.1. Nanosecond REMPI and ZEKE studies

Hickman *et al.* [63] noted that the 13^1 band in their fluorescence excitation spectrum appeared to contain two or three overlapped transitions. In this work, a nanosecond REMPI spectrum has been used to characterise the S_1 vibrational levels (see Fig. 9.2). Three distinct peaks are resolved at 1198, 1193 and 1185 cm^{-1}, which will be denoted as $|1\rangle$, $|2\rangle$ and $|3\rangle$ respectively.

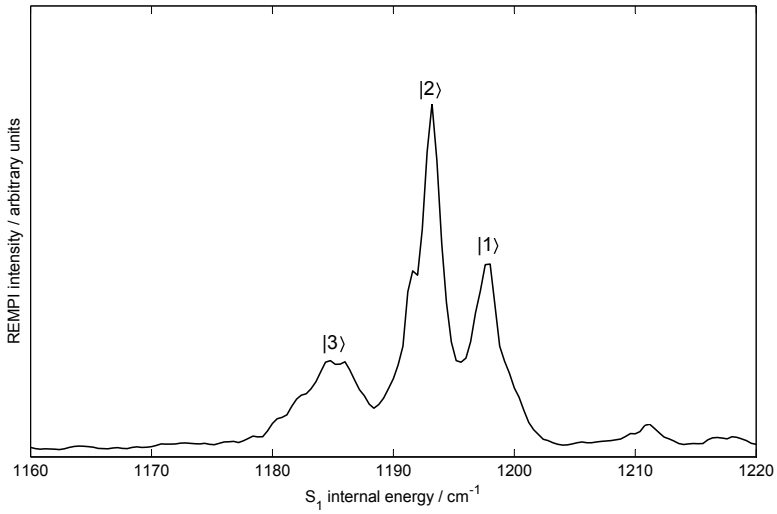

Fig. 9.2. Nanosecond REMPI spectrum of toluene in the vicinity of S_1 13^1.

Nanosecond ZEKE spectra were recorded *via* levels $|1\rangle$ and $|2\rangle$, although unfortunately no ZEKE signal could be observed following excitation to level $|3\rangle$. The two

ZEKE spectra are compared with a Franck-Condon simulation *via* S_1 13^1 in Fig. 9.3. Both experimental spectra show a strong ion 13^1 peak, suggesting that this zero-order state makes a significant contribution to at least two different vibrational eigenstates in S_1. Other peaks are also present which cannot be accounted for by the Franck-Condon simulation, providing further evidence that 13^1 is significantly coupled to at least one other zero-order state. Although the peaks themselves are sharp and well-resolved, they are superimposed upon a broad, unstructured 'hump' which may be attributed to the effects of IVR. This is in contrast to the ZEKE spectrum via S_1 13^1 in the closely-related molecule *para*-fluorotoluene [96], which showed an almost flat baseline and no direct evidence of IVR.

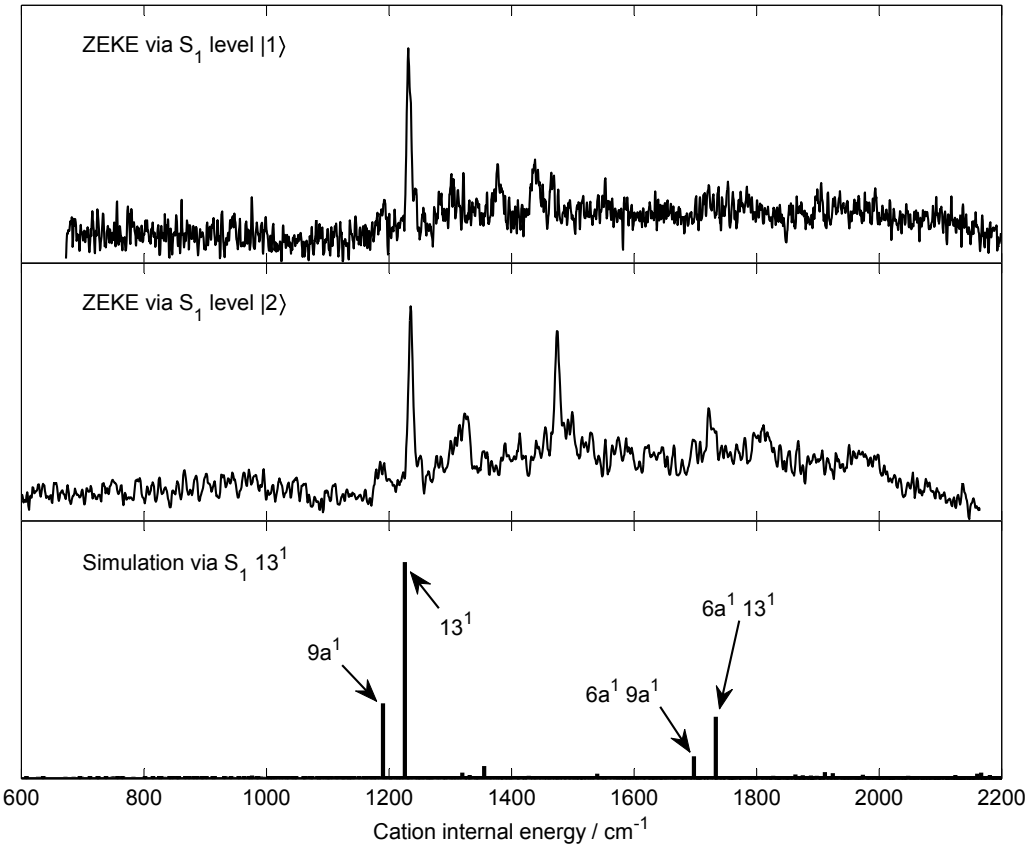

Fig. 9.3. Nanosecond ZEKE spectra via two S_1 vibrational levels in the vicinity of 13^1, compared with a Franck-Condon simulation via 13^1.

9.1.2. Picosecond time-resolved SEVI spectra

Photoelectron images were recorded via the S_1 13^1 level using probe laser wavelengths of 294.36, 290.31 and 286.31 nm, for pump-probe time delays of 0–20 ps in 1 ps steps, and also at 30, 50, 100, 200 and 500 ps. The resulting SEVI spectra are shown in Fig. 9.4 for time delays of 0–6 ps, and Fig. 9.5 for selected longer time delays. Initially oscillatory behaviour is seen, similar to that observed in Chapter 7 following coherent excitation of

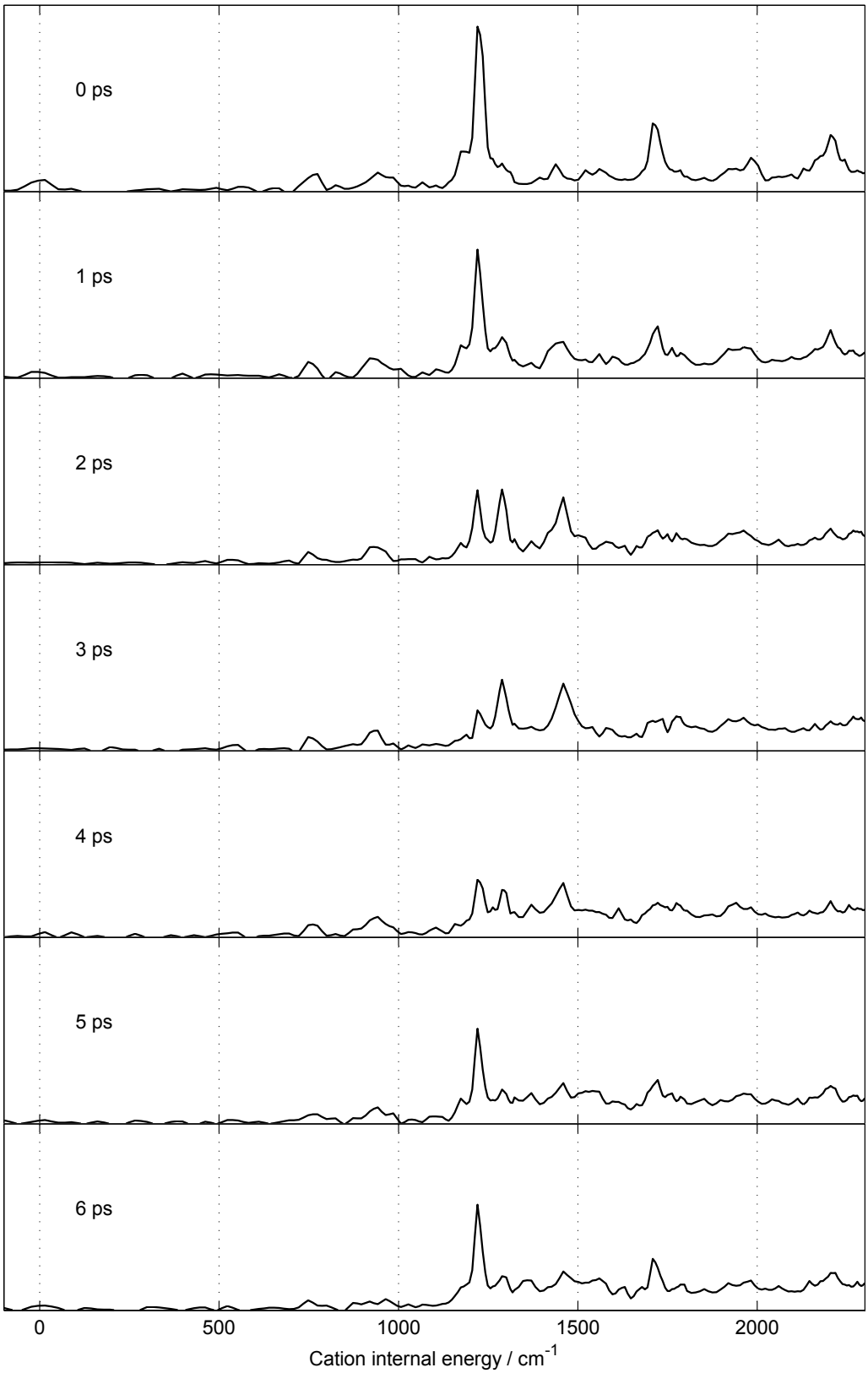

Fig. 9.4. Picosecond SEVI spectra via S_1 13^1 at short time delays.

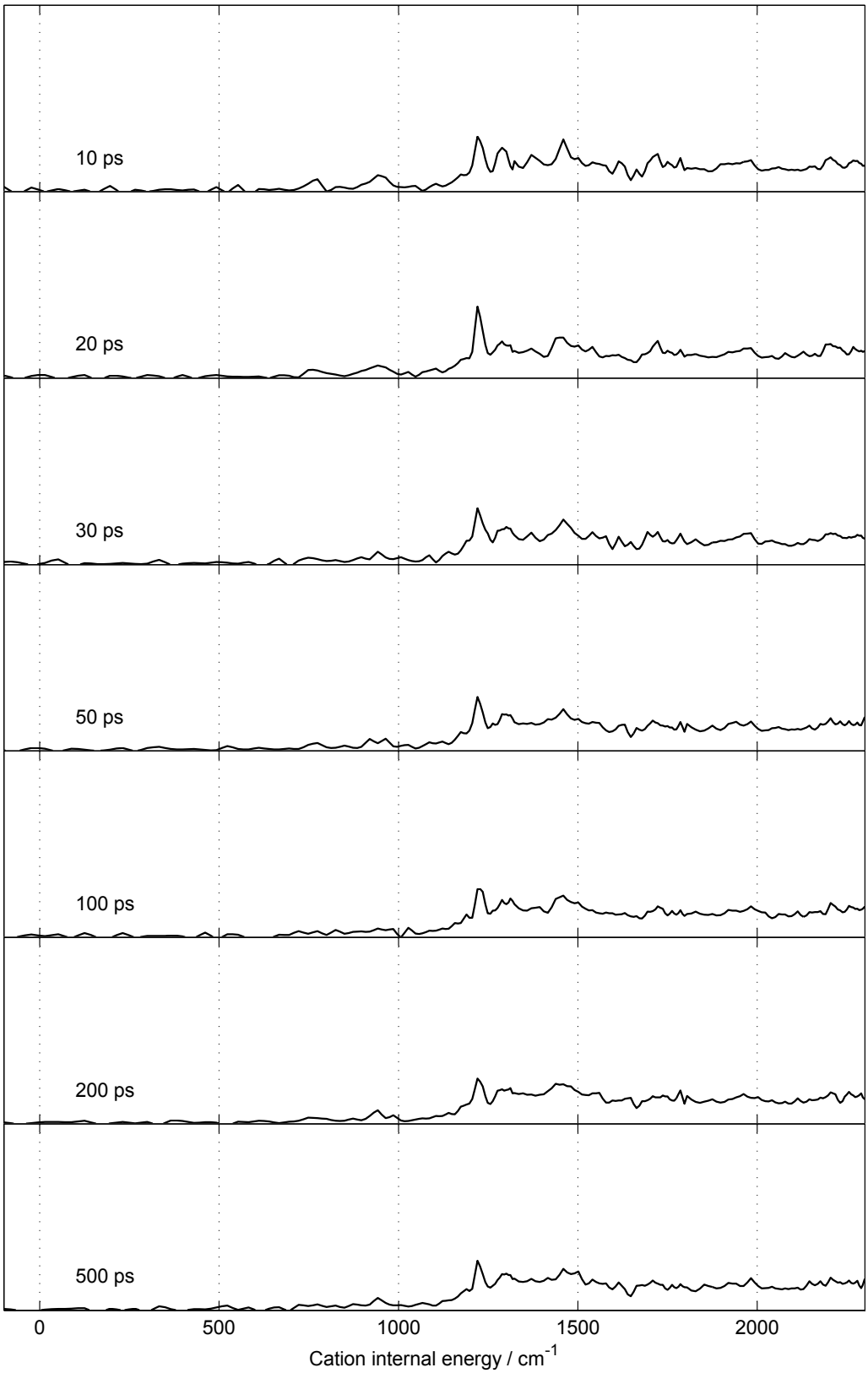

Fig. 9.5. Picosecond SEVI spectra via S_1 13^1 at long time delays.

the S_1 $16a^2$ / $6a^1$ / $10b^1 16b^1$ levels. Over the first 3 ps, two peaks grow in at 1289 and 1460 cm^{-1}, which correspond to ionisation from a "dark" vibrational state. Meanwhile the intensity of the 13^1 peak decreases, indicating loss of population from the zero-order bright state. Between 3 and 6 ps, the opposite trend is observed. By 6 ps the spectrum is similar to that at 0 ps, except for a slightly higher baseline and a correspondingly smaller 13^1 peak. At longer time delays the portion of the SEVI spectrum above ~1250 cm^{-1} internal energy becomes increasingly congested, with little structure discernible beyond 50 ps. This would suggest that vibrational energy has been transferred into a "bath" of many different dark states. Nonetheless the 13^1 peak remains visible even after 500 ps, indicating that complete dissipative IVR has not been achieved.

An estimate of the population of the 13^1 zero-order bright state may be obtained by using the Trapezium Rule to integrate the $\Delta v = 0$ peak over the internal energy range 1200–1260 cm^{-1}. When the population is plotted as a function of time, a clear pattern of quantum beats is revealed over the first 20 ps (see Fig. 9.6). These can be modelled empirically using an exponentially decaying cosine wave superimposed upon an overall exponential decay of population:

$$I(t) = A + Be^{-t/\tau_1} + Ce^{-t/\tau_2}\cos(\omega t)\,. \tag{9.1}$$

A non-linear least-squares fitting routine in Matlab was used to fit the oscillations to Equation (9.1), yielding decay lifetimes $\tau_1 = 19.9$ ps and $\tau_2 = 4.6$ ps. The fitted oscillation frequency, $\omega = 0.975$ rad $ps^{-1} \equiv 5.2\,cm^{-1}$, matches the observed energy spacing of vibrational levels $|1\rangle$ and $|2\rangle$ in the nanosecond REMPI spectrum (Fig. 9.2).

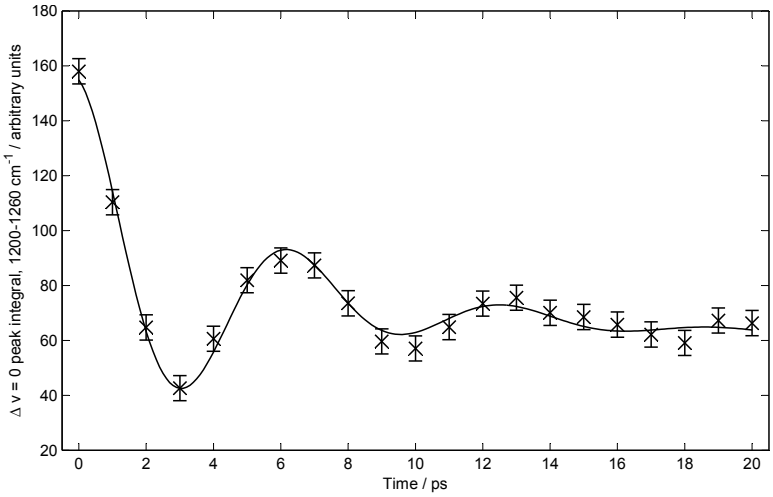

Fig. 9.6. Bright state population as a function of time, with fit to Equation (9.1). The population is estimated using the integral from 1200–1260 cm^{-1}, calculated by the Trapezium Rule. Error bars are equal to the range of measured integrals for six images taken at 0 ps.

Two other peaks, from 1260–1320 and 1400–1530 cm^{-1}, reveal the population of the "doorway" states as a function of time (see Fig. 9.7). Attempts to model their oscillations with Equation (9.1) were unsuccessful; however a much better fit can be achieved by adding a second cosine term:

$$I(t) = A + Be^{-t/\tau_1} + e^{-t/\tau_2}\left[C\cos(\omega_1 t) + D\cos(\omega_2 t)\right]. \tag{9.2}$$

In contrast to the 13^1 bright state, which has an overall exponential decay of population, the dark states can be expected to have an *increase* in population over the first few picoseconds, leading to a negative value for the coefficient B. In fitting the oscillation patterns to Equation (9.2), the frequency ω_1 was held fixed to the value of $0.975\,\mathrm{rad\,ps^{-1}}$ determined for the bright state peak. The resulting fitted values for ω_2 were $1.272\,\mathrm{rad\,ps^{-1}} \equiv 6.8\,\mathrm{cm^{-1}}$ and $1.313\,\mathrm{rad\,ps^{-1}} \equiv 7.0\,\mathrm{cm^{-1}}$ for the 1260–1320 and 1400–1530 cm^{-1} peaks respectively. These values are both consistent with the observed energy spacing between S_1 vibrational levels $|2\rangle$ and $|3\rangle$. In Fig. 9.7 the beat patterns of all three peaks have been fitted to Equation (9.2), with ω_2 fixed to the average of these two values. The other fitted parameters are listed in Table 9.1. From the coefficients C and D, it can be seen that the 1260–1320 cm^{-1} peak is the most sensitive to ω_2, whereas the 13^1 peak (1200–1260 cm^{-1}) has a negligible contribution from this frequency component. It therefore appears that the bright state coupled more strongly to one doorway state than to the other.

Table 9.1. Parameters given by fit of peak oscillations to Equation (9.2), with $\omega_1 = 0.975\ \mathrm{rad\,ps^{-1}} = 5.2\,\mathrm{cm^{-1}}$ and $\omega_2 = 1.293\ \mathrm{rad\,ps^{-1}} = 6.9\,\mathrm{cm^{-1}}$.

Peak range / cm^{-1}	A	B	C	D	τ_1 / ps	τ_2 / ps
1200–1260	51.3	32.8	66.3	4.5	19.2	5.0
1260–1320	55.0	0.0	-10.5	-12.7	—	14.7
1400–1530	116.0	-9.9	-35.2	-15.3	10.0	6.8

9.1.3. Assignment of the "doorway" state

Examination of the time-resolved SEVI spectra plotted in Fig. 9.4 shows that the contribution of the "doorway" vibrational state must be greatest at 3 ps, since the intensity of the $\Delta v = 0$ peak is minimised and the two "dark state" peaks at 1289 and 1461 cm^{-1} are maximised. A small contribution from the 13^1 bright state nonetheless remains. For the purposes of analysis, this can be removed by making the approximation that the spectrum at 0 ps represents the pure bright state, and scaling it appropriately to match the intensity of the 13^1 peak at 3 ps (see Fig. 9.8a). Subtraction of this scaled bright

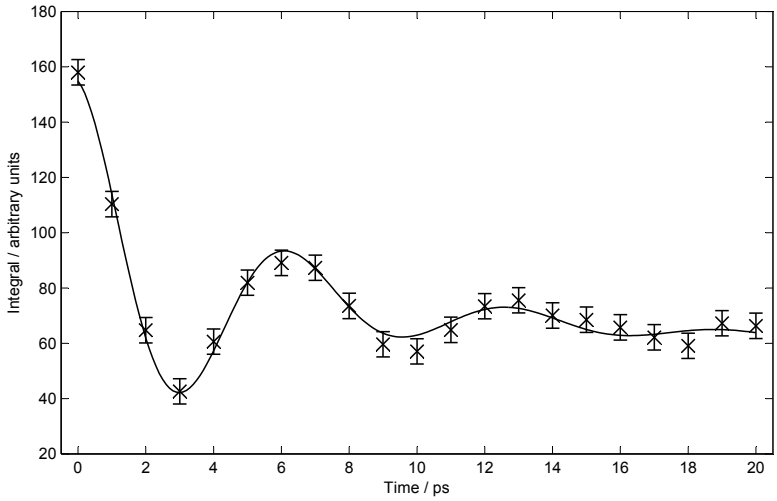

(a) Bright state, 1200–1260 cm^{-1}.

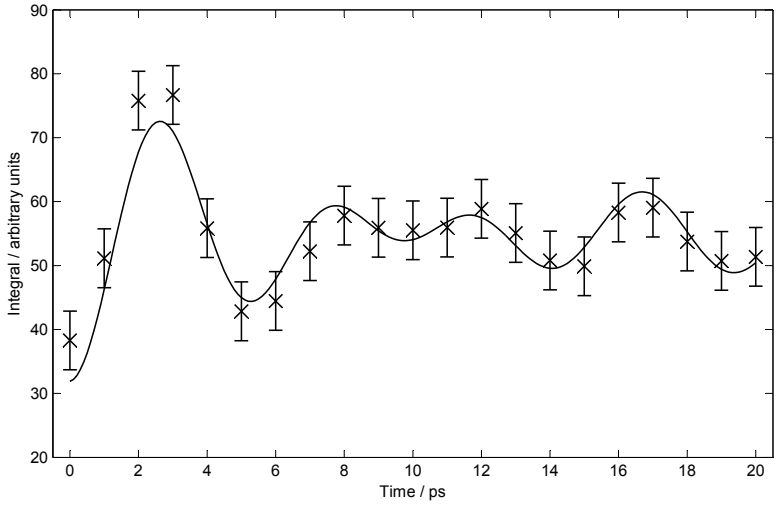

(b) Dark state, 1260–1320 cm^{-1}.

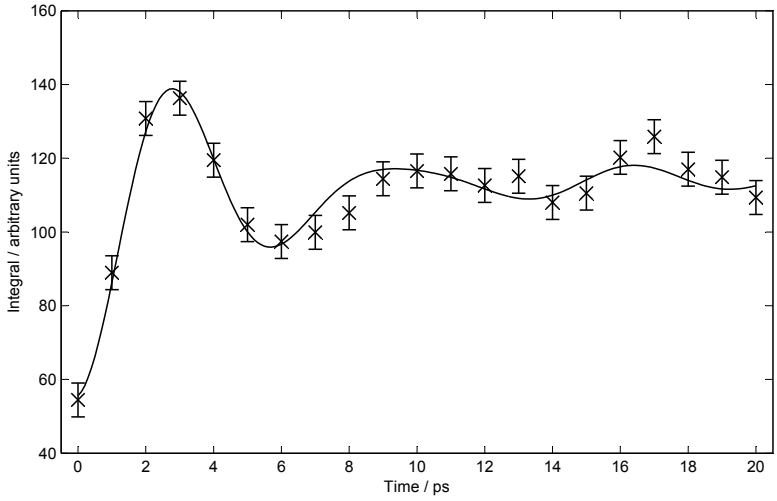

(c) Dark state, 1400–1530 cm^{-1}.

Fig. 9.7. Fits of peak oscillations to Equation (9.2), with $\omega_1 = 0.975\ \text{rad}\,\text{ps}^{-1} = 5.2\,\text{cm}^{-1}$ and $\omega_2 = 1.293\ \text{rad}\,\text{ps}^{-1} = 6.9\,\text{cm}^{-1}$. All error bars are equal to the range of measured bright state integrals for six images taken at 0 ps.

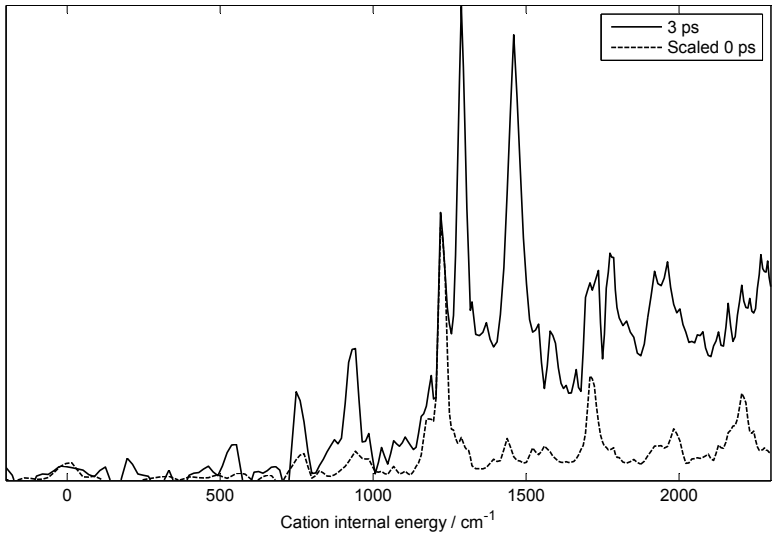

(a) SEVI spectrum at 3 ps, with 0 ps spectrum scaled to match intensity of the ion 13^1 peak.

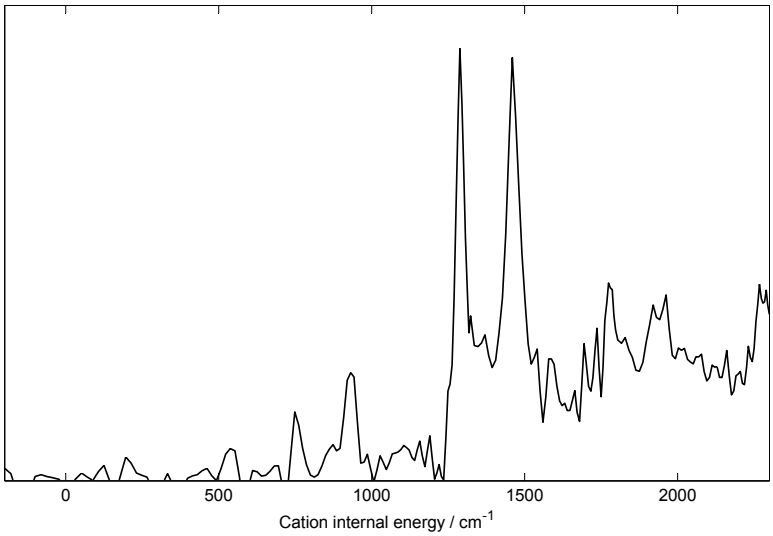

(b) Result of subtraction to give the photoelectron spectrum from the "doorway" state.

Fig. 9.8. Isolation of the photoelectron spectrum from the "doorway" vibrational state.

state spectrum from the spectrum at 3 ps leaves behind only those features which act as a "fingerprint" for the doorway vibrational state (Fig. 9.8b).

The backtracking algorithm described in Section 5.3.2 can be used to identify possible candidates for the identity of the doorway states. These states must have an energy within approximately ± 15 cm^{-1} of the S_1 13^1 vibrational level in order for their associated eigenstates to be coherently excited by the pump laser. The corresponding cation frequencies should match at least one of the peaks seen in the "doorway state" SEVI spectrum of Fig. 9.8. Assuming an approximate C_{2v} point group for the toluene molecule, the doorway state must be of A_1 symmetry in order to couple to 13^1 through anharmonicity. Significant coupling is only expected for a relatively small change in the

total number of vibrational quanta, and so only states with three or fewer quanta will be considered.

The S_1 frequencies for use in the backtracking algorithm were taken from the TD-B3LYP / aug-cc-pVTZ calculation with a scaling factor of 0.97 (see Section 5.1.2 and Table 5.3). The experimental values of Hickman *et al.* [63] were used in place of the calculated values, where available. Vibrational levels within $\pm 25\ \mathrm{cm}^{-1}$ of S_1 13^1 were accepted as plausible candidates. This frequency range was chosen to be greater than the bandwidth of the pump laser ($\sim 15\,\mathrm{cm}^{-1}$) because the calculated S_1 frequencies are typically in error by $\sim 10\,\mathrm{cm}^{-1}$.

Cation frequencies were taken from the ZEKE experiments where available (see Chapter 6), with the remaining frequencies given by the anharmonic B3LYP / aug-cc-pVTZ calculation (Table 5.2). States with ion frequencies in the ranges 1200–1350 and 1400–1550 cm^{-1} were accepted as plausible candidates for the two "doorway state" peaks seen in Fig. 9.8. The states meeting all of the criteria for coupling to $|13^1, m = 0\rangle$ are listed in Table 9.2, and those which could potentially couple to $|13^1, m = 1\rangle$ are given in Table 9.3.

Table 9.2. List of vibrational states with suitable energy and symmetry for coupling to $|13^1, m = 0\rangle$.

(a) Candidates for the dark state peak at $\sim 1290\,\mathrm{cm}^{-1}$.

Quanta	State	S_1 energy / cm^{-1}	Ion energy / cm^{-1}
1	13^1	1193	1235
2	$1^1 6a^1$	1202	1260
	$16a^1\delta_{\mathrm{as}}^{-1}, m = 3$	1203	1338
3	$1^1 10b^1 16a^1, m = 3$	1178	1280

(b) Candidates for the dark state peak at $1475\,\mathrm{cm}^{-1}$.

Quanta	State	S_1 energy / cm^{-1}	Ion energy / cm^{-1}
2	$15^1 17b^1, m = 6$	1218	1465
	$6a^1 10a^1, m = 6$	1210	1468
	$6a^1 17b^1, m = 3$	1200	1476
	$16b^1 17b^1, m = 6$	1206	1501
	$4^1 11^1, m = 6$	1195	1505
3	$4^1 15^1 16a^1, m = 6$	1174	1433
	$4^1 16b^1 6a^1$	1200	1436
	$1^1 16a^2$	1201	1438
	$10b^2 17a^1, m = 6$	1192	1459
	$10b^1 15^1 17a^1$	1176	1478
	$4^1 10b^1 11^1, m = 3$	1209	1492
	$10a^1 15^1 16b^1$	1214	1499
	$10a^1 15^1 16a^1, m = 3$	1170	1507

Having thus obtained a shortlist of potential doorway states, a series of Franck-Condon simulations were performed and compared with the observed doorway state spectrum.

Table 9.3. List of vibrational states with suitable energy and symmetry for coupling to $|13^1, m = 1\rangle$.

(a) Candidates for the dark state peak at $\sim$1290 cm^{-1}.

Quanta	State	S_1 energy / cm^{-1}	Ion energy / cm^{-1}
1	$18a^1, m = 7$	1195	1238
2	$6a^2, m = 7$	1174	1248
	$1^1 6a^1, m = 1$	1207	1265
3	$6b^1 10b^1 16a^1, m = 7$	1177	1211
	$6a^1 10b^1 16b^1, m = 7$	1194	1260

(b) Candidates for the dark state peak at 1475 cm^{-1}.

Quanta	State	S_1 energy / cm^{-1}	Ion energy / cm^{-1}
2	$5^1 10b^1, m = 7$	1214	1425
3	$6a^1 16a^2, m = 7$	1173	1426
	$4^1 6a^1 16b^1, m = 1$	1205	1441
	$1^1 16a^2, m = 1$	1206	1443
	$10b^1 15^1 17a^1, m = 1$	1181	1483

Simulations *via* four of the most likely candidates from Tables 9.2a and 9.3a for the peak at $\sim$1290 cm^{-1} are plotted in Fig. 9.9. The state $|1^1 10b^1 16a^1, m = 3\rangle$ might plausibly account for this feature, and is the only one of the four that would be able to couple to $|13^1, m = 0\rangle$. Two other possibilities, $|1^1 6a^1, m = 1\rangle$ and $|6a^1 10b^1 16b^1, m = 7\rangle$, can be ruled out because they would produce additional strong peaks which are not observed in the experiment. However, coupling of $|18a^1, m = 7\rangle$ to $|13^1, m = 1\rangle$ could also account for the 1290 cm^{-1} peak.

In Fig. 9.10 Franck-Condon simulations are presented for selected states from the list in Table 9.2b, which should produce $\Delta v = 0$ peaks matching the dark state feature seen at 1475 cm^{-1} in both the SEVI and ZEKE experiments. Interestingly two of the simulations, *via* $|15^1 17b^1, m = 6\rangle$ and $|16b^1 17b^1, m = 6\rangle$, are able to reproduce *both* of the dark state features seen in the SEVI spectrum at 3 ps. The 1475 cm^{-1} peak could also be accounted for by ionisation from $|4^1 11^1, m = 6\rangle$ or $|10b^1 15^1 17a^1\rangle$, with the latter being a particularly close match to the observed peak position. By contrast, the simulations *via* $|6a^1 10a^1, m = 6\rangle$ and $|6a^1 17b^1, m = 3\rangle$ are not consistent with the observed doorway state spectrum, suggesting that these two S_1 vibrational levels are probably not coupled directly to 13^1.

The five most likely doorway states suggested by the simulations are listed in Table 9.4. All but one of these require torsion-vibration coupling to be invoked. The sole exception is the pure vibration $10b^1 15^1 17a^1$, which can account for the dark state SEVI and ZEKE features at 1475 cm^{-1} but not the SEVI peak at 1290 cm^{-1}. If torsion-vibration

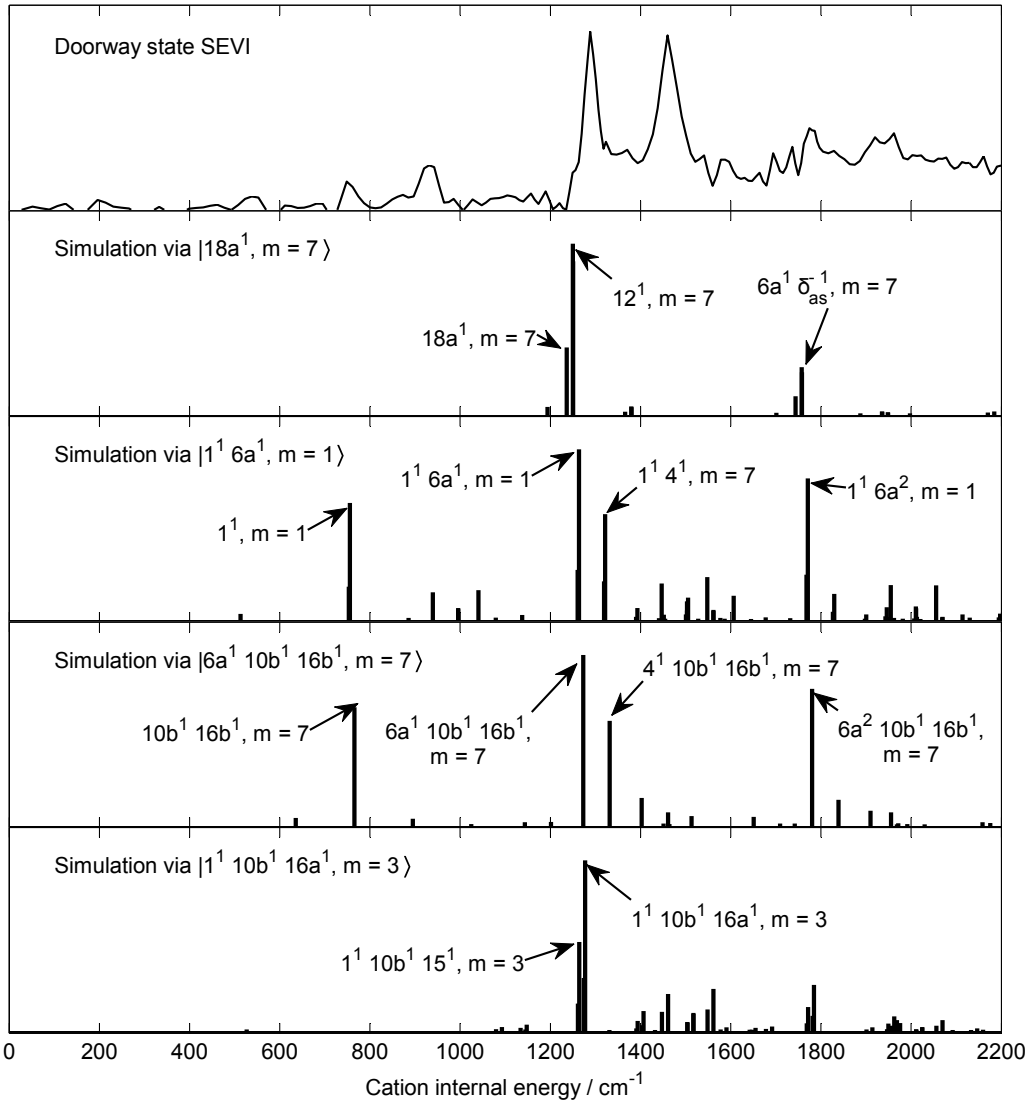

Fig. 9.9. Comparison of the "doorway" SEVI spectrum with Franck-Condon simulations from possible doorway states which could give rise to a peak at $\sim$1290 cm^{-1}.

Table 9.4. Summary of the most plausible candidates for the identity of the doorway state(s) coupled to 13^1.

Vibrational state	m	Calculated S_1 frequency / cm^{-1}	Calculated SEVI peak positions / cm^{-1}
$1^1 10b^1 16a^1$	3	1178	1280
$15^1 17b^1$	6	1218	1277 and 1465
$16b^1 17b^1$	6	1206	1317 and 1501
$4^1 11^1$	6	1195	1505
$10b^1 15^1 17a^1$	0	1176	1478

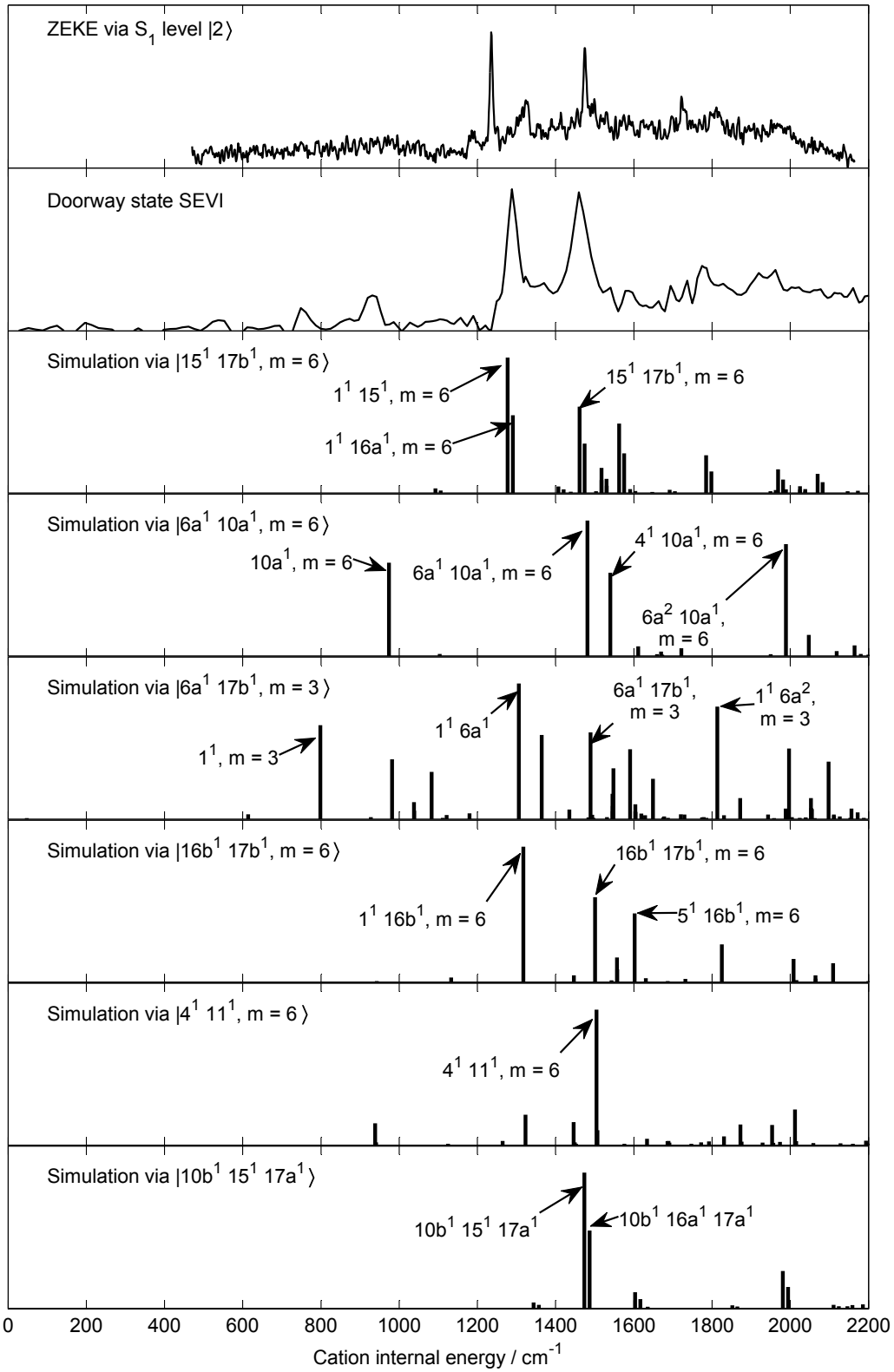

Fig. 9.10. Comparison of the ZEKE and "doorway" SEVI spectra with Franck-Condon simulations from six candidate doorway states that could give rise to a peak at $\sim$1475 cm^{-1}.

coupling is indeed crucial to reaching the doorway state, then this would explain why a $\Delta v = 0$ peak remains visible in the SEVI spectrum even after 500 ps, when all other structure has been lost. All of the states listed in Table 9.4 have overall A_1 symmetry, which is appropriate for coupling to $|13^1, m = 0\rangle$ but not $|13^1, m = 1\rangle$. As discussed in Section 2.7.6, the Boltzmann populations of the $m = 0$ and $m = 1$ torsional levels are roughly equal at the 10 K temperature of the molecular beam. Approximately half of the molecules would therefore remain trapped in $|13^1, m = 1\rangle$, unable to couple to any nearby dark states.

9.2. C−CD_3 stretch: 13^1 in toluene-D_3

It is interesting to compare the IVR behaviour of S_1 13^1 in toluene with that of the isotopologue $C_6H_5CD_3$, in which the three methyl hydrogens are replaced by deuterium. One might expect the frequency of a C−CD_3 stretch to be red-shifted with respect to the corresponding C−CH_3 stretch in toluene. However the DFT calculations described in Section 5.1 suggest that, in all three electronic states, the 13^1 vibrational level is in fact *blue*-shifted by deuteration. Examination of the calculated normal modes shows that there is significant "umbrella" motion associated with the C−CD_3 stretch, which may explain the increased frequency (see Fig. 9.11).

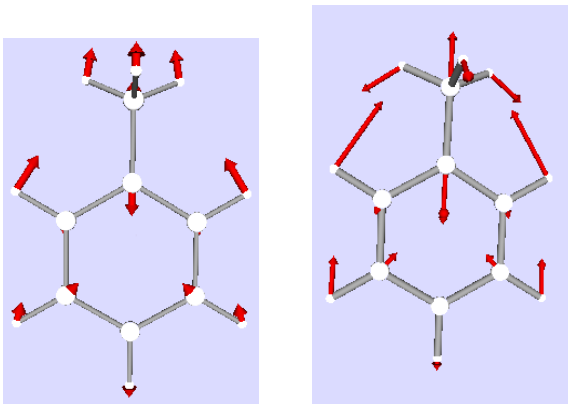

(a) $C_6H_5CH_3$ **(b)** $C_6H_5CD_3$

Fig. 9.11. Comparison of atomic motions for Varsányi mode 13 in the two isotopomers.

Balfour and co-workers [119, 120] have confirmed that, in the S_0 electronic state, 13^1 is indeed blue-shifted on deuteration. These authors conducted a study of the liquid-phase infra-red and ultraviolet absorption spectra of toluene and seven deuterated isomers. The infrared spectra indicated S_0 13^1 frequencies of 1208 and 1225 cm^{-1} in $C_6H_5CH_3$

and $C_6H_5CD_3$ respectively.[2] In the S_1 electronic state, however, these authors suggest that the 13^1 level is red-shifted from 1189 to 1166 cm^{-1} on deuteration of the methyl group. This is a surprising result since it would require the direction of the isotopic shift to be reversed in the excited state. As the assigned frequencies are based purely upon the UV absorption bands, and have not been confirmed by (*e.g.*) dispersed fluorescence measurements, the possibility of a misassignment cannot be ruled out.

The nanosecond REMPI spectrum of $C_6H_5CD_3$ recorded as part of the present work shows an intense absorption feature at ∼1241 cm^{-1} above the S_1 origin (Fig. 9.12). Unfortunately no ZEKE spectrum was recorded *via* this vibrational level; however the picosecond SEVI spectrum is strikingly similar to that recorded via S_1 13^1 in toluene-H_8 (Fig. 9.13). This result suggests that deuteration of the methyl group blue-shifts the 13^1 level by some 48 cm^{-1} in the S_1 electronic state, and by 46 cm^{-1} in the ion. The isotopic shift is in fact almost twice as large as that predicted by the DFT calculations (∼25 cm^{-1} in both electronic states).

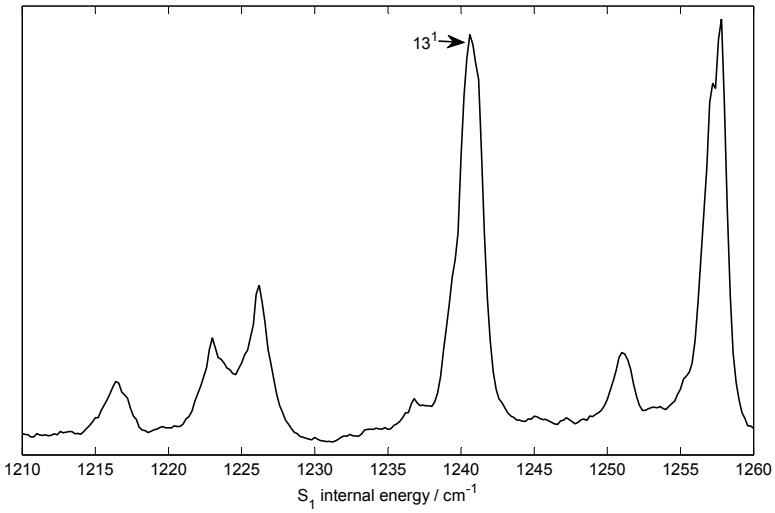

Fig. 9.12. Portion of the nanosecond REMPI spectrum of $C_6H_5CD_3$ in the vicinity of S_1 13^1.

A series of two-colour picosecond VMI photoelectron spectra was recorded *via* S_1 13^1 in toluene-D_3, using a fixed probe wavelength of 290.27 nm and time delays of 0–30, 50, 100, 200 and 500 ps. Some of these spectra are plotted in Fig. 9.14. As in toluene-H_8 the intensity of the main $\Delta v = 0$ peak is seen to oscillate initially, suggesting a transfer of population back and forth between 13^1 and a "doorway" state. At later time delays the spectrum becomes congested, and little structure can be discerned after 100 ps.

The oscillations of the $\Delta v = 0$ peak can be quantified by measuring the time-dependent integral from 1160–1347 cm^{-1} using the Trapezium Rule. A clear pattern of quantum

[2] The assignment is given here in Varsányi notation, but Balfour and co-workers use a different numbering scheme in which the same vibration is referred to as mode "7a".

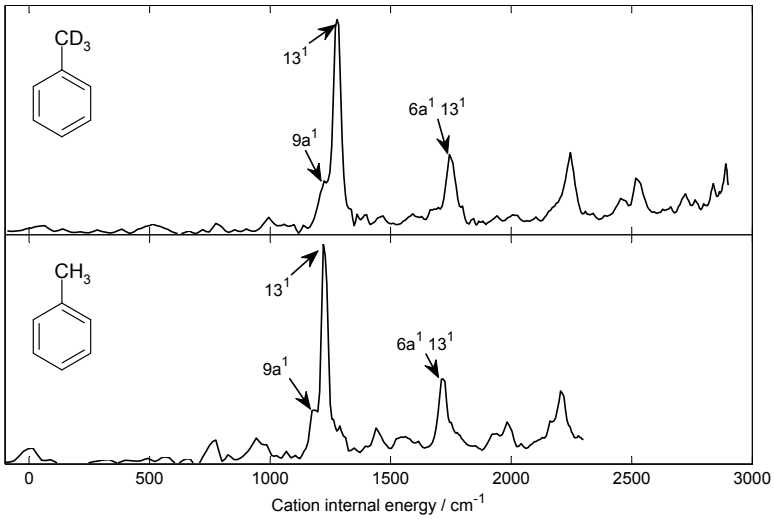

Fig. 9.13. SEVI spectra at 0 ps *via* S_1 13^1 in the two isotopomers.

beats is revealed which can be modelled successfully using Equation (9.1) (see Fig. 9.15). The fitted parameters are listed and compared with those for toluene-H_8 in Table 9.5.

Table 9.5. Parameters obtained from fits of 13^1 peak oscillations to Equation (9.1) for the two isotopomers. $\tilde{\nu}$ is the wavenumber equivalent of the fitted value ω.

Molecule	A	B	C	τ_1 / ps	τ_2 / ps	ω / rad ps^{-1}	$\tilde{\nu}$ / cm^{-1}
$C_6H_5CH_3$	51.1	32.4	71.3	19.9	4.6	0.975	5.2
$C_6H_5CD_3$	239.7	133.8	98.5	5.0	13.7	0.582	3.1

A signature of the doorway state appears in the 6 ps spectrum as a weak, partially resolved feature at ∼1400 cm^{-1}. This can be seen more clearly in a SEVI spectrum, produced by splicing together VMI spectra for probe wavelengths of 294.30, 290.27, 286.33 and 282.35 nm. Three such SEVI spectra were obtained in this work, for time delays of 0, 6 and 12 ps (Fig. 9.16). The SEVI spectrum at 6 ps gives a more accurate energy for the doorway state feature of 1391 cm^{-1}.

A search using the backtracking algorithm suggests only five vibrational states which lie within ±25 cm^{-1} of 13^1, have the correct symmetry for coupling to $|13^1, m = 0\rangle$ and could produce a $\Delta v = 0$ SEVI peak close to 1391 cm^{-1}. These are listed in Table 9.6 and Franck-Condon simulations via each of the five candidate doorway states are presented in Fig. 9.17. There is one other possibility, $|10b^1 16a^1 \delta_{as}^{-1}, m = 7\rangle$, which might potentially couple to $|13^1, m = 1\rangle$ (see Fig. 9.18). Since the SEVI spectrum is rather congested above ∼1500 cm^{-1} internal energy it is not possible to give a definitive assignment for the doorway state; however the calculations do suggest that it may be different from the doorway state that is coupled to 13^1 in toluene-H_8.

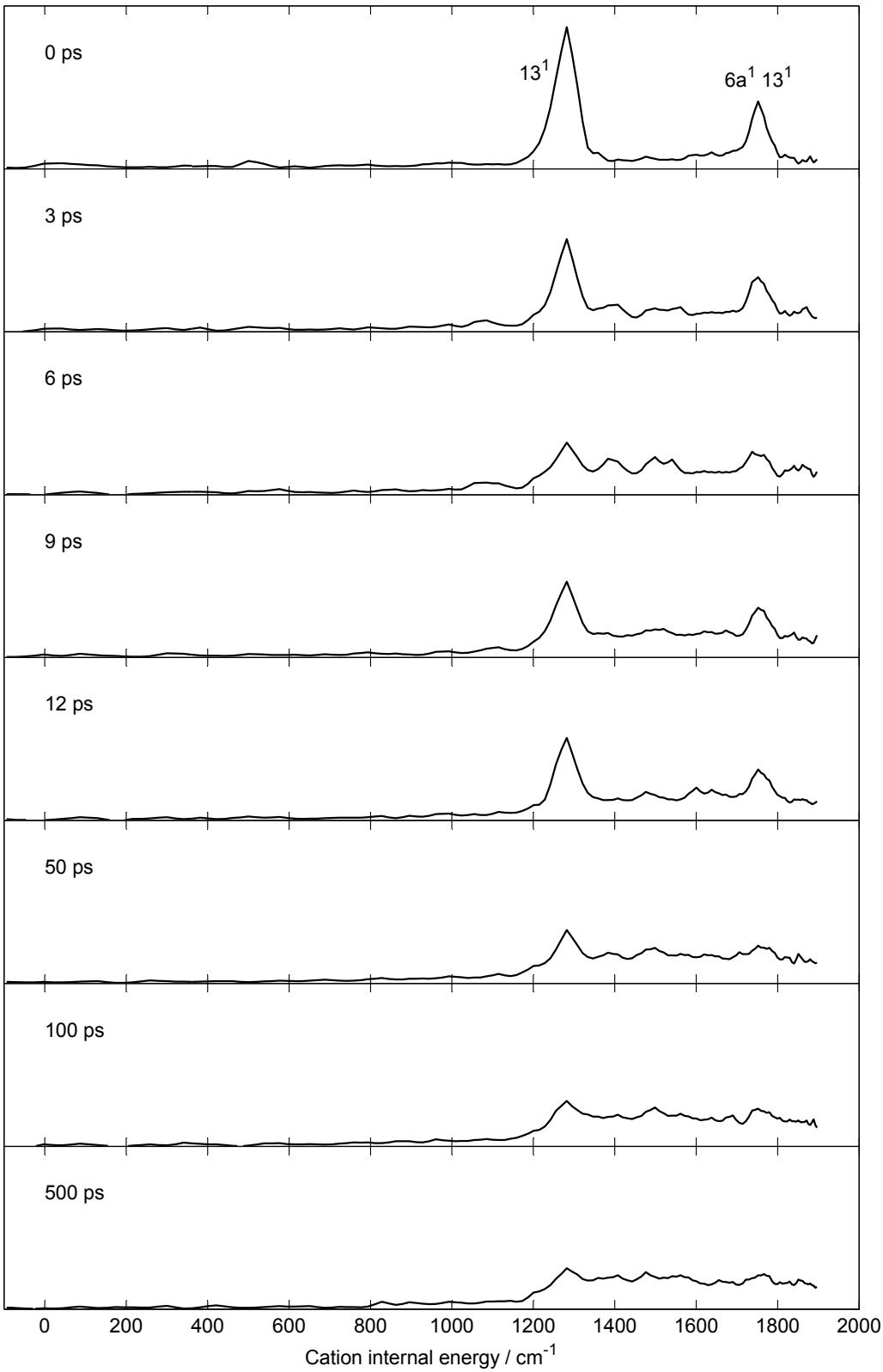

Fig. 9.14. Two-colour VMI photoelectron spectra *via* S_1 13^1 in toluene-D_3 at selected pump-probe time delays. The probe wavelength, measured using the monochromator, was 290.27 nm.

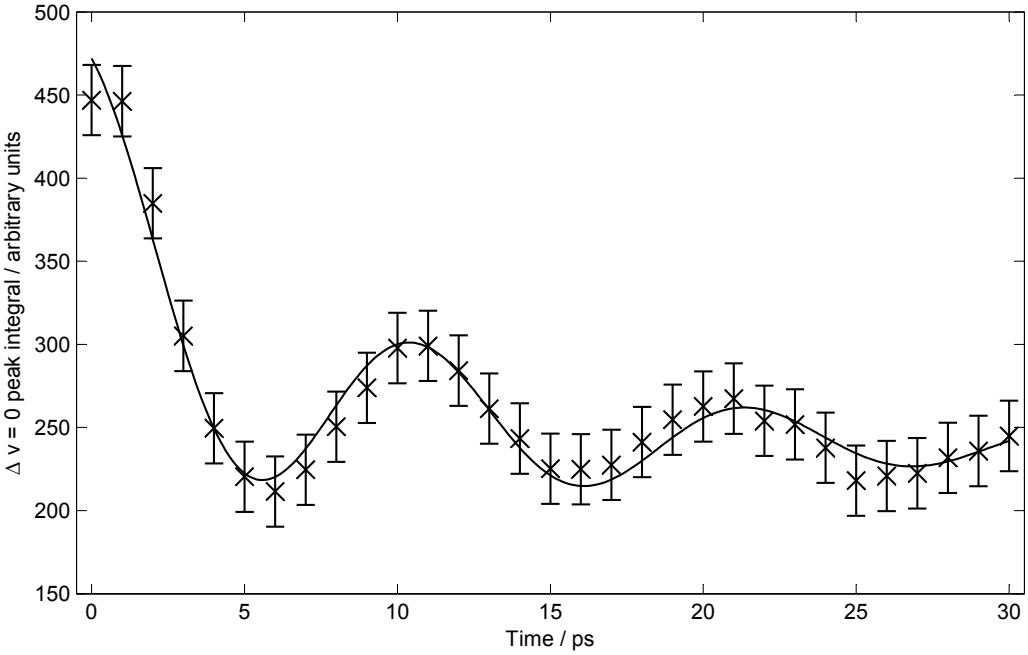

Fig. 9.15. Time-resolved oscillations of the $\Delta v = 0$ peak (1160–1347 cm^{-1}) in spectra via S_1 13^1 in toluene-D_3. The solid line represents a fit to Equation (9.1). Error bars are taken from the range of measured integrals for three repeat images at 0 ps.

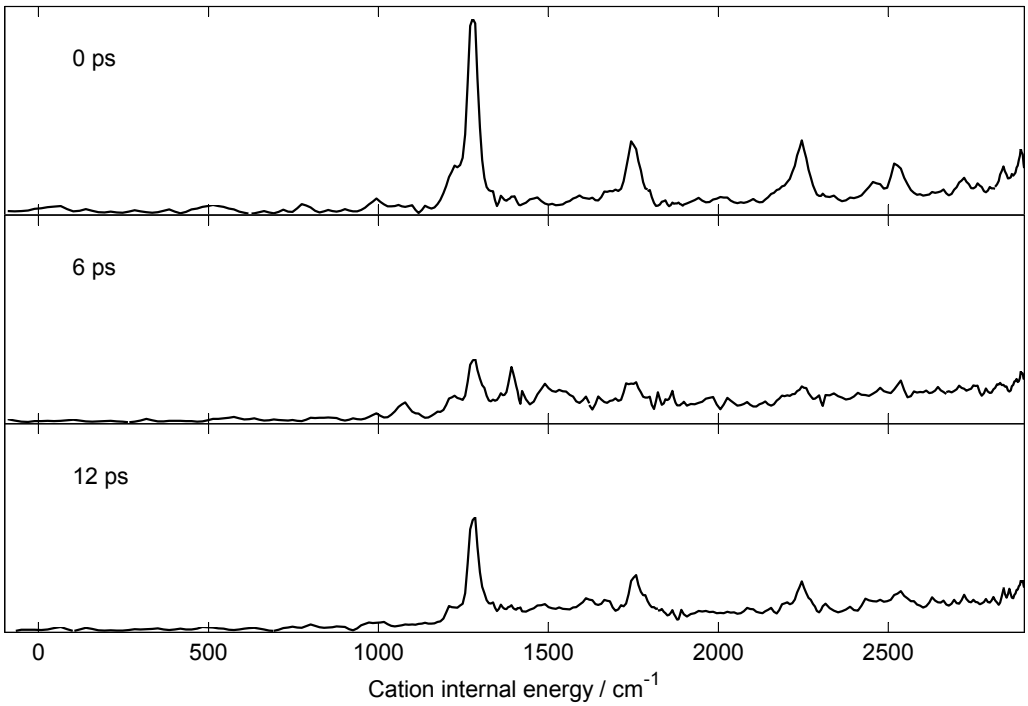

Fig. 9.16. Time-resolved picosecond SEVI spectra *via* S_1 13^1 in toluene-D_3.

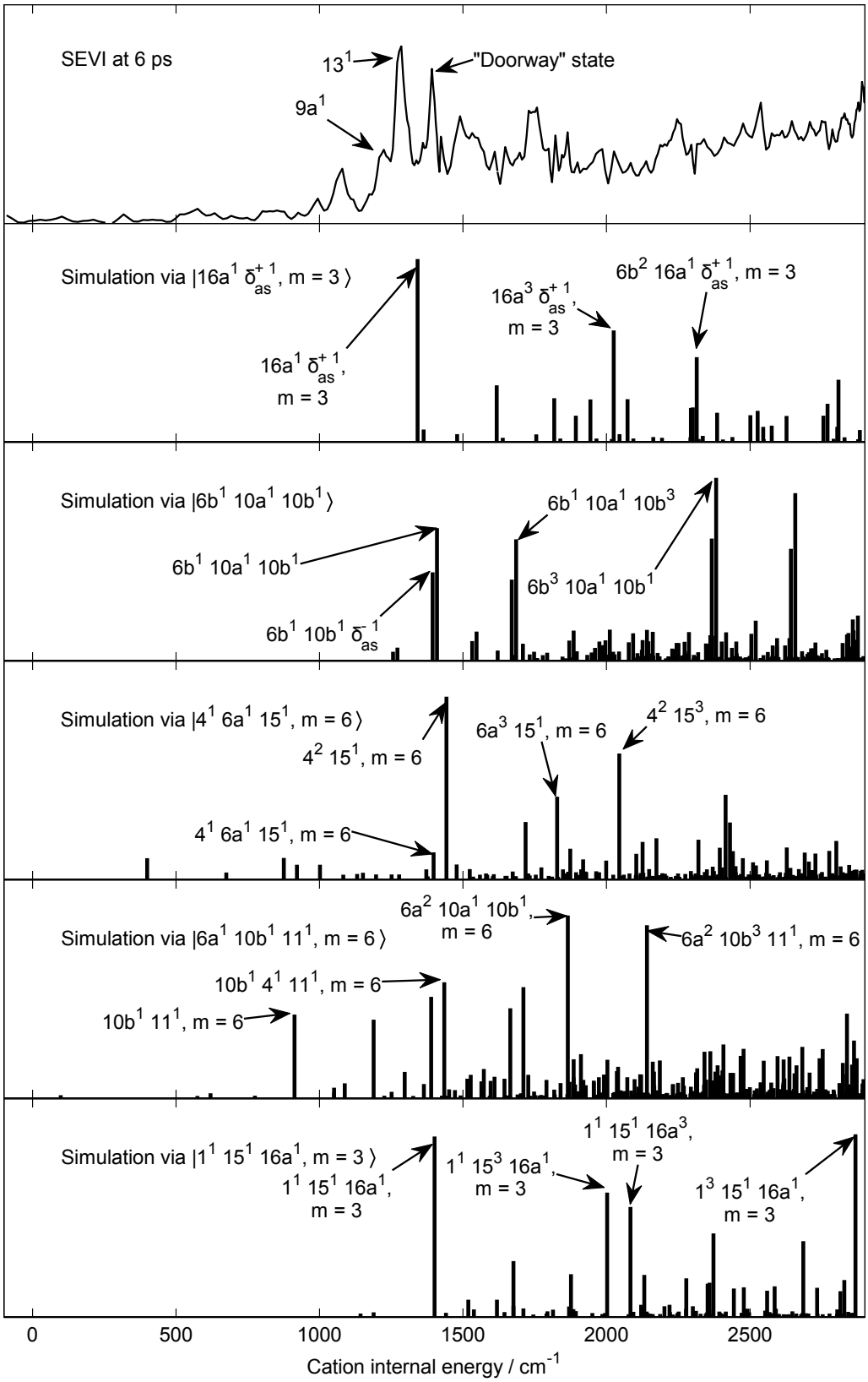

Fig. 9.17. Comparison of SEVI spectrum *via* S_1 13^1 in toluene-D_3 at 6 ps with simulations from the candidate doorway states. Harmonic frequencies for the cation have been scaled by a factor of 0.97.

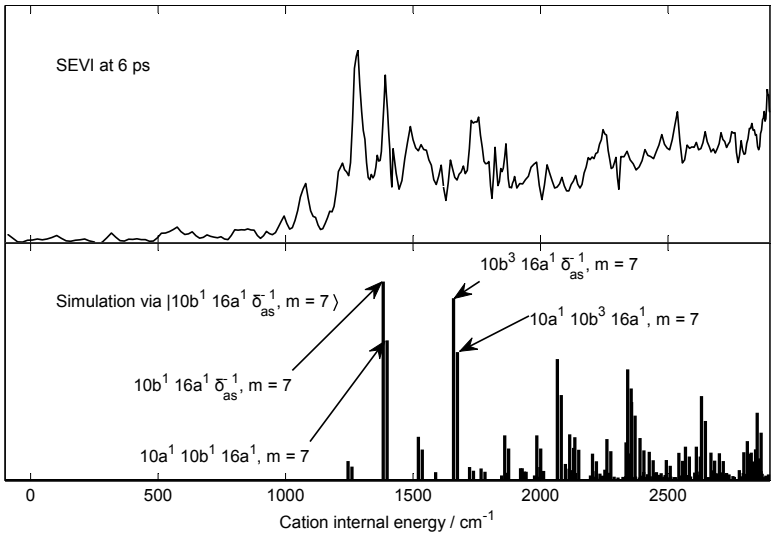

Fig. 9.18. Simulation *via* a state which could potentially couple to S_1 $|13^1, m = 1\rangle$ in $C_6H_5CD_3$.

Table 9.6. Candidate doorway states with suitable energy and symmetry for coupling to $|13^1, m = 0\rangle$ in S_1 toluene-D_3.

Quanta	State	S_1 energy / cm^{-1}	Ion energy / cm^{-1}
2	$16a^1\delta_{as}^{+1}; m = 3$	1246	1409
3	$10b^1 6b^1 10a^1$	1219	1410
	$15^1 6a^1 4^1; m = -6$	1244	1398
	$15^1 16a^1 1^1; m = 3$	1246	1400
	$10b^1 6a^1 11^1; m = 6$	1248	1389

9.3. Ring breathing: $1^1 6a^1$ in toluene-D_3

In Chapter 7 it was shown that the "bright" zero-order state $6a^1$, which is a stretching motion of the benzene ring, couples to the bending combination $10b^1 16b^1$ and the twisting overtone $16a^2$ to produce a set of three eigenstates. When these are coherently excited by the picosecond laser, the resulting time-resolved photoelectron spectra show a quantum beat pattern that persists for at least 500 ps, which is characteristic of restricted IVR. In the nanosecond REMPI spectrum of $C_6H_5CD_3$ obtained in this work, those three levels can also be seen in combination with the 1^1 zero-order state, which is a totally symmetric ring breathing motion. An enlarged portion of the REMPI spectrum in the vicinity of these levels is shown in Fig. 9.19. Each vibrational level has been labelled according to the zero-order state which it resembles most closely, although in reality each eigenstate is expected to have some contribution from all three zero-order states.

The nanosecond ZEKE spectra obtained following excitation of the S_1 1^1 ($6a^1$ / $10b^1 16b^1$ / $16a^2$) levels were found to be unstructured, suggesting the possibility of rapid IVR. Picosecond SEVI spectra were also recorded with pump-probe time delays of 0–20,

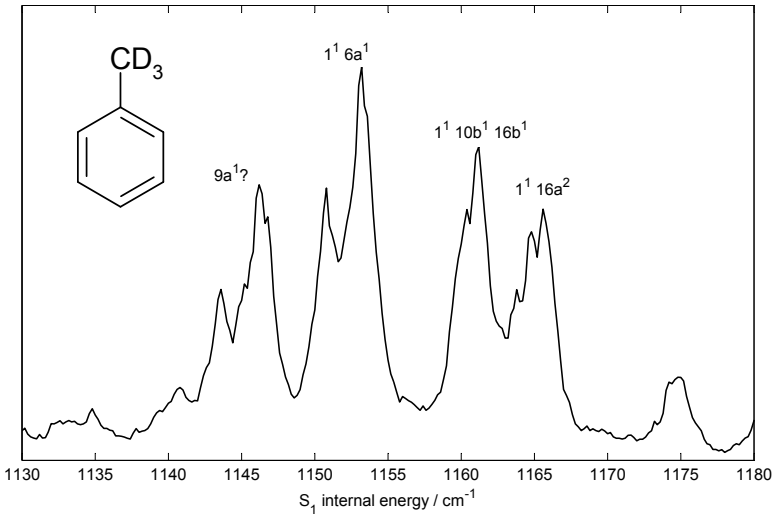

Fig. 9.19. Portion of the nanosecond REMPI spectrum of toluene-D_3 in the vicinity of the $1^1 6a^1$ vibrational level.

25, 30, 40, 50, 70, 100, 150, 200, 300, 400 and 500 ps. Due to the broader bandwith of the picosecond laser, all three levels were excited coherently and at 0 ps the vibrational wavepacket could be expected to resemble the zero-order bright state $1^1 6a^1$. The spectra for time delays of 0–6 ps are presented in Fig. 9.20 and show clear vibrational structure, with evidence of oscillatory behaviour. At longer time delays, however, the spectra become very congested and little structure remains beyond 20 ps, indicating that dissipative IVR has taken place (Fig. 9.21).

In Fig. 9.22 the SEVI spectra at 0 and 2 ps are compared with Franck-Condon simulations *via* each of the three zero-order states. At 0 ps the spectrum closely resembles that predicted for ionisation from $1^1 6a^1$, as would be expected if this is the "bright" state. After 2 ps, the intensity of the $1^1 6a^1$ peak is minimised and so the SEVI spectrum must be mainly due to ionisation from "dark" states. The simulations indicate that all of the main features in this spectrum can be accounted for by ionisation from either $1^1 10b^1 16b^1$ or $1^1 16a^2$, suggesting that both of these states are significantly coupled to $1^1 6a^1$.

The quantum beats seen in the spectra for time delays of 0–20 ps can be studied in more detail by examining the integral of the 1^1 peak, which is measured using the Trapezium Rule over the range 650–791 cm^{-1}. This feature is chosen because it remains isolated at 20 ps, whereas the peaks above $\sim$1000 cm^{-1} are rapidly obscured by the increasing congestion. The resulting oscillation pattern, which is plotted in Fig. 9.23, is well described by Equation (9.1) with fitted decay lifetimes $\tau_1 = 1.7$ and $\tau_2 = 6.7$ ps. The fitted beat frequency, $\omega = 1.397$ rad $\mathrm{ps}^{-1} \equiv 7.4\,\mathrm{cm}^{-1}$, is consistent with the separation of the S_1 "$1^1 6a^1$" and "$1^1 10b^1 16b^1$" vibrational levels observed in the nanosecond REMPI spectrum (Fig. 9.19). This would seem to suggest that $1^1 10b^1 16b^1$ acts as the main

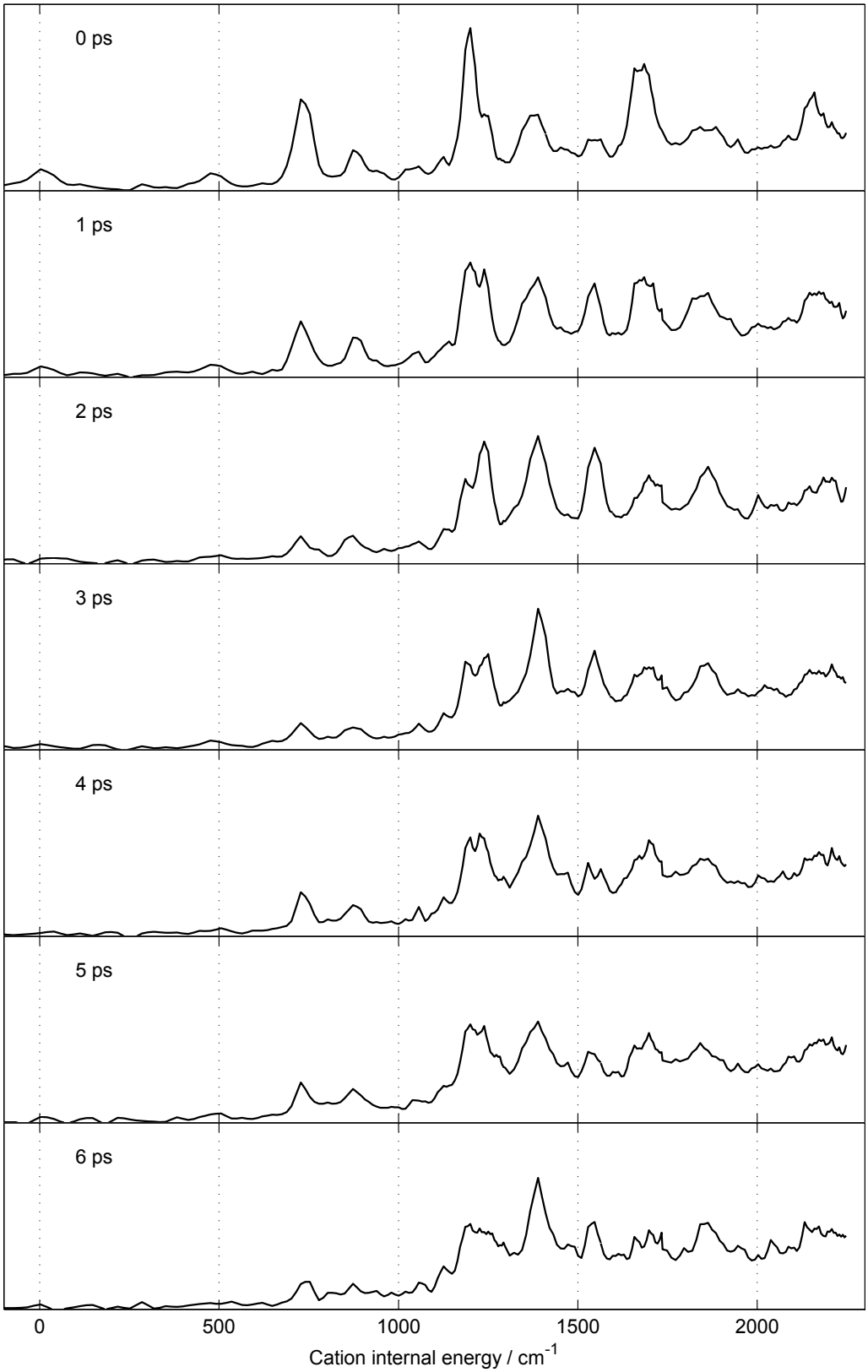

Fig. 9.20. Picosecond SEVI spectra via S_1 $1^1\left(6a^1/10b^1 16b^1/16a^2\right)$ in $C_6H_5CD_3$ at short time delays.

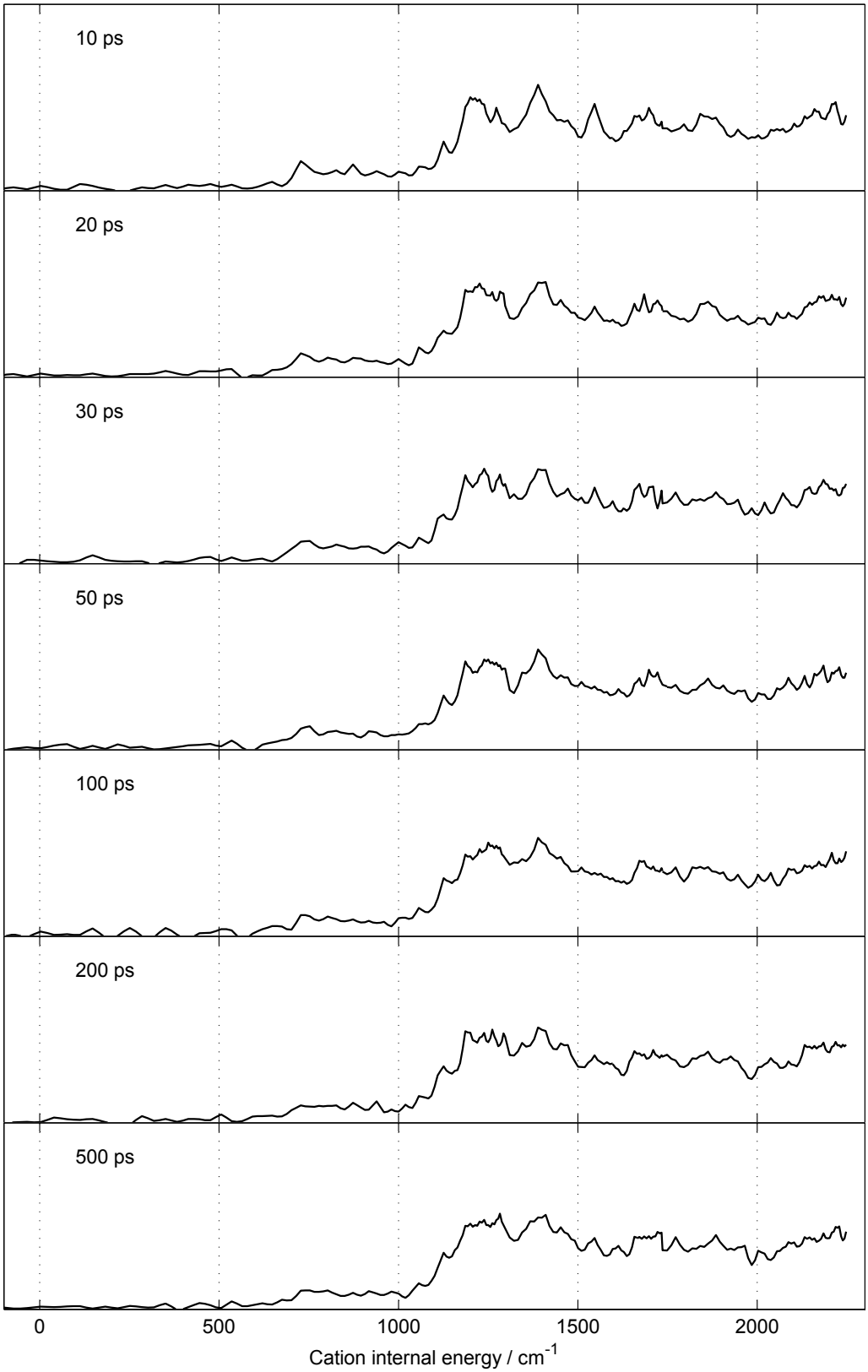

Fig. 9.21. Picosecond SEVI spectra via S_1 $1^1\left(6a^1/10b^1 16b^1/16a^2\right)$ in $C_6H_5CD_3$ at long time delays.

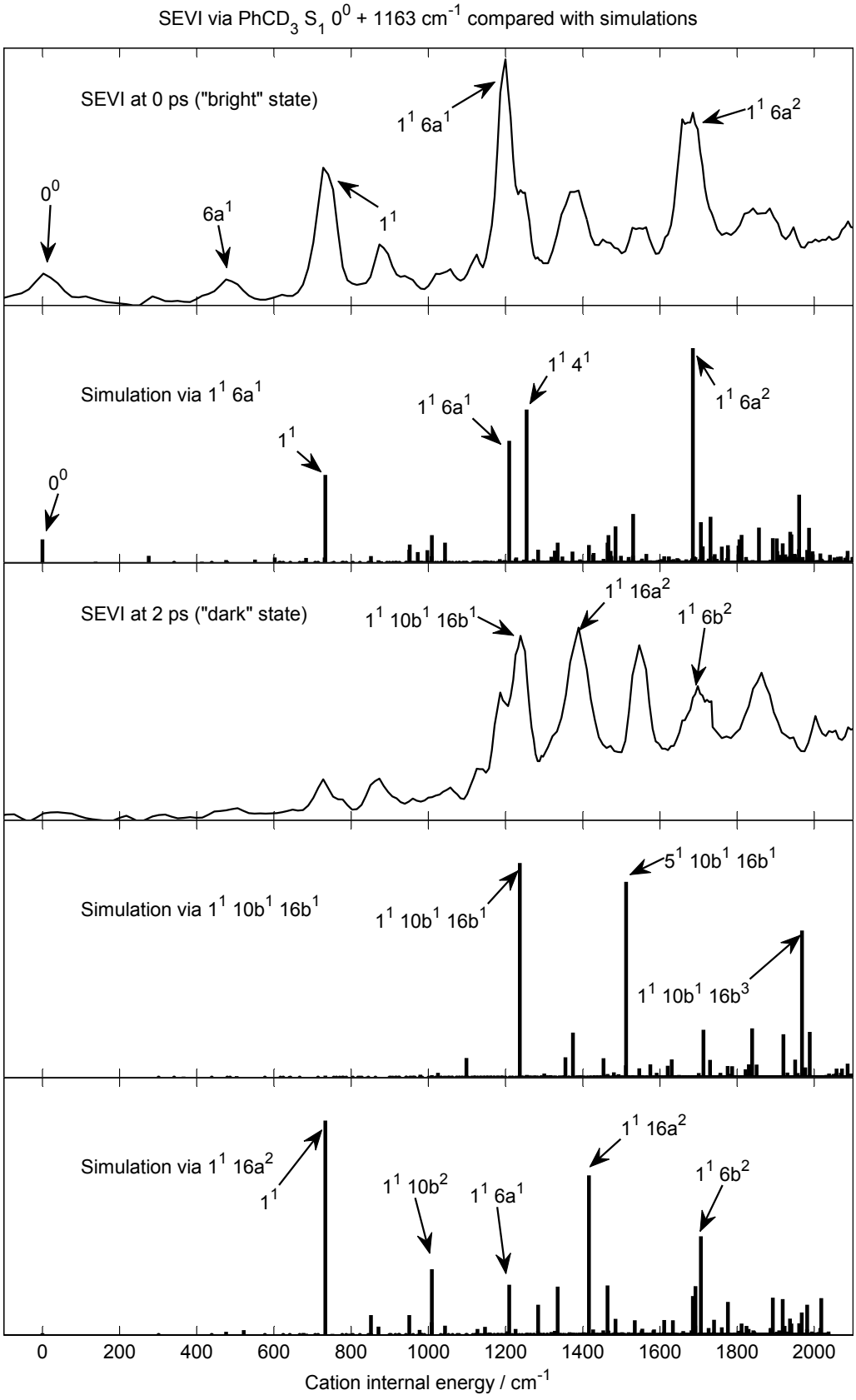

Fig. 9.22. Comparison of SEVI spectra *via* S_1 $1^1 6a^1$ in $C_6H_5CD_3$ with Franck-Condon simulations.

"doorway" state through which dissipative IVR is achieved.

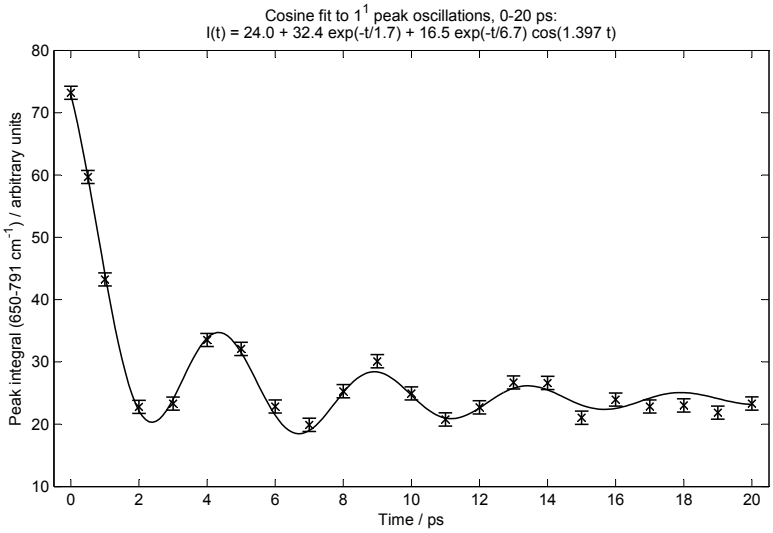

Fig. 9.23. Oscillations of the 1^1 peak in the SEVI spectra via S_1 $1^1\left(6a^1/10b^116b^1/16a^2\right)$ for $C_6H_5CD_3$, with fit to Equation (9.1).

9.4. Conclusions

The results presented in this chapter provide direct evidence for the existence of so-called "doorway states" which facilitate dissipative IVR from certain initially prepared states. In the case of 1^16a^1, the use of time-resolved photoelectron spectroscopy in conjunction with Franck-Condon simulations has given a clear assignment for the doorway state: peaks are seen to appear after two picoseconds which are consistent with ionisation from a mixture of $1^110b^116b^1$ and 1^116a^2. By comparing the quantum beat frequency with the energy spacings of the three vibrational levels seen in the nanosecond REMPI spectrum, it has been shown that the 1^16a^1 bright state is coupled mainly to $1^110b^116b^1$. This means that vibrational energy initially flows from an in-plane ring breathing motion to an out-of-plane bending motion. The bending then leads on rapidly to a twisting motion (1^116a^2) and ultimately to many other dark vibrational states. At present, the IVR dynamics from 1^16a^1 have only been studied for toluene-D_3 and it would be interesting in future work to perform a comparison with toluene-H_8.

The results for the 13^1 vibrational level highlight the importance of achieving adequate resolution in the photoelectron spectrum. Whereas previous studies using time-of-flight and one-colour velocity map imaging detection were unable to resolve vibrational structure after 10 ps, giving the impression of very rapid dissipative IVR, in this work the superior resolution of SEVI has shown that quantum beats are present and therefore that the IVR must proceed *via* a doorway state. Five possible candidates for the identity

of this state have been found which could explain the observed time dependence of the SEVI spectra, although the assignment is not as clear-cut as for $1^1 6a^1$. The internal rotation of the methyl group seems to play a key role: four of the proposed doorway states involve an excitation to the $m = 3$ or $m = 6$ torsional level, and due to symmetry restrictions all five doorway states are only accessible to molecules which initially have $m = 0$. This may explain why the $\Delta v = 0$ peak is retained in the SEVI spectra even after 500 ps: approximately half of the molecules are trapped in $|13^1, m = 1\rangle$ and are unable to couple to the doorway state. In future work, this theory could be tested by varying the temperature of the molecular beam: raising the temperature should inhibit IVR by increasing the populations of $m = 1$ and higher torsional levels relative to $m = 0$.

In the deuterated isotopologue $C_6H_5CD_3$, the SEVI spectrum at 0 ps shows that a feature seen in the nanosecond REMPI at $1241\,\mathrm{cm}^{-1}$ above the S_1 origin must be 13^1, contrary to the assignment of $13^1 = 1166\,\mathrm{cm}^{-1}$ postulated by Balfour and Ram [120]. Although the time dependence of the picosecond spectra is superficially similar to that seen in $C_6H_5CH_3$, the doorway state must be different since 13^1 is no longer close in energy to any of the doorway states proposed for toluene-H_8. Five possibilities have been identified which could account for the peak at $1391\,\mathrm{cm}^{-1}$ that appears in the SEVI spectrum after 6 ps. The quantum beat frequency is lower for $C_6H_5CHD_3$ than for $C_6H_5CH_3$, indicating that the doorway state is closer in energy to 13^1 in the deuterated molecule.

At present only a single probe wavelength has been used for the time-resolved spectra. In future the resolution could be improved by employing SEVI, *i.e.* splicing together spectra recorded with different probe wavelengths, at a greater range of time delays. Further insights could also potentially be gained by measuring nanosecond ZEKE spectra *via* the 13^1 level in toluene-D_3. This level was overlooked in the present ZEKE experiments due to an initial misassignment of the REMPI peak at $1153\,\mathrm{cm}^{-1}$ (now known to be $1^1 6a^1$) as 13^1. Due to the relatively fast IVR, no structure could be discerned in the ZEKE spectra recorded *via* $1^1 6a^1$, $1^1 10b^1 16b^1$ and $1^1 16a^2$.

10. Conclusions and future work

In this work, a powerful combination of experimental and theoretical methods has been applied to gain new insights into the IVR dynamics of toluene. Picosecond laser pulses, in conjunction with velocity map imaging of the photoelectrons produced, have given a direct view of the vibrational redistribution process in the time domain. The use of slow electron velocity map imaging (SEVI), in which the spectra are combined from images recorded at different probe photon energies, has given a substantial improvement in resolution over previous studies in which a single laser wavelength was used to excite and ionise. Nonetheless, since a superposition of vibrational states was prepared in S_1, full vibrational resolution could not be expected and in some cases the SEVI peaks were seen to be composites of two or more unresolved features.

ZEKE photoelectron spectroscopy with nanosecond laser pulses gave better energy resolution, at the expense of time resolution. The ZEKE spectra yielded information that was complementary to the picosecond SEVI experiments, due to the different nature of the vibrational state prepared in S_1. Because of their broad bandwidth, the picosecond pulses excited a coherent superposition of vibrational eigenstates which, at time zero, corresponded to a zero-order bright state. By contrast, the narrow bandwidth of the nanosecond pulses resulted in the excitation of a single vibrational level.[1] Consequently, the S_1 vibrational state did not evolve in time, and did not correspond to any particular localised motion; instead the vibrational state was best pictured as a mixture of zero-order states.

The third approach has been the theoretical calculations described in Chapter 5. Using a combination of density functional theory and the Configuration Interaction Singles (CIS) method, the normal modes and vibrational frequencies of toluene and the isotopologue $C_6H_5CD_3$ have been calculated in the S_0 and S_1 electronic states, as well as the D_0 ground state of the cation. From these, Franck-Condon factors have been calculated in order to simulate the photoelectron spectra out of different vibrational states in S_1. The simulations act as a valuable aid to the assignment of features seen in the experimental spectra, particularly those which correspond to ionisation from "dark" S_1 vibrational states that cannot be prepared directly.

[1] Strictly speaking, the nanosecond laser pulses did not prepare an eigenstate in S_1 because individual rotational levels were not resolved.

By bringing together the results obtained from the picosecond time-resolved spectra, nanosecond spectra and computer simulations, it has been possible to achieve an understanding of the dynamics that could not have been reached using any one of these techniques alone. In this chapter, the most important findings will be summarised and the prospects for future work will be discussed.

10.1. Spectroscopy of the toluene cation

As discussed in Chapter 6, prior to this work only a few of the normal mode frequencies were known experimentally for the toluene cation, and even less information was available for $C_6H_5CD_3^+$. In the present investigation, ZEKE photoelectron spectra were recorded for the first time *via* eleven excited vibrational levels in S_1 toluene-H_8 and toluene-D_3, yielding accurate frequencies for eight normal modes in the cation (see Table 6.1). Additionally, the ZEKE spectra *via* the S_1 origin enabled the determination of the adiabatic ionisation energy. For toluene, the measured value of 71201 ± 5 cm^{-1} was in good agreement with values given in the literature [92, 123]. In the case of $C_6H_5CD_3$, for which no published value could be found, the ionisation energy was determined to be 71247 ± 5 cm^{-1}.

10.2. Regimes of IVR dynamics

The IVR dynamics of the vibrational levels in S_1 toluene studied in this work can be classified into three distinct regimes, which are illustrated in Fig. 10.1. We see restricted or no IVR for S_1 vibrational levels below $\sim$1100 cm^{-1}, and dissipative IVR above 1260 cm^{-1}. In between these two limiting cases, the 13^1 vibrational level at 1193 cm^{-1} undergoes intermediate IVR, as discussed in Chapter 9. The picosecond time-resolved spectra show evidence that vibrational energy initially flows back and forth between 13^1 and a "doorway" state, but within about 200 ps it becomes spread out among many different dark states.

These three regimes can be rationalised on the basis of the density of vibrational states. When the density of states is low there will be few, if any, dark states with suitable energies and symmetries for coupling to the zero-order bright state. However, according to the theoretical calculations described in Chapter 5, the density of states rises rapidly as the vibrational energy is increased beyond about 1000 cm^{-1}. Consequently the number of dark states available for coupling to the zero-order bright state also increases sharply, making dissipative IVR possible.

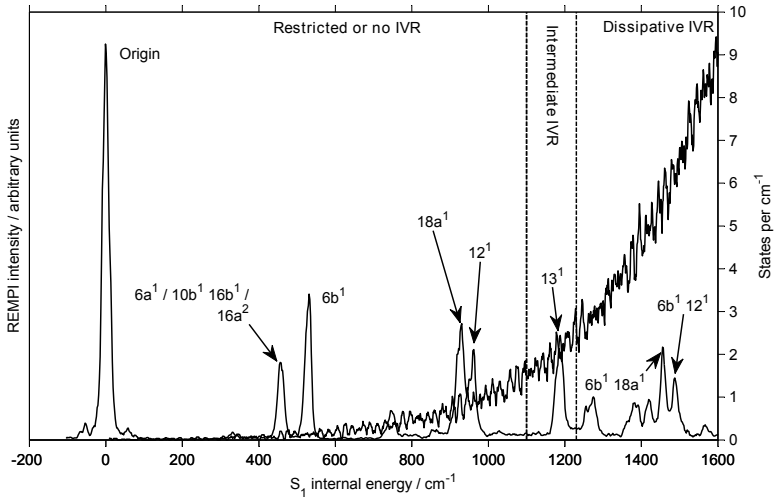

Fig. 10.1. Picosecond REMPI spectrum of toluene and calculated density of vibrational states, showing the three distinct regimes of IVR observed in this work.

10.2.1. Restricted IVR

As would be expected, no time dependence was observed in the SEVI spectrum following excitation to the S_1 origin, for which IVR is by definition impossible. The picosecond SEVI spectrum from S_1 $6b^1$ was also found to be invariant with pump-probe time delay, and the nanosecond ZEKE spectrum was consistent with a Franck-Condon simulation *via* $6b^1$ (see Section 6.4). It therefore appears that in this case the zero-order state given by the harmonic oscillator model is a good approximation to the true vibrational eigenstate, and thus $6b^1$ is not significantly coupled to any other zero-order states.

The Fermi resonance couple 1^1 / $4^1 16b^1$ (736 / 754 cm^{-1}) was also investigated using both picosecond SEVI and nanosecond ZEKE spectroscopy. In this case, strong coupling of the two zero-order states had been clearly indicated by the dispersed fluorescence spectra of Hickman *et al.* [63]. The SEVI and ZEKE spectra showed evidence of this coupling, with features corresponding to both zero-order states in the ion being seen in the spectra following excitation of either Fermi resonance component in S_1. However, since the spacing of the vibrational eigenstates in S_1 exceeded the bandwidth of the picosecond laser, it was not possible to prepare the necessary coherent superposition to observe time dependence. This example serves as a warning that a lack of time dependence does not necessarily imply an absence of coupling between the zero-order states.

The most interesting result was seen for the REMPI peak at $\sim$460 cm^{-1}, which is the $6a^1$ / $10b^1 16b^1$ / $16a^2$ system explored in Chapter 7. In this case, three vibrational eigenstates were sufficiently close in energy to be coherently excited by the picosecond pump laser. Prior to the present study, the system had been believed to be a simple Fermi

resonance between the $6a^1$ and $10b^1 16b^1$ zero-order states, comprising two eigenstates at 457 and 462 cm^{-1} above the S_1 origin. Hickman *et al.* [63] recorded dispersed fluorescence spectra from both of these levels, which clearly indicated the coupling between $6a^1$ and $10b^1 16b^1$. Fluorescence was also seen into several other vibrational levels of the ground electronic state, including $16a^2$. However it could not be concluded from this whether $16a^2$ was involved in the coupling, or merely a spectator to the dynamics. A preliminary time-resolved photoelectron imaging study by Hammond *et al.*, in which spectra were obtained using 1 ps laser pulses of equal wavelength to excite and ionise, had given results consistent with the two-level picture [13, 57, 58]. In that work, as the pump-probe time delay was varied between 0 and 10 ps, a regular oscillation was seen between photoelectron spectra characteristic of ionisation from $6a^1$ and from $10b^1 16b^1$.

The laser system used in the present work had a narrower, better-defined bandwidth than that employed by Hammond *et al.* This, in conjunction with the use of SEVI, brought about a great improvement in the resolution of the photoelectron spectra. With the increased beam time made available by an in-house laser system, it was possible to record photoelectron images at time delays up to 510 ps, including 0–100 ps in 1 ps steps. A small feature emerged in the spectra corresponding to ionisation from S_1 $16a^2$, and its oscillation pattern in time showed a definite phase relationship to the oscillations of the peaks originating from S_1 $6a^1$ and $10b^1 16b^1$. The time-resolved data thus revealed a weak coupling to $16a^2$ that could not be seen either in the frequency-resolved experiments of Hickman *et al.*, or in the nanosecond ZEKE spectra recorded in the present work. Fourier transformation of the time-resolved oscillations for each photoelectron peak yielded frequency components corresponding to the energy spacings of the coherently excited vibrational levels. Using these frequencies, the oscillation patterns were fitted to an exponentially decaying sum of cosine waves. From the relative amplitudes of the fitted cosines it was then possible to derive the vibrational coupling matrix, giving the composition of each eigenstate as a linear combination of the $6a^1$, $10b^1 16b^1$ and $16a^2$ zero-order wavefunctions. This is believed to be the first example of the use of time-resolved photoelectron spectroscopy to gain *quantitative* information about vibrational couplings.

The time-resolved oscillations and their Fourier transforms also revealed an unexpected "doubling" of the frequency components. Normally, one cosine term would be seen corresponding to each of the energy spacings between the eigenstates, but instead two were observed. This result was attributed to the fact that, at the 10 K temperature of the molecular beam, approximately half of the toluene molecules exist in the lowest

torsional energy level of the methyl rotor ($m = 0$), and half possess one quantum of torsional excitation ($m = 1$). Consequently there were two "torsional ladders" of vibrational eigenstates which were incoherently excited by the pump laser. It is assumed that the energy spacings of the vibrational levels in the two ladders are slightly different, leading to the observed splitting of the frequency components. Although it is not yet clear why this should be the case, it will be important to consider the role of the different torsional ladders in any future investigation of a molecule with a torsional degree of freedom.

10.2.2. Intermediate IVR

For two of the vibrational levels studied in this work, the picosecond time-resolved photoelectron spectra show direct evidence of IVR proceeding *via* a "doorway" state. In these cases, the $\Delta v = 0$ peak from the zero-order bright state is initially seen to oscillate in time, with the opposite phase to other peaks which correspond to ionisation from the doorway state. The spectra become increasingly congested with increasing pump-probe time delay, as many other dark states are accessed.

The most readily interpreted result is for the $1^1 6a^1$ vibrational level, which is a combination of a totally symmetric ring breathing mode with a ring stretching motion. This level has been studied only in the deuterated isotopomer $C_6H_5CD_3$, for which it occurs at $\sim$1153 cm^{-1} above the S_1 origin. By analogy with the $6a^1$ / $10b^1 16b^1$ / $16a^2$ system discussed above, $1^1 6a^1$ can be expected to couple strongly to $1^1 10b^1 16b^1$ and weakly to $1^1 16a^2$. A comparison of the time-resolved SEVI spectra with Franck-Condon simulations shows that, after 2 ps, peaks are present due to ionisation from all three of these zero-order states. The frequency of the time-resolved oscillations of the 1^1 peak, which is due to ionisation from $1^1 6a^1$, indicates that the zero-order bright state is coupled mainly to a level whose frequency lies $\sim$7 cm^{-1} away. Examination of the nanosecond REMPI spectrum, in which all three vibrational levels are resolved, reveals that the lower two levels are separated by 7 cm^{-1}. The oscillation frequency therefore suggests that $1^1 6a^1$ is primarily coupled to $1^1 10b^1 16b^1$, which then acts as the doorway state for dissipative IVR.

For the 13^1 level (C$-$CH$_3$ or C$-$CD$_3$ stretch), which has been studied in both isotopomers, the assignment of the doorway state is less clear-cut. Franck-Condon simulations revealed five possible candidates for each isotopologue which could explain the dark state peaks seen in the time-resolved spectra. Due to the large blue-shift of the S_1 13^1 level on deuteration, the doorway state(s) cannot be the same in $C_6H_5CH_3$ and $C_6H_5CD_3$. For both molecules, however, it seems likely that the torsional motion of the

methyl group is of key importance, with many of the proposed doorway states involving a torsional excitation to $m = 3$ or $m = 6$. Due to symmetry restrictions, most of the proposed doorway states can couple to $|13^1, m = 0\rangle$, but not to the torsionally excited level $|13^1, m = 1\rangle$. This could explain why a $\Delta v = 0$ peak can still be discerned in the SEVI spectrum at 500 ps for toluene-H_8: approximately half of the molecules remain "trapped" in $|13^1, m = 1\rangle$, unable to couple to the doorway state.

The present studies of 13^1 also underline the importance of obtaining photoelectron spectra with sufficient resolution. In previous work using time-of-flight [52, 53] and one-colour velocity map imaging [13, 58] detection of the photoelectrons, the closely-spaced peaks could not be resolved. The time-resolved oscillations which reveal the coupling to a doorway state were therefore not observed. Within 10 ps the spectra had become unstructured, giving the misleading impression of very rapid and complete dissipative IVR.

10.2.3. Dissipative IVR

Four zero-order states at energies above 1260 cm^{-1} were examined in Chapter 8. The time-resolved experiments indicate that dissipative IVR takes place on a time-scale of tens of picoseconds. The vibrational energy flows irreversibly out of the initially-prepared zero-order bright state, becoming spread among many different dark states. In the time-resolved spectra, the IVR is manifested as a decrease in the intensity of the main $\Delta v = 0$ peak and a loss of structure over time. The rate of IVR was found to vary according to the vibrational mode excited by the pump laser, but did not have a simple relationship to either the vibrational energy or the density of states. The insensitivity of the IVR rate to the density of states suggests that only a subset of the dark states are significantly coupled to the bright state; in other words the IVR mechanism proceeds *via* certain doorway states. However, in contrast to the results for 13^1 and $1^1 6a^1$, the doorway states are too short-lived to leave a clear signature in the time-resolved photoelectron spectra. Interestingly, dissipative IVR from the $6b^1 18a^1$ level was found to occur faster in toluene-H_8 than in toluene-D_3, even though the vibrational motion was initially localised in the benzene ring and not in the methyl group. This observation strongly suggests that the doorway state does involve motion of the methyl group, and is more strongly coupled to the bright state in the non-deuterated case.

10.3. Future directions

The results summarised above provide a proof of concept for the use of nano- and picosecond photoelectron spectroscopy in studies of intramolecular vibrational redistribution. Time-resolved SEVI experiments can provide especially rich information about the dynamics, and in some cases allow the identification of dark states that are coupled to the initially prepared bright state. These techniques therefore show great promise for use in future investigations.

As remarked above in Section 10.2.1, one of the more surprising observations in the present work was the splitting of the frequency components in the time-resolved oscillations of the SEVI spectra *via* $6a^1$ / $10b^1 16b^1$ / $16a^2$. The proposed explanation is the incoherent excitation of two separate "torsional ladders" of vibrational eigenstates, one in the torsional ground state ($m = 0$) and the other with $m = 1$, in which the eigenstate spacings are slightly different. However, at present the evidence for this is indirect. By changing the backing gas and / or the backing pressure, it should be possible to alter the rotational temperature of the molecular beam. If the torsional ladder molecule is correct, then the resulting change in the relative populations of the $m = 0$ and $m = 1$ torsional levels should affect the relative amplitudes of the two frequency components associated with each eigenstate spacing. More complicated quantum beat patterns may emerge as the $m = 3$ and higher torsional levels become significantly populated at warmer temperatures. Similar temperature dependence studies could also prove illuminating for further investigation of the IVR dynamics from 13^1 and $6b^1 18a^1$, both of which are likely to be coupled to torsionally-excited doorway states. In the case of 13^1, it is anticipated that a higher rotational temperature would inhibit IVR by increasing the relative population of the $m = 1$ torsional level, which is prevented by symmetry from coupling to the proposed doorway states.

More general insights could be gained by comparing the IVR dynamics of analogous vibrational states across families of related molecules. One interesting group for further study would be the three isomers of fluorotoluene (*ortho*, *meta* and *para*). Chemical timing experiments by Timbers, Parmenter and Moss [23] have shown that, following excitation of a C−F stretching mode in the S_1 electronic state, IVR proceeds approximately twelve times faster in the *meta* isomer than in the *para* isomer. These authors point out that the lower symmetry of *meta*-fluorotoluene leads to an approximate doubling of the density of states available for anharmonic coupling to the bright state, but this is not sufficient in itself to explain the order-of-magnitude increase in the IVR rate. They therefore hypothesise that increased torsion-vibration and torsion-rotation couplings may also

play a part. In order to test these ideas, it will be necessary in future work to examine how the IVR rate depends upon the mode excited in these molecules, and also to perform comparisons with the *ortho* isomer. Picosecond time-resolved studies of IVR dynamics in the S_1 electronic state of *para*-fluorotoluene are already underway. Very recently, Davies and Reid [128] have used time-resolved SEVI to observe intermediate IVR following the excitation of S_1 $18a^1$ in this molecule and to identify two doorway states which are coupled to it.

In the longer term, once a fuller understanding has been achieved of the role of the methyl group in promoting IVR, it would be interesting to investigate systems containing multiple rotors. A comparison of the IVR dynamics in the three isomers of xylene (dimethylbenzene) could give an insight into the effect of interactions between the rotors, which would be strong in the *ortho* isomer but essentially absent in the *para* isomer. Another option is to replace the methyl group with an isopropyl ($CH(CH_3)_2$) or tertiary butyl ($C(CH_3)_3$) group, which would increase the number of torsional degrees of freedom whilst retaining a structure closely analogous to that of toluene.

As so often happens in science, each new discovery in the field of IVR dynamics raises further questions and suggests more avenues of investigation. This work represents an incremental step along the road to an understanding of vibrational redistribution, but the journey ahead remains a long one. Whilst we cannot predict where it will ultimately take us, the one certainty is that there are many more intriguing phenomena waiting to be uncovered.

Part IV.

Appendices

A. Normal modes of toluene

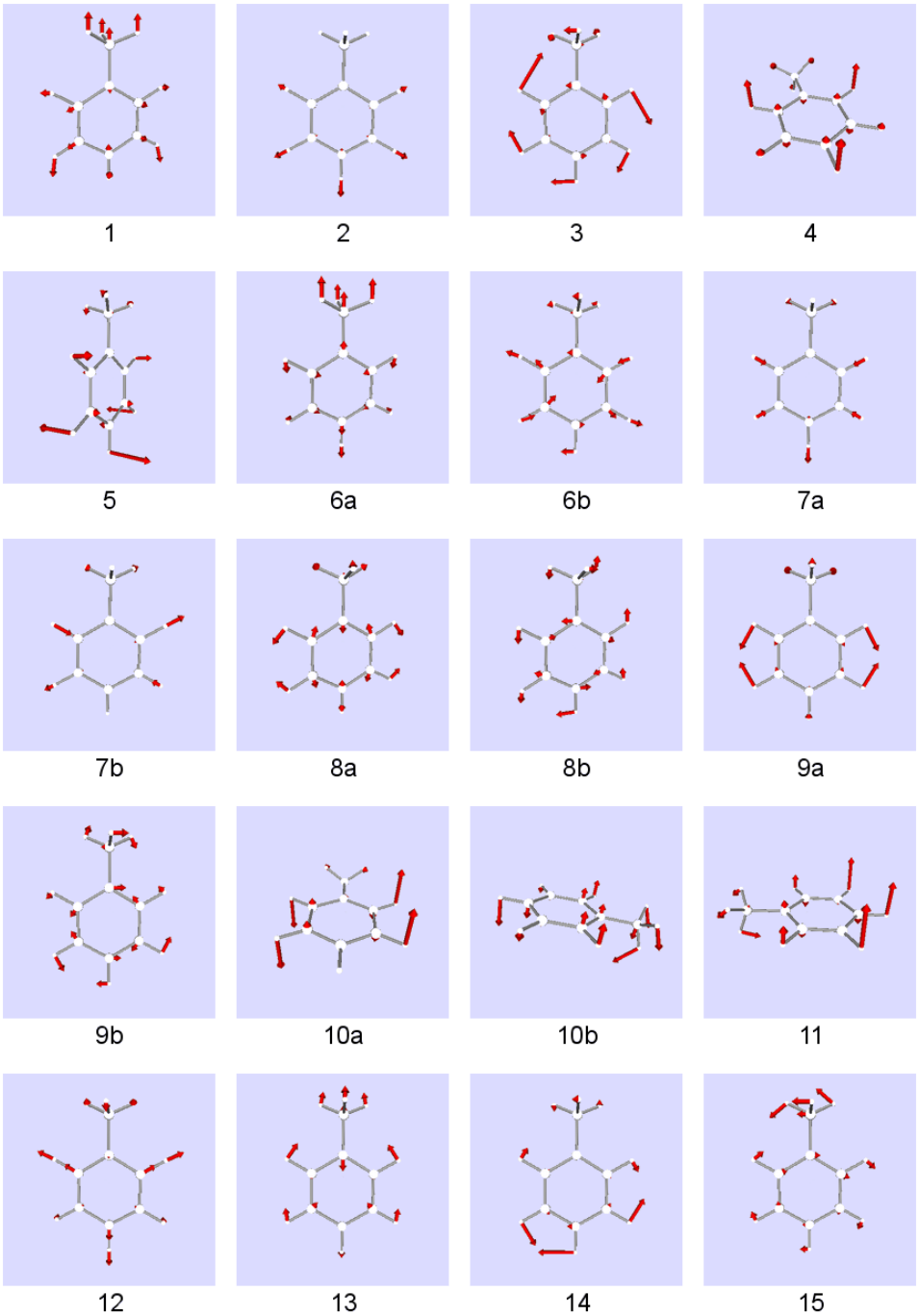

Fig. A.1. Normal modes of toluene in the S_0 electronic state (part 1)

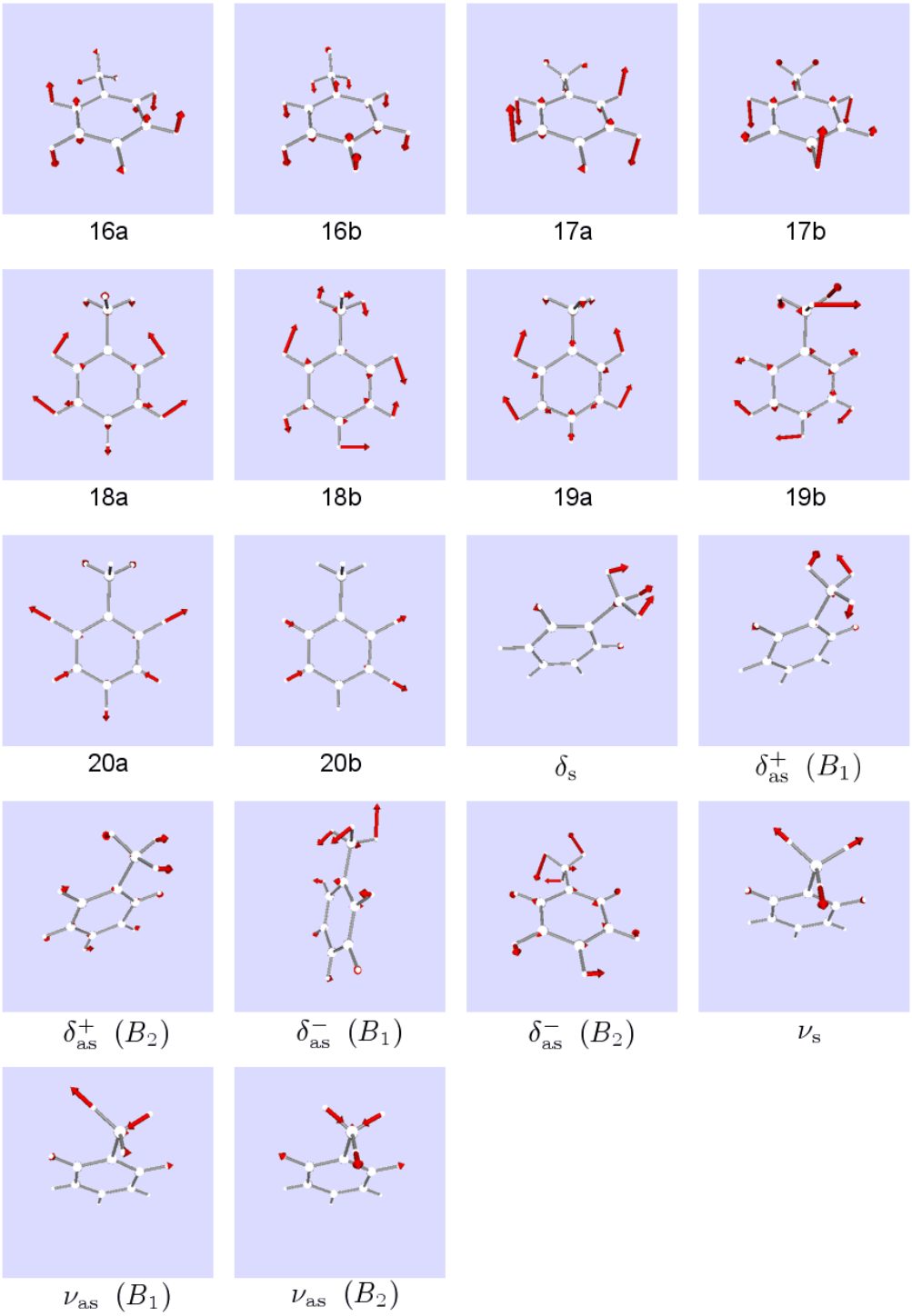

Fig. A.2. Normal modes of toluene in the S_0 electronic state (part 2)

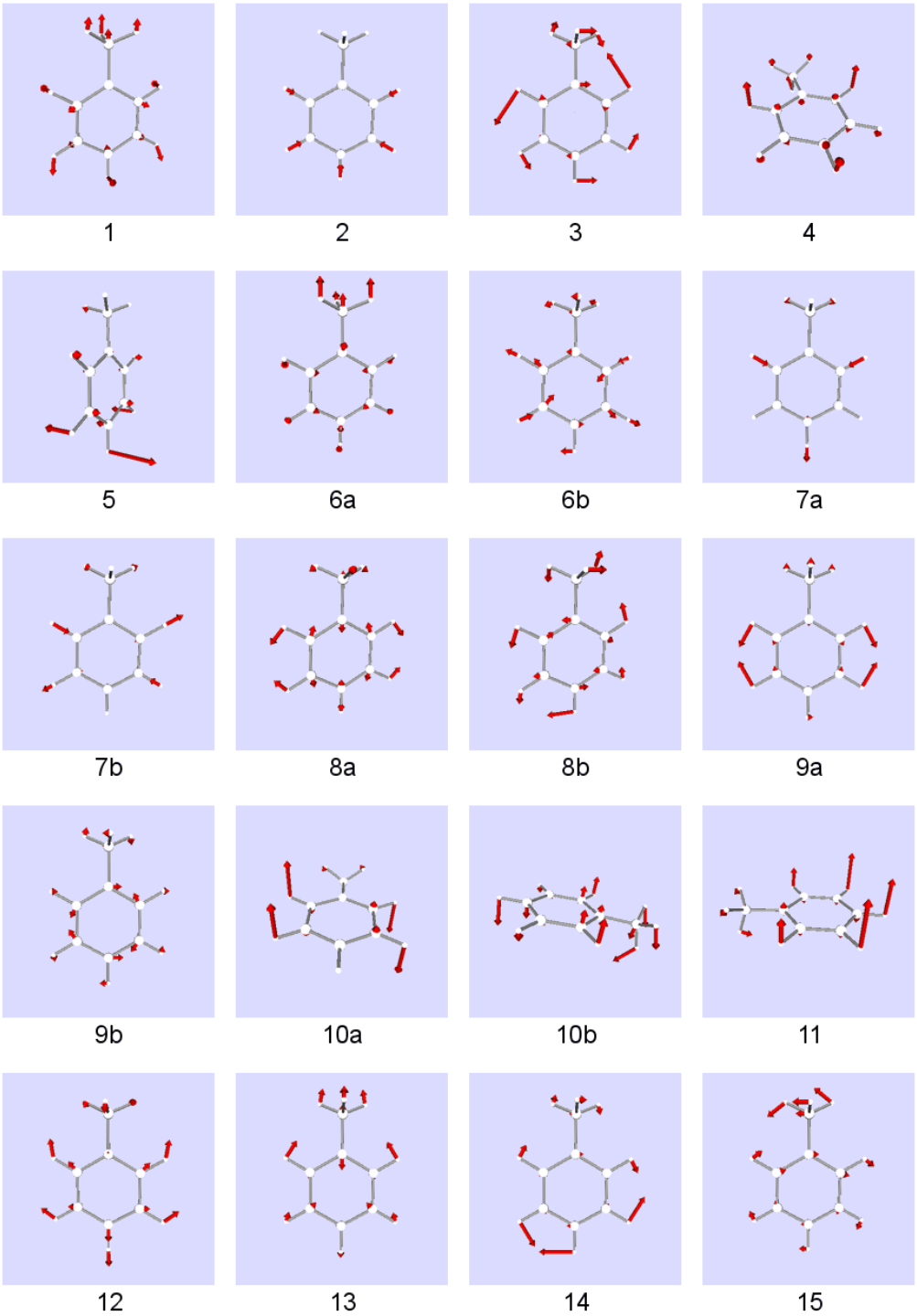

Fig. A.3. Normal modes of toluene in the S_1 electronic state (part 1)

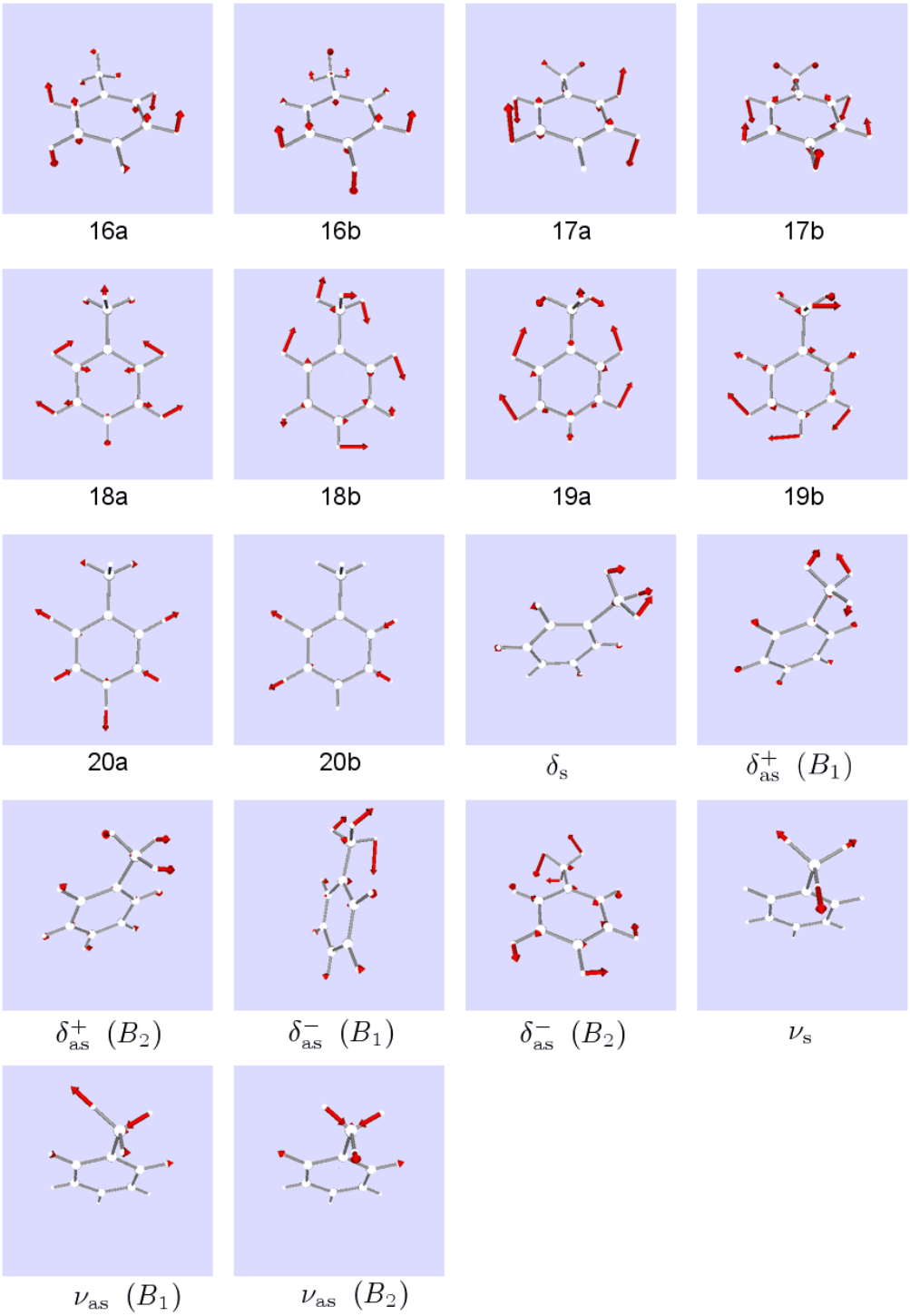

Fig. A.4. Normal modes of toluene in the S_1 electronic state (part 2)

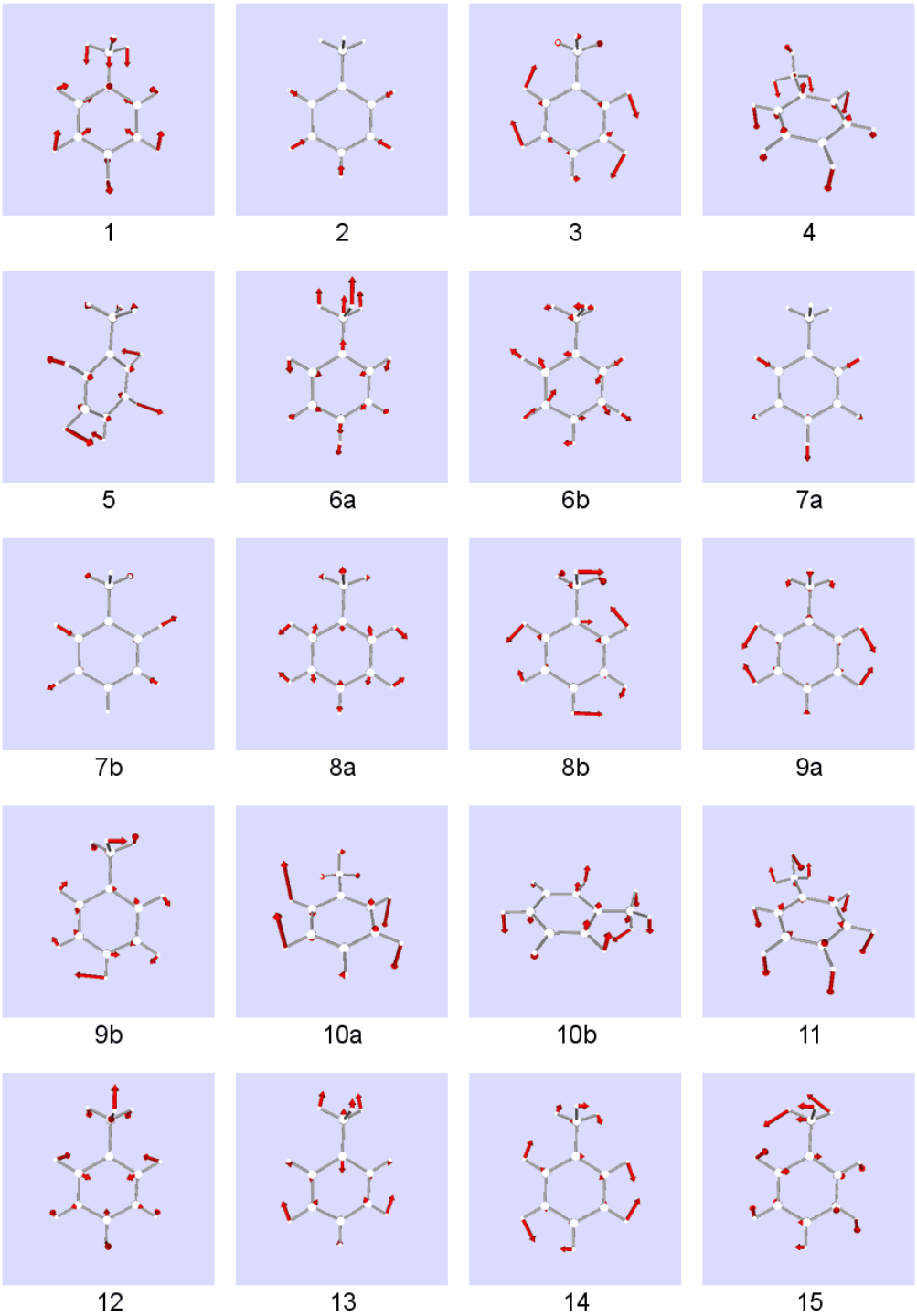

Fig. A.5. Normal modes of the toluene cation (part 1)

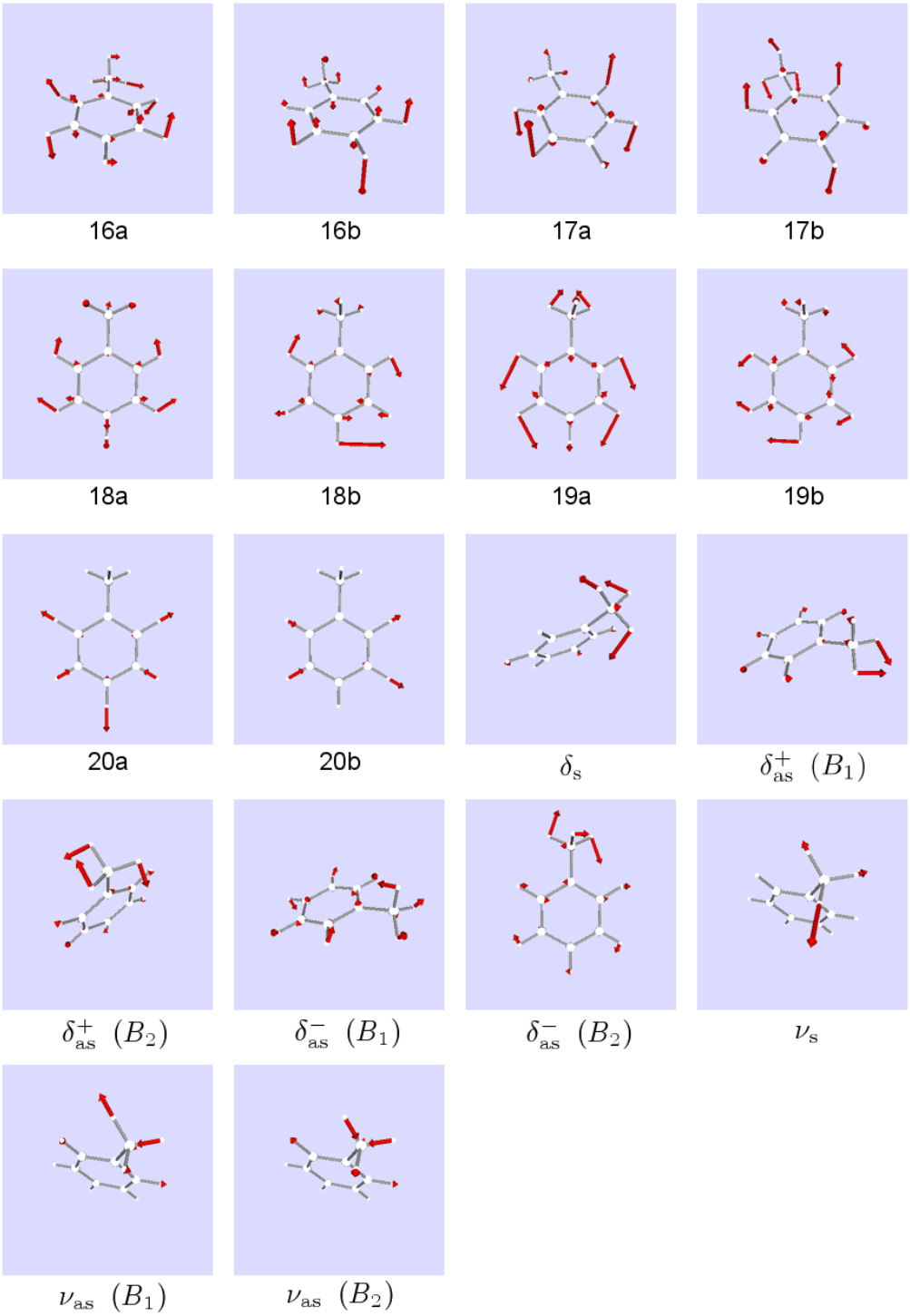

Fig. A.6. Normal modes of the toluene cation (part 2)

B. Normal modes of toluene-D_3

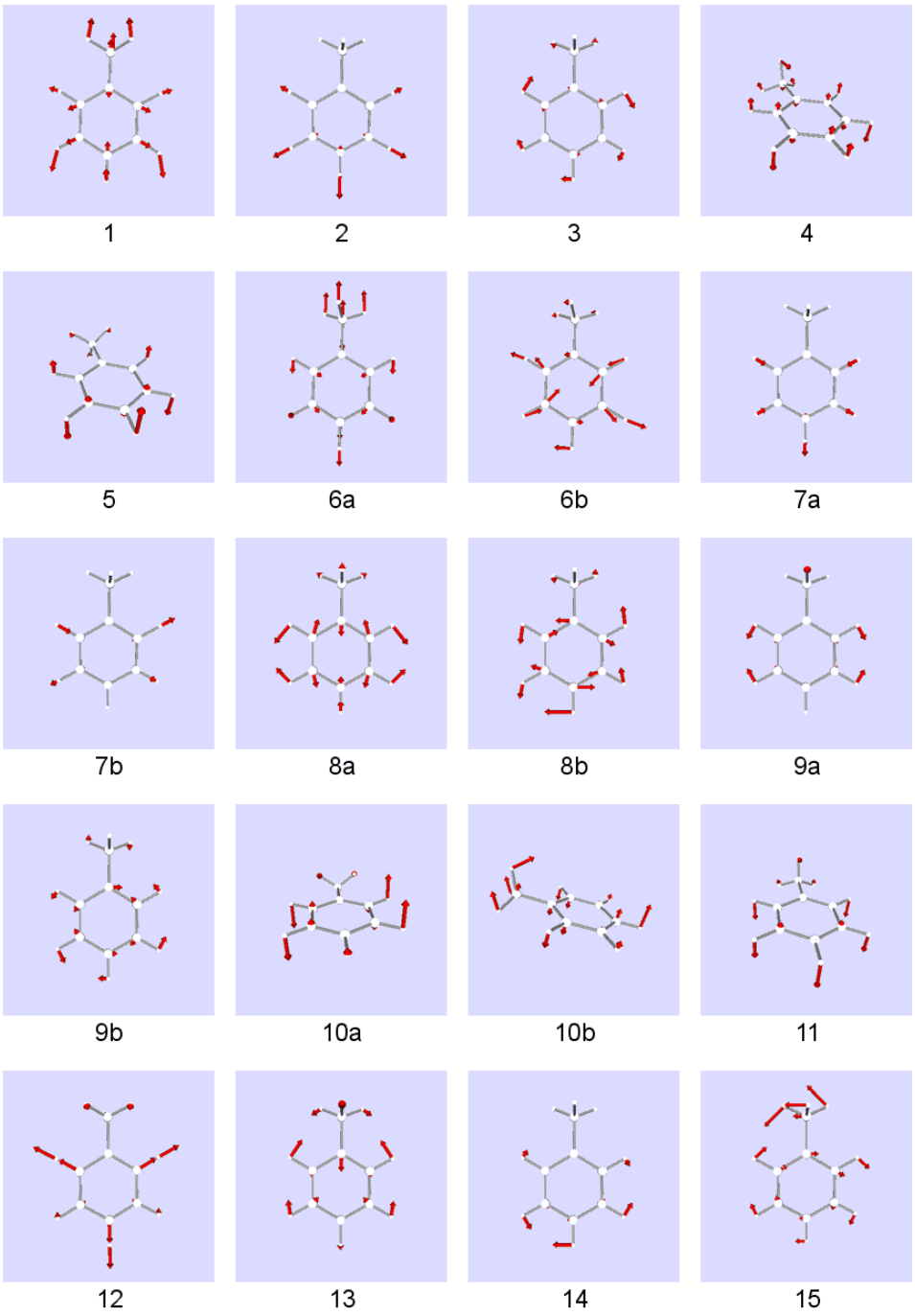

Fig. B.1. Normal modes of $C_6H_5CD_3$ in the S_0 electronic state (part 1)

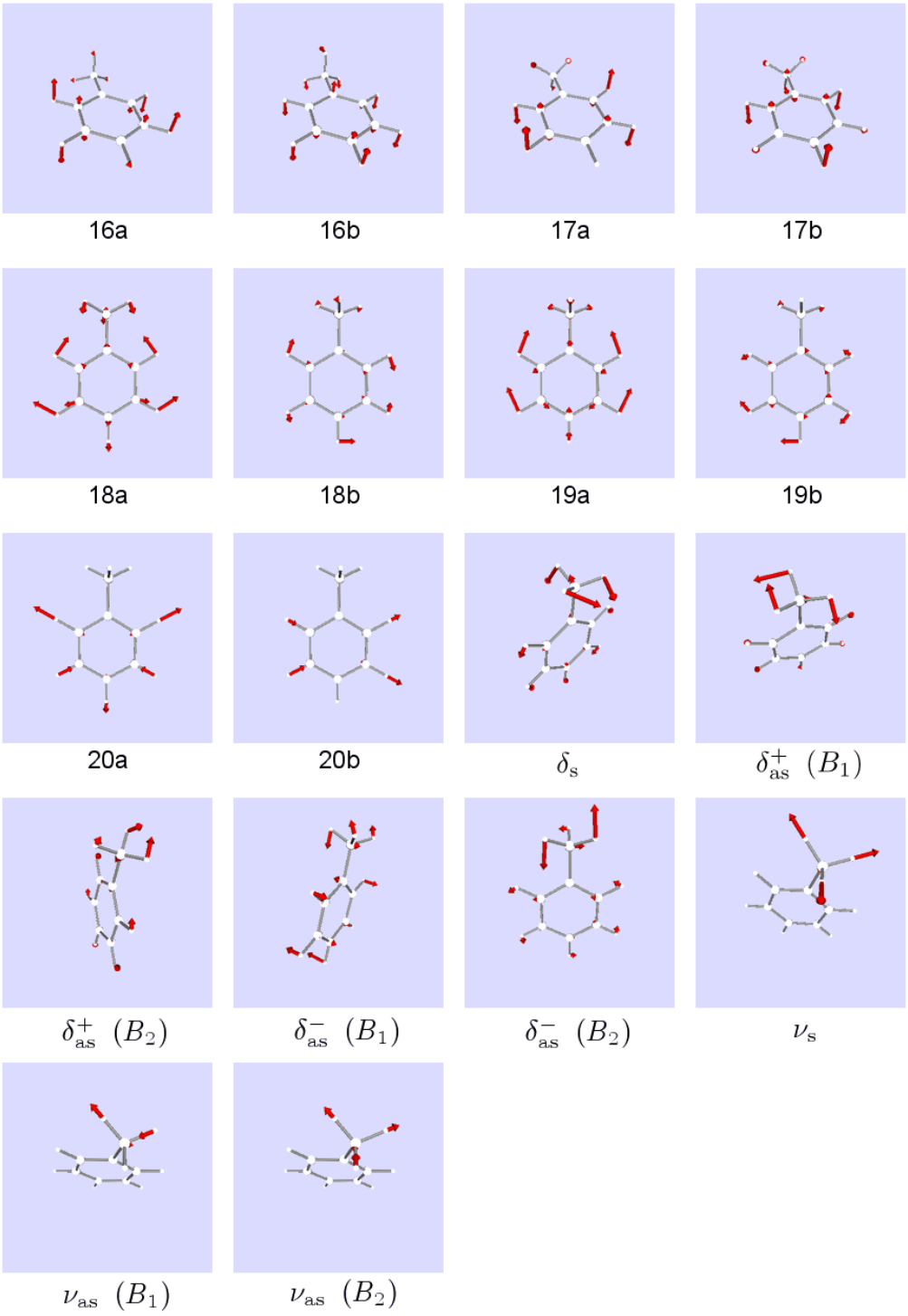

Fig. B.2. Normal modes of $C_6H_5CD_3$ in the S_0 electronic state (part 2)

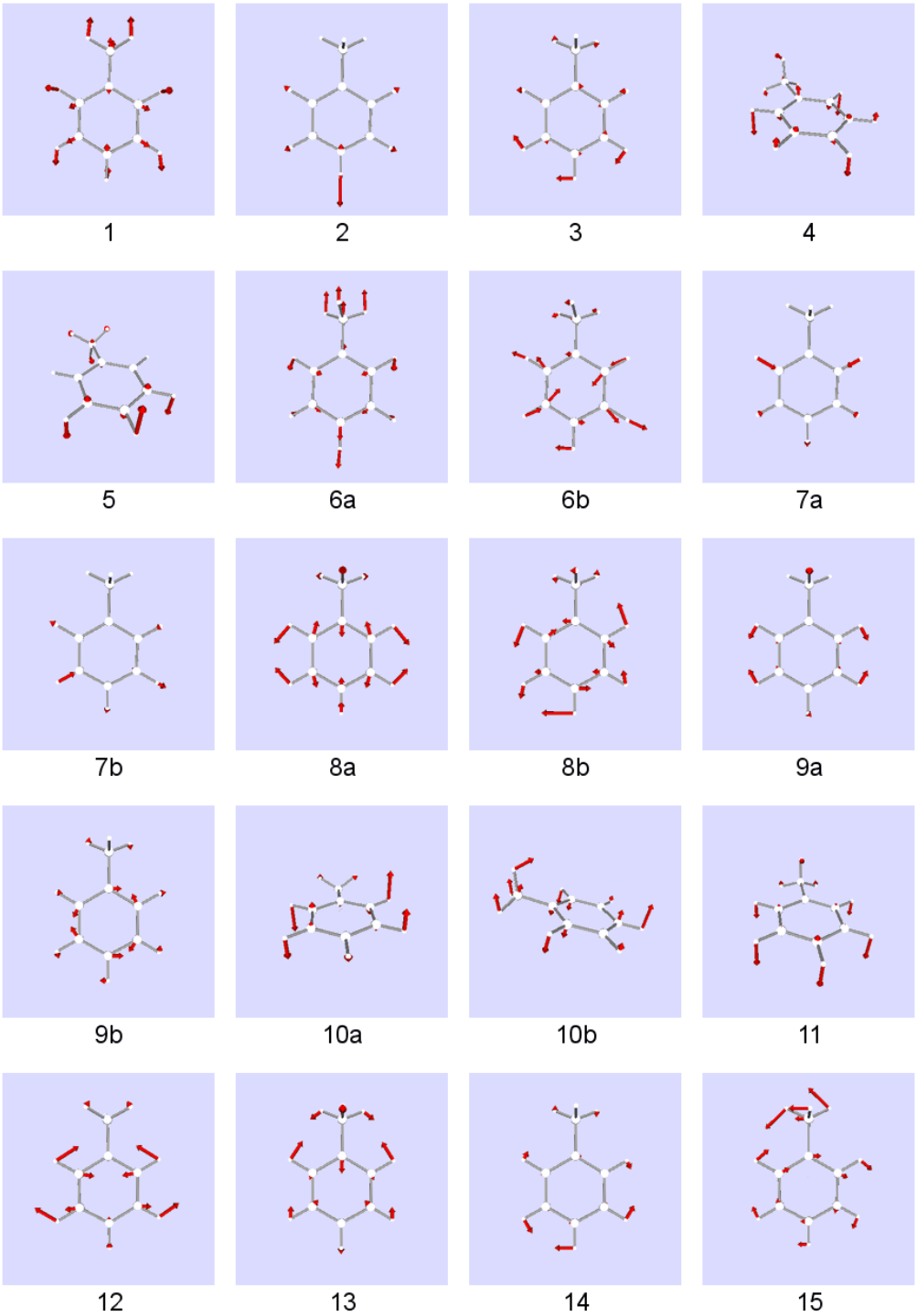

Fig. B.3. Normal modes of $C_6H_5CD_3$ in the S_1 electronic state (part 1)

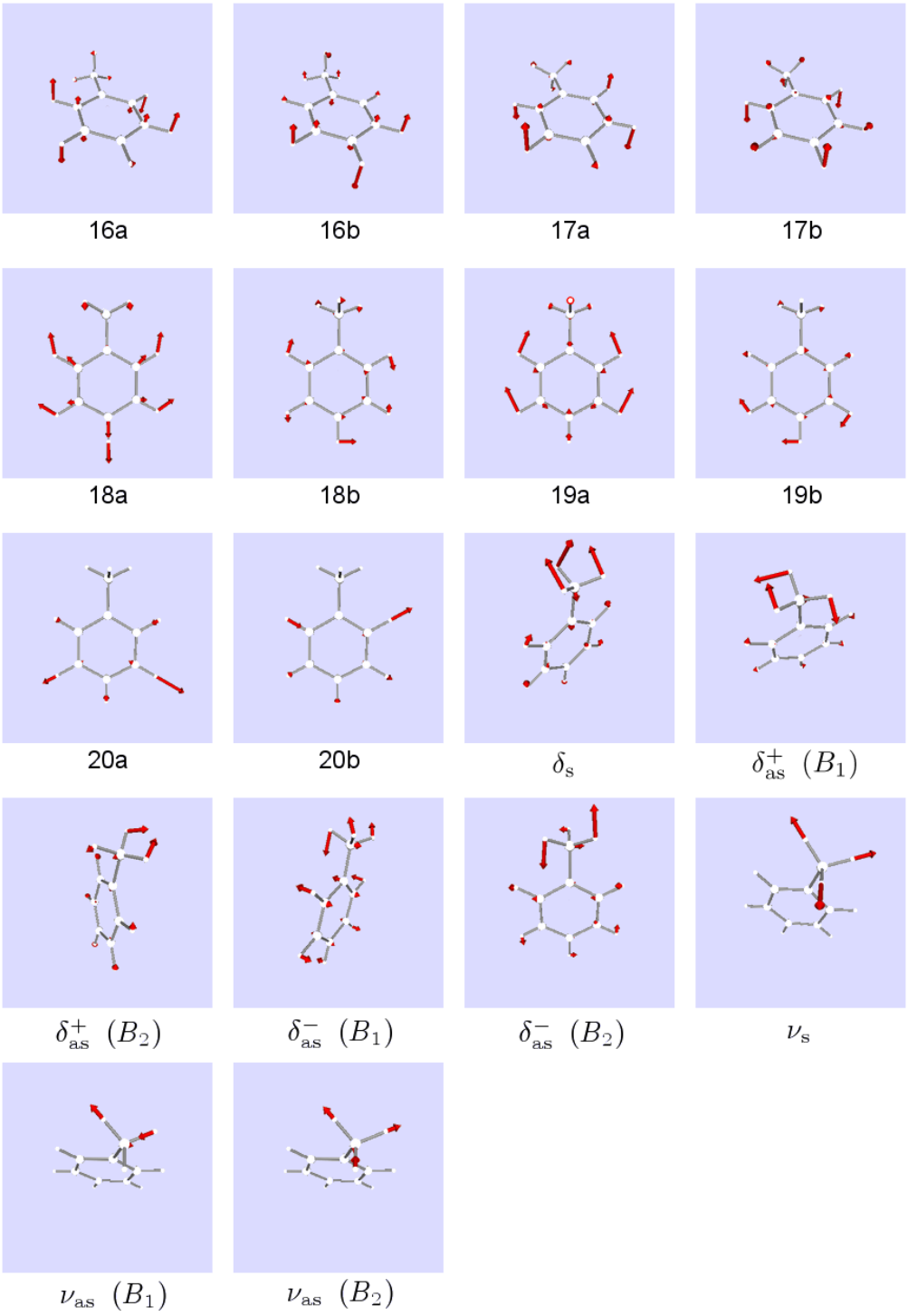

Fig. B.4. Normal modes of $C_6H_5CD_3$ in the S_1 electronic state (part 2)

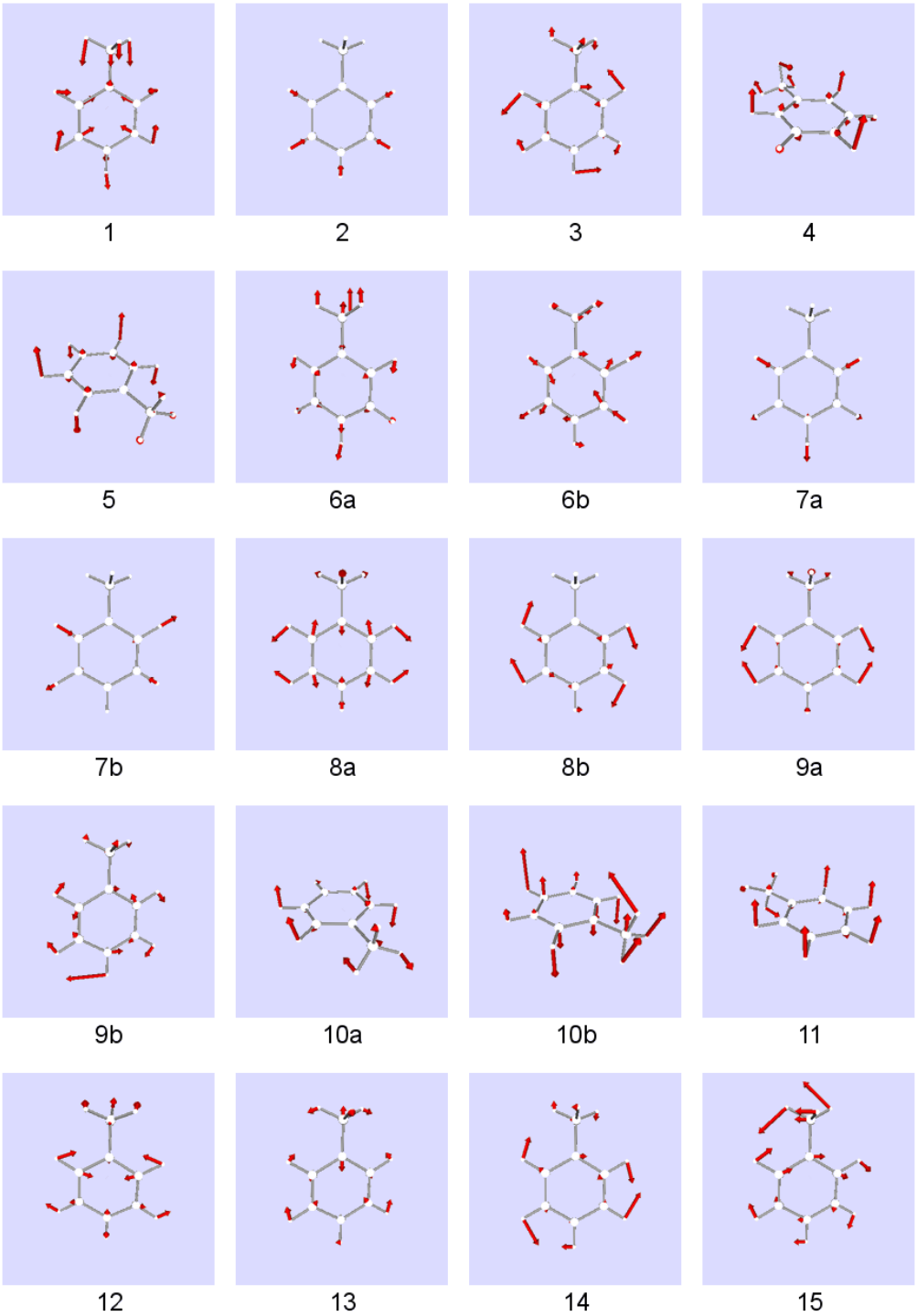

Fig. B.5. Normal modes of $C_6H_5CD_3^+$ (part 1)

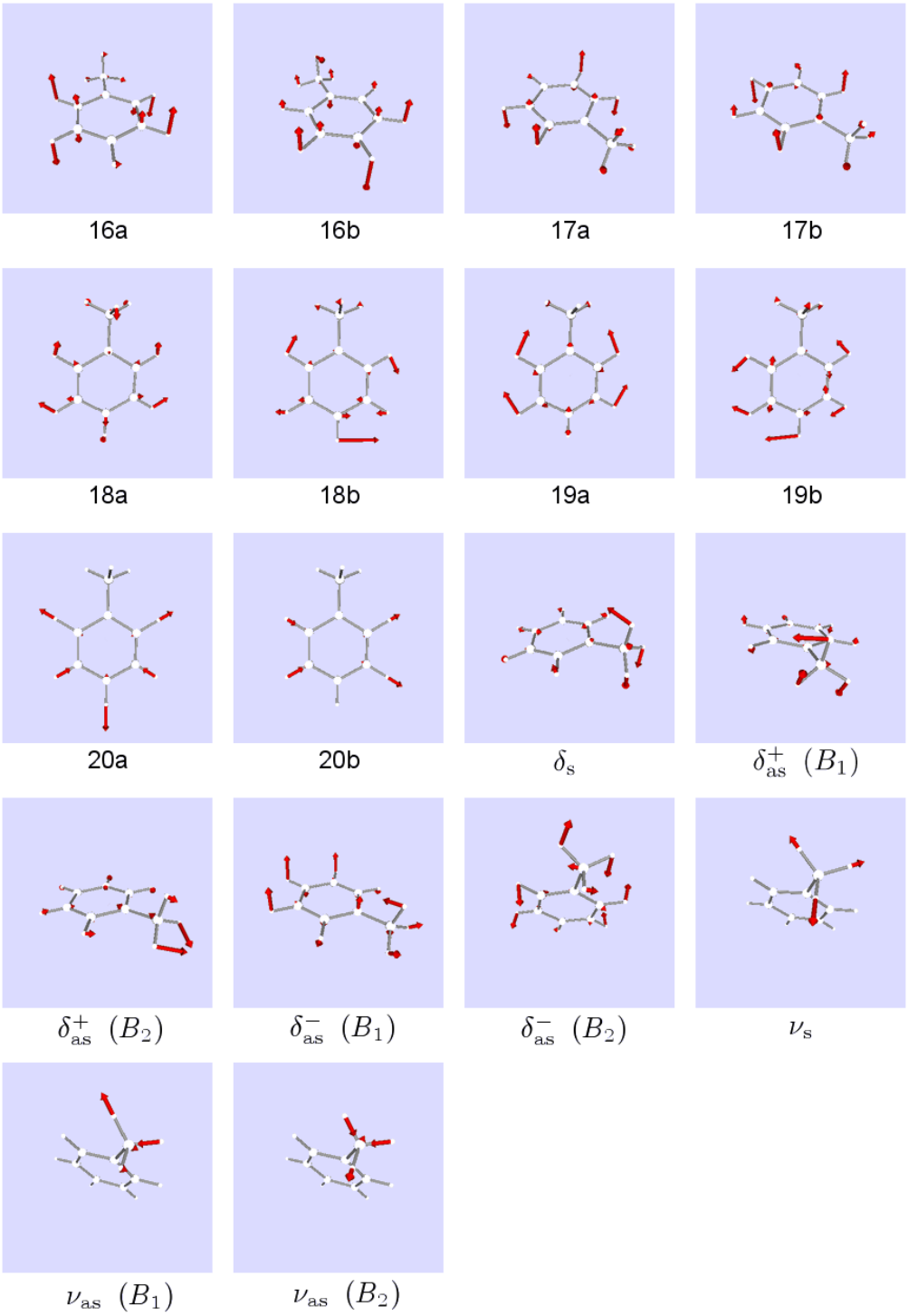

Fig. B.6. Normal modes of $C_6H_5CD_3^+$ (part 2)

Bibliography

[1] J. C. Polanyi, *Acc. Chem. Res.*, 1972, **5**, 161–168.

[2] M. Brouard, *Reaction Dynamics*, Oxford University Press, 1998.

[3] F. F. Crim, in *Tutorials in Molecular Reaction Dynamics*, ed. M. Brouard and C. Vallance, RSC Publishing, Cambridge, 2010, ch. 7, pp. 214–239.

[4] R. G. Gilbert and S. C. Smith, *Theory of unimolecular and recombination reactions*, Blackwell Scientific Publications, Oxford, 1990.

[5] T. Baer and W. L. Hase, *Unimolecular Reaction Dynamics: Theory and Experiments*, Oxford University Press, 1996.

[6] J. N. Butler and G. B. Kistiakowsky, *J. Am. Chem. Soc.*, 1960, **82**, 759–765.

[7] (*a*) J. D. Rynbrandt and B. S. Rabinovitch, *J. Chem. Phys.*, 1971, **54**, 2275–2276; (*b*) B. S. Rabinovitch and J. D. Rynbrandt, *J. Phys. Chem.*, 1971, **75**, 2164–2171.

[8] H. H. Fielding and A. D. G. Nunn, in *Tutorials in Molecular Reaction Dynamics*, ed. M. Brouard and C. Vallance, RSC Publishing, Cambridge, 2010, ch. 11, pp. 363–391.

[9] R. N. Zare, *Science*, 1998, **279**, 1875–1879.

[10] K. K. Lehmann, G. Scoles and B. H. Pate, *Annu. Rev. Phys. Chem.*, 1994, **45**, 241–274.

[11] D. Boyall and K. L. Reid, *Chem. Soc. Rev.*, 1997, **26**, 223–232.

[12] D. Nesbitt and R. Field, *Journal of Physical Chemistry*, 1996, **100**, 12735–12756.

[13] K. L. Reid, *Int. Rev. Phys. Chem.*, 2008, **37**, 607–628.

[14] P. W. Atkins and R. S. Friedman, *Molecular Quantum Mechanics*, Oxford University Press, 3rd edn., 1997.

[15] C. N. Banwell and E. M. McCash, *Fundamentals of molecular spectroscopy*, McGraw-Hill, London, 4th edn., 1994.

[16] J. C. Keske and B. H. Pate, *Annu. Rev. Phys. Chem.*, 2000, **51**, 323–353.

[17] D. R. Borst and D. W. Pratt, *J. Chem. Phys.*, 2000, **113**, 3658–3669.

[18] R. A. Coveleskie, D. A. Dolson and C. S. Parmenter, *J. Chem. Phys.*, 1980, **72**, 5774–5775.

[19] R. A. Coveleskie, D. A. Dolson and C. S. Parmenter, *J. Phys. Chem.*, 1985, **89**, 645–654.

[20] K. W. Holtzclaw and C. S. Parmenter, *J. Phys. Chem.*, 1984, **88**, 3182–3185.

[21] C. S. Parmenter and B. M. Stone, *J. Chem. Phys.*, 1986, **84**, 4710–4711.

[22] D. B. Moss and C. S. Parmenter, *J. Chem. Phys.*, 1993, **98**, 6897–6905.

[23] P. J. Timbers, C. S. Parmenter and D. B. Moss, *J. Chem. Phys.*, 1994, **100**, 1028–1034.

[24] W. R. Lambert, P. M. Felker and A. H. Zewail, *J. Chem. Phys.*, 1981, **75**, 5958–5960.

[25] A. H. Zewail, *Faraday Discuss. Chem. Soc.*, 1983, **75**, 315–330.

[26] P. M. Felker and A. H. Zewail, *Phys. Rev. Lett.*, 1984, **53**, 501–504.

[27] P. M. Felker and A. H. Zewail, *J. Chem. Phys.*, 1985, **82**, 2961–2974.

[28] P. M. Felker and A. H. Zewail, *J. Chem. Phys.*, 1985, **82**, 2975–2993.

[29] P. M. Felker and A. H. Zewail, *J. Chem. Phys.*, 1985, **82**, 2994–3002.

[30] P. M. Felker, W. R. Lambert and A. H. Zewail, *J. Chem. Phys.*, 1985, **82**, 3003–3010.

[31] P. M. Felker and A. H. Zewail, *Adv. Chem. Phys.*, 1988, **70**, 265–364.

[32] P. M. Felker and A. H. Zewail, in *Jet Spectroscopy and Molecular Dynamics*, ed. J. M. Hollas and D. Phillips, Blackie, Glasgow, 1995, ch. 7, pp. 222–308.

[33] J. S. Baskin, T. S. Rose and A. H. Zewail, *J. Chem. Phys.*, 1988, **88**, 1458–1459.

[34] M. J. Côté, J. F. Kauffman, P. G. Smith and J. D. McDonald, *J. Chem. Phys.*, 1989, **90**, 2865–2873.

[35] J. F. Kauffman, M. J. Côté, P. G. Smith and J. D. McDonald, *J. Chem. Phys.*, 1989, **90**, 2874–2891.

[36] (*a*) P. G. Smith and J. D. McDonald, *J. Chem. Phys.*, 1990, **92**, 1004–1014; (*b*) P. G. Smith and J. D. McDonald, *J. Chem. Phys.*, 1990, **92**, 6337–6337.

[37] P. G. Smith and J. D. McDonald, *J. Chem. Phys.*, 1990, **93**, 6350–6356.

[38] Y. Yamada, Y. Katsumoto and T. Ebata, *Phys. Chem. Chem. Phys.*, 2007, **9**, 1170–1185.

[39] A. Stolow, *Annu. Rev. Phys. Chem.*, 2003, **54**, 89–119.

[40] A. Stolow, A. E. Bragg and D. M. Neumark, *Chem. Rev.*, 2004, **104**, 1719–1758.

[41] T. Suzuki, *Annu. Rev. Phys. Chem.*, 2006, **57**, 555–592.

[42] X. Song, C. W. Wilkerson, J. Lucia, S. Pauls and J. P. Reilly, *Chem. Phys. Lett.*, 1990, **174**, 377 – 384.

[43] J. M. Smith, C. Lakshminarayan and J. L. Knee, *J. Chem. Phys.*, 1990, **93**, 4475–4476.

[44] J. L. Knee, in *High resolution laser photoionization and photoelectron studies*, ed. T. Baer, C.-Y. Ng and I. Powis, Wiley, Chichester, 1995, ch. 10, pp. 369–406.

[45] J. M. Smith, X. Zhang and J. L. Knee, *Proceedings of SPIE*, 1993, **1858**, 217–225.

[46] J. Smith, X. Zhang and J. Knee, *J. Chem. Phys.*, 1993, **99**, 2550–2559.

[47] X. Zhang and J. Knee, *Faraday Discussions*, 1994, **97**, 299–313.

[48] X. Zhang, J. Smith and J. Knee, *J. Chem. Phys.*, 1994, **100**, 2429–2436.

[49] J. Smith, X. Zhang and J. Knee, *J. Phys. Chem.*, 1995, **99**, 1768–1775.

[50] J. A. Davies, K. L. Reid, M. Towrie and P. Matousek, *J. Chem. Phys.*, 2002, **117**, 9099–9102.

[51] D. Dolson, C. Parmenter and B. Stone, *Chem. Phys. Lett.*, 1981, **81**, 360 – 364.

[52] P. T. Whiteside, A. K. King, J. A. Davies, K. L. Reid, M. Towrie and P. Matousek, *J. Chem. Phys.*, 2005, **123**, 204317.

[53] P. T. Whiteside, *Ph.D. thesis*, University of Nottingham, 2005.

[54] A. T. J. B. Eppink and D. H. Parker, *Rev. Sci. Instrum.*, 1997, **68**, 3477–3484.

[55] K. L. Reid, *Annu. Rev. Phys. Chem.*, 2003, **54**, 397–424.

[56] A. K. King, S. M. Bellm, C. J. Hammond, K. L. Reid, M. Towrie and P. Matousek, *Molecular Physics*, 2005, **103**, 1821–1827.

[57] C. J. Hammond, K. L. Reid and K. L. Ronayne, *J. Chem. Phys.*, 2006, **124**, 201102.

[58] C. J. Hammond, *Ph.D. thesis*, University of Nottingham, 2008.

[59] A. Osterwalder, M. J. Nee, J. Zhou and D. M. Neumark, *J. Chem. Phys.*, 2004, **121**, 6317–6322.

[60] C. J. Hammond and K. L. Reid, *Phys. Chem. Chem. Phys.*, 2008, **10**, 6762–6769.

[61] J. A. Davies, A. M. Green and K. L. Reid, *Phys. Chem. Chem. Phys.*, 2010, **12**, 9872–9883.

[62] R. S. Mulliken, *J. Chem. Phys.*, 1955, **23**, 1997–2011.

[63] C. G. Hickman, J. R. Gascooke and W. D. Lawrance, *J. Chem. Phys.*, 1996, **104**, 4887–4901.

[64] E. B. Wilson, Jr., *Physical Review*, 1934, **45**, 706–714.

[65] G. Varsányi, *Assignments for vibrational spectra of seven hundred benzene derivatives*, Adam Hilger, London, 1974.

[66] G. Herzberg, *Molecular Spectra and Molecular Structure*, Krieger, Malabar, Florida, 2nd edn., 1991, vol. 2.

[67] P. W. Atkins, M. S. Child and C. S. G. Phillips, *Tables for Group Theory*, Oxford University Press, 1970.

[68] W. D. Lawrance and A. E. W. Knight, *J. Phys. Chem.*, 1988, **92**, 5900–5908.

[69] F. Duschinsky, *Acta Physico-Chimica URSS*, 1937, **7**, 551–566.

[70] İ. Özkan, *J. Mol. Spectrosc.*, 1990, **139**, 147–162.

[71] T. G. Dietz, M. A. Duncan and R. E. Smalley, *J. Chem. Phys.*, 1982, **76**, 1227–1232.

[72] M. Bixon and J. Jortner, *J. Chem. Phys.*, 1968, **48**, 715–726.

[73] A. A. Stuchebrukhov and R. A. Marcus, *J. Chem. Phys.*, 1993, **98**, 6044–6061.

[74] D. B. Moss, C. S. Parmenter and G. E. Ewing, *J. Chem. Phys.*, 1987, **86**, 51–61.

[75] R. J. Longfellow and C. S. Parmenter, *J. Chem. Soc. Faraday Trans. 2*, 1988, **84**, 1499–1510.

[76] Z.-Q. Zhao, C. S. Parmenter, D. B. Moss, A. J. Bradley, A. E. W. Knight and K. G. Owens, *J. Chem. Phys.*, 1992, **96**, 6362–6377.

[77] P. J. Breen, J. A. Warren, E. R. Bernstein and J. I. Seeman, *J. Chem. Phys.*, 1987, **87**, 1917–1926.

[78] H. D. Rudolph, H. Dreizler, A. Jaeschke, and P. Wendling, *Zeitschrift für Naturforschung A*, 1967, **22**, 940.

[79] J. D. Lewis, T. B. Malloy, Jr., T. H. Chao and J. Laane, *J. Mol. Struct.*, 1972, **12**, 427–449.

[80] P. R. Bunker and P. Jensen, *Molecular symmetry and spectroscopy*, NRC Research Press, Ottawa, Ontario, Canada, 2nd edn., 1998.

[81] Z.-Q. Zhao, *Ph.D. thesis*, Indiana University, 1992.

[82] K.-T. Lu, G. C. Eiden, J. K. Badenhoop, F. A. Weinhold and J. C. Weisshaar, in *High resolution laser photoionization and photoelectron studies*, ed. T. Baer, C.-Y. Ng and I. Powis, Wiley, Chichester, 1995, ch. 9, pp. 331–367.

[83] National Instruments Corporation, Austin, TX, USA, *LabVIEW 8.5*, 2007.

[84] D. H. Parker and A. T. J. B. Eppink, in *Imaging in molecular dynamics: Technology and applications*, ed. B. Whitaker, Cambridge University Press, 2003, ch. 2, pp. 20–64.

[85] D. W. Chandler and P. L. Houston, *J. Chem. Phys.*, 1987, **87**, 1445–1447.

[86] S. M. Bellm and K. L. Reid, *Chemical Physics Letters*, 2004, **395**, 253 – 258.

[87] R. J. Hanisch, A. Farris, E. W. Greisen, W. D. Pence, B. M. Schlesinger, P. J. Teuben, R. W. Thompson and A. Warnock III, *Astronomy & Astrophysics*, 2001, **376**, 359–380.

[88] NASA, *The FITS Support Office*, `http://fits.gsfc.nasa.gov/`.

[89] A. T. J. B. Eppink, S.-M. Wu and B. J. Whitaker, in *Imaging in molecular dynamics: Technology and applications*, ed. B. Whitaker, Cambridge University Press, 2003, ch. 3, pp. 65–112.

[90] G. A. Garcia, L. Nahon and I. Powis, *Rev. Sci. Instrum.*, 2004, **75**, 4989–4996.

[91] The MathWorks, Inc., Natick, Massachusetts, *MATLAB 7.6.0.324*, 2008.

[92] K. T. Lu, G. C. Eiden and J. C. Weisshaar, *J. Phys. Chem.*, 1992, **96**, 9742–9748.

[93] W. D. Pence, *CFITSIO 3.09*, 2008, `http://heasarc.gsfc.nasa.gov/docs/software/fitsio/`.

[94] A. R. Weeks, Jr., *Fundamentals of electronic image processing*, IEEE Press, 1996.

[95] E. W. Schlag, *ZEKE Spectroscopy*, Cambridge University Press, 1998.

[96] C. J. Hammond, V. L. Ayles, D. E. Bergeron, K. L. Reid and T. G. Wright, *J. Chem. Phys.*, 2006, **125**, 124308.

[97] V. L. Ayles, C. J. Hammond, D. E. Bergeron, O. J. Richards and T. G. Wright, *J. Chem. Phys.*, 2007, **126**, 244304.

[98] V. L. Ayles, *Ph.D. thesis*, University of Nottingham, 2008.

[99] S. D. Gamblin, S. E. Daire, J. Lozeille and T. G. Wright, *Chemical Physics Letters*, 2000, **325**, 232 – 240.

[100] M. J. Frisch, G. W. Trucks, H. B. Schlegel, G. E. Scuseria, M. A. Robb, J. R. Cheeseman, G. Scalmani, V. Barone, B. Mennucci, G. A. Petersson, H. Nakatsuji, M. Caricato, X. Li, H. P. Hratchian, A. F. Izmaylov, J. Bloino, G. Zheng, J. L. Sonnenberg, M. Hada, M. Ehara, K. Toyota, R. Fukuda, J. Hasegawa, M. Ishida, T. Nakajima, Y. Honda, O. Kitao, H. Nakai, T. Vreven, J. A. Montgomery, Jr., J. E. Peralta, F. Ogliaro, M. Bearpark, J. J. Heyd, E. Brothers, K. N. Kudin, V. N. Staroverov, R. Kobayashi, J. Normand, K. Raghavachari, A. Rendell, J. C. Burant, S. S. Iyengar, J. Tomasi, M. Cossi, N. Rega, J. M. Millam, M. Klene, J. E. Knox, J. B. Cross, V. Bakken, C. Adamo, J. Jaramillo, R. Gomperts, R. E. Stratmann, O. Yazyev, A. J. Austin, R. Cammi, C. Pomelli, J. W. Ochterski, R. L. Martin, K. Morokuma, V. G. Zakrzewski, G. A. Voth, P. Salvador, J. J. Dannenberg, S. Dapprich, A. D. Daniels, . Farkas, J. B. Foresman, J. V. Ortiz, J. Cioslowski and D. J. Fox, *Gaussian 09 Revision A.1*, 2009, Gaussian Inc., Wallingford, CT.

[101] *National Service for Computational Chemistry Software*, `http://www.nsccs.ac.uk/`.

[102] K. S. Pitzer and D. W. Scott, *J. Am. Chem. Soc.*, 1943, **65**, 803.

[103] N. Fuson, C. Garrigou-Lagrange and M. L. Josien, *Spectrochimica Acta*, 1960, **16**, 106.

[104] L. M. Sverdlov, M. A. Kovner and E. P. Krainov, *Vibrational spectra of polyatomic molecules*, Wiley, New York, 1973.

[105] C. J. Cramer, *Essentials of Computational Chemistry: Theories and Models*, Wiley, Chichester, 2nd edn., 2004.

[106] J. P. Merrick, D. Moran and L. Radom, *J. Phys. Chem. A*, 2007, **111**, 11683–11700.

[107] F.-t. Chau, J. M. Dyke, E. P.-f. Lee and D.-c. Wang, *Journal of Electron Spectroscopy and Related Phenomena*, 1998, **97**, 33–47.

[108] All Franck–Condon simulations have been carried out using FC-LabII Version 2009.a, a computational package developed by C. Schriever, M.C.R. Cockett and I. Pugliesi. The latest information on program updates, a basic introduction to Franck–Condon simulations and a free download of the software can be found at `http://www.fclab2.net/`.

[109] I. Pugliesi and K. Müller-Dethlefs, *J. Phys. Chem. A*, 2006, **110**, 4657–4667.

[110] T. Beyer and D. Swinehart, *Communications of the Association for Computing Machinery*, 1973, **16**, 379.

[111] S. E. Stein and B. S. Rabinovitch, *J. Chem. Phys.*, 1973, **58**, 2438–2445.

[112] (*a*) J. R. Barker, N. F. Ortiz, J. M. Preses, L. L. Lohr, A. Maranzana, P. J. Stimac, T. L. Nguyen and T. J. D. Kumar, *MultiWell-2011 Software*, University of Michigan, Ann Arbor, MI, 2011, `http://aoss.engin.umich.edu/multiwell/`; (*b*) J. R. Barker, *Int. J. Chem. Kinetics*, 2001, **33**, 232–245; (*c*) J. R. Barker, *Int. J. Chem. Kinetics*, 2009, **41**, 748–763.

[113] M. J. H. Kemper, J. M. F. Van Dijk and H. M. Buck, *Chem. Phys. Lett.*, 1978, **53**, 121–124.

[114] J. K. Wilmshurst and H. J. Bernstein, *Can. J. Chem.*, 1957, **35**, 911.

[115] C. La Lau and R. G. Snyder, *Spectrochimica Acta*, 1971, **27A**, 2073.

[116] A. M. Bogomolov, *Optical Spectroscopy*, 1960, **9**, 162.

[117] J. A. Draeger, *Spectrochimica Acta*, 1985, **41A**, 607.

[118] M. Tasumi, T. Urano and M. Nakata, *J. Mol. Struct.*, 1986, **146**, 383.

[119] W. J. Balfour and Y. Fried, *Canadian Journal of Physics*, 1994, **72**, 1218–1224.

[120] W. J. Balfour and R. S. Ram, *Canadian Journal of Physics*, 1994, **72**, 1225–1235.

[121] J. T. Meek, S. R. Long and J. P. Reilly, *J. Phys. Chem.*, 1982, **86**, 2809–2811.

[122] P. T. Whiteside, A. K. King and K. L. Reid, *J. Chem. Phys.*, 2005, **123**, 204316.

[123] F. Gunzer and J. Grotemeyer, *Phys. Chem. Chem. Phys.*, 2002, **4**, 5966–5972.

[124] A. M. Gardner, A. M. Green, J. A. Davies, K. L. Reid and T. G. Wright, In preparation.

[125] R. W. Ramirez, *The FFT: Fundamentals and Concepts*, Prentice-Hall, Englewood Cliffs, NJ, 1985.

[126] (*a*) M. Frigo and S. G. Johnson, *The Fastest Fourier Transform in the West*, `http://www.fftw.org/`; (*b*) M. Frigo and S. G. Johnson, *Proceedings of the IEEE*, 2005, **93**, 216–231.

[127] R. J. Doyle, E. S. J. Love, R. Da Campo and S. R. Mackenzie, *J. Chem. Phys.*, 2005, **122**, 194315.

[128] J. A. Davies and K. L. Reid, Accepted by *J. Chem. Phys.*, 2011.